NUREG/CR–6288

Geochemical Investigations Related to the Yucca Mountain Environment and Potential Nuclear Waste Repository

Manuscript Completed: September 1994
Date Published: November 1994

Prepared by
W. M. Murphy, R. T. Pabalan

Southwest Research Institute
Center for Nuclear Waste Regulatory Analyses
6220 Culebra Road
San Antonio, TX 78228–0510

Prepared for
Division of Regulatory Applications
Office of Nuclear Regulatory Research
U.S. Nuclear Regulatory Commission
Washington, DC 20555–0001
NRC JCN B6666

DISCLAIMER

ABSTRACT

This report presents final results of the Geochemistry Research Project conducted at the Center for Nuclear Waste Regulatory Analyses (CNWRA) for the Nuclear Regulatory Commission (NRC) Office of Nuclear Regulatory Research. The study focused on experimental determinations and theoretical interpretations of fundamental thermodynamic and kinetic properties of minerals and reactions that characterize geochemical processes at the proposed nuclear waste repository site at Yucca Mountain and that could affect the capacity of the site to isolate nuclear waste. Technical results are presented in three major sections covering (i) cation exchange studies on clinoptilolite, (ii) kinetic and solubility studies on analcime and Na-clinoptilolite, and (iii) conceptual and numerical geochemical modeling of natural and repository systems. Experimental studies were designed to advance knowledge of the fundamental properties of the zeolite minerals clinoptilolite and analcime through controlled tests at 25 °C, and to interpret the data in the context of the geochemical system at Yucca Mountain. Cation exchange equilibria were determined for clinoptilolite and binary solutions of Na^+ with K^+, Ca^{2+}, and Sr^{2+} at several solution concentrations. Results were interpreted using a Margules solid solution model for clinoptilolite coupled with a Pitzer activity coefficient model for aqueous solutions. Experimental data for analcime and clinoptilolite dissolution rates were interpreted using postulated rate mechanisms, and corresponding rate constants were determined. Dissolution rate data for analcime can be rationalized by alternate mechanisms which invoke either the presence of ultrareactive material or rate dependence on aqueous aluminum. Reversed solubility determinations were interpreted to obtain equilibrium constants for dissolution reactions and standard state Gibbs free energies of formation of the minerals. The measured solubility of analcime differs significantly from values based on thermodynamic data reported in the literature. A provisional equilibrium constant for the Na-clinoptilolite dissolution reaction is comparable to an estimated value reported in the literature and employed in reaction-path modeling in this report. Derived thermodynamic properties permit evaluations of waters from the Yucca Mountain environment. In some circumstances, zeolite compositions can be used to determine coexisting water compositions. Limited chemical analyses indicate that the natural groundwaters appear to be at equilibrium with analcime. Employing principles of thermodynamics, reaction kinetics, mass transfer, and mass transport, computational models were developed using EQ3/6 to explore the evolution of the natural geochemical system, and the geochemical processes that are likely to occur under repository conditions. The natural system model for Yucca Mountain was based on interpretations of geochemical data from the site. Models for dissolution of volcanic glass in water with a calcium-enriched initial composition, coupled with growth of secondary clinoptilolite and smectite, provide reasonable representations of observed groundwater and clinoptilolite compositions at Yucca Mountain. Reaction-path models of the heated repository system and for a boiling groundwater solution predict feldspar dissolution; precipitation of calcite, clinoptilolite, and smectite, and evolution of solution compositions toward increased sodium bicarbonate concentrations and pH. When vaporization is 95- to 99.6-percent complete the model solution becomes dominated by mixed sodium bicarbonate and sodium carbonate at $pH > 9$. All initial project objectives were substantially achieved. The understanding gained will be useful in resolution of key technical uncertainties related to repository licensing that have been identified by the NRC.

CONTENTS

Section		Page
FIGURES		viii
TABLES		x
1	INTRODUCTION	1-1
	1.1 REFERENCES	1-4
2	ION-EXCHANGE EXPERIMENTS BETWEEN CLINOPTILOLITE AND AQUEOUS SOLUTIONS OF Na^+, K^+, Ca^{2+}, AND Sr^{2+}	2-1
	2.1 EXPERIMENTAL PROTOCOL	2-2
	2.1.1 Materials Characterization and Pretreatment	2-2
	2.1.2 Ion-Exchange Experiments	2-4
	2.2 THERMODYNAMIC MODEL	2-5
	2.3 ION-EXCHANGE RESULTS AND DISCUSSION	2-9
	2.4 SOLUTION COMPOSITIONS CALCULATED FROM ZEOLITE ANALYSIS	2-30
	2.4.1 Equations for Calculating Solution Compositions from Zeolite Data	2-34
	2.4.2 Measured Solution Compositions versus Values Predicted from Zeolite Data: Laboratory Ion-Exchange Data	2-35
	2.4.3 Yucca Mountain Groundwater Compositions Predicted from Zeolite Analytical Data	2-44
	2.5 CONCLUSIONS	2-49
	2.6 REFERENCES	2-49
3	REACTION KINETICS AND THERMODYNAMICS OF DISSOLUTION AND GROWTH OF ANALCIME AND CLINOPTILOLITE AT 25 °C	3-1
	3.1 INTRODUCTION	3-1
	3.2 REVIEW OF ANALCIME THERMODYNAMICS AND DISSOLUTION	3-2
	3.2.1 Calorimetric Data	3-2
	3.2.2 Hydrothermal Phase Equilibrium Data	3-3
	3.2.3 Solubility Data	3-3
	3.2.4 Dissolution Reaction and Aqueous Species	3-4
	3.3 REVIEW OF THE THERMODYNAMIC PROPERTIES OF CLINOPTILOLITE AT 25 °C	3-4
	3.4 SAMPLE CHARACTERIZATION AND PREPARATION	3-6
	3.4.1 Analcime	3-6
	3.4.2 Clinoptilolite	3-7
	3.4.3 Initial Solutions	3-7
	3.4.4 Analytical Procedure	3-9
	3.5 ANALCIME DISSOLUTION MECHANISM AND RATE	3-10
	3.5.1 Mass Transfer Relations	3-10
	3.5.2 Kinetic Analysis	3-15

CONTENTS (Cont'd)

Section			Page
		3.5.2.1 Variably Reactive Materials Hypothesis	3-18
		3.5.2.2 Aluminate Dependence Hypothesis	3-19
	3.6	ANALCIME SOLUBILITY	3-20
	3.7	CLINOPTILOLITE DISSOLUTION AND GROWTH	3-26
	3.8	CLINOPTILOLITE SOLUBILITY	3-29
	3.9	EQUILIBRATION OF ANALCIME AND CLINOPTILOLITE	3-32
	3.10	GROUNDWATER IN THE VICINITY OF YUCCA MOUNTAIN	3-33
	3.11	SUMMARY OF CONCLUSIONS	3-37
	3.12	REFERENCES	3-39
4		CONCEPTUAL AND NUMERICAL GEOCHEMICAL MODELING OF THE ENVIRONMENT OF THE PROPOSED NUCLEAR WASTE REPOSITORY AT YUCCA MOUNTAIN	4-1
	4.1	INTRODUCTION	4-1
	4.2	SUMMARY OF THE NATURAL GEOCHEMICAL SYSTEM AT YUCCA MOUNTAIN	4-2
		4.2.1 Bulk Rock Geochemistry and Mineralogy	4-2
		4.2.2 Origin of Alteration at Yucca Mountain	4-4
		4.2.3 Gas Chemistry	4-6
		4.2.4 Hydrochemical Characteristics	4-6
		4.2.5 Aqueous Geochemistry in the Saturated and Unsaturated Zones	4-15
		4.2.5.1 Oxidation State	4-15
		4.2.5.2 pH	4-15
		4.2.5.3 CO_2 and Bicarbonate	4-16
		4.2.5.4 Chloride and Sulfate	4-17
		4.2.5.5 Fluoride	4-17
		4.2.5.6 Nitrate	4-18
		4.2.5.7 Silica	4-18
		4.2.5.8 Major Cations: Na, K, Ca, Mg	4-19
		4.2.5.9 Minor Components: Al, Fe, Sr, Mn	4-21
		4.2.6 Construction of a Quantitative Geochemical Model for the Natural System	4-21
		4.2.7 Natural System Model Results	4-24
	4.3	HEATED REPOSITORY MODEL	4-28
		4.3.1 Geochemical Scenario for a Heated Repository Environment	4-28
		4.3.2 Construction of a Geochemical Model for the Heated Repository	4-29
		4.3.3 Heated Repository Model Results	4-31

CONTENTS (Cont'd)

Section			Page
		4.3.4 Heated Repository Model Sensitivity to Reaction Rates and CO_2 Pressures	4-34
		4.3.5 Geochemical Model for Boiling Evolved Water	4-35
	4.4	DISCUSSION OF MODEL APPROXIMATIONS AND UNCERTAINTY	4-36
	4.5	CONCLUSIONS	4-39
	4.6	REFERENCES	4-41
5		PROGRAMMATIC CONCLUSIONS	5-1
	5.1	PROJECT OBJECTIVES AND ACCOMPLISHMENTS	5-1
	5.2	PROJECT RESULTS AND NRC REGULATORY NEEDS	5-4
	5.3	REFERENCES	5-7

APPENDIX A — ESTIMATED OVERALL UNCERTAINTY IN ISOTHERM DATA
APPENDIX B — EXPERIMENTAL CONDITIONS AND ANALYTICAL DATA FOR ANALCIME AND CLINOPTILOLITE DISSOLUTION AND PRECIPITATION STUDIES
APPENDIX C — SUMMARY AND USE OF THE EQ3/6 SOFTWARE PACKAGE

FIGURES

Figure		Page
2-1	Isotherms for ion-exchange at 25 °C between clinoptilolite and NaCl/KCl aqueous mixtures at total solution concentrations of (a) 0.5-N, (b) 0.05-N, and (c) 0.005-N	2-20
2-2	Isotherms for ion-exchange at 25 °C between clinoptilolite and NaCl/$CaCl_2$ aqueous mixtures at total solution concentrations of (a) 0.5-N, (b) 0.05-N, and (c) 0.005-N	2-21
2-3	Isotherms for ion-exchange at 25 °C between clinoptilolite and NaCl/$SrCl_2$ aqueous mixtures at total solution concentrations of (a) 0.5-N, (b) 0.05-N, and (c) 0.005-N	2-22
2-4	Vanselow corrected selectivity coefficient versus zeolite composition calculated from the 0.5-N NaCl/KCl isotherm data given in Table 2-2. Circles and squares were	2-25
2-5	Vanselow corrected selectivity coefficient versus zeolite composition calculated from the 0.5-N NaCl/$CaCl_2$ isotherm data given in Table 2-5. Circles and squares were	2-26
2-6	Vanselow corrected selectivity coefficient versus zeolite composition calculated from the 0.5-N NaCl/$SrCl_2$ isotherm data given in Table 2-8. Circles and squares were	2-27
2-7	Excess Gibbs energy of mixing for (K^+, Na^+), (Ca^{2+}, Na^+) and (Sr^{2+}, Na^+) clinoptilolite solid solutions calculated using Margules parameters derived from the . . .	2-28
2-8	Activity coefficients for zeolite components of (K^+, Na^+), (Ca^{2+}, Na^+) and (Sr^{2+}, Na^+) clinoptilolite solid solutions (solid, long dashed, and short dashed lines, ...	2-29
2-9	Isotherms for ion-exchange at 25 °C between clinoptilolite and aqueous mixtures of (a) NaCl/$CaCl_2$ and (b) NaCl/$SrCl_2$ for solution concentrations of 0.0005 to 1.0 N	2-31
2-10	Isotherms for ion-exchange at 25 °C between clinoptilolite and 0.05-N $NaNO_3$/KNO_3 aqueous mixtures. Circles and squares represent isotherm points calculated from	2-32
2-11	Isotherms for ion-exchange at 25 °C between clinoptilolite and 0.05-N $NaNO_3$/$Ca(NO_3)_2$ aqueous mixtures. Circles and squares represent isotherm points calculated from	2-33
2-12	Comparison of measured K^+ and Na^+ solution molarities versus values predicted from measured clinoptilolite Na and K content. Error bars in predicted K^+ and Na^+	2-40
2-13	Comparison of measured Ca^{2+} and Na^+ solution molarities versus values predicted from measured clinoptilolite Na and Ca content. Error bars in predicted Ca^{2+} and Na^+	2-43
3-1	Concentrations of Al and Si in the analcime dissolution experiment reported by Caullet et al. (1980). The initial period of reaction is illustrated in A, and complete data	3-5
3-2	Scanning electron photomicrographs of analcime powder: before (A) and after (B) ultrasonic cleaning, and after reaction with NaCl-$NaHCO_3$ solutions in the ACDTIIA . . .	3-8
3-3	Structural interpretation of analcime chemical analyses. Moles of Al (+Fe) and Na (+K+2Ca+2Mg) per 6 moles of structural O are plotted as a function of moles of . . .	3-10
3-4	Moles of Al (triangles) and Si (circles) released as a function of time in ACDT A series analcime dissolution experiments. Lines in figures for the ACDTIA and ACDTIIA . . .	3-13
3-5	Relative numbers of moles of Al and Si released in ACDT A series analcime dissolution experiments. The slopes of the lines correspond to the analyzed ratio of Al (and Na) . .	3-14
3-6	Na molality in the ACDTIA analcime dissolution experiment. Circle symbols represent analytical measurements using a sodium ion specific electrode	3-16
3-7	Calculated moles of Si (circles) and Al (triangles) released based on analytical data from experiment ACDTIA. Curves are computed by numerical integration of rate	3-19
3-8	Calculated moles of Si (circles) and Al (triangles) released based on analytical data from experiment ACDTIA. Curves are computed by numerical integration of rate	3-21

FIGURES (Cont'd)

Figure		Page
3-9	Moles of Si (A) and Al (B) precipitated in RACDT series analcime precipitation experiments as a function of time	3-22
3-10	Moles of Al precipitated as a function of moles of Si precipitated in RACDT and RASH series analcime precipitation experiments. The line has a slope corresponding to the	3-23
3-11	Logarithmic activity diagram illustrating experimental reversal of the analcime solubility limit. Symbols represent solution properties derived from ACDT, ASE, and ASEA	3-24
3-12	Moles of Si (A) and Al (B) released in CDVSE series clinoptilolite dissolution experiments as a function of time. Al release is roughly three orders of	3-27
3-13	Net moles of Si and Al released in RCDV series clinoptilolite precipitation experiments as a function of time. Net precipitation is indicated by negative values and dissolution	3-30
3-14	Ion activity product for clinoptilolite dissolution and precipitation reactions derived from CDVSE and RCDV series experimental results as a function of time. The line is	3-31
3-15	Moles of Si and Al released in ACDTB series experiments as a function of time. Analcime dissolved during the first 5,640 hr. Then clinoptilolite was added to the	3-33
3-16	Interpretation of analcime and clinoptilolite dissolution and precipitation experiments in logarithmic activity coordinates. Arrows mimic the evolution of solution	3-34
3-17	Logarithmic activity diagram representing natural groundwater chemistry from the vicinity of Yucca Mountain (open squares) and Oasis Valley (open circles) in relation	3-35
3-18	Logarithmic activity diagram representing natural groundwater chemistry from the vicinity of Yucca Mountain (open squares) and Oasis Valley (open circles) in relation	3-36
4-1	Locations of wells in the vicinity of Yucca Mountain for which water chemistry is regarded as characteristic of the saturated zone tuffaceous aquifer. Topography is	4-8
4-2	Comparison of water chemistry from the saturated zone tuffaceous aquifer in the vicinity of Yucca Mountain highlighting J-13 well water (Kerrisk, 1987) from unsaturated	4-9
4-3	Isothermal reaction-path model results and analytical solution compositions. Aqueous concentrations of Na (A), K (B), Si (C), and HCO_3^- (D) are shown as functions of	4-25
4-4	Isothermal reaction-path model results. Solution pH (A), moles of secondary minerals (B), and secondary clinoptilolite (C) are shown as functions of the concentration	4-26
4-5	Model temperature and CO_2 fugacity at a point 75 m above the repository horizon as a function of time (Codell and Murphy, 1992). CO_2 fugacity shown as curve A was	4-30
4-6	Heated repository model results for the aqueous (A,B,C) and mineral systems (D,E,F) as a function of time	4-33
4-7	Sensitivity of the heated repository model results to reaction rate and CO_2 pressure. Dotted curves are results from the heated repository model based on higher CO_2	4-35
4-8	Boiling reaction-path model. Solution characteristics are shown as a function of the fraction of the original H_2O that has been volatilized	4-37

TABLES

Table		Page
2-1	Results of ICP analysis of clinoptilolite samples*, the Na-form was used in the ion-exchange experiments	2-4
2-2	Experimental data for ion-exchange between clinoptilolite and 0.5-N NaCl/KCl solutions	2-10
2-3	Experimental data for ion-exchange between clinoptilolite and 0.05-N NaCl/KCl solutions	2-11
2-4	Experimental data for ion-exchange between clinoptilolite and 0.005-N NaCl/KCl solutions	2-12
2-5	Experimental data for ion-exchange between clinoptilolite and 0.5-N $NaCl/CaCl_2$ solutions	2-13
2-6	Experimental data for ion-exchange between clinoptilolite and 0.05-N $NaCl/CaCl_2$ solutions	2-14
2-7	Experimental data for ion-exchange between clinoptilolite and 0.005-N $NaCl/CaCl_2$ solutions	2-15
2-8	Experimental data for ion-exchange between clinoptilolite and 0.5-N $NaCl/SrCl_2$ solutions	2-16
2-9	Experimental data for ion-exchange between clinoptilolite and 0.05-N $NaCl/SrCl_2$ solutions	2-17
2-10	Experimental data for ion-exchange between clinoptilolite and 0.005-N $NaCl/SrCl_2$ solutions	2-18
2-11	Ion-interaction parameters used in this study to calculate aqueous activity coefficients using the Pitzer equations	2-24
2-12	Thermodynamic parameters for ion-exchange reactions represented by Eq. (2-1) derived from 0.5N data	2-30
2-13	Chemical composition of clinoptilolites recovered from ion-exchange equilibrium experiments. For comparison, the composition of the starting material (Na-form)	2-36
2-14	Comparison of measured K^+ and Na^+ solution molarities versus values predicted from measured clinoptilolite Na and K content. Also tabulated are cationic mole fractions	2-38
2-15	Comparison of measured Ca^{2+} and Na^+ solution molarities versus values predicted from measured clinoptilolite Na and Ca content. Also tablulated are cationic mole fractions	2-41
2-16	Comparison of K^+ and Ca^{2+} molarities predicted from zeolite compositions using either activity coefficient ratios for the actual solution normality or activity coefficient	2-45
2-17	Comparison of predicted versus measured K^+, Ca^{2+}, and Na^+ molarities for Yucca Mountain well water samples that are possibly spatially correlated with zeolite	2-48
3-1	Standard state thermodynamic properties of analcime at 25 °C and 1 bar	3-3
3-2	Standard state thermodynamic properties of clinoptilolite at 25 °C and 1 bar	3-6
3-3	Analcime chemical analyses (weight percent)	3-9
3-4	Summary of analcime and clinoptilolite experimental studies	3-11
4-1	Bulk rock compositions for tuffs at Yucca Mountain (Broxton et al., 1986)	4-3
4-2	Reactants and products in reaction-path models	4-23
4-3	Rate expressions and parameters	4-32

EXECUTIVE SUMMARY

This report presents final results of the Geochemistry Research Project conducted at the Center for Nuclear Waste Regulatory Analyses (CNWRA) for the Nuclear Regulatory Commission (NRC) Office of Nuclear Regulatory Research. The study focused on experimental determinations and theoretical interpretations of fundamental thermodynamic and kinetic properties of minerals and reactions that characterize geochemical processes at the proposed nuclear waste repository site at Yucca Mountain and that could affect the capacity of the site to isolate nuclear waste. Following a brief introduction giving the programmatic context of the research and a list of project objectives, technical results are presented in three major sections covering (i) cation exchange studies on clinoptilolite, (ii) kinetic and solubility studies on analcime and Na-clinoptilolite, and (iii) conceptual and numerical geochemical modeling of natural and repository systems. A concluding section summarizes the manner in which each of the initial project objectives was addressed and the relations between research results and regulatory requirements identified by the NRC.

The presence of zeolite minerals has been widely cited as a favorable characteristic with regard to isolation of nuclear wastes at Yucca Mountain. Generally this class of minerals possesses a large potential for ion exchange. Hence their widespread occurrence at Yucca Mountain may constitute a barrier to radionuclide migration. In addition, zeolites are the dominant product of natural geochemical alteration of the rocks at Yucca Mountain. Understanding this alteration process provides an indication of changes to the Yucca Mountain system that may occur as a consequence of repository-induced thermal loading and fluid circulation. Furthermore, groundwater chemistry would have a fundamental influence on repository performance through impacts on container and waste form alteration and radionuclide solubility and speciation. Interactions with zeolites are likely to provide an important control on groundwater chemistry, and zeolite chemistry may yield indications of the chemical properties of groundwater in the natural system.

The objective of original experimental studies was to advance knowledge of the fundamental properties of the zeolite minerals clinoptilolite and analcime through controlled experimentation at 25 °C, and to interpret the data in the context of the geochemical system at Yucca Mountain. Experiments were designed and conducted to measure cation exchange equilibria between clinoptilolite and binary solutions of Na^+ with K^+, Ca^{2+}, and Sr^{2+} at a variety of total solution concentrations. Results of ion exchange experiments and interpretations demonstrate that a solid solution model for zeolite minerals based on a Margules-type of thermodynamic formulation, coupled with an activity coefficient model for aqueous solutions (e.g., Pitzer model), can successfully describe and predict ion exchange equilibria between aqueous solutions and clinoptilolite over a wide range of solution composition and concentration, at least for binary ion exchange reactions. The model also permits prediction of groundwater cationic compositions based on compositions of zeolites that equilibrated with the solutions, at least for systems that are close to binary (two-cation) mixtures.

Experimental data show that analcime dissolution and growth are approximately stoichiometric in experimental solutions with elevated pH and Na^+ concentrations. Mass transfer data indicate that no solid phases other than analcime influenced analcime dissolution and growth experiments at aqueous SiO_2 concentrations less than approximately 4 ppm. However, attempts to precipitate analcime from supersaturated solutions at SiO_2 concentration of approximately 30 ppm apparently led to precipitation of a mineral other than analcime with lower solubility.

The dissolution rate data for analcime cannot be rationalized using a fixed preaffinity rate constant. Two dissolution mechanisms were hypothesized to account for this result, and both provide reasonable regressions of the mass transfer rate data. The variably reactive materials hypothesis invokes the presence of a significant mass of material that reacts rapidly and dissolves completely. Its rate of dissolution decreases as its mass and surface area decrease. The bulk material is hypothesized to react in parallel with the ultrareactive material but accords to a much smaller rate constant. In the aluminate-dependent reaction hypothesis the reaction rate is presumed to be inversely proportional to the square of the $Al(OH)_4^-$ activity. Existing data do not permit a selection among these models or other possible mechanisms that would decrease reaction rate under conditions that are far from equilibrium.

The equilibrium solubility of analcime was closely approached from both undersaturation and supersaturation. Interpretation of the aqueous solution data permits extraction of the equilibrium constant and standard state Gibbs free energy for the analcime dissolution reaction. The standard state Gibbs free energy of formation of analcime can also be extracted using established properties for the aqueous species. However, this value depends strongly on the stoichiometry adopted for the equilibrated analcime. The equilibrium solubility of analcime obtained in this study differs significantly from values based on thermodynamic data reported in the literature.

Release of Si in Na-clinoptilolite dissolution studies follows a systematic pattern of decreasing rate with increasing solution concentration and approach to equilibrium. The time-dependent data can be rationalized using a conventional dissolution rate equation. Release of Al, however, is orders of magnitude less than that of Si, indicating incongruent dissolution.

Attempts to determine the solubility of Na-clinoptilolite were complicated by precipitation of an unidentified, low-solubility, Al-bearing phase in the experiments, as indicated by mass transfer relations and thermodynamic interpretation of the data. Nevertheless, the data were interpreted as providing a reversal of the equilibrium state. A provisional equilibrium constant and corresponding standard Gibbs free energy for the dissolution reaction were extracted from the data, adopting plausible assumptions about the composition of the equilibrated clinoptilolite. Within limits of reasonable uncertainty, the value of the equilibrium constant is equivalent to one based on theoretical estimates of the properties of Na-clinoptilolite reported in the literature and employed in reaction-path modeling in this report.

Natural groundwater chemical data from the vicinity of Yucca Mountain and from Oasis Valley were interpreted thermodynamically. Solutions have aqueous silica activities that vary over a small range at a value greater than that corresponding to mutual equilibration of analcime and Na-clinoptilolite. Limited groundwater chemical analyses that include data for aluminum indicate that the natural waters appear to be at equilibrium with analcime using thermodynamic data derived in this study. However, the natural waters are supersaturated with respect to the provisional Na-clinoptilolite solubility and with respect to the solubility of analcime based on thermodynamic data reported in the literature.

Conceptual and numerical modeling of the environment of the proposed repository at Yucca Mountain provides insights into geochemical processes of significance to repository performance. Modeling also provides predictions of the evolution of the geochemical environment through the period of repository perturbations and regulatory concern. A general description of the geochemical system at Yucca Mountain was developed based on literature review to identify geochemical processes that are important in the evolution of this system. This framework was used to develop the conceptual basis for quantitative reaction-path models for the natural Yucca Mountain system and the heated repository system. Employing principles of thermodynamics, reaction kinetics, mass transfer, and mass transport, computational models

were developed using EQ3/6 to explore the evolution of the natural geochemical system and the geochemical processes that are likely to occur under repository conditions.

The dominant geochemical process at Yucca Mountain is alteration of volcanic glass to clinoptilolite and, with increasing depth, to analcime. Several lines of evidence indicate that altered rocks at Yucca Mountain are enriched in calcium derived from the ground surface and transported to depth in infiltrating groundwater. Calcite is an occasional secondary mineral, occurring notably in fractures and as coatings near the ground surface. Young calcite with isotopic characteristics similar to soil-zone calcite occurs at depth in the unsaturated zone. Unaltered Paintbrush Tuff from Yucca Mountain generally contains less than 1 percent CaO by weight, whereas rocks that have been partially altered to zeolites and/or clays typically contain CaO at 3 to 4 percent. The large differences in calcium concentrations indicate that it is added to the altered rocks from an external source. In general, alteration minerals, notably zeolites, are enriched in calcium at higher positions in the volcanic section above the water table, and become richer in potassium and sodium with depth. Similar relations are observed for other alkaline earth metals, including magnesium and strontium. Variations in groundwater compositions also support a mechanism of alkaline earth metasomatism.

A numerical mass-transfer model for the genesis and evolution of groundwater and alteration minerals like those at Yucca Mountain consists of irreversible dissolution of alkali feldspar, as a chemical analog of volcanic glass in a silica-buffered system, in water with a calcium enriched initial composition, coupled with reversible growth of a secondary stable or metastable solid phase assemblage. Dominant secondary minerals in the upper diagenetic levels of Yucca Mountain are clinoptilolite and smectite. This set of minerals precipitates in the model when solutions are calculated to be saturated with respect to them. After calibration, the natural system reaction-path model reasonably represents observed ranges and relative variations of major groundwater components of the saturated zone tuffaceous aquifer at Yucca Mountain. Computed clinoptilolite compositions also correspond well to those observed at Yucca Mountain. The absence of calcite precipitation is consistent with its sparse occurrence in tuffs at Yucca Mountain, and general undersaturation with respect to calcite of the saturated zone tuffaceous aquifer groundwaters at Yucca Mountain. Smectites in the unsaturated zone at Yucca Mountain are commonly rich in sodium, which is also consistent with model results.

Two likely changes to the mineralogical system at Yucca Mountain due to repository heating would be precipitation of calcite and partial alteration of glass or feldspars to secondary minerals such as zeolites. Transient calcite precipitation due to heating may occur over widespread areas of the mountain over long time periods. Alteration of volcanic glass is the dominant diagenetic process that has occurred naturally at Yucca Mountain, and additional alteration is likely to be provoked by heating and heat-induced fluid circulation. Mineralogical changes would in turn have potential effects on fluid flow and retardation of radionuclide migration as well as on water chemistry.

Reaction-path models of the heated repository system, and for a boiling groundwater solution, illustrate plausible variations in gas, water, and rock geochemistry that could affect container and waste form performance and radionuclide migration in a repository at Yucca Mountain. Initial conditions for the heated repository model were based on results of the natural system model. Temperature and CO_2 fugacity variations as a function of time were imposed on the modeled geochemical system at a point above the repository horizon. Dominant model predictions include feldspar dissolution, precipitation of calcite, clinoptilolite and smectite, and evolution of solution compositions toward increased sodium bicarbonate concentrations and pH. Alternate computations showed that model results for the heated repository system are somewhat sensitive to reaction rate parameters and strongly sensitive to CO_2

pressures which influence pH and reaction rates. A reaction-path model for vaporization of water in the heated repository indicates precipitation of calcite, clinoptilolite, and cristobalite. Changes in aqueous solution composition are relatively small until over 80 percent of the water is vaporized. Dramatic changes occur between 95- and 99.6-percent evaporation, as the solution becomes dominated by mixed sodium bicarbonate and sodium carbonate at $pH > 9$.

All initial project objectives have been substantially achieved through an integrated and multifaceted approach of original experimentation, theoretical interpretation of experimental and field data, and geochemical system modeling. An improved understanding has been developed of the properties of minerals and reactions that characterize natural alteration processes at the proposed nuclear waste repository site at Yucca Mountain and that could affect the capacity of the site to isolate nuclear waste. This understanding will be useful in resolution of key technical uncertainties (KTUs) related to repository licensing that have been identified by the NRC.

FOREWORD

This technical report was prepared by the Center for Nuclear Waste Regulatory Analyses (JCN B6666) under its Geochemistry Research Project with the Waste Management Branch in the Office of Nuclear Regulatory Research. The report presents the project's final results, focusing on experimental determinations and theoretical interpretations of fundamental thermodynamic and chemical properties of minerals and reactions that characterize geochemical processes at the proposed high-level radioactive waste (HLW) site at Yucca Mountain, NV, and could affect the capacity of the site to isolate HLW.

NUREG/CR-6288 is not a substitute for NRC regulations, and compliance is not required. The approaches and/or methods described in the NUREG/CR are provided for information only. Publication of this report does not necessarily constitute NRC approval of or agreement with the information contained herein.

ACKNOWLEDGMENTS

Many people have contributed to the success of this research project. Notably J.D. Prikryl conducted the analcime/clinoptilolite dissolution experiments, and T. Griffin and F.P. Bertetti performed the ion-exchange experiments. Mineral preparation, characterization, and analyses were done mainly by J.D. Prikryl and T. Griffin, with assistance from F.P. Bertetti, M. Barnes, W. Shannon, and S.J. Birnbaum. C.J. Goulet, F.P. Bertetti, and J.A. Roberts contributed to interpretation of analytical and literature data. R.B. Codell collaborated on a related project in which supporting models were generated. R.H. Martin assisted with computer programming. Technical reviews of this report have been provided by D.R. Turner, P.C. Lichtner, G.A. Cragnolino, B. Sagar, W.C. Patrick, and H.L. McKague. Peer reviews were provided by D.A. Sverjenski, J.A. Apps, and J.V. Walther. Clerical and editorial assistance have been provided by P.A. Smith, E. Cantu, C. Garcia, A. Ramos, T. Fischer, and C. Gray. Program guidance has been provided by G.F. Birchard and J.L. Russell. This report documents work performed at the Center for Nuclear Waste Regulatory Analyses (CNWRA) for the Nuclear Regulatory Commission (NRC) under Contract No. NRC-02-93-005. The activities reported here were performed on behalf of the NRC Office of Nuclear Regulatory Research, Division of Regulatory Applications. The report is an independent product of the CNWRA and does not necessarily reflect the views or regulatory position of the NRC. Sources of data are referenced in each section. CNWRA-generated laboratory data contained in this report meet quality assurance requirements described in the CNWRA Quality Assurance Manual. For all other data, their respective sources should be consulted for determining their level of quality assurance. Scientific/engineering computer codes used in analyses contained in this report are: EQ3/6 Version 7.1 and SUPCRT92. Neither is presently controlled under the CNWRA Software Configuration Procedure TOP-018.

1 INTRODUCTION

The Nuclear Regulatory Commission (NRC) is mandated by the Nuclear Waste Policy Act (NWPA), as amended, to review the U.S. Department of Energy's (DOE) license application to construct and operate a mined geologic repository for the disposal of high-level radioactive waste (HLW), to conduct a licensing hearing, and to make a construction authorization decision. Relevant to this mission, the NRC HLW program undertakes independent research to develop the licensing tools and technical bases necessary to judge the adequacy of the DOE license application, to ensure a sufficient understanding of the basic physical processes that occur or may occur at the proposed geologic repository, and to maintain an independent, but limited, confirmatory research capability.

The regulatory requirements set forth in Title 10 Part 60 of the Code of Federal Regulations (10 CFR Part 60) require the geologic setting of a HLW repository to exhibit an appropriate combination of geochemical conditions to provide determination of reasonable assurance of isolation of the waste. At present, Yucca Mountain, Nevada, is being investigated as a possible site for a HLW repository. Information on the geochemistry of the proposed site is important in many areas of the HLW program, such as site characterization, performance assessment, and design. For example, geochemical conditions and processes may significantly affect the performance of both the natural and engineered components of the multiple barrier system for waste containment and isolation. Groundwater interactions with the waste form, waste package, and surrounding rocks may influence the release rates of radionuclides from the waste form and engineered barriers. The long-term stability of seals, backfills, and other underground facility components are affected by geochemical processes. Furthermore, migration of radionuclides as dissolved constituents or particulates/colloids in groundwater or in the gas phase is strongly affected by the chemical characteristics of the geologic system and by geochemical processes such as sorption, dissolution/precipitation, and ion exchange reactions. Thus, understanding the geochemistry of the geologic system is fundamentally important in evaluating the suitability of Yucca Mountain, Nevada, as a HLW repository.

In support of the NRC HLW program, the Center for Nuclear Waste Regulatory Analyses (CNWRA) has conducted research activities during the period 1988 to 1994, as part of the NRC-funded Geochemistry Research Project. The general objectives of the project were to:

- Understand the ambient geochemical conditions and processes at the proposed HLW repository site
- Understand the geochemical conditions and processes affecting the transport of radionuclides through the geologic setting and the release of radionuclides to the accessible environment
- Understand the geochemical conditions and processes which may affect the performance of the waste packages and engineered barrier system and therefore affect the radionuclide source term
- Recognize and evaluate issues and uncertainties in predictive geochemical models used in assessment of the performance of the proposed HLW repository in regard to isolation of the waste

Information derived from the Geochemistry Research Project will aid in identifying and resolving technical issues and uncertainties associated with the NRC licensing of the proposed repository. The goal of the project was to develop the technical knowledge base and to perform investigations which will give the CNWRA the capabilities to support the NRC provision of appropriate, timely prelicensing guidance to the DOE, and to support the NRC in evaluation of geochemical information presented in the DOE licensing submittals. These capabilities will enable the NRC to regulate and make licensing decisions from an appropriately informed technical position concerning the disposal of HLW, as dictated by the NWPA.

The Geochemistry Research Project was initiated with both experimental and modeling tasks and the following specific objectives were identified at the outset of the project.

- Establish similarities and differences between chemical compositions of water in the unsaturated zone in the tuff, and water in nearby similar rocks that are fully saturated
- Establish a reference chemical composition (or range of compositions) for water in unsaturated, fractured rock that can be used to constrain the initial solvent composition in experimental work, and in corrosion studies performed in the CNWRA Integrated Waste Package Research Project
- Assess potential effects of open-system CO_2 behavior on the chemical composition of fluids and solids in unsaturated, fractured tuff
- Identify and characterize solid phases in the tuff that may control groundwater chemistry and/or radionuclide mobility
- Evaluate conceptual models of the geochemical evolution of water in the unsaturated, fractured tuffs at the repository candidate site from prior to waste emplacement through operation, closure, and post-emplacement time
- Develop a theoretically based understanding of relevant gas-water-rock reactions, and the capacity to make predictions of the evolution of the geochemical systems of concern
- Interpret and evaluate experimental and field data from studies of gas-water-rock interactions, including those conducted for and by the DOE HLW program
- Identify key geochemical parameters for which data are either lacking or inadequate and for which experimental studies are necessary
- Develop constraints of initial conditions, time periods, water-rock ratios, fluid and gas compositions, etc., in order to support and direct experimental activities in this project and research in other CNWRA projects such as natural analog and waste package performance studies
- Directly measure key parameters for characterizing the relevant geochemical systems and their evolution for which necessary data are either lacking or of insufficient accuracy
- Support and validate the geochemical modeling described in the modeling task

- Provide an experimental database with which to independently judge the geochemical work by the DOE on HLW isolation

These objectives have been addressed through an integrated, multifaceted research project focusing on the fundamental properties of major mineralogical constituents and the processes of geochemical alteration at Yucca Mountain. In particular, the presence of zeolite minerals has been widely cited as a favorable characteristic with regard to isolation of nuclear wastes at Yucca Mountain. Generally this class of minerals possesses a large potential for ion exchange. Hence their widespread occurrence at Yucca Mountain may constitute a barrier to radionuclide migration. In addition, zeolites are the dominant product of natural geochemical alteration of the rocks at Yucca Mountain. Understanding this alteration process provides an indication of changes to the Yucca Mountain system that may occur as a consequence of repository-induced thermal loading and fluid circulation. Furthermore, groundwater chemistry would have a fundamental influence on repository performance through impacts on container and waste form alteration, and radionuclide solubility and speciation. Interactions with zeolites are likely to provide an important control on groundwater chemistry, and zeolite chemistry may yield indications of the chemical properties of groundwater in the natural system. Despite these basic geochemical issues with regard to HLW disposal at Yucca Mountain, the fundamental properties of the primary zeolite minerals at Yucca Mountain remained poorly understood at the outset of this project. Geochemical modeling studies focused on development of multicomponent system models calibrated on mineral, water, and gas chemistry from the site and extrapolated to predict the geochemical evolution of the nonisothermal repository system over thousands of years. Geochemical modeling of the repository system provides a necessary basis for assessments of waste package and waste form alteration processes, radioelement solubilities and speciation, and retardation of radionuclide migration. Nevertheless, quantitative representations of the genesis of mineral alteration at Yucca Mountain had received limited development, and theoretically based predictive models were lacking for gas-water-rock interactions in the natural and potential repository systems at Yucca Mountain. These basic technical issues were addressed in an effort to achieve the objectives of the project.

This report presents major technical results and information derived from the Geochemistry Research Project in three sections. Section 2 presents original experimental and thermodynamic modeling studies on ion-exchange reactions between aqueous solutions and the zeolite mineral clinoptilolite. Section 3 presents new experimental and modeling results on the dissolution kinetics and solubility of analcime and clinoptilolite. Section 4 presents conceptual and numerical models for the natural geochemical environment at Yucca Mountain. Numerical geochemical models are then extended to provide predictions of the behavior of the gas-water-rock system at Yucca Mountain under potential repository conditions. The final section (Section 5) addresses the results of the research project from the perspective of the NRC regulatory concerns and needs. Also in Section 5 is a discussion of the manner in which each of the specific objectives established at the inception of the project was addressed in this research project.

Intermediate results of the project have been published in NRC and CNWRA research progress reports, peer-reviewed publications, and conference proceedings [Pabalan and Murphy (1990); Patrick (1990 a,b,c; 1991 a,b,c,d; and 1993 a,b); Sagar (1993 a,b); Murphy et al. (1992); Murphy (1994); Pabalan (1991, 1994); Pabalan and Bertetti (1994); and Murphy et al. (1994)[1]]. Additional papers are in preparation. Nevertheless, this document is basically self-contained.

---

[1]Murphy, W.M., R.T. Pabalan, J.D. Prikryl, and C.J. Goulet. 1994. Reaction kinetics and thermodynamics of aqueous dissolution and growth of analcime and clinoptilolite at 25 °C. Submitted to *American Journal of Science*.

1.1 REFERENCES

Murphy, W.M. 1994. Geochemical models for gas-water-rock interactions in a proposed nuclear waste repository at Yucca Mountain, Nevada. *Proceedings of the Site Characterization and Model Validation FOCUS '93*. La Grange Park, IL: American Nuclear Society. 115-121.

Murphy, W.M., R.T. Pabalan, J.D. Prikryl, and C.J. Goulet. 1992. Dissolution rate and solubility of analcime at 25 °C. *Water-Rock Interaction*. Y.K. Kharaka and A.S. Maest, eds. Rotterdam, Holland: A.A. Balkema: 107-110.

Pabalan, R.T. 1991. Nonideality effects on the ion-exchange behavior of the zeolite mineral clinoptilolite. *Scientific Basis for Nuclear Waste Management XIV*. T. Abrajano, Jr., and L.H. Johnson, eds. Pittsburgh, PA: Materials Research Society: MRS Symposium Proceedings 212: 559-567.

Pabalan, R.T. 1994. Thermodynamics of ion-exchange between clinoptilolite and aqueous solutions of Na^+/K^+ and Na^+/Ca^{2+}. *Geochimica et Cosmochimica Acta 58.*

Pabalan, R.T., and W.M. Murphy. 1990. *Progress in Experimental Studies on the Thermodynamic and Ion Exchange Properties of Clinoptilolite*. CNWRA 89-006. San Antonio, TX: Center for Nuclear Waste Regulatory Analyses.

Pabalan, R.T., and F.P. Bertetti. 1994. Thermodynamics of ion-exchange between Na^+/Sr^{2+} solutions and the zeolite mineral clinoptilolite. *Scientific Basis for Nuclear Waste Management XVII*. A. Barkatt and R. Van Konynenburg, eds. Pittsburgh, PA: Materials Research Society: MRS Symposium Proceedings 333: 731-738.

Patrick, W.C. (ed.). 1990a. *Report on Research Activities for the Quarter January 1 through March 31, 1990*. CNWRA 90-01Q. San Antonio, TX: Center for Nuclear Waste Regulatory Analyses.

Patrick, W.C. (ed.). 1990b. *Report on Research Activities for the Quarter April 1 through June 30, 1990*. CNWRA 90-02Q. San Antonio, TX: Center for Nuclear Waste Regulatory Analyses.

Patrick, W.C. (ed.). 1990c. *Report on Research Activities for the Quarter July 1 through September 30, 1990*. CNWRA 90-03Q. San Antonio, TX: Center for Nuclear Waste Regulatory Analyses.

Patrick, W.C. (ed.). 1991a. *Report on Research Activities for Calendar Year 1990*. NUREG/CR-5817, CNWRA 90-01A. Washington, DC: Nuclear Regulatory Commission.

Patrick, W.C. (ed.). 1991b. *Report on Research Activities for the Quarter January 1 through March 31, 1991*. CNWRA 91-01Q. San Antonio, TX: Center for Nuclear Waste Regulatory Analyses.

Patrick, W.C. (ed.). 1991c. *Report on Research Activities for the Quarter April 1 through June 30, 1991*. CNWRA 91-02Q. San Antonio, TX: Center for Nuclear Waste Regulatory Analyses.

Patrick, W.C. (ed.). 1991d. *Report on Research Activities for the Quarter July 1 through September 30, 1991*. CNWRA 91-03Q. San Antonio, TX: Center for Nuclear Waste Regulatory Analyses.

Patrick, W.C. (ed.). 1993a. *NRC High-Level Radioactive Waste Research at CNWRA Calendar Year 1991*. NUREG/CR-5817, CNWRA 91-01A. Washington, DC: Nuclear Regulatory Commission: 2.

Patrick, W.C. (ed.). 1993b. *NRC High-Level Radioactive Waste Research at CNWRA January through June 1992*. NUREG/CR-5817, CNWRA 92-01S. Washington, DC: Nuclear Regulatory Commission: 3(1).

Sagar, B. (ed.). 1993a. *NRC High-Level Radioactive Waste Research at CNWRA June through December 1992*. NUREG/CR-5817, CNWRA 92-02S. Washington, DC: Nuclear Regulatory Commission: 3(2).

Sagar, B. (ed.). 1993b. *NRC High-Level Radioactive Waste Research at CNWRA January through June 1993*. CNWRA 93-01S. San Antonio, TX: Center for Nuclear Waste Regulatory Analyses.

2 ION-EXCHANGE EXPERIMENTS BETWEEN CLINOPTILOLITE AND AQUEOUS SOLUTIONS OF Na^+, K^+, Ca^{2+}, AND Sr^{2+} [1]

Zeolite minerals are recognized as some of the most important authigenic silicates in altered pyroclastic and volcaniclastic rocks (Surdam, 1977; Hay, 1977, 1978; Mumpton, 1978; Surdam and Sheppard, 1978). These are mostly formed by reaction of pore waters with volcanic glass, and by alteration of pre-existing feldspars, feldspathoids, poorly-crystalline clays, and biogenic silica (Hay, 1978; Mumpton, 1978; Tschernich, 1992). Because of their well-known ion-exchange properties and favorable selectivities toward alkali and alkaline earth radionuclides such as ^{135}Cs, ^{137}Cs, and ^{90}Sr (Ames, 1964 a,b), the potential siting of a geologic repository for HLW at Yucca Mountain, Nevada, which is underlain by diagenetically-altered, zeolite-rich rhyolitic tuffs (Broxton et al., 1986, 1987), has focused attention on the possible importance of zeolite minerals such as clinoptilolite, heulandite, and mordenite as barriers to radionuclide migration from the repository horizon to the accessible environment. Measured compositions of zeolite minerals at Yucca Mountain show lateral and vertical variations, for example, Na-K-bearing and increasingly Na-rich with depth on the western side and Ca-K-bearing and increasingly Ca-rich with depth on the eastern side of Yucca Mountain (Broxton et al., 1986, 1987). Because ion-exchange properties of zeolites depend on factors including solid and aqueous phase compositions as well as aqueous solution concentrations, spatial variations in zeolite composition that have been observed at Yucca Mountain and natural or repository-induced changes in groundwater chemistry may influence the effectiveness of zeolite minerals as agents for retardation of radionuclide migration.

In addition, because the characteristic three-dimensional pore system and large pore apertures of zeolites allow relatively easy exchange of certain cations between aqueous solutions and intracrystalline exchange sites, groundwater chemistry can be altered by ion-exchange interactions with zeolite minerals. For example, a study by Sturchio et al. (1989) demonstrated that ion-exchange interactions between thermal waters and zeolites controlled the distribution of ^{226}Ra and Ba in the Yellowstone hydrothermal environment. White et al. (1980) showed that groundwater compositions at Rainier Mesa, which is located 50 km north-northeast of Yucca Mountain, became enriched in Na and depleted in Ca and Mg after passing through alteration zones containing zeolites and smectites. Also, the observed systematic compositional variations in zeolite minerals at Yucca Mountain have been attributed partly to ion-exchange interactions with groundwater (Broxton et al., 1987). The alteration of groundwater chemistry by interactions with zeolite minerals can potentially affect the stability of engineered materials in the near field and the transport/retardation of radionuclides in the far-field environments of the proposed repository.

Furthermore, uncertainties exist in determining groundwater chemistries in the vadose zone at Yucca Mountain due to problems inherent in current techniques used to sample pore waters from unsaturated media (Yang et al., 1988; Edmunds et al., 1992; Peters et al., 1992; Puchelt and Bergfeldt, 1992). It may be possible to reduce these uncertainties by investigating groundwater/zeolite equilibria through ion-exchange experiments coupled with thermodynamic modeling. Through these studies, it may be possible to calculate groundwater compositions based on chemical analysis of coexisting zeolite phases.

---

[1]Parts of this chapter have been published in Pabalan (1991, 1994) and Pabalan and Bertetti (1994).

To provide a thermodynamic basis for understanding zeolite-water interactions in geologic systems, ion-exchange experiments were conducted between the zeolite mineral clinoptilolite and aqueous solutions of Na^+, K^+, Ca^{2+}, and Sr^{2+}. Clinoptilolite was selected for study because it is the predominant zeolite mineral present in altered pyroclastic and volcaniclastic rocks (Mumpton, 1978; Mumpton and Ormsby, 1978), particularly those present at Yucca Mountain, Nevada (Broxton et al., 1986, 1987). Na^+, K^+, and Ca^{2+} are commonly the major cationic constituents of groundwater, including those at Yucca Mountain (Ogard and Kerrisk, 1984), whereas ^{90}Sr ($t_{1/2}$=29.1 yr) is an important fission product (Kerrisk, 1985) whose potential release to the environment, particularly at $t < 300$ yr after disposal, poses a serious health risk due to its high fission yield and mobility in aqueous systems. Although some data on ion-exchange between clinoptilolite and aqueous solutions of Na^+, K^+, Ca^{2+}, and Sr^{2+} are available (Ames, 1964 a,b; White, 1988), these were derived for single-solution concentrations only. In addition, the experiments of White (1988) indicated nonreversibility for exchanges involving Na^+/K^+ and Na^+/Ca^{2+}; hence, equilibrium thermodynamics were not applied to these data.

The present study was designed to investigate the effects on the exchange equilibrium of changes in total solution concentration, relative concentrations of exchangeable cations in solution, and anionic composition. Another goal was to test the use of an empirical Margules thermodynamic formulation for zeolite solid solutions for describing and predicting ion-exchange equilibria. Because the Margules formulation can be easily extended to ternary and more complicated systems, it may be useful for modeling ion-exchange equilibria in multicomponent geochemical systems such as that of Yucca Mountain, Nevada.

2.1 EXPERIMENTAL PROTOCOL

2.1.1 Materials Characterization and Pretreatment

Although clinoptilolite is a common mineral in volcanic-sedimentary rocks, its occurrence in macrocrystalline form is rare (Gottardi and Galli, 1985; Tschernich, 1992). Therefore, ion-exchange studies on clinoptilolite typically used specimens of clinoptilolite-rich zeolitic tuffs. In this study, zeolitized tuffs from six localities were initially characterized by x-ray diffraction (XRD), petrographic analysis, and scanning electron microscopy (SEM). Specimens from four localities, namely: (i) Hector, California; (ii) Barstow, California; (iii) Death Valley Junction, California; and (iv) Castle Creek, Idaho, were obtained from Minerals Research Company. Additional specimens from Tilden, Texas, and Buckhorn, Grant County, New Mexico, were obtained from Zeotech Corporation. The samples from different localities contained differing amounts of clinoptilolite, which is mostly well-crystallized and has replaced the glass in poorly welded tuffs. The clinoptilolite, however, is very fine-grained, and well-formed crystals on the order of 10 to 30 μm in length occur only in vugs or in voids previously occupied by glass shards. Other phases identified in the specimens are mordenite, quartz, smectite, illite, plagioclase, K-feldspar, gypsum, dolomite, calcite, halite, and unaltered volcanic glass.

The samples from Death Valley Junction, California, contained the fewest impurities and were selected for use in preparing purified clinoptilolite for the ion-exchange experiments. Powdered material was prepared by first using a rock hammer to break the as-received samples into pieces less than one-third of an inch in diameter. These small pieces were then ground in a Spex #8000 Mixer/Mill using a tungsten carbide vial and sieved using a Ro-Tap sieve shaker and 8-in.-diameter stainless-steel sieves into five size ranges: (i) 35–100 mesh (500–150 μm), (ii) 100–200 mesh (150–75 μm), (iii) 200–325 mesh

(75–45 μm), (iv) 325–450 mesh (45–32 μm), and (v) <450 mesh (<32 μm). Sieving was repeated several times to minimize the retention of grains of a particular size with grains in a larger size range.

Using the 100–200 mesh-size fraction, the material was first treated with 1 N sodium acetate buffer (pH adjusted to 5) to dissolve any carbonate minerals. Other mineral impurities were then separated from clinoptilolite by density separation using heavy liquid mixtures of tetrabromoethane and NN-dimethyl formamide (Hutchison, 1974). The 100–200 mesh-size fraction was found to provide good separation between clinoptilolite and other solid phases. The clinoptilolite was washed several times with acetone with the aid of an ultrasonic cleaner, and was rinsed with deionized water. Subsequently, iron oxide minerals were dissolved using a sodium dithionite-citrate-bicarbonate mixture (Mehra and Jackson, 1960).

Near homoionic Na-clinoptilolite was generated by treating 40-g batches of the purified material with 400 ml of 3-m NaCl solution in 500-ml polypropylene bottles. The bottles were continuously agitated in a constant-temperature shaker water bath maintained at 90 °C for about 2 wk. The NaCl solution was replaced every 2 days. The clinoptilolite powders thus treated were washed several times with deionized water at 90 °C to eliminate excess NaCl, dried in an oven at about 65 °C, and then equilibrated with water vapor over saturated NaCl solution in a desiccator until constant mass was attained (~10 days). This last step was necessary to provide a constant zeolite water content prior to both chemical analysis and initiation of ion-exchange experiments. No secondary mineral phases were observed to have formed during pretreatment as determined by SEM and XRD.

Subsequent to lithium metaborate fusion and dissolution in an HCl/HNO_3 matrix, the compositions of the original (untreated), the purified, and the Na-form clinoptilolite samples were analyzed by inductively-coupled plasma (ICP) emission spectrometry. The results are given in Table 2-1. The water content of Na-clinoptilolite was determined by weighing three samples in self-sealing quartz crucibles before and after heating at 900 °C for 2 hr. The resulting weight percent of H_2O is 15.21 ± 0.18. The chemical formula of the Na-clinoptilolite sample calculated from the analytical data corresponds to $(Na_{1.804}K_{0.123})(Ca_{0.003}Mg_{0.035})(Al_{1.947}Fe^{3+}_{0.044})(Si_{10.002}Ti_{0.004})O_{24} \cdot 7.43H_2O$, based on 24 oxygens per unit cell. For comparison, the idealized formula for the sodium-endmember of clinoptilolite is $Na_2Al_2Si_{10}O_{24} \cdot 8H_2O$.

The cation exchange capacity (CEC) of Na-clinoptilolite was derived from the zeolite analysis given in Table 2-1. The calculation of CEC is based on the following assumptions: (i) negligible mineral impurities are present in the sample; (ii) Al^{3+} and Fe^{3+} substitute for Si^{4+} in the tetrahedral site and result in a negatively charged structure; and (iii) this negative charge is balanced by alkali and alkaline earth ions such as Na^+, K^+, Ca^{2+}, and Mg^{2+} in intracrystalline cation exchange sites. An additional assumption is that the K^+, Ca^{2+}, and Mg^{2+} present in the Na-clinoptilolite are in inaccessible exchange sites and do not participate in the ion-exchange process. This last assumption seems reasonable considering the Na-clinoptilolite was generated by reacting the purified clinoptilolite with NaCl solutions at 90 °C for 2 wk, whereas the ion-exchange experiments were conducted at 25 °C. Thus, CEC is equal to the moles of $(Al^{3+}+Fe^{3+})$ per gram of zeolite less the equivalents of $(K^+ + Ca^{2+} + Mg^{2+})$ per gram, or 2.04 ± 0.02 meq/g. Alternatively, the CEC is equal to the equivalents of Na^+ per gram of zeolite or 2.05 ± 0.01 meq/g, which is equal to the former value within analytical uncertainty. The value of 2.04 meq/g was used in the following calculations.

Table 2-1. Results of ICP analysis of clinoptilolite samples*, the Na-form was used in the ion-exchange experiments

Component	Weight Percent		
	Untreated	Purified	Na-form
SiO_2	67.26 ±0.36	69.13 ±0.34	68.28 ±0.57
Al_2O_3	11.10 ±0.12	11.38 ±0.06	11.28 ±0.09
TiO_2	0.10 ±0.00	0.06 ±0.03	0.04 ±0.03
Fe_2O_3	0.84 ±0.01	0.47 ±0.01	0.40 ±0.02
MgO	0.36 ±0.01	0.27 ±0.02	0.16 ±0.03
CaO	0.73 ±0.04	0.09 ±0.02	0.02 ±0.01
Na_2O	3.47 ±0.08	4.83 ±0.02	6.36 ±0.04
K_2O	3.51 ±0.06	2.77 ±0.05	0.66 ±0.05
TOTAL	87.37 ±0.03	89.00 ±0.42	87.20 ±0.66

*Standard deviations are based on analysis of 2, 4, and 6 samples, respectively, of untreated, purified, and Na-exchanged clinoptilolite. Measured strontium concentrations are 169±4, 58±4, and 8±2 ppm Sr for the untreated, purified, and Na-form clinoptilolite, respectively.

2.1.2 Ion-Exchange Experiments

Experiments were conducted at 25 °C for the binary systems K^+-Na^+, Ca^{2+}-Na^+, and Sr^{2+}-Na^+ by equilibrating weighed amounts of Na-clinoptilolite with a series of solutions containing the two competing cations at different equivalent concentration ratios, but at a constant normality equal to 0.005, 0.05, or 0.50 N (eq/L). Aqueous mixtures of K^+-Na^+, Ca^{2+}-Na^+, and Sr^{2+}-Na^+ at 0.50 N and with equivalent cationic mole fractions of K^+, Ca^{2+}, or Sr^{2+} equal to 0.1, 0.2, ..., 1.0, were prepared by mass from reagent-grade KCl, NaCl, $CaCl_2 \cdot 2H_2O$, or $SrCl_2 \cdot 6H_2O$. The 0.05- and 0.005-N solutions were prepared by ten-factor dilutions of the 0.50- and 0.05-N mixtures, respectively. The normality of the 0.5-N chloride solutions was checked by gravimetric titration with $AgNO_3$. A separate set of 0.05-N K^+-Na^+ and Ca^{2+}-Na^+ aqueous solutions was also prepared from reagent-grade KNO_3, $NaNO_3$, and

$Ca(NO_3)_2 \cdot 4H_2O$. Experiments using these nitrate solutions serve to check for possible effects of anionic composition on the ion-exchange equilibria.

The masses of clinoptilolite powder used in the experiments ranged from 0.03 to 1.8 g, and solution volumes ranged from 5 to 250 ml. The zeolite-mass to solution-volume ratios and the aqueous mixture compositions used in the experiments were designed to yield significant differences in the initial and final concentrations of the cations in solution and a relatively evenly-spaced distribution of points along the ion-exchange isotherm. The clinoptilolite + solution mixtures were contained in 5- to 250-ml capped polypropylene bottles that were agitated and thermostatted at 25 °C in a shaker water bath for at least 1 wk. Kinetics tests indicated that ion-exchange equilibrium is closely approached in about 2 to 3 days. After equilibrium was established, aliquots of the reference and experimental solutions were taken and analyzed for Na^+, K^+, Ca^{2+}, or Sr^{2+}. Several isotherm points were reversed by adding to the remaining solutions known volumes of an aqueous mixture of equal total normality but with a higher proportion of Na^+. In addition, known volumes of aqueous mixtures with higher proportions of K^+, Ca^{2+}, or Sr^{2+} were added to some of the other remaining solutions to check the reproducibility of the isotherms. The new mixtures were reequilibrated for about a week, then samples were taken for Na^+, K^+, Ca^{2+}, or Sr^{2+} analysis.

Analyses for Na^+, K^+, or Ca^{2+} were done using Orion ion-selective electrodes (ISE) and an Orion 920A pH/mV/ISE/°C meter. Some samples were also taken for atomic absorption (AA) analysis using a Perkin-Elmer Model 3100 AA analyzer, the results of which agreed very well with the ISE analysis. Sr^{2+} concentrations in solution were determined by liquid scintillation analysis (Cerenkov counting) of $^{90}Sr/^{90}Y$ using a Packard Tri-Carb Model 1900TR liquid scintillation analyzer (LSA) after secular equilibrium had been reached between ^{90}Sr and ^{90}Y in the aqueous samples. Overall uncertainties in the measured concentrations of Na^+, K^+, and Ca^{2+} are estimated to be ± 2, ± 3, and ± 4 percent, respectively, based on the reproducibility of replicate analyses and reported uncertainty in the standard solutions. Uncertainties in Sr^{2+} concentrations are estimated to be ± 1 percent based on the LSA counting error.

2.2 THERMODYNAMIC MODEL

The theoretical treatment of zeolite ion-exchange equilibria has been discussed in a number of publications (Helfferich, 1962; Howery and Thomas, 1965; Barrer and Klinowski, 1972, 1974, 1979; Barrer et al., 1973; Dyer et al., 1981; Fletcher et al., 1984). For a binary exchange reaction involving cations A^{z_A+} and B^{z_B+}, the equilibrium reaction may be written as

$$z_B\, A^{z_A+} + z_A BL_{z_B} \rightleftharpoons z_A B^{z_B+} + z_B AL_{z_A} \qquad (2\text{-}1)$$

where z_A+ and z_B+ are the valences of the respective ions, and L is defined as a portion of zeolite framework holding unit negative charge. The usual thermodynamic equilibrium constant, K, for this reaction is given by

$$K = \left[(\bar{a}_A)^{z_B}(a_B)^{z_A}\right] / \left[(a_A)^{z_B}(\bar{a}_B)^{z_A}\right] \qquad (2\text{-}2)$$

where a represents activities of the aqueous species and $\bar{a}$ represents activities of the zeolite components. The zeolite may be considered as a solid solution of two components AL_{z_A} and BL_{z_B}

(Ekedahl et al., 1950; Freeman, 1961; Barrer and Klinowski, 1977), where L_{z_A} is the amount of anionic framework associated with an A^{z_A+} ion and carrying anionic charge z_A- and L_{z_B} is this amount of framework associated with B^{z_B+} and carrying anionic charge z_B-. The number of moles of AL_{z_A} and BL_{z_B} are then respectively equal to the total number of moles $\bar{n}_A$ and $\bar{n}_B$ of ions A^{z_A+} and B^{z_B+} in the zeolite, and solid phase compositions can be described in terms of cationic mole fractions of A^{z_A+} and B^{z_B+} in the zeolite

$$\bar{X}_A = \bar{n}_A/(\bar{n}_A + \bar{n}_B);\ \bar{X}_B = \bar{n}_B/(\bar{n}_A + \bar{n}_B) \tag{2-3}$$

A convenient standard state for each solid phase component is the appropriate homoionic zeolite component in equilibrium with a solution with $a_{H_2O} = 1$ (Gaines and Thomas, 1953; Sposito, 1981). Then the criterion for ideal behavior in the zeolite solid solution is that $\bar{a}_i = \bar{X}_i$ for all $\bar{X}_i$. For the aqueous electrolyte solution, the standard state adopted is a hypothetical, one-molar solution referenced to infinite dilution. Equation (2-2) may be expanded to give

$$K = \left[(\bar{X}_A)^{z_B}(M_B)^{z_A}\right] / \left[(\bar{X}_B)^{z_A}(M_A)^{z_B}\right]\left[(f_A)^{z_B} / (f_B)^{z_A}\right]\left[(\gamma_B)^{z_A} / (\gamma_A)^{z_B}\right] \tag{2-4}$$

or

$$K = K_v\left[(f_A)^{z_B}/(f_B)^{z_A}\right];\ K_v = \left[(\bar{X}_A)^{z_B}(M_B)^{z_A}\right]/\left[(\bar{X}_B)^{z_A}(M_A)^{z_B}\right]\left[(\gamma_B)^{z_A}/(\gamma_A)^{z_B}\right] \tag{2-5}$$

where K_v is the Vanselow corrected selectivity coefficient (Vanselow, 1932; Townsend, 1986), and M_A and M_B are the molarities of A^{z_A+} and B^{z_B+} in the aqueous phase. The quantities γ_A and γ_B are single-ion activity coefficients for the aqueous ions, and f_A and f_B are activity coefficients for the zeolite components. The ratio $\left[(\gamma_B)^{z_A}/(\gamma_A)^{z_B}\right]$ is therefore a nonideality correction for the aqueous solution phase, whereas $\left[(f_A)^{z_B}/(f_B)^{z_A}\right]$ is a correction for nonideal behavior in the zeolite phase.

The evaluation of K, f_A, and f_B from experimental data results from an appropriate integration of the Gibbs-Duhem relation (Argersinger et al., 1950). Together with Eq. (2-5), the Gibbs-Duhem equation gives the following expressions for calculating zeolite phase activity coefficients and the value of K

$$\ln K = \int_0^1 \ln K_v \, d(\bar{E}_A) \tag{2-6}$$

$$\ln f_A^{z_B} = -\bar{E}_B \ln K_v + \int_{\bar{E}_A}^{1} \ln K_v \, d(\bar{E}_A) \tag{2-7}$$

and

$$\ln f_B^{z_A} = \bar{E}_A \ln K_v - \int_{0}^{\bar{E}_A} \ln K_v \, d(\bar{E}_A) \tag{2-8}$$

where $\bar{E}_A$ and $\bar{E}_B$ are the equivalent cationic fractions of A^{z_A+} and B^{z_B+}, respectively, in the zeolite phase defined as

$$\bar{E}_A = z_A\bar{n}_A/(z_A\bar{n}_A + z_B\bar{n}_B); \; \bar{E}_B = z_B\bar{n}_B/(z_A\bar{n}_A + z_B\bar{n}_B) \tag{2-9}$$

Equivalent cationic fractions in the aqueous solution can be defined similarly as

$$E_A = z_A n_A/(z_A n_A + z_B n_B); \; E_B = z_B n_B/(z_A n_A + z_B n_B) \tag{2-10}$$

where n_A and n_B are the number of moles of A^{z_A+} and B^{z_B+}, respectively, in the aqueous solution. Note that although K_v is defined in terms of $\bar{X}_i$, Eqs. (2-6), (2-7), and (2-8) also require values of the charge fraction $\bar{E}_i$. The relationship between $\bar{X}_i$ and $\bar{E}_i$ is shown by

$$\bar{X}_A = (\bar{E}_A/z_A)/[(\bar{E}_A/z_A) + (\bar{E}_B/z_B)]; \; \bar{X}_B = (\bar{E}_B/z_B)/[(\bar{E}_A/z_A) + (\bar{E}_B/z_B)] \tag{2-11}$$

The standard free energy of the exchange reaction represented by (2-1) is given by

$$\Delta G^\circ = -RT \ln K \tag{2-12}$$

where R is the gas constant and T is temperature (K), and, per equivalent of exchange, the standard free energy is

$$\Delta G^\ominus = \Delta G^\circ/(z_A z_B) \tag{2-13}$$

The above thermodynamic formulations are valid under conditions where imbibition of neutral electrolyte is negligible, which for zeolites is at solution concentrations approximately <1.0 m (Dyer et al., 1981). An additional condition is that the overall contribution made by water activity changes in the zeolite are insignificant. Barrer and Klinowski (1974) demonstrated that the water activity terms are not significant for most cases of ion-exchange equilibria. However, for ion-exchange reactions involving concentrated electrolyte solutions, the Gibbs-Duhem equation and the thermodynamic relationships derived from it can be expanded to include terms for the effects of sorbed or imbibed solvent and of imbibed salts (Gaines and Thomas, 1953).

It is apparent from Eqs. (2-4) to (2-13) that equilibrium constants, Gibbs energies of exchange reactions, and zeolite phase activity coefficients evaluated from isotherm data depend on the values used for aqueous phase activity coefficients. Ion-exchange studies by Fletcher and Townsend (1985) demonstrated the importance of correctly evaluating aqueous solution activity coefficients for accurate interpretation of exchange equilibria, particularly on studies with mixed background anions. In principle, γ's, which account for nonideal behavior in the aqueous solution, can be calculated from well-established electrolyte solution theories (Bronsted, 1922 a,b; Guggenheim, 1935; Scatchard, 1936, 1968; Glueckauf, 1949; Pitzer, 1973, 1987, 1991). Because it would be useful to investigate multicomponent exchange reactions over wide ranges of concentration and temperature, the ion-interaction model developed by Pitzer (1973, 1987, 1991) was used here to calculate single-ion activity coefficients of the aqueous species[2]. This model has the advantage of having a large database of parameters at 25 °C and above, and demonstrated success in applications to multicomponent systems over wide ranges of solution compositions, concentrations, and temperatures (Clegg and Whitfield, 1991; Pabalan and Pitzer, 1991). For details on the ion-interaction model, the papers by Pitzer (1973, 1987, 1991) and the references cited therein should be consulted.

Nonideal behavior in the zeolite phase is reflected in the activity coefficients f_A and f_B. However, there is no generally accepted activity coefficient model for exchangeable ions or solid solutions. Commonly used models are based on general equations for the molar excess Gibbs energy (g^{ex}) of mixing (Grant and Sparks, 1989), which may be defined as

$$g^{ex}/RT = \sum_{i=1}^{n} \bar{X}_i \ln f_i \qquad (2\text{-}14)$$

A thermodynamic model that has been found useful for both solid and liquid solutions is the Margules formulation. For a two-component system, the Margules model [also referred to as a subregular solution model (Hardy, 1953; Grover, 1977; Ganguly and Saxena, 1987)] describes g^{ex} as

$$g^{ex}/RT = \bar{X}_A \bar{X}_B \left(\bar{X}_B W_A + \bar{X}_A W_B\right) \qquad (2\text{-}15)$$

where W_A and W_B are empirical parameters that are functions only of temperature and pressure.

Representation of solid phase nonideality in terms of a g^{ex} model such as Eq. (2-15) makes convenient the calculation of zeolite solid solution and ion-exchange properties over the whole range of zeolite composition and the prediction of ion-exchange equilibria, which will be demonstrated in a

---

[2]The ion-interaction activity coefficient model uses a molal (moles/kg H_2O) concentration scale, whereas the solution concentrations in this study are in normal (equivalents/liter solution) or molar (moles/liter solution) units. The relationship between molarity- and molality-based mean activity coefficients ($\gamma_{\pm,M}$ and $\gamma_{\pm,m}$ respectively) is given by: $\gamma_{\pm,m} = \gamma_{\pm,M} \cdot M/(m \cdot \rho_o)$, where ρ_o is the density of water. At the highest ionic strength used in this study (I=0.75 for 0.5 N $CaCl_2$ solution), this correction amounts to less than 0.8 percent, which affects derived ion-exchange thermodynamic parameters by amounts which are small relative to errors introduced by analytical uncertainties. For convenience, molal activity coefficients were not converted to a molar basis, but were assigned uncertainties of ± 3 percent for the purpose of error propagation.

following section. Using the Gibbs-Duhem equation and Eqs. (2-14) and (2-15), ln f_A and ln f_B can be expressed in terms of W_A and W_B by

$$\ln f_A = \bar{X}_B^2\left[W_A + 2\bar{X}_A(W_B - W_A)\right]; \ln f_B = \bar{X}_A^2\left[W_B + 2\bar{X}_B(W_A - W_B)\right] \quad (2\text{-}16)$$

Similar expressions can be derived for systems with three or more components (Ganguly and Saxena, 1987; Grant and Sparks, 1989). The Vanselow selectivity coefficient, K_v, for the reaction represented by (2-1) can then be calculated from

$$\ln K_v = \ln K + z_A\bar{X}_A^2\left[W_B + 2\bar{X}_B(W_A - W_B)\right] - z_B\bar{X}_B^2\left[W_A + 2\bar{X}_A(W_B - W_A)\right] \quad (2\text{-}17)$$

K can be derived either by using Eq. (2-6) or by nonlinear regression of Eq. (2-17) to isotherm data (Grant and Sparks, 1989). If the zeolite phase behaves ideally, $f_A = f_B = 1$ and $g^{ex} = 0$ for all values of $\bar{X}_A$ (and $\bar{X}_B$), and $K = K_v$.

2.3 ION-EXCHANGE RESULTS AND DISCUSSION

The measured initial and final concentrations of Na^+, K^+, Ca^{2+}, or Sr^{2+} of the experimental solutions from the forward experiments are given in Tables 2-2 to 2-10. Also tabulated are the zeolite masses and solution volumes used in the experiments. Results of these binary ion-exchange experiments can be represented conveniently by ion-exchange isotherms, which are plots of the equilibrium fraction of an exchanging ion in solution versus the equilibrium fraction of that same ion in the zeolite at constant temperature and total solution concentration. The isotherm is usually plotted in terms of the equivalent cationic fraction of the ion in solution [Eq. (2-10)] against that in the solid [Eq. (2-9)] (Dyer et al., 1981). Values of $\bar{E}_K$, E_K, $\bar{E}_{Ca}$, E_{Ca}, $\bar{E}_{Sr}$, and E_{Sr} were calculated from the zeolite mass (W, grams), the solution volume (V, liters), and the initial (i) and final (f) molar concentrations (M, moles/liter solution) of K^+, Ca^{2+}, or Sr^{2+} given in Tables 2-2 to 2-10 using the equation

$$\bar{E}_A = z_A\left(M_{A,i} - M_{A,f}\right)V/(W \bullet CEC); \; E_A = z_A M_{A,f} / TN \quad (2\text{-}18)$$

where TN is the total cation normality of the aqueous phase and the subscript A refers to K^+, Ca^{2+}, or Sr^{2+}.

In most ion-exchange studies the initial and final solution concentrations of only one of the competing cations are measured. For example, both Ames (1964 a,b) and White (1988) measured only the solution concentrations of ^{22}Na in their study of K^+-Na^+ and Ca^{2+}-Na^+ ion-exchange equilibria. However, recent investigators have emphasized the need to analyze for each exchanging ion when constructing exchange isotherms (Townsend, 1986) because small errors in the analysis of an ion can cause large errors in the calculated isotherm points, particularly at the extremes of the isotherm plot. This is made clearer in the uncertainty analysis of isotherm data discussed in Appendix A. In this study, therefore, solution concentrations of Na^+ were analyzed in addition to those of K^+, Ca^{2+}, and Sr^{2+}. The Na^+ data permitted values of $\bar{E}_K$, E_K, $\bar{E}_{Ca}$, E_{Ca}, $\bar{E}_{Sr}$, and E_{Sr} to be independently calculated from the equation

Table 2-2. Experimental data for ion-exchange between clinoptilolite and 0.5 N NaCl/KCl solutions

Sample No.	Mass Zeolite (g)	Volume Solution ($L \times 10^{-3}$)	Initial Solution Concentration ($M \times 10^{-3}$)		Final Solution Concentration ($M \times 10^{-3}$)	
			Na^+	K^+	Na^+	K^+
1	1.0371	10	452	48.6	499	2.98
2	0.6143	10	452	48.6	490	6.15
3	0.4031	10	452	48.6	486	12.9
4	0.2259	10	452	48.6	475	24.4
5	0.4801	10	401	97.3	460	38.0
6	0.3960	10	401	97.3	453	43.4
7	0.3518	10	401	97.3	448	49.0
8	0.2306	10	401	97.3	431	64.3
9	0.4737	10	349	148	420	77.0
10	0.3686	10	349	148	403	93.0
11	0.2991	10	349	148	395	99.4
12	0.4606	10	300	197	376	123
13	0.2794	10	300	197	349	149
14	0.4067	10	252	242	321	175
15	0.5295	10	202	293	295	196
16	0.5150	10	151	336	243	241
17	0.7517	10	52.1	448	197	300
18	0.7354	10	0.0	494	141	346
19	0.6064	10	0.0	494	118	370
20	0.4800	10	0.0	494	94.5	398
21	0.2353	10	0.0	494	46.1	457

Table 2-3. Experimental data for ion-exchange between clinoptilolite and 0.05 N NaCl/KCl solutions

Sample No.	Mass Zeolite (g)	Volume Solution ($L \times 10^{-3}$)	Initial Solution Concentration ($M \times 10^{-3}$)		Final Solution Concentration ($M \times 10^{-3}$)	
			Na^+	K^+	Na^+	K^+
1	0.2592	25	45.2	5.09	49.2	0.248
2	0.1535	25	45.2	5.09	49.3	0.618
3	0.1007	25	45.2	5.09	49.3	1.15
4	0.1695	25	30.0	9.97	47.6	2.21
5	0.2160	25	34.8	14.9	46.0	3.64
6	0.1891	25	34.8	14.9	45.7	4.68
7	0.1760	25	34.8	14.9	44.8	5.01
8	0.1398	25	34.8	14.9	43.2	6.50
9	0.1972	25	30.1	19.8	42.1	7.75
10	0.1691	25	30.1	19.8	40.9	9.19
11	0.1495	25	30.1	19.8	39.8	9.94
12	0.1151	25	30.1	19.8	37.6	12.3
13	0.1396	25	25.1	25.2	34.7	15.1
14	0.1693	25	20.2	29.4	31.9	18.2
15	0.1897	25	15.0	34.0	29.1	20.9
16	0.1932	25	10.1	39.0	24.7	23.9
17	0.1880	25	4.94	44.0	19.5	29.0
18	0.1837	25	0.0	49.7	14.5	35.2
19	0.1518	25	0.0	49.7	12.1	37.3
20	0.1199	25	0.0	49.7	9.70	39.8
21	0.0587	25	0.0	49.7	4.89	42.2

Table 2-4. Experimental data for ion-exchange between clinoptilolite and 0.005 N NaCl/KCl solutions

Sample No.	Mass Zeolite (g)	Volume Solution ($L \times 10^{-3}$)	Initial Solution Concentration ($M \times 10^{-3}$)		Final Solution Concentration ($M \times 10^{-3}$)	
			Na^+	K^+	Na^+	K^+
1	0.1093	50	4.03	0.941	4.94	0.0263
2	0.1077	50	3.61	1.41	4.93	0.0610
3	0.0777	50	3.61	1.41	4.90	0.114
4	0.0790	50	3.03	1.89	4.77	0.214
5	0.0817	50	2.52	2.39	4.64	0.372
6	0.0738	50	2.52	2.39	4.51	0.462
7	0.0880	50	2.03	2.85	4.49	0.531
8	0.0774	50	2.03	2.85	4.28	0.719
9	0.0867	50	1.50	3.38	4.16	0.826
10	0.0799	50	1.50	3.38	4.05	0.949
11	0.0899	50	1.02	3.89	3.93	1.06
12	0.0806	50	1.02	3.89	3.66	1.29
13	0.0838	50	0.516	4.34	3.40	1.57
14	0.0745	50	0.516	4.34	3.12	1.85
15	0.0795	50	0.0	4.80	2.88	2.00
16	0.0645	50	0.0	4.80	2.45	2.47
17	0.1002	100	0.0	4.80	1.93	2.95
18	0.0736	100	0.0	4.80	1.48	3.47
19	0.0606	100	0.0	4.80	1.19	3.76
20	0.1202	250	0.0	4.80	0.974	3.99
21	0.0589	250	0.0	4.80	0.479	4.32

Table 2-5. Experimental data for ion-exchange between clinoptilolite and 0.5 N $NaCl/CaCl_2$ solutions

Sample No.	Mass Zeolite (g)	Volume Solution ($L\times10^{-3}$)	Initial Solution Concentration ($M\times10^{-3}$)		Final Solution Concentration ($M\times10^{-3}$)	
			Na^+	Ca^{2+}	Na^+	Ca^{2+}
1	1.5359	5	452	23.8	496	5.91
2	1.8430	5	396	47.9	480	12.3
3	1.3441	5	396	47.9	465	16.6
4	0.8639	5	396	47.9	458	23.7
5	1.2801	5	358	72.1	447	30.2
6	1.3072	5	358	72.1	428	34.9
7	0.7680	5	358	72.1	422	40.2
8	0.9599	5	306	96.3	388	52.1
9	0.6399	5	306	96.3	372	60.6
10	0.7946	5	251	122	346	76.1
11	0.6876	5	203	146	297	97.1
12	0.5984	5	153	174	247	124
13	0.5240	5	102	196	197	147
14	0.3677	5	102	196	167	161
15	0.4653	5	51.3	224	151	174
16	0.3292	5	51.3	224	124	186
17	0.4191	5	0.0	252	101	203
18	0.3377	5	0.0	252	85.6	208
19	0.4911	10	0.0	252	65.2	211
20	0.3439	10	0.0	252	48.7	223
21	0.2209	10	0.0	252	34.1	233
22	0.1459	10	0.0	252	23.8	238

Table 2-6. Experimental data for ion-exchange between clinoptilolite and 0.05 N $NaCl/CaCl_2$ solutions

Sample No.	Mass Zeolite (g)	Volume Solution ($L\times10^{-3}$)	Initial Solution Concentration ($M\times10^{-3}$)		Final Solution Concentration ($M\times10^{-3}$)	
			Na^+	Ca^{2+}	Na^+	Ca^{2+}
1	0.2446	25	44.8	2.36	49.2	0.484
2	0.1492	25	44.8	2.36	48.7	0.898
3	0.2879	25	40.0	4.87	47.4	1.40
4	0.2034	25	40.0	4.87	46.1	2.04
5	0.1555	25	40.0	4.87	45.2	2.54
6	0.2057	25	35.2	7.39	41.3	3.84
7	0.2559	25	30.3	9.76	40.0	5.06
8	0.1800	25	30.3	9.76	37.4	6.21
9	0.2304	25	25.4	12.0	35.2	7.36
10	0.2174	25	20.3	14.6	30.0	9.63
11	0.2022	25	15.2	17.3	25.2	12.2
12	0.1465	25	15.2	17.3	22.6	13.5
13	0.1858	25	10.2	20.3	20.0	14.6
14	0.2321	25	5.09	22.6	17.4	16.0
15	0.2541	25	0.0	25.4	15.2	17.3
16	0.1999	25	0.0	25.4	12.6	18.6
17	0.1516	25	0.0	25.4	10.0	20.06
18	0.2136	50	0.0	25.4	7.39	21.5
19	0.1356	50	0.0	25.4	5.22	22.9
20	0.0640	50	0.0	25.4	2.61	23.8

Table 2-7. Experimental data for ion-exchange between clinoptilolite and 0.005 N $NaCl/CaCl_2$ solutions

Sample No.	Mass Zeolite (g)	Volume Solution ($L\times10^{-3}$)	Initial Solution Concentration ($M\times10^{-3}$)		Final Solution Concentration ($M\times10^{-3}$)	
			Na^+	Ca^{2+}	Na^+	Ca^{2+}
1	0.1453	50	3.50	0.760	4.94	0.0483
2	0.0916	50	3.45	0.760	4.89	0.0765
3	0.1008	50	3.00	1.01	4.65	0.145
4	0.0802	50	3.00	1.01	4.70	0.180
5	0.0940	50	2.51	1.26	4.55	0.245
6	0.0806	50	2.51	1.26	4.35	0.328
7	0.0803	50	2.00	1.53	4.13	0.447
8	0.0711	50	2.00	1.53	3.97	0.526
9	0.0902	50	1.49	1.77	3.93	0.536
10	0.0800	50	1.49	1.77	3.71	0.621
11	0.0914	50	0.983	2.02	3.60	0.695
12	0.0798	50	0.983	2.02	3.34	0.802
13	0.0862	50	0.484	2.27	3.06	0.797
14	0.0759	50	0.484	2.27	2.82	1.07
15	0.0822	50	0.0	2.48	2.51	1.21
16	0.0624	50	0.0	2.48	2.03	1.46
17	0.1055	100	0.0	2.48	1.75	1.59
18	0.0888	100	0.0	2.48	1.50	1.70
19	0.0712	100	0.0	2.48	1.24	1.81
20	0.0555	100	0.0	2.48	0.966	1.99
21	0.0992	250	0.0	2.48	0.7163	2.10
22	0.0640	250	0.0	2.48	0.4724	2.25
23	0.0308	250	0.0	2.48	0.2379	2.33

Table 2-8. Experimental data for ion-exchange between clinoptilolite and 0.5 N $NaCl/SrCl_2$ solutions

Sample No.	Mass Zeolite (g)	Volume Solution ($L \times 10^{-3}$)	Initial Solution Concentration ($M \times 10^{-3}$)		Final Solution Concentration ($M \times 10^{-3}$)	
			Na^+	Sr^{2+}	Na^+	Sr^{2+}
1	1.6259	10	475	12.5	492	1.66
2	1.4012	10	450	25.0	478	6.02
3	1.9243	10	400	50.0	468	12.8
4	0.8024	10	400	50.0	435	28.1
5	0.9146	10	350	75.0	404	45.2
6	1.1063	10	300	100	373	59.6
7	0.5315	10	300	100	345	77.8
8	0.7589	10	250	125	315	91.3
9	0.6069	10	200	150	262	119
10	0.5759	10	150	175	214	144
11	0.6163	10	100	200	173	162
12	0.6093	10	50.0	225	128	185
13	0.7200	10	0.0	250	97.9	203
14	0.4967	10	0.0	250	71.8	217
15	0.8588	25	0.0	250	51.3	224
16	0.5877	25	0.0	250	36.4	232
17	0.3931	25	0.0	250	24.4	237
18	0.2460	100	0.0	250	4.74	248

Table 2-9. Experimental data for ion-exchange between clinoptilolite and 0.05 N $NaCl/SrCl_2$ solutions

Sample No.	Mass Zeolite (g)	Volume Solution ($L\times10^{-3}$)	Initial Solution Concentration ($M\times10^{-3}$)		Final Solution Concentration ($M\times10^{-3}$)	
			Na^+	Sr^{2+}	Na^+	Sr^{2+}
1	0.3102	25	45.7	2.50	50.2	0.188
2	0.1659	25	45.7	2.50	49.4	0.419
3	0.1032	25	45.7	2.50	48.8	0.906
4	0.2321	25	40.6	5.00	47.7	1.16
5	0.1519	25	40.6	5.00	46.5	2.14
6	0.1941	25	35.5	7.50	43.6	3.43
7	0.2186	25	30.4	10.00	40.4	5.04
8	0.2658	25	25.4	12.5	37.9	6.19
9	0.2809	25	20.3	15.0	34.2	7.92
10	0.3182	25	15.3	17.5	31.5	9.37
11	0.2756	25	10.3	20.0	25.7	12.5
12	0.3035	25	5.09	22.5	22.4	14.1
13	0.2867	25	0.0	25.0	17.1	16.3
14	0.2005	25	0.0	25.0	12.7	18.7
15	0.3088	50	0.0	25.0	9.96	20.3
16	0.2407	50	0.0	25.0	8.22	21.2
17	0.1893	50	0.0	25.0	6.39	21.9
18	0.1269	50	0.0	25.0	4.52	22.8

Table 2-10. Experimental data for ion-exchange between clinoptilolite and 0.005 N NaCl/$SrCl_2$ solutions

Sample No.	Mass Zeolite (g)	Volume Solution ($L\times10^{-3}$)	Initial Solution Concentration ($M\times10^{-3}$)		Final Solution Concentration ($M\times10^{-3}$)	
			Na^+	Sr^{2+}	Na^+	Sr^{2+}
1	0.0957	50	4.524	0.251	5.133	0.001
2	0.1023	100	4.524	0.251	5.089	0.006
3	0.1621	100	4.015	0.502	5.046	0.008
4	0.1061	100	4.015	0.502	5.002	0.039
5	0.1363	100	3.493	0.753	4.959	0.050
6	0.1520	100	3.006	1.004	4.872	0.090
7	0.1746	100	2.492	1.255	4.785	0.148
8	0.1532	100	2.492	1.255	4.611	0.239
9	0.1628	100	2.001	1.495	4.345	0.375
10	0.1727	100	1.514	1.746	4.076	0.488
11	0.1831	100	1.000	1.997	3.789	0.638
12	0.1821	100	0.496	2.248	3.371	0.843
13	0.1704	100	0.0	2.499	2.736	1.134
14	0.1478	100	0.0	2.499	2.431	1.289
15	0.1280	100	0.0	2.499	2.127	1.445
16	0.1011	100	0.0	2.499	1.696	1.634
17	0.0729	100	0.0	2.499	1.266	1.887
18	0.1124	250	0.0	2.499	0.779	2.085
19	0.0574	250	0.0	2.499	0.418	2.306
20	0.0303	250	0.0	2.499	0.226	2.412

$$\bar{E}_A = z_B(M_{B,f} - M_{B,i})V/(W \bullet CEC); \; E_A = 1 - z_B M_{B,f} / TN \qquad (2\text{-}19)$$

where the subscript B refers to Na^+.

The isotherm data for the NaCl/KCl, NaCl/$CaCl_2$, and NaCl/$SrCl_2$ mixtures are plotted in Figures 2-1, 2-2, and 2-3, respectively. In these figures, the circles are equivalent cationic fractions calculated from either the K^+, Ca^{2+}, or Sr^{2+} analytical data, whereas the squares are equivalent cationic fractions calculated from the Na^+ analytical results. Isotherm points calculated using the two methods generally agree with each other within experimental uncertainty. Error bars, which were calculated using equations given in Appendix A, are shown for some isotherm points (for clarity not all error bars are indicated). The open symbols in these figures represent forward isotherm data, whereas solid symbols represent reversed isotherm data. For clarity of the figures, data on reproducibility of the isotherms are not plotted. The symbols are numbered to identify corresponding points from the forward and reverse experiments. These data indicate that ion-exchange reactions between clinoptilolite and aqueous solutions of Na^+/K^+, Na^+/Ca^{2+}, and Na^+/Sr^{2+} are reversible.

The results shown in Figures 2-2 and 2-3 indicate a strong dependence of isotherm shape on total solution concentrations for the systems Ca^{2+}-Na^+ and Sr^{2+}-Na^+, which involve ion-exchange between a monovalent and a divalent cation. On the other hand this dependence is small for K^+-Na^+ ion-exchange, which involves two monovalent cations. The strong dependence of isotherm shapes on solution concentration for heterovalent ion-exchange reactions is a consequence of the law of mass action for isotherms plotted in terms of equivalent cationic mole fractions. This is discussed in detail by Barrer and Klinowski (1974) and Sposito (1981). Figures 2-2 and 2-3 illustrate that with increasing dilution clinoptilolite exhibits increasing preference ("selectivity") for the cation of higher charge. This behavior, commonly referred to as "concentration-valency effect", gives rise to isotherms that become more rectangular and selective to the ion of higher charge with increasing dilution for ion-exchange reactions where $z_A \neq z_B$. It illustrates the reason Ca^{2+} can be removed from dilute aqueous solutions by synthetic ion-exchangers such as water softeners, whereas an exhausted exchanger in Ca^{2+} form can be regenerated into Na^+ form with concentrated NaCl solution.

It is possible to predict ion-exchange equilibria for a wide range of phase compositions and aqueous concentrations based on thermodynamic parameters derived from a single experimental isotherm. These predictions rest on the assumption that the ratio of activity coefficients for the zeolite components varies little as the total concentration of the aqueous phase changes. It is also assumed that the effects of water activity changes and salt imbibition are negligible. The only requirement is that aqueous solution activity coefficients can be calculated by some thermodynamic means. To evaluate the use of the Margules model to describe and predict ion-exchange equilibria between clinoptilolite and aqueous solutions, Eq. (2-17) was fit to values of ln K_v versus $\bar{X}_i$, derived from the 0.5-N isotherm data. In a manner analogous to that used in calculating the isotherm points, one set of ln K_v versus $\bar{X}_i$ values was calculated from the K^+, Ca^{2+}, or Sr^{2+} analytical data and another set from the Na^+ data using the respective equations

$$K_v = \left\{\left(\bar{X}_A\right)^{z_B}\left[\left(TN - z_A M_A\right)/z_B\right]^{z_A}\right\} / \left[\left(1 - \bar{X}_A\right)^{z_A}\left(M_A\right)^{z_B}\right]\left[\left(\gamma_B\right)^{z_A} / \left(\gamma_A\right)^{z_B}\right] \qquad (2\text{-}20)$$

and

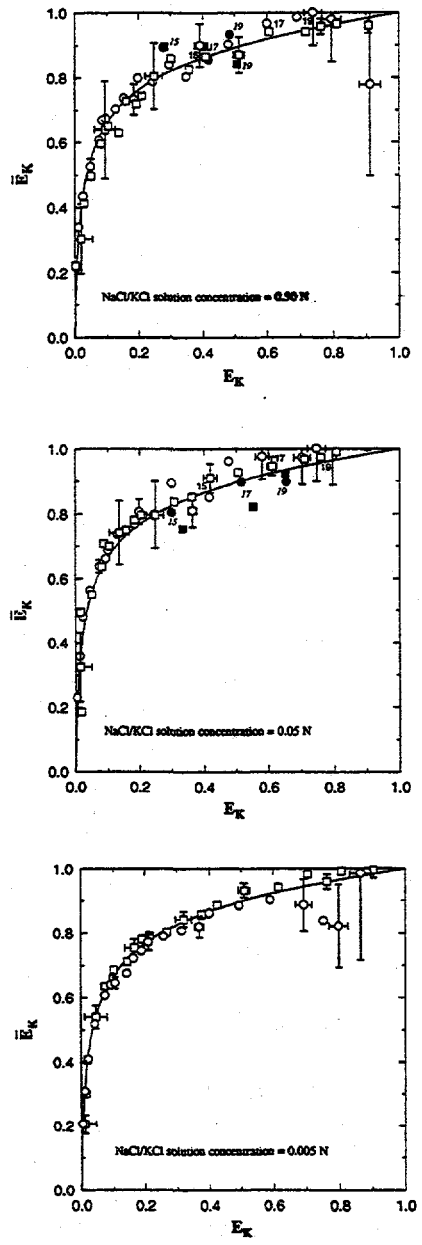

Figure 2-1. Isotherms for ion-exchange at 25 °C between clinoptilolite and NaCl/KCl aqueous mixtures at total solution concentrations of (a) 0.5, (b) 0.05, and (c) 0.005 N. Circles and squares represent isotherm points calculated from solution concentrations of K^+ and Na^+, respectively. Open and solid symbols are isotherm data from forward and reverse experiments, respectively. Numbers identify corresponding points from the two experiments. Error bars for some points are indicated. The curve in Figure 2-1(a) was fit to the 0.5-N isotherm data using a Margules solid solution model. The curves in Figures 2-1(b) and 2-1(c) represent isotherm points predicted using a Margules solid solution model with parameters derived from the 0.5-N isotherm data.

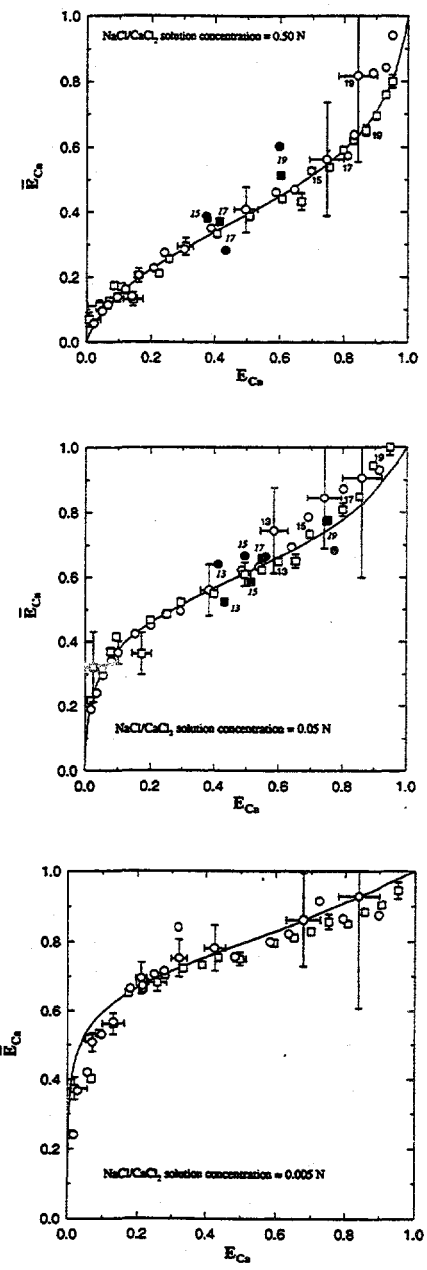

Figure 2-2. Isotherms for ion-exchange at 25 °C between clinoptilolite and NaCl/$CaCl_2$ aqueous mixtures at total solution concentrations of (a) 0.5, (b) 0.05, and (c) 0.005 N. Circles and squares represent isotherm points calculated from solution concentrations of Ca^{2+} and Na^{+}, respectively. Open and solid symbols are isotherm data from forward and reverse experiments, respectively. Numbers identify corresponding points from the two experiments. Error bars for some points are indicated. The curve in Figure 2-2(a) was fit to the 0.5-N isotherm data using a Margules solid solution model. The curves in Figures 2-2(b) and 2-2(c) represent isotherm points predicted using a Margules solid solution model with parameters derived from the 0.5-N isotherm data.

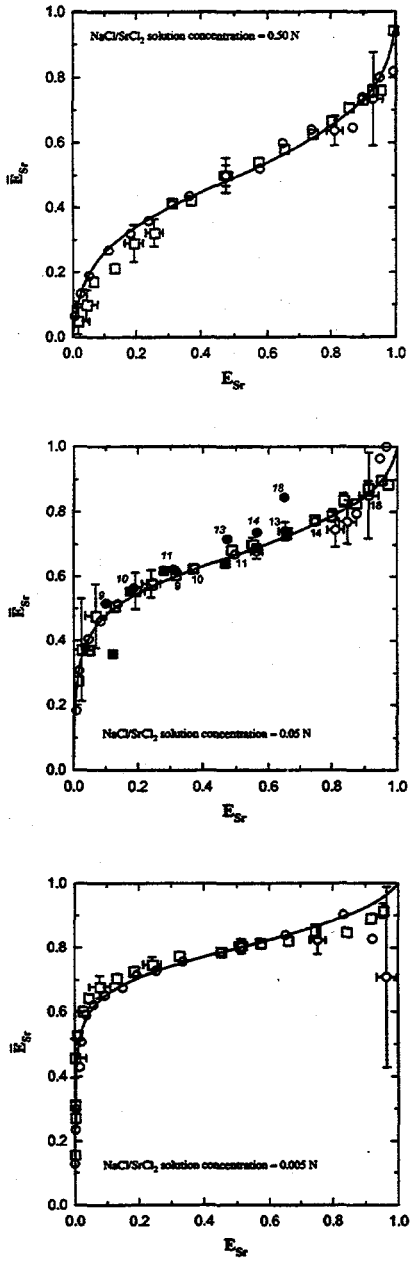

Figure 2-3. Isotherms for ion-exchange at 25 °C between clinoptilolite and $NaCl/SrCl_2$ aqueous mixtures at total solution concentrations of (a) 0.5, (b) 0.05, and (c) 0.005 N. Circles and squares represent isotherm points calculated from solution concentrations of Sr^{2+} and Na^+, respectively. Open and solid symbols are isotherm data from forward and reverse experiments, respectively. Numbers identify corresponding points from the two experiments. Error bars for some points are indicated. The curve in Figure 2-3(a) was fit to the 0.5-N isotherm data using a Margules solid solution model. The curves in Figures 2-3(b) and 2-3(c) represent isotherm points predicted using a Margules solid solution model with parameters derived from the 0.5-N isotherm data.

$$K_v = \left[(1-\bar{X}_B)^{z_B}(M_B)^{z_A}\right] / \left\{(\bar{X}_B)^{z_A}\left[(TN - z_B M_B)/z_A\right]^{z_B}\right\} \left[(\gamma_B)^{z_A}/(\gamma_A)^{z_B}\right] \qquad (2\text{-}21)$$

where subscript A represents K^+, Ca^{2+}, or Sr^{2+} and subscript B represents Na^+. Aqueous activity coefficients were calculated using the ion-interaction model and the parameters listed in Table 2-11. Values of ln K_v versus $\bar{X}_i$ for the NaCl/KCl, NaCl/$CaCl_2$, and NaCl/$SrCl_2$ mixtures are plotted in Figures 2-4, 2-5, and 2-6, respectively, where the circles represent values calculated either from the K^+, Ca^{2+}, or Sr^{2+} analysis and the squares represent values derived from the Na^+ data. In the regression ln K_v was weighted inversely to the square of its estimated overall uncertainty (see Appendix A).

Regression of Eq. (2-17) to the 0.5-N NaCl/KCl data resulted in values of W_{Na} and W_K equal to -1.41 ± 0.12 and -0.99 ± 0.11, respectively. Values of W_{Na} and W_{Ca} equal to -1.22 ± 0.30 and -2.67 ± 0.07, respectively, were derived from the 0.5-N NaCl/$CaCl_2$ data. Regression of the 0.5-N NaCl/$SrCl_2$ data resulted in values of W_{Na} and W_{Sr} equal to -2.73 ± 0.36 and -3.37 ± 0.09, respectively. Excess Gibbs energies (g^{ex}) and zeolite component activity coefficients calculated from these parameters and Eqs. (2-15) and (2-16) are plotted in Figures 2-7 and 2-8, respectively. For reaction (2-1) where A and B correspond to K^+ and Na^+, respectively, the ln K derived by fitting Eq. (2-17) to isotherm data is equal to 3.22 ± 0.03; the corresponding value of $\Delta G°$ is $-7{,}980\pm80$ J/mol. Where A and B correspond to Ca^{2+} and Na^+, respectively, the derived ln K and $\Delta G°$ for reaction (2-1) are -1.65 ± 0.08 and $4{,}090\pm200$ J/mol. For reaction (2-1) where A and B correspond to Sr^{2+} and Na^+, respectively, the derived ln K and $\Delta G°$ are -0.891 ± 0.095 and $2{,}210\pm240$ J/mol. The derived parameters are summarized in Table 2-12.

From the known values of the equilibrium constant, K, and the Margules parameter, W_i, values of K_v can be calculated for a given zeolite composition, $\bar{X}_i$, using Eq. (2-17). If the total solution normality is known and aqueous activity coefficients can be calculated, then the composition of the aqueous solution in equilibrium with the zeolite can be solved from Eq. (2-5). The curves in Figures 2-1a, 2-2a, and 2-3a represent 0.5-N isotherm values calculated from the parameters given previously. The curves in Figures 2-1b, 2-1c, 2-2b, 2-2c, 2-3b, and 2-3c represent predicted isotherms at 0.05 or 0.005-N solution concentration calculated using the parameters derived from the 0.5-N data. As shown in these figures, there is very good agreement between experimental values and those calculated using the Margules model. Ca^{2+}-Na^+ and Sr^{2+}-Na^+ isotherms calculated using the Margules model for aqueous concentrations from 0.0005 to 1.0 N are plotted in Figure 2-9, which also illustrates the strong dependence of isotherm shape on solution concentration for heterovalent exchange reactions.

Although the use of monoanionic electrolyte solution is adequate for thermodynamic characterization of ion-exchange phenomena (Fletcher and Townsend, 1985), ion-exchange reactions that occur in geochemical systems involve aqueous solutions with variable anionic species. As an initial test of the possible effect of anionic composition on ion-exchange equilibria, isotherm experiments were also conducted in this study using 0.05-N mixtures of $NaNO_3/KNO_3$ and $NaNO_3/Ca(NO_3)_2$. The results of these experiments are plotted in Figures 2-10 and 2-11. The solid curves in these figures represent isotherms predicted using Margules parameters derived previously from data in Cl^- systems, and using γ's calculated for $NaNO_3/KNO_3$ or $NaNO_3/Ca(NO_3)_2$ solutions. A comparison of Figures 2-1b and 2-2b with Figures 2-10 and 2-11 indicates that for exchanges involving Na^+/K^+ or Na^+/Ca^{2+} solutions and clinoptilolite, the isotherm for systems with Cl^- as the aqueous anion is essentially identical to that for systems with NO_3^- as the anion. Fletcher and Townsend (1985) similarly observed that the isotherm for

Table 2-11. Ion-interaction parameters used in this study to calculate aqueous activity coefficients using the Pitzer equations*

Single Electrolyte Parameters			
Electrolyte	$\beta^{(0)}$	$\beta^{(1)}$	C^{ϕ}
NaCl	0.0765	0.2664	0.00127
KCl	0.04835	0.2122	−0.00084
$CaCl_2$	0.3159	1.614	−0.00034
$SrCl_2$	0.2858	1.6673	−0.00130
$NaNO_3$	0.0068	0.1783	−0.00072
KNO_3	−0.0816	0.0494	0.00660
$Ca(NO_3)_2$	0.2108	1.409	−0.02014

Mixture parameters					
$\theta_{Na,K}$	= −0.012	$\theta_{Na,Ca}$	= 0.07	$\theta_{Na,Sr}$	= 0.051
$\psi_{Na,K,Cl}$	= −0.0018	ψ_{Na,K,NO_3}	= −0.0012	$\psi_{Na,Sr,Cl}$	= −0.0021
$\psi_{Na,Ca,Cl}$	= −0.007	ψ_{Na,Ca,NO_3}	= −0.007		

*Values were taken from Pitzer (1991), except for $\theta_{Na,Ca}$, $\psi_{Na,Sr,Cl}$, and ψ_{Na,Ca,NO_3}. Values of $\theta_{Na,Sr}$ and $\psi_{Na,Sr,Cl}$ were taken from Reardon and Armstrong (1987), and the value of ψ_{Na,Ca,NO_3} is based on the $NaNO_3$+$Ca(NO_3)_2$ solution activity coefficient data of Smith et al. (1993).

ion-exchange between zeolite X and $NaNO_3/Ca(NO_3)_2$ solutions is indistinguishable from that for ion-exchange involving $NaClO_4/Ca(ClO_4)_2$ solutions. Their study indicated that the solution activity ratios for Na^+ and Ca^{2+} ions in Eqs. (2-4) and (2-5) are not very much different for NO_3^- and ClO_4^- solutions. This is also apparently the case for the Cl^- and NO_3^- solutions of Na^+/K^+ and Na^+/Ca^{2+} used in this study. However, ion-exchange data on zeolite X and Na^+/Cd^{2+} solutions showed that the activity coefficient ratios in Cl^-, NO_3^-, and mixed Cl^-/NO_3^- matrix are sufficiently different to result in different isotherms for different anionic compositions (Fletcher and Townsend, 1985). In cases such as this, failure to use correct mixed electrolyte solution activity coefficients would lead to a serious error in derived K and $\Delta G°$ for the ion-exchange reaction, particularly for ternary or more complicated ion-exchange reactions (Fletcher and Townsend, 1981, 1983).

Equilibrium constants derived from this study are different from those determined by Ames (1964 a,b), who gives ln K values of 2.54, −0.161, and 0.255 for the K^+-Na^+, Ca^{2+}-Na^+, and Sr^{2+}-Na^+ systems, respectively, based on his experiments at a total solution concentration of 1.0 N. The differences are largely due to his use of a different activity coefficient model for the aqueous solution, and partly due to his use of a different clinoptilolite material. A reevaluation of his isotherm data using the Pitzer equations for aqueous activity coefficients yields ln K's for K^+-Na^+, Ca^{2+}-Na^+, and Sr^{2+}-

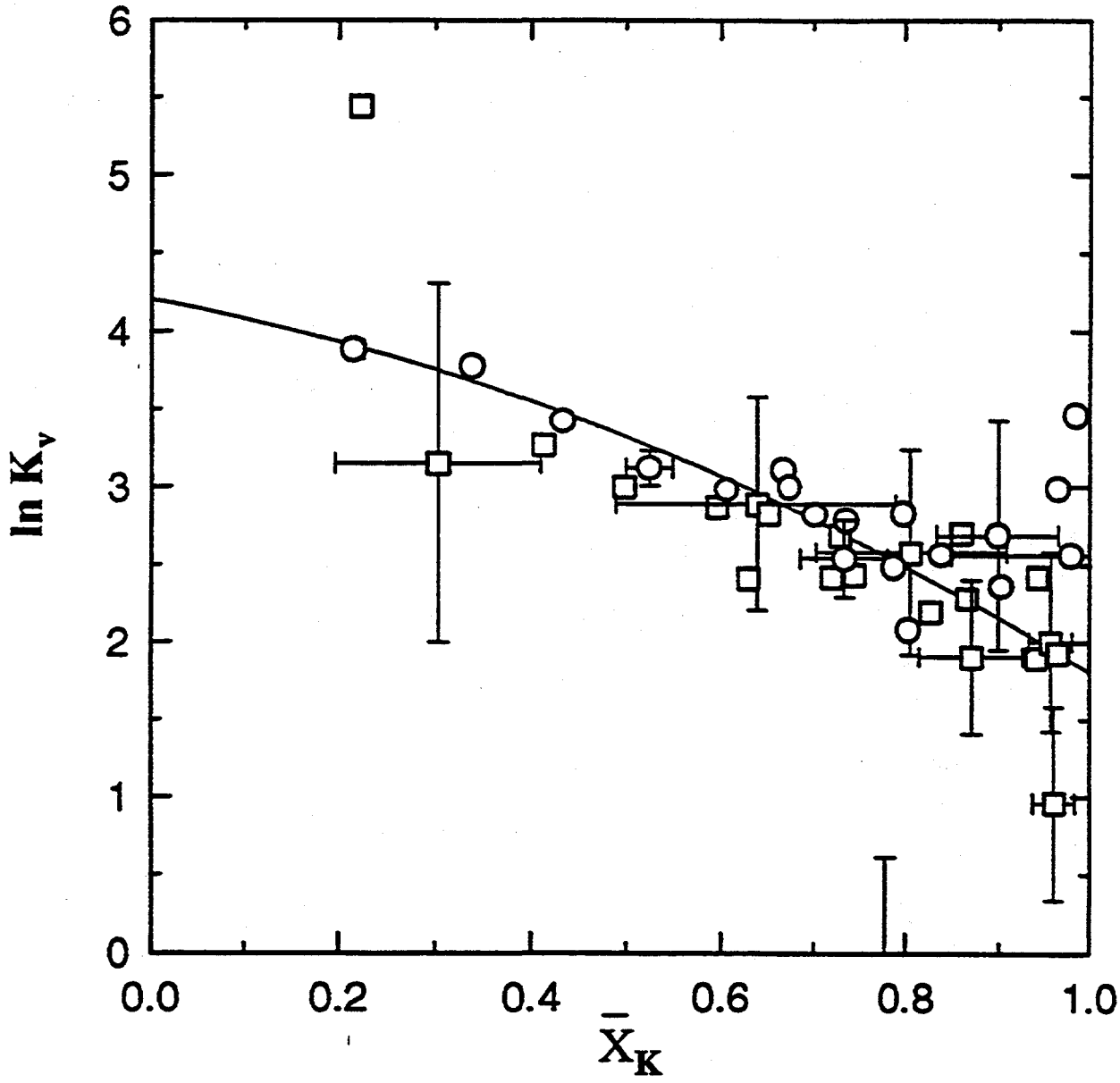

Figure 2-4. Vanselow corrected selectivity coefficient versus zeolite composition calculated from the 0.5-N NaCl/KCl isotherm data given in Table 2-2. Circles and squares were calculated from K^+ and Na^+ data, respectively. Error bars are indicated for some isotherm points. The curve was calculated using a Margules model, the parameters of which were derived by fitting to data represented by the symbols.

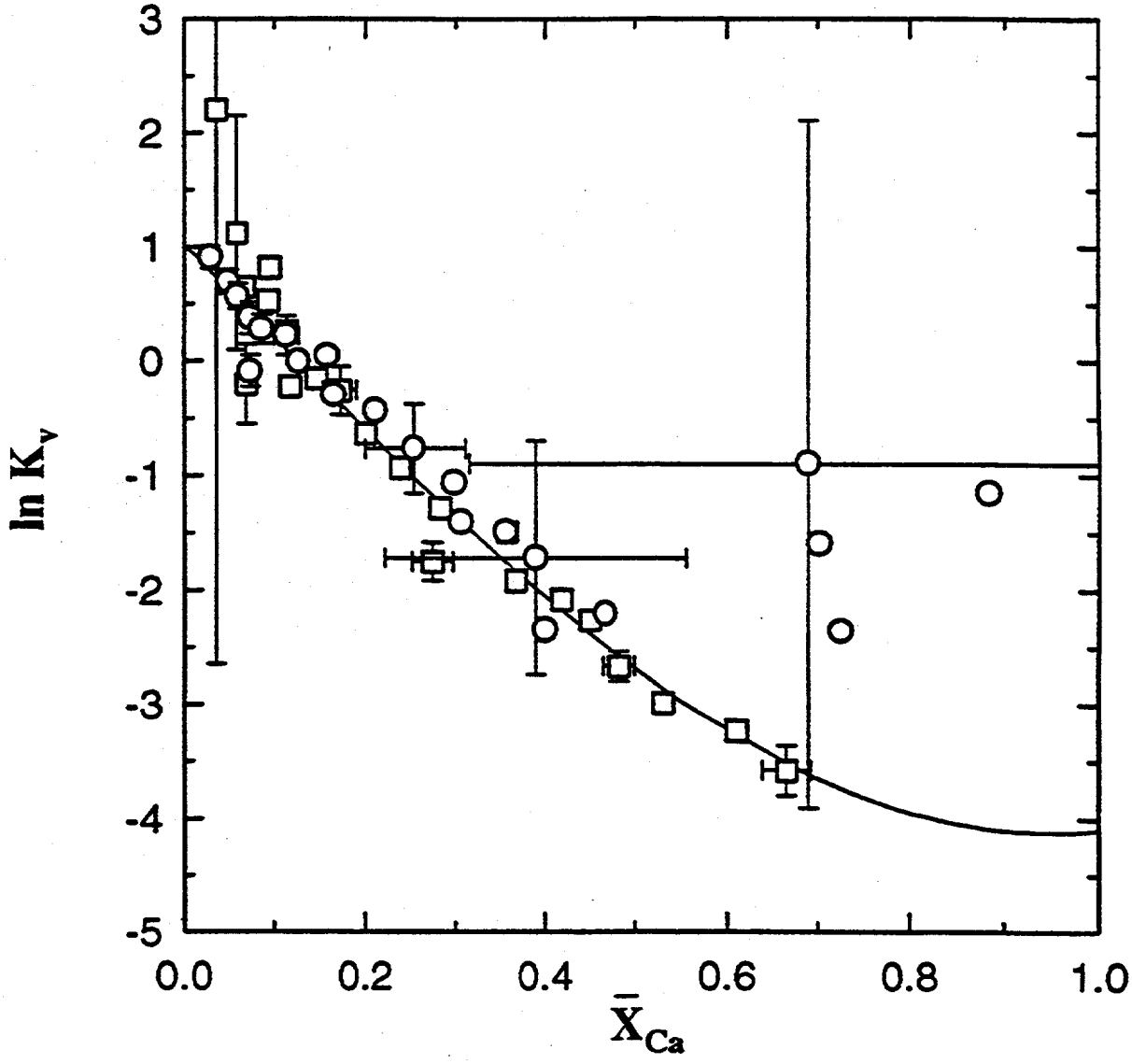

Figure 2-5. Vanselow corrected selectivity coefficient versus zeolite composition calculated from the 0.5-N NaCl/$CaCl_2$ isotherm data given in Table 2-5. Circles and squares were calculated from Ca^{2+} and Na^+ data, respectively. Error bars are indicated for some isotherm points. The curve was calculated using a Margules model, the parameters of which were derived by fitting to data represented by the symbols.

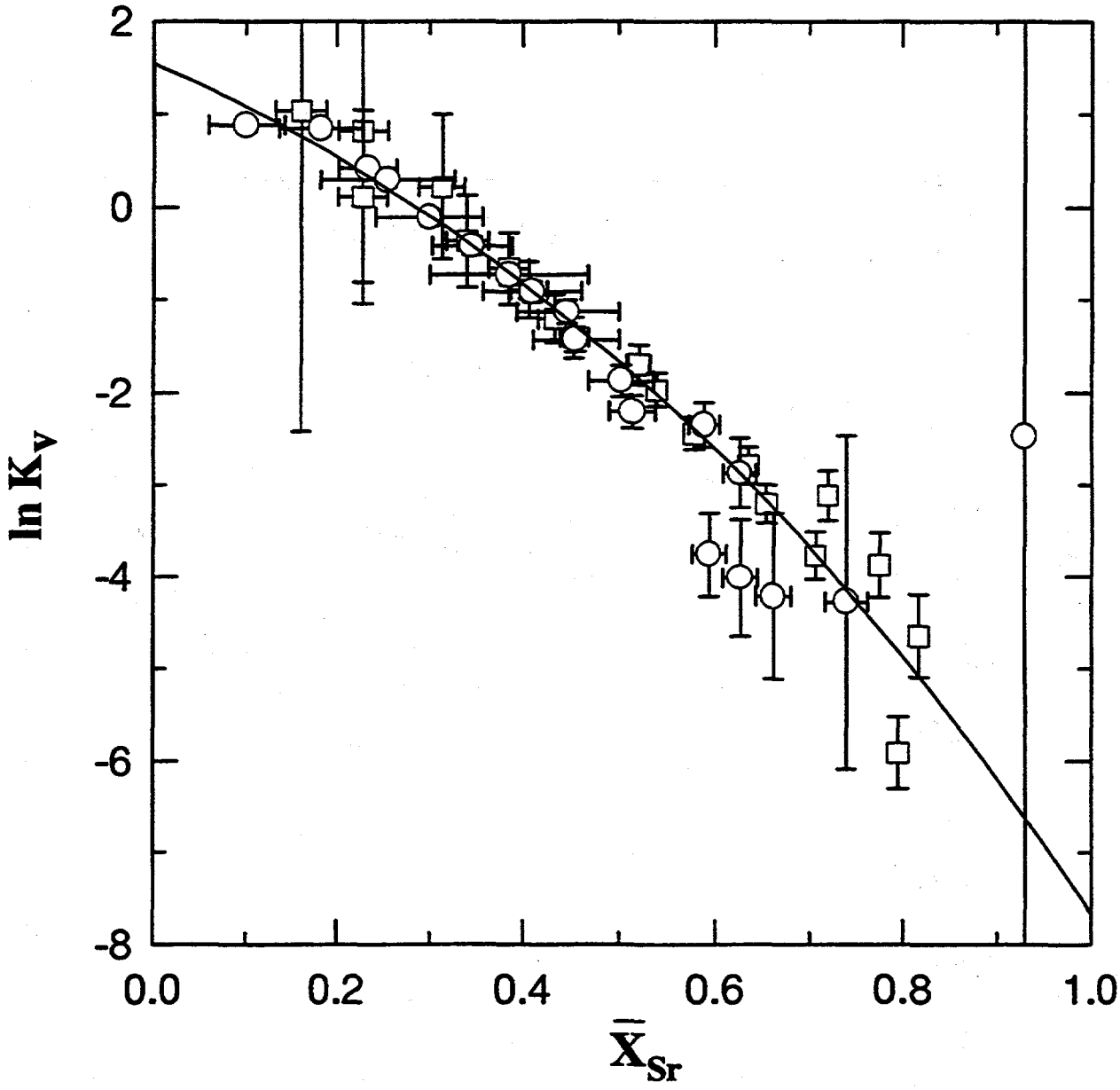

Figure 2-6. Vanselow corrected selectivity coefficient versus zeolite composition calculated from the 0.5-N NaCl/$SrCl_2$ isotherm data given in Table 2–8. Circles and squares were calculated from Sr^{2+} and Na^+ data, respectively. Error bars are indicated for some isotherm points. The curve was calculated using a Margules model, the parameters of which were derived by fitting to data represented by the symbols.

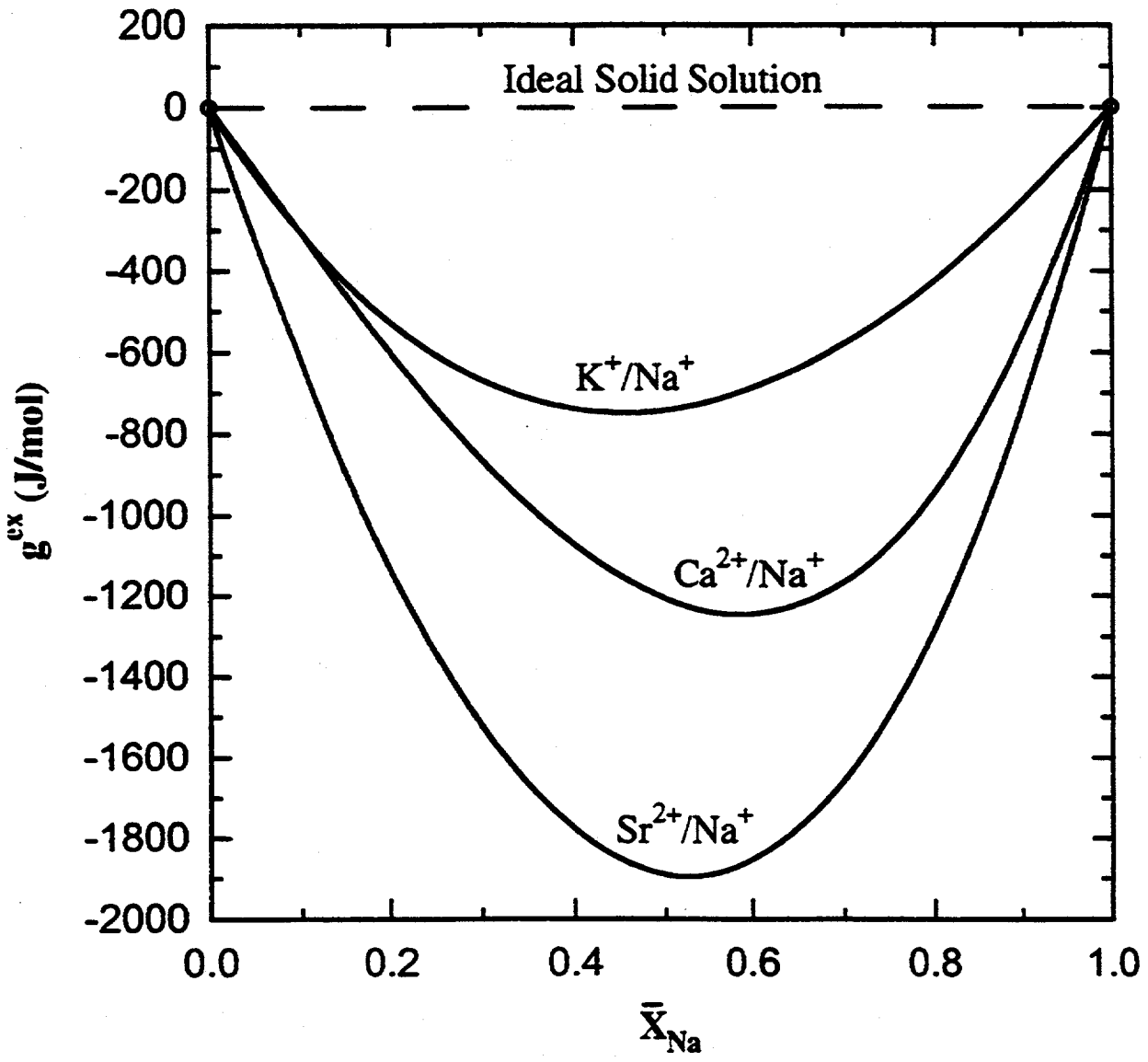

Figure 2-7. Excess Gibbs energy of mixing for (K^+, Na^+), (Ca^{2+}, Na^+) and (Sr^{2+}, Na^+) clinoptilolite solid solutions calculated using Margules parameters derived from the 0.5-N isotherm data

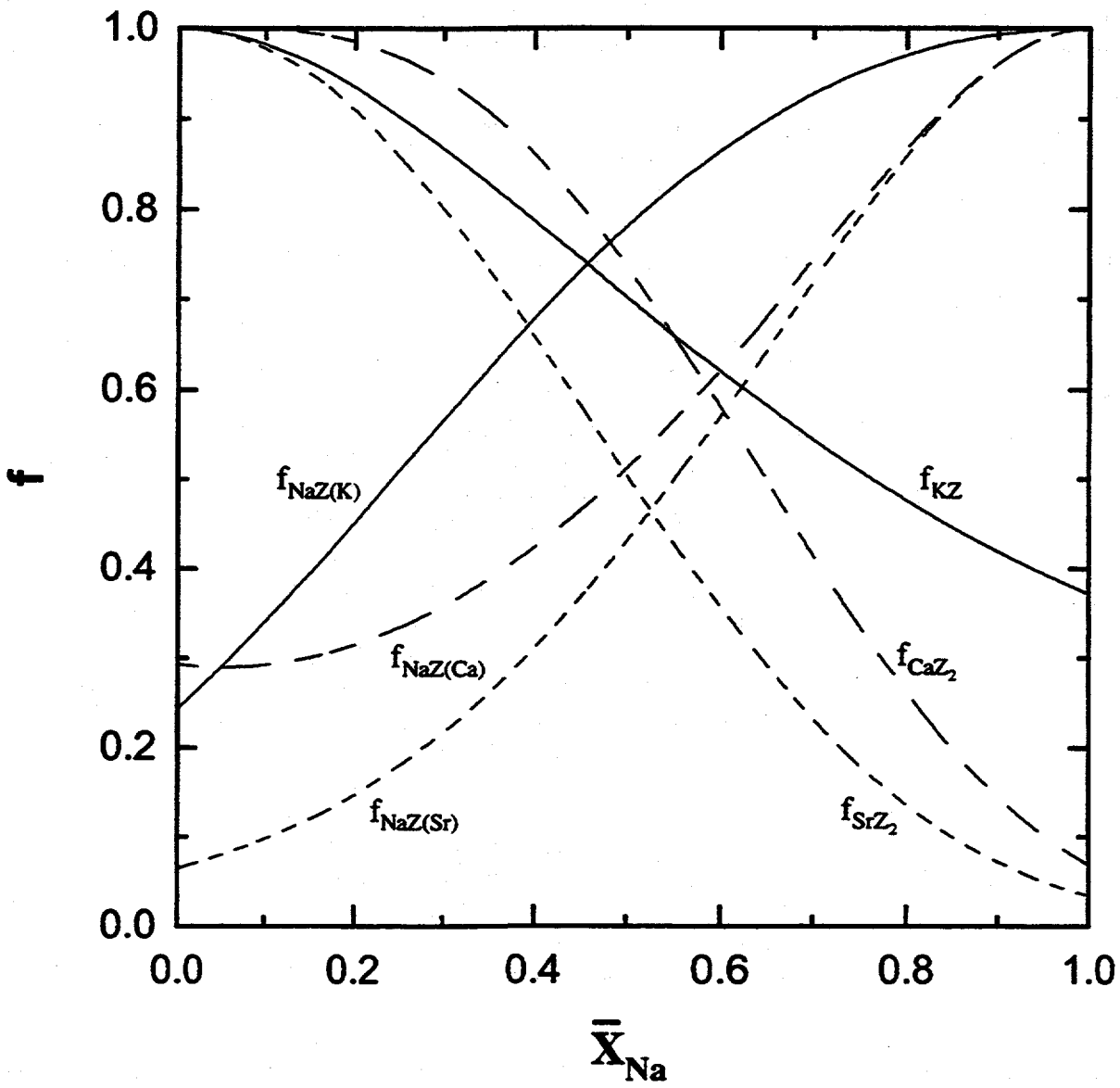

Figure 2-8. Activity coefficients for zeolite components of (K^+, Na^+), (Ca^{2+}, Na^+) and (Sr^{2+}, Na^+) clinoptilolite solid solutions (solid, long dashed, and short dashed lines, respectively) calculated using Margules parameters derived from the 0.5-N isotherm data

Table 2-12. Thermodynamic parameters for ion-exchange reactions represented by Eq. (2-1) derived from 0.5N data

A^{ZA+}/B^{ZB+}	ln K	$\Delta G°$(J/mol)	W_A	W_B
K^+/Na^+	3.22±.03	−7,980±80	−0.99±0.11	−1.41±0.12
Ca^{2+}/Na^+	−1.65±.08	4,090±200	−2.67±0.07	−1.22±0.30
Sr^{2+}/Na^+	−0.891±.095	2,210±240	−3.37±0.09	−2.73±0.36

Na^+ equal to 3.0, −1.69, and −1.04, respectively, which are very close to values determined in this study. The recalculated $\Delta G°$ values for exchanges involving K^+-Na^+, Ca^{2+}-Na^+, and Sr^{2+}-Na^+ are −7,510, 4,190, and 2,590 J/mol, respectively.

2.4 SOLUTION COMPOSITIONS CALCULATED FROM ZEOLITE ANALYSIS

Little information is available on the groundwater chemistry for the hydrologically unsaturated zone of Yucca Mountain, Nevada. Although some efforts have been made to extract aqueous solutions by high-pressure triaxial compression of rock samples taken from the vadose zone of Yucca Mountain (Yang et al., 1988; Peters et al., 1992; see Section 4.2.4), there are large variabilities in the chemical composition of solutions derived using this technique. Aqueous samples have also been extracted from unsaturated soils and sands by ultracentrifugation techniques (Edmunds et al., 1992; Puchelt and Bergfeldt, 1992). It is uncertain whether compositions of water extracted from rock pores by ultracentrifugation or by high-pressure squeezing methods accurately represent the compositions of *in situ* water. Water extracted in these manners are likely to have compositions different from those of *in situ* water due to several possible processes (Peters et al., 1992): (i) dilution of pore solutions by water desorbed from hydrated minerals like zeolites and clays, (ii) dissolution reactions due to increased mineral solubility and/or higher carbon dioxide concentration at higher pressures, (iii) membrane filtration by clays and zeolites, and (iv) ion-exchange with the zeolites and clays.

The thermodynamic model for ion-exchange equilibria discussed in Section 2.2 may provide a foundation for reducing uncertainties associated with groundwater compositions in the unsaturated stratigraphic horizons of Yucca Mountain, Nevada. Using the thermodynamic model, it may be possible to constrain the water cation chemistry based on composition data on natural zeolites, such as those derived by electron microprobe techniques. Such studies may provide useful information on past flow and transport and on the aqueous chemistry of groundwater in the unsaturated zone of Yucca Mountain.

In this section, the possibility of calculating solution cationic compositions based on chemical data on zeolite minerals is investigated. Initially, relatively well-constrained zeolite and aqueous solution data derived from laboratory ion-exchange equilibrium experiments presented in Section 2.3 are used. Following these best case calculations, cationic compositions are predicted for saturated zone Yucca Mountain groundwaters based on reported chemical data for clinoptilolite minerals and are compared with measured values.

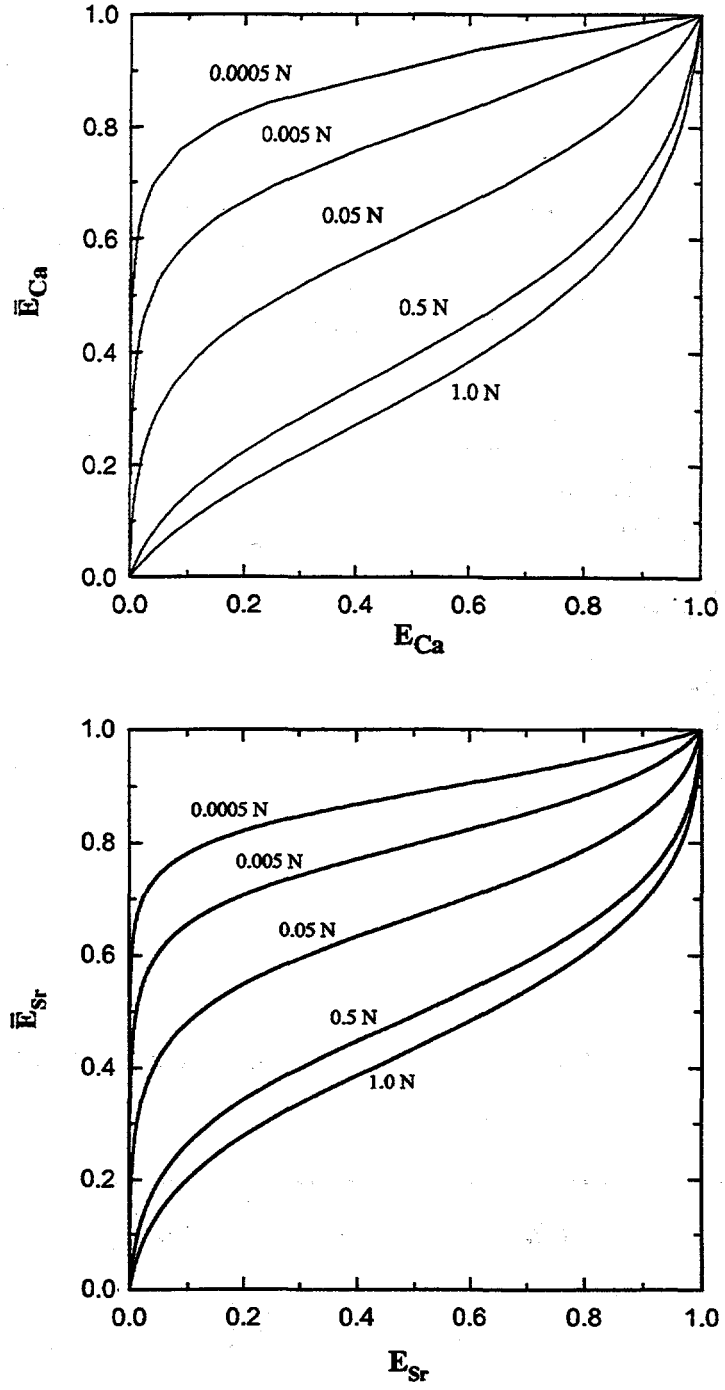

Figure 2-9. Isotherms for ion-exchange at 25 °C between clinoptilolite and aqueous mixtures of (a) $NaCl/CaCl_2$ and (b) $NaCl/SrCl_2$ for solution concentrations of 0.0005 to 1.0 N calculated using a Margules solid solution model with parameters derived from the 0.5-N isotherm data

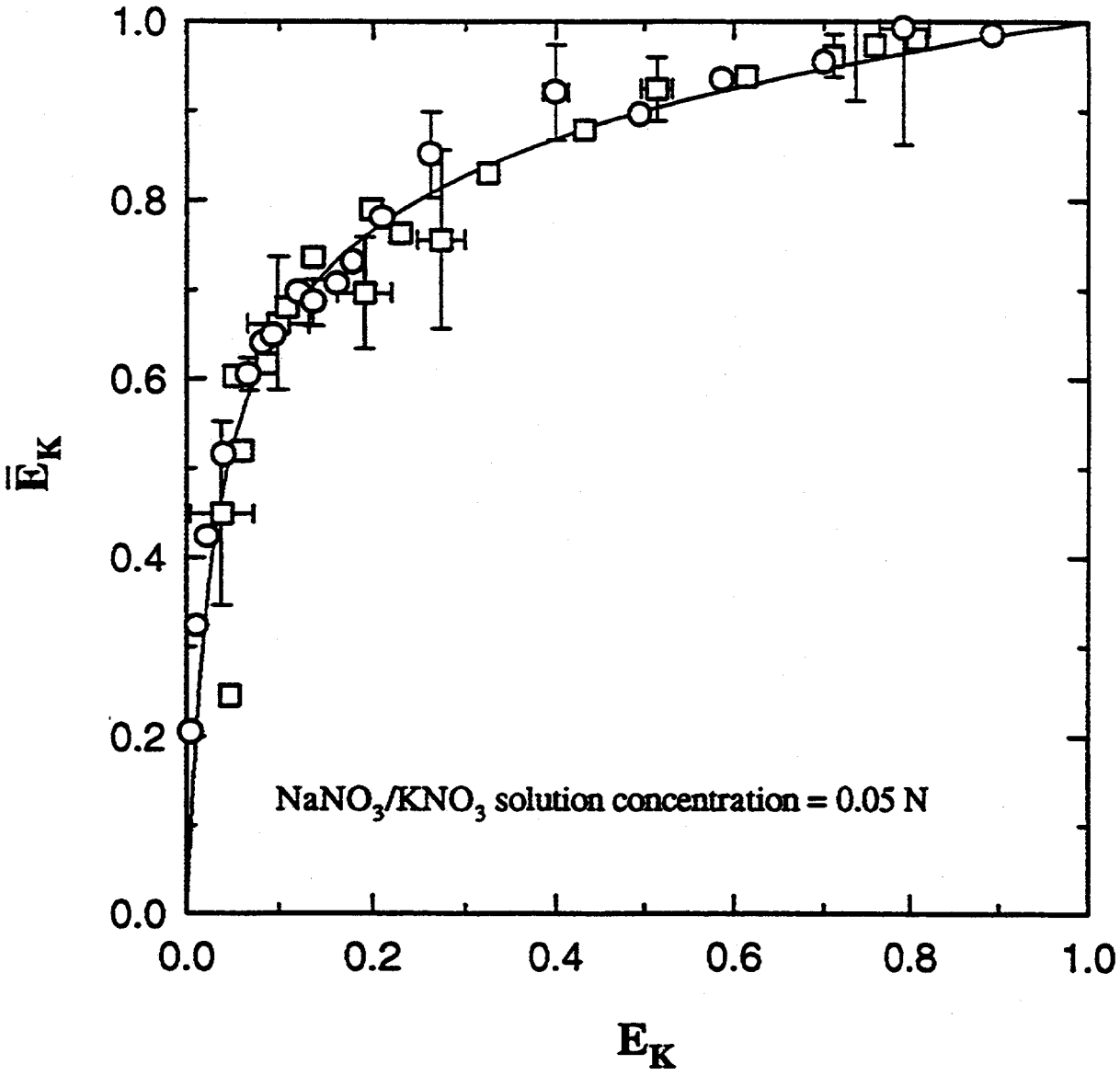

Figure 2-10. Isotherms for ion-exchange at 25 °C between clinoptilolite and 0.05-N $NaNO_3/KNO_3$ aqueous mixtures. Circles and squares represent isotherm points calculated from solution concentrations of K^+ and Na^+, respectively. The curve represents isotherm points predicted using a Margules solid solution model with parameters derived from the 0.5-N NaCl/KCl isotherm data.

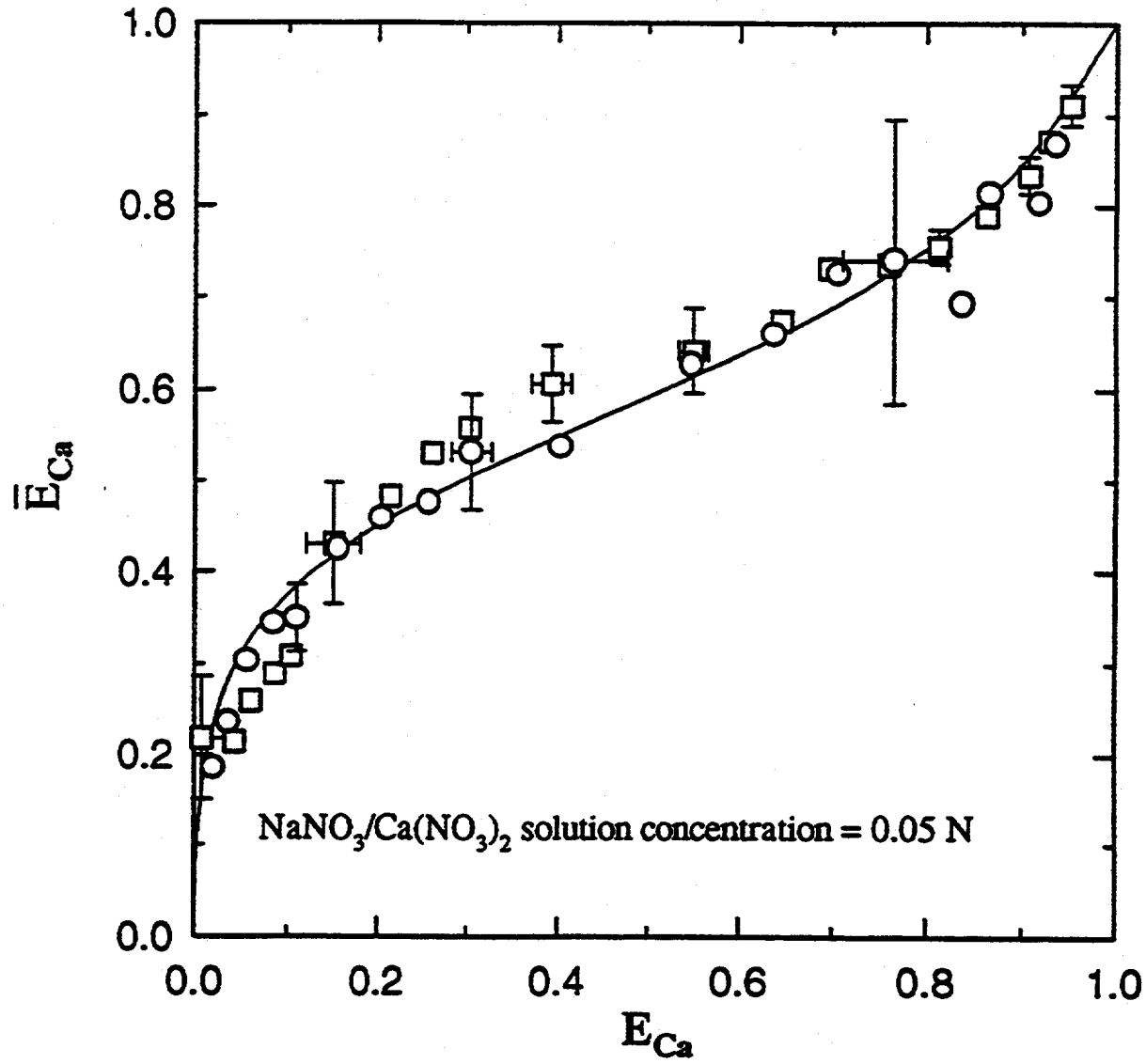

Figure 2-11. Isotherms for ion-exchange at 25 °C between clinoptilolite and 0.05-N $NaNO_3/Ca(NO_3)_2$ aqueous mixtures. Circles and squares represent isotherm points calculated from solution concentrations of Ca^{2+} and Na^+, respectively. The curve represents isotherm points predicted using a Margules solid solution model with parameters derived from the 0.5-N $NaCl/CaCl_2$ isotherm data.

2.4.1 Equations for Calculating Solution Compositions from Zeolite Data

The ratio of the aqueous activities of two cations, A^{z_A+} and B^{z_B+}, participating in an ion-exchange reaction such as that represented by reaction (2-1) can be written as

$$(a_B)^{z_A}/(a_A)^{z_B} = \left[(M_B)^{z_A}(\gamma_B)^{z_A}\right]/\left[(M_A)^{z_B}(\gamma_A)^{z_B}\right] = K_v(\overline{X}_B)^{z_A}/(\overline{X}_A)^{z_B} \qquad (2\text{-}22)$$

Substituting Eq. (2-17) for K_v and writing the zeolite composition in terms of $\overline{X}_A$ only, the aqueous activity ratio can be represented in terms of the equilibrium constant, K, for the binary exchange reaction and the Margules parameters, W_A and W_B, for the zeolite solid solution

$$\begin{aligned}(a_B)^{z_A}/(a_A)^{z_B} &= \left\{(1-\overline{X}_A)^{z_A}/(\overline{X}_A)^{z_B}\right\} \\ \exp\Big\{\ln K &+ z_A(\overline{X}_A)^2\left[W_B + 2(1-\overline{X}_A)(W_A - W_B)\right] \\ &- z_B(1-\overline{X}_A)^2\left[W_A + 2(\overline{X}_A)(W_B - W_A)\right]\Big\}\end{aligned} \qquad (2\text{-}23)$$

Since the total normality of a binary aqueous solution, TN, can be calculated from

$$TN = z_A M_A + z_B M_B \qquad (2\text{-}24)$$

the ratio of the molarities of A^{z_A+} and B^{z_B+} can be written in terms of the molarity of either A^{z_A+} only or B^{z_B+} only. Thus,

$$\begin{aligned}(M_B)^{z_A}/(M_A)^{z_B} &= \left[(TN - z_A M_A)/z_B\right]^{z_A}/(M_A)^{z_B} \\ &= \left[(a_B)^{z_A}/(a_A)^{z_B}\right]\left[(\gamma_A)^{z_B}/(\gamma_B)^{z_A}\right]\end{aligned} \qquad (2\text{-}25)$$

For binary ion-exchange reactions involving monovalent cations, $(z_A = z_B = 1)$, one can derive from Eq. (2-25) expressions for M_A and M_B that are fairly simple:

$$M_A = TN/(1 + k);\ M_B = TN - M_A \qquad (2\text{-}26)$$

where

$$k = \left[(a_B)^{z_A}/(a_A)^{z_B}\right]\left[(\gamma_A)^{z_B}/(\gamma_B)^{z_A}\right] \qquad (2\text{-}27)$$

For exchange reactions where $z_A = 2$ and $z_b = 1$, the solution compositions can be solved by making use of a quadratic equation

$$M_A = \left(-b \pm\sqrt{b^2-4ac}\right)/2a;\ M_B = TN - 2M_A \qquad (2\text{-}28)$$

where

$$a = 1;\ b = [-4(TN) - k]/4;\ \text{and}\ c = (TN/2)^2 \qquad (2\text{-}29)$$

Using Eqs. (2-23) to (2-29), together with the equilibrium constants and Margules parameters derived from the ion-exchange experiments, values of M_A and M_B can be calculated if the value of TN is known or can be estimated by independent means. A value of TN is required not only as input into Eqs. (2-26) and (2-28), but also in calculating the aqueous activity coefficient ratios, $(\gamma_A)^{z_B}/(\gamma_B)^{z_A}$. For a specific value of TN, a range of values corresponding to the activity coefficient ratios for solutions of almost pure A^{z_A+} to almost pure B^{z_B+} can be calculated. The aqueous activity coefficient ratios do not change very much for a particular TN. For example, for a $NaCl/CaCl_2$ solution at TN=0.5-N, $(\gamma_{Na^+})^2/(\gamma_{Ca^{2+}})$ changes by only 6.1 percent, from 1.913 to 2.030, for solutions with M_{Na^+}: $M_{Ca^{2+}}$ ranging from 0.49495:0.002525 to 0.00504:0.24748. The change in activity coefficient ratios for different solution compositions is smaller for lower total normalities and also for solutions containing homovalent cations only (e.g., Na^+/K^+). Thus, although aqueous activity coefficient ratios are required to calculate solution compositions from zeolite data, one can use a value corresponding to that of a solution of median composition (e.g., equal normalities of A^{z_A+} and B^{z_B+}). For dilute solutions typical of Yucca Mountain groundwaters (ionic strength $\approx$ 0.003 molal), it may be sufficient to use an activity coefficient ratio equal to one and still get reasonable predictions of solution compositions (see Section 2.4.3).

2.4.2 Measured Solution Compositions versus Values Predicted from Zeolite Data: Laboratory Ion-Exchange Data

Laboratory ion-exchange experiments conducted in this study provide useful data for evaluating the predictive model discussed in Section 2.4.1. Table 2-13 presents the chemical compositions of clinoptilolite powders that were equilibrated with the Na^+/K^+ or Na^+/Ca^{2+} solutions. The data for the NaCl-KCl and $NaCl-CaCl_2$ mixtures at 0.05 and 0.5-N are for zeolites recovered at the end of the reversibility/reproducibility experiments, whereas the data for the $NaNO_3$-KNO_3 and $NaNO_3$-$Ca(NO_3)_2$ mixtures were recovered at the end of the forward experiments. These clinoptilolite powders were recovered using standard filtration methods. However, to avoid altering the clinoptilolite compositions, the zeolites were washed only with the solutions with which they equilibrated. This is particularly important for the Na^+/Ca^{2+} system because, due to the concentration-valency effect discussed in Section 2.3, zeolite compositions may change significantly if the solids were contacted with deionized water. The compositions presented in Table 2-13 were derived by ICP methods. Because of the very small amounts of zeolite powder used in the ion-exchange experiments, no duplicate samples were analyzed. For example, only about 0.1 g or less of the clinoptilolite powders from the 0.05-N experiments were available for the ICP analysis, instead of the minimum 0.2 to 0.5 g typically used in the procedure.

Table 2-14 and Figure 2-12 compare the molarities of Na^+ and K^+ predicted from the measured zeolite composition versus those measured with the ISEs. Table 2-15 and Figure 2-13 compare the predicted versus measured Na^+ and Ca^{2+} solution concentrations. The cationic mole fractions of Na^+ and K^+ in the zeolite from the Na^+/K^+ ion-exchange experiments were normalized to the molar amounts of Na and K only, whereas the zeolite mole fractions of Na^+ and Ca^{2+} from the Na^+/Ca^{2+} experiments were normalized to the molar amounts of Na and Ca only. This assumes that the small amounts of Ca^{2+} and Mg^{2+} present in the zeolite did not participate in the exchange process for the Na^+/K^+ system, and

Table 2-13. Chemical composition of clinoptilolites recovered from ion-exchange equilibrium experiments. For comparison, the composition of the starting material (Na-form) is included.

Na^+/K^+ or Na^+/Ca^{2+} Mixtures	wt% SiO_2	wt% TiO_2	wt% Al_2O_3	wt% Fe_2O_3	wt% MgO	wt% Na_2O	wt% K_2O	wt% CaO	Total wt%
Na/K/Cl 0.5 N #1	67.81	0.06	11.17	0.36	0.17	1.91	7.52	0.00	89.00
Na/K/Cl 0.5 N #3	66.95	0.06	10.98	0.36	0.17	1.23	8.55	0.00	88.30
Na/K/Cl 0.5 N #11	65.82	0.06	10.75	0.35	0.16	0.55	9.29	0.01	86.99
Na/K/Cl 0.5 N #17	67.80	0.06	10.91	0.34	0.17	0.81	9.34	0.00	89.44
Na/K/Cl 0.05 N #1	67.48	0.06	10.63	0.35	0.17	2.35	6.20	0.01	87.25
Na/K/Cl 0.05 N #5	67.58	0.04	10.55	0.25	0.25	0.55	8.43	0.00	87.65
Na/K/Cl 0.05 N #9	67.48	0.06	10.66	0.35	0.17	0.56	9.29	0.01	88.58
Na/K/Cl 0.05 N #19	67.34	0.06	10.58	0.35	0.17	0.32	9.64	0.00	88.46
$Na/K/NO_3$ 0.05 N #1	68.00	0.06	10.78	0.35	0.17	4.83	2.66	0.00	86.85
$Na/K/NO_3$ 0.05 N #5	68.00	0.06	10.77	0.38	0.18	2.24	6.71	0.00	88.34
$Na/K/NO_3$ 0.05 N #9	67.30	0.06	10.79	0.35	0.17	1.52	7.59	0.00	87.78
$Na/K/NO_3$ 0.05 N #14	66.76	0.06	10.49	0.35	0.17	0.78	8.70	0.01	87.32
$Na/K/NO_3$ 0.05 N #16	65.65	0.06	10.46	0.34	0.16	0.46	8.85	0.01	85.99
$Na/K/NO_3$ 0.05 N #19	67.00	0.06	10.72	0.40	0.18	0.17	9.60	0.00	88.13

Table 2-13. Chemical composition of clinoptilolites recovered from ion-exchange equilibrium experiments. For comparison, the composition of the starting material (Na-form) is included. (cont'd)

Na^+/K^+ or Na^+/Ca^{2+} Mixtures	wt% SiO_2	wt% TiO_2	wt% Al_2O_3	wt% Fe_2O_3	wt% MgO	wt% Na_2O	wt% K_2O	wt% CaO	Total wt%
Na/Ca/Cl 0.5 N #1	68.46	0.06	11.25	0.36	0.18	5.00	0.61	1.32	87.24
Na/Ca/Cl 0.5 N #5	67.02	0.06	10.95	0.4	0.19	4.43	0.62	1.79	85.46
Na/Ca/Cl 0.5 N #7	66.13	0.06	10.57	0.36	0.18	3.79	0.61	2.14	83.84
Na/Ca/Cl 0.5 N #11	67.17	0.06	10.73	0.36	0.19	3.03	0.63	3.10	85.27
Na/Ca/Cl 0.5 N #13	67.32	0.06	10.74	0.36	0.18	2.47	0.63	3.60	85.36
Na/Ca/Cl 0.05 N #1	67.62	0.06	11.10	0.36	0.18	3.57	0.63	2.56	86.08
Na/Ca/Cl 0.05 N #5	67.54	0.05	11.00	0.36	0.20	2.55	0.58	3.52	85.80
Na/Ca/Cl 0.05 N #9	68.03	0.06	11.08	0.36	0.19	2.12	0.61	3.91	86.36
Na/Ca/Cl 0.05 N #11	68.62	0.06	11.33	0.36	0.19	1.72	0.62	4.36	87.26
Na/Ca/Cl 0.05 N #19	67.41	0.06	11.05	0.35	0.20	1.39	0.55	4.51	85.52
$Na/Ca/NO_3$ 0.05 N #1	69.09	0.06	11.30	0.36	0.19	5.10	0.62	1.21	87.93
$Na/Ca/NO_3$ 0.05 N #7	66.08	0.06	10.89	0.35	0.18	3.28	0.60	2.66	84.10
$Na/Ca/NO_3$ 0.05 N #10	65.74	0.06	10.86	0.38	0.18	2.55	0.62	3.46	83.85
$Na/Ca/NO_3$ 0.05 N #14	66.17	0.06	10.98	0.37	0.19	1.90	0.60	4.13	84.40
Na-clinoptilolite	68.28	0.04	11.28	0.40	0.16	6.36	0.66	0.02	87.20

Table 2-14. Comparison of measured K^+ and Na^+ solution molarities versus values predicted from measured clinoptilolite Na and K content. Also tabulated are cationic mole fractions of K^+ in the zeolite, $\bar{X}_K$, and predicted solution activity ratios of Na^+ and K^+.

Na^+/K^+ Mixtures	wt% Na_2O	wt% K_2O	$\bar{X}_K$	a_{Na}/a_K	M_K Calc.	M_K Meas.	M_{Na} Calc.	M_{Na} Meas.
Na/K/Cl 0.5 N #1	1.91	7.52	0.721	5.906	0.076 ±0.019	0.061	0.424 ±0.019	0.444
Na/K/Cl 0.5 N #3	1.23	8.55	0.821	2.463	0.150 ±0.030	0.130	0.350 ±0.030	0.366
Na/K/Cl 0.5 N #11	0.55	9.29	0.917	0.7338	0.295 ±0.032	0.258	0.205 ±0.032	0.238
Na/K/Cl 0.5 N #17	0.81	9.34	0.884	1.207	0.233 ±0.034	0.209	0.267 ±0.034	0.298
Na/K/Cl 0.05 N #1	2.35	6.20	0.634	11.30	0.0041 ±0.0011	0.0033	0.0459 ±0.0011	0.0465
Na/K/Cl 0.05 N #5	0.55	8.43	0.910	0.8303	0.0274 ±0.0033	0.0194	0.0226 ±0.0033	0.0306
Na/K/Cl 0.05 N #9	0.56	9.29	0.916	0.7507	0.0287 ±0.0032	0.0239	0.0213 ±0.0032	0.0271
Na/K/Cl 0.05 N #19	0.32	9.64	0.952	0.3646	0.0367 ±0.0024	0.0327	0.0133 ±0.0024	0.0174

Table 2-14. Comparison of measured K^+ and Na^+ solution molarities versus values predicted from measured clinoptilolite Na and K content. Also tabulated are cationic mole fractions of K^+ in the zeolite, $\bar{X}_K$, and predicted solution activity ratios of Na^+ and K^+. (cont'd)

Na^+/K^+ Mixtures	wt% Na_2O	wt% K_2O	$\bar{X}_K$	a_{Na}/a_K	M_K Calc.	M_K Meas.	M_{Na} Calc.	M_{Na} Meas.
$Na/K/NO_3$ 0.05 N #1	4.83	2.66	0.266	125.1	0.0004 ±0.0001	0.0003	0.0496 ±0.0001	0.0476
$Na/K/NO_3$ 0.05 N #5	2.24	6.71	0.663	9.181	0.0049 ±0.0013	0.0034	0.0451 ±0.0013	0.0457
$Na/K/NO_3$ 0.05 N #9	1.52	7.59	0.767	4.063	0.0099 ±0.0023	0.0069	0.0401 ±0.0023	0.0404
$Na/K/NO_3$ 0.05 N #14	0.78	8.70	0.880	1.262	0.0222 ±0.0033	0.0154	0.0278 ±0.0033	0.0314
$Na/K/NO_3$ 0.05 N #16	0.46	8.85	0.927	0.6237	0.0309 ±0.0031	0.0248	0.0191 ±0.0031	0.0243
$Na/K/NO_3$ 0.05 N #19	0.17	9.60	0.974	0.1799	0.0424 ±0.0015	0.0368	0.0076 ±0.0015	0.0121

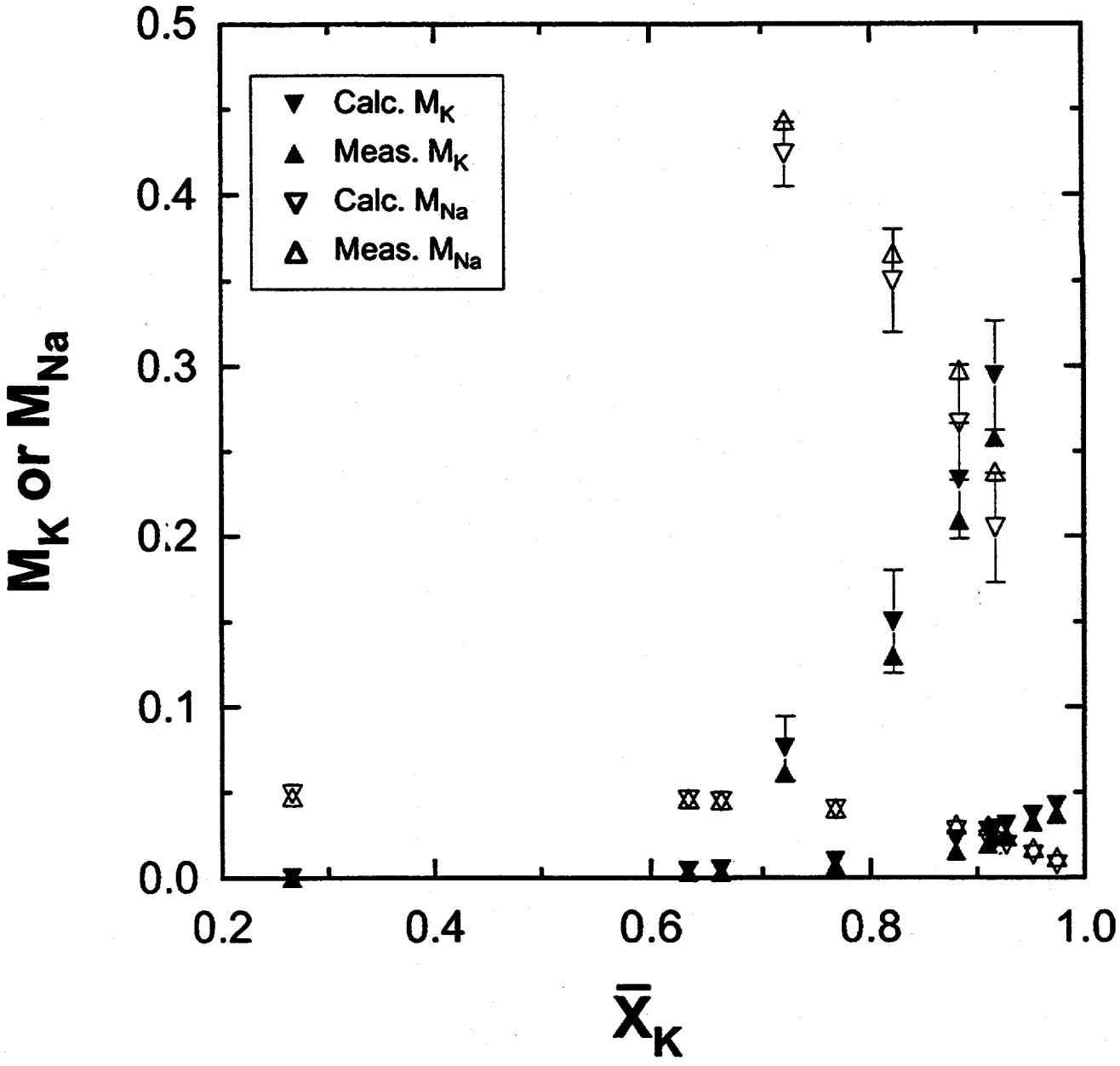

Figure 2-12. Comparison of measured K^+ and Na^+ solution molarities versus values predicted from measured clinoptilolite Na and K content. Error bars in predicted K^+ and Na^+ molarities were propagated assuming ±10 percent errors in measured K_2O and Na_2O weight percent of the zeolite.

Table 2-15. Comparison of measured Ca^{2+} and Na^{+} solution molarities versus values predicted from measured clinoptilolite Na and Ca content. Also tabulated are cationic mole fractions of Ca^{2+} in the zeolite, $\bar{X}_{Ca}$, and predicted solution activity ratios of Na^{+} and Ca^{2+}.

Na^{+}/Ca^{2+} Mixtures	wt% Na_2O	wt% CaO	$\bar{X}_{Ca}$	$(a_{Na})^2/(a_{Ca})$	M_{Ca} Calc.	M_{Ca} Meas.	M_{Na} Calc.	M_{Na} Meas.
Na/Ca/Cl 0.5 N #1	5	1.32	0.127	5.868	0.052 ±0.012	0.051	0.395 ±0.025	0.409
Na/Ca/Cl 0.5 N #5	4.43	1.79	0.183	2.314	0.089 ±0.019	0.085	0.323 ±0.037	0.345
Na/Ca/Cl 0.5 N #7	3.79	2.14	0.238	1.005	0.124 ±0.022	0.118	0.252 ±0.043	0.260
Na/Ca/Cl 0.5 N #11	3.03	3.1	0.361	0.1885	0.184 ±0.018	0.180	0.133 ±0.036	0.155
Na/Ca/Cl 0.5 N #13	2.47	3.6	0.446	0.06527	0.208 ±0.013	0.199	0.083 ±0.026	0.100
Na/Ca/Cl 0.05 N #1	3.57	2.56	0.284	0.5259	0.0047 ±0.0016	0.0039	0.0406 ±0.0031	0.0406
Na/Ca/Cl 0.05 N #5	2.55	3.52	0.433	0.07686	0.0124 ±0.0026	0.0105	0.0252 ±0.0052	0.0285
Na/Ca/Cl 0.05 N #9	2.12	3.91	0.505	0.03232	0.0158 ±0.0023	0.0136	0.0184 ±0.0046	0.0214
Na/Ca/Cl 0.05 N #11	1.72	4.36	0.583	0.01291	0.0187 ±0.0018	0.0173	0.0126 ±0.0035	0.0159
Na/Ca/Cl 0.05 N #19	1.39	4.51	0.642	0.00658	0.0203 ±0.0013	0.0194	0.0094 ±0.0026	0.0124

Table 2-15. Comparison of measured Ca^{2+} and Na^{+} solution molarities versus values predicted from measured clinoptilolite Na and Ca content. Also tabulated are cationic mole fractions of Ca^{2+} in the zeolite, $\bar{X}_{Ca}$, and predicted solution activity ratios of Na^{+} and Ca^{2+}. (cont'd)

Na^{+}/Ca^{2+} Mixtures	wt% Na_2O	wt% CaO	$\bar{X}_{Ca}$	$(a_{Na})^2/(a_{Ca})$	M_{Ca} Calc.	M_{Ca} Meas.	M_{Na} Calc.	M_{Na} Meas.
$Na/Ca/NO_3$ 0.05 N #1	5.1	1.21	0.116	7.251	0.0005 ±0.0002	0.0005	0.0490 ±0.0003	0.0496
$Na/Ca/NO_3$ 0.05 N #7	3.28	2.66	0.309	0.3714	0.0059 ±0.0019	0.0051	0.0382 ±0.0037	0.0392
$Na/Ca/NO_3$ 0.05 N #10	2.55	3.46	0.429	0.0809	0.0122 ±0.0026	0.0101	0.0257 ±0.0051	0.0303
$Na/Ca/NO_3$ 0.05 N #14	1.9	4.13	0.546	0.01999	0.0174 ±0.0020	0.0159	0.0153 ±0.0040	0.0177
$Na/Ca/NO_3$ 0.05 N #18	1.02	4.92	0.727	0.00243	0.0220 ±0.0008	0.0217	0.0060 ±0.0015	0.0069

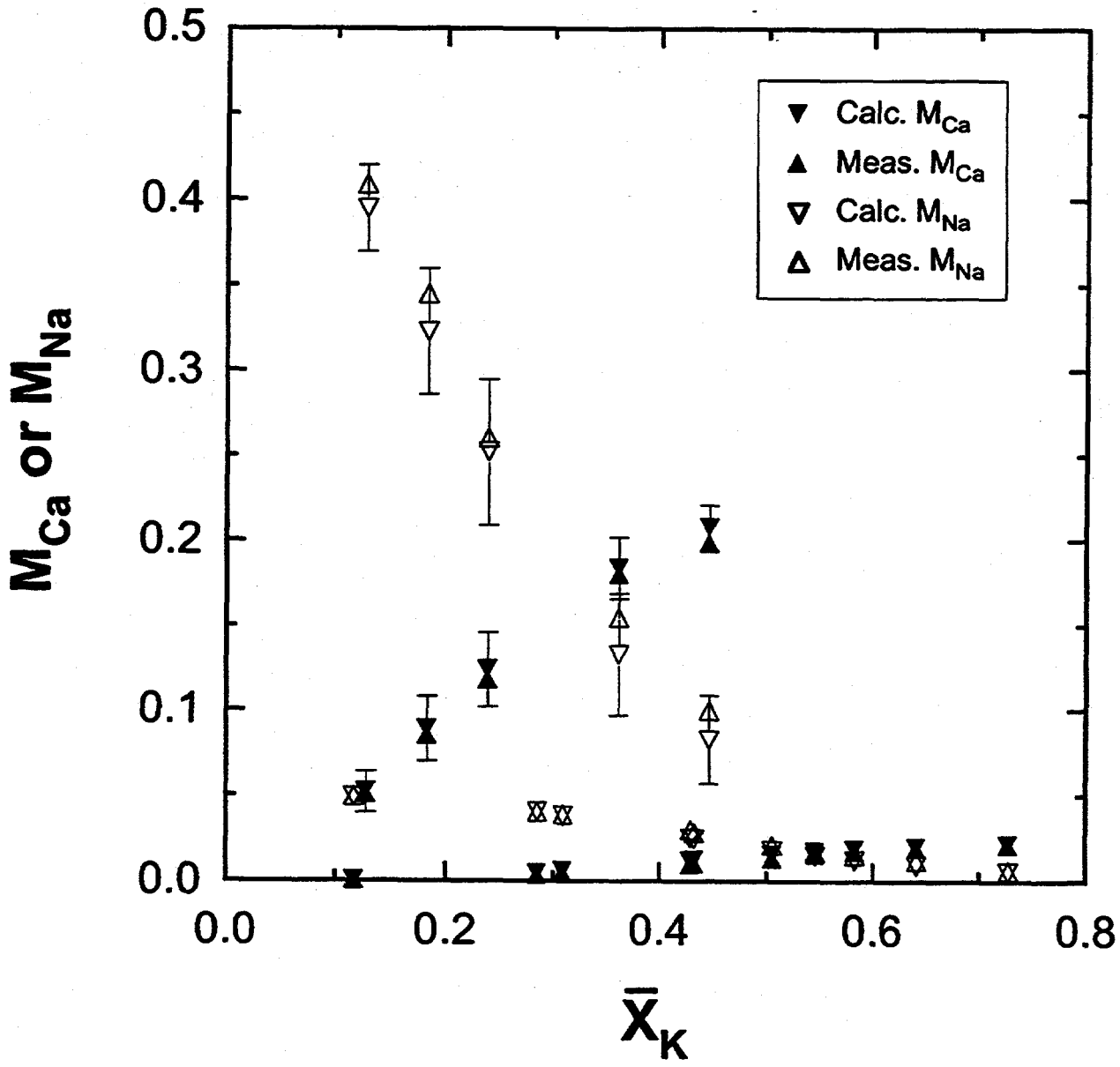

Figure 2-13. Comparison of measured Ca^{2+} and Na^{+} solution molarities versus values predicted from measured clinoptilolite Na and Ca content. Error bars in predicted Ca^{2+} and Na^{+} molarities were propagated assuming ± 10 percent errors in measured CaO and Na_2O weight percent of the zeolite.

K^+ and Mg^{2+} did not participate in the exchange for the Na^+/Ca^{2+} mixture. This is justified by the zeolite compositions given in Table 2-13 which show that, within analytical uncertainty, the MgO and CaO contents of all zeolites from the Na^+/K^+ ion-exchange experiments are the same and are equal to the MgO and CaO contents of the original Na-clinoptilolite (Table 2-1). Likewise, the K_2O and MgO contents of the zeolites from the Na^+/Ca^{2+} experiments and of the Na-clinoptilolite are the same.

The uncertainties in molarities of Na^+, K^+, and Ca^{2+} predicted from zeolite analytical data were propagated assuming ± 10 percent error in measured weight percent of Na_2O, K_2O, and CaO, but neglecting the regression errors for ln K, W_A, and W_B. The results listed in Tables 2-14 and 2-15, and illustrated in Figures 2-12 and 2-13 show that the predicted solution compositions agree very well with measured values, mostly within analytical uncertainty, and demonstrate that it is possible to predict with confidence the cationic composition of an aqueous solution based on chemical analysis of zeolites with which it equilibrated, at least for simple two-cation systems for which the solution normality is well known.

The predicted molarities were calculated using Eqs. (2-23) to (2-29) and values of ln K, W_A, and W_B derived from the Na^+/K^+ and Na^+/Ca^{2+} ion-exchange experiments. Based on the Pitzer equations and the parameters listed in Table 2-11, values for $\gamma_{Na^+}/\gamma_{K^+}$ equal to 1.05 and 1.008 were used for the Na^+/K^+ mixtures at 0.5 and 0.05 N, respectively. For Na^+/Ca^{2+} solutions, $(\gamma_{Na^+})^2/(\gamma_{Ca^{2+}})$ equal to 1.97 and 1.49 were used at total normalities of 0.5 and 0.05, respectively. For many natural aqueous systems, uncertainties are present with respect to the total concentration of the solution; thus, accurate values of activity ratios cannot be calculated. In some cases, especially when solutions are dilute, it may be useful to assume a value equal to 1.0 for the activity coefficient ratios. Table 2-16 compares predicted solution compositions that were calculated either using activity coefficient ratios for the correct solution concentrations (0.5 or 0.05 N) or using activity coefficient ratios equal to 1.0. The results in Table 2-16 indicate that for aqueous solutions consisting only of monovalent cations, the solution compositions predicted using either activity coefficient ratio value do not differ very much. On the other hand, for aqueous solutions involving heterovalent cations, significant differences occur between predicted solution compositions. However, these differences become smaller at lower solution concentrations. For example, at solution normalities equal to 0.05 N, compositions predicted using activity coefficient ratios equal to 1.0 are reasonably close to values calculated using more accurate values. Thus, for typical Yucca Mountain groundwaters with an ionic strength of $\approx$ 0.003 m, a value of 1.0 for the activity coefficient ratio is a relatively good approximation.

2.4.3 Yucca Mountain Groundwater Compositions Predicted from Zeolite Analytical Data

The examples presented in Tables 2-14 and 2-15 are ideal case examples since the exchange reactions are known to be binary in nature, total normalities of the solutions are known, and aqueous activity coefficient ratios can be calculated with good certainty. To test the application of the predictive model to more complex mixtures, zeolite and groundwater chemistry data from Yucca Mountain were used. It should be noted that this test is only preliminary because the equilibrium constants and Margules parameters used in the calculations strictly apply only to the binary exchange reactions. Additional experimental data on ternary mixtures are needed to better constrain the calculations. Nevertheless, it is interesting to determine whether reasonable predictions of cationic compositions of multicomponent groundwaters can be made using only parameters derived for binary systems.

Table 2-16. Comparison of K^+ and Ca^{2+} molarities predicted from zeolite compositions using either activity coefficient ratios for the actual solution normality or activity coefficient ratios set equal to 1.0

Na^+/K^+ Mixtures	M_K Calc. Using 0.5 or 0.05 N γ's	M_K Calc. Using $\gamma_{Na^+}/\gamma_{K^+} = 1$	M_{Na} Calc. Using 0.5 or 0.05 N γ's	M_{Na} Calc. Using $\gamma_{Na^+} / \gamma_{K^+} = 1$
Na/K/Cl 0.5 N #1	0.076	0.072	0.424	0.428
Na/K/Cl 0.5 N #3	0.150	0.144	0.350	0.356
Na/K/Cl 0.5 N #11	0.295	0.288	0.205	0.212
Na/K/Cl 0.5 N #17	0.233	0.227	0.267	0.273
Na/KCl 0.05 N #1	0.0041	0.0041	0.0459	0.0459
Na/KCl 0.05 N #5	0.0274	0.0273	0.0226	0.0227
Na/KCl 0.05 N #9	0.0287	0.0286	0.0213	0.0214
Na/KCl 0.05 N #19	0.0367	0.0366	0.0133	0.0134
Na^+/Ca^{2+} Mixtures	M_{Ca} Calc. Using 0.5 or 0.05 N γ's	M_{Ca} Calc. Using $(\gamma_{Na^+})^2 / (\gamma_{Ca^{2+}}) = 1$	M_{Na} Calc. Using 0.5 or 0.05 N γ's	M_{Na} Calc. Using $(\gamma_{Na^+})^2 / (\gamma_{Ca^{2+}}) = 1$
Na/Ca/Cl 0.5 N #1	0.052	0.032	0.395	0.435
Na/Ca/Cl 0.5 N #5	0.089	0.061	0.323	0.377
Na/Ca/Cl 0.5 N #7	0.124	0.095	0.252	0.309
Na/Ca/Cl 0.5 N #11	0.184	0.162	0.133	0.175
Na/Ca/Cl 0.5 N #13	0.208	0.194	0.083	0.112

Table 2-16. Comparison of K^+ and Ca^{2+} molarities predicted from zeolite compositions using either activity coefficient ratios for the actual solution normality or activity coefficient ratios set equal to 1.0 (cont'd)

Na^+/Ca^{2+} Mixtures	M_{Ca} Calc. Using 0.5 or 0.05 N γ's	M_{Ca_2} Calc. Using $(\gamma_{Na^+})^2 / (\gamma_{Ca^{2+}}) = 1$	M_{Na} Calc. Using 0.5 or 0.05 N γ's	M_{Na_2} Calc. Using $(\gamma_{Na^+})^2 / (\gamma_{Ca^{2+}}) = 1$
Na/Ca/Cl 0.05 N #1	0.0047	0.0035	0.0406	0.0430
Na/Ca/Cl 0.05 N #5	0.0124	0.0107	0.0252	0.0286
Na/Ca/Cl 0.05 N #9	0.0158	0.0143	0.0184	0.0215
Na/Ca/Cl 0.05 N #11	0.0187	0.0175	0.0126	0.0150
Na/Ca/Cl 0.05 N #19	0.0203	0.0194	0.0094	0.0113

Abundant water and mineral chemistry data have been collected from the hydrologically saturated zone of Yucca Mountain, Nevada. However, as reflected in the literature, there has been little attempt to correlate the chemistry of coexisting waters and minerals. An effort has been made previously to identify sets of mineral and water chemistry data from the same location at Yucca Mountain and to examine the data for correlations that may represent equilibrium controls (Pabalan and Murphy, 1990). That effort identified several combinations of water and clinoptilolite chemistry data from tuffaceous units at Yucca Mountain that possibly represent samples from spatially correlated sources. Two integrated water samples from well UE-25b#1, with producing zones at the 810- to 825-m and 860- to 875-m depths in the upper Bullfrog Member of the Crater Flat Tuff and the 480- to 650-m zone encompassing the Calico Hills Tuff and the Prow Pass Member of the Crater Flat Tuff (Lahoud et al., 1984; Benson et al., 1983), and an interval sample from the 863- to 875-m depth may be spatially correlated to two clinoptilolite samples taken at the 863.2- and 877.5-m depths of the same well. The integrated water sample from the J-13 well, with a producing zone in the lower Topopah Spring Member of the Paintbrush Tuff [approximately 282- to 450-m depth, (Benson et al., 1983)], is spatially correlated to three clinoptilolite specimens at the 406.9-, 433.1-, and 444.1-m depths, and to one clinoptilolite sample from a fracture at 432.8-m depth. The water from the producing zone in the Crater Flat Tuff (600- to 900-m depth) in well USW H-4 (Whitfield et al., 1985; Benson et al., 1983) is correlated to a clinoptilolite from the 603.5-m depth. Thus a total of seven clinoptilolite drillhole samples can be spatially correlated with groundwater samples from the same hole and approximately the same depth.

Table 2-17 lists these seven samples together with the average and standard deviation of several analyses. The zeolite data were taken from Appendix F of Broxton et al. (1986), except the zeolite analyses for the J-13 fracture sample that were taken from Carlos (1989). Water chemistry data were taken from Benson et al. (1983) [the same data excluding Li^+ and Sr^{2+} also tabulated in Kerrisk (1987)]. In cases where two or more groundwater specimens are possibly spatially correlated with one zeolite sample, the range in measured K^+, Ca^{2+}, and Na^+ molarities are listed in the table. Also listed in Table 2-17 are the predicted and measured K^+, Ca^{2+}, and Na^+ molarities of Yucca Mountain groundwater samples. The predicted concentrations were calculated from the zeolite data in a manner similar to that described in Section 2.4.2. The total solution concentration of the Yucca Mountain groundwaters tabulated by Benson et al. (1983) ranges from about 0.0025 to 0.0042 N (mean=0.0031; standard deviation=0.0006). To simplify the calculations presented here, a value for TN equal to 0.003 was used and activity coefficient ratios were assumed to be 1.0. Because the predictions used parameters derived from binary Na^+/K^+ and Na^+/Ca^{2+} ion-exchange data, nonunique values of Na^+ molarities were calculated from the thermodynamic model. Thus, two sets of predicted Na^+ molarities, one calculated using the Na^+/K^+ and the other using the Na^+/Ca^{2+} parameters, are listed in the table. The uncertainties in predicted molarities were propagated from the standard deviations of the zeolite composition.

The results show that there is good agreement between measured groundwater compositions and those predicted from zeolite data using thermodynamic models that account for nonideal behavior in the zeolite phases. Predicted Na^+ concentrations are all within a factor of two of the measured values, whereas predicted K^+ and Ca^{2+} are mostly within a factor of three of measured concentrations. Only one predicted value substantially disagreed with the measured value: the calculated Ca^{2+} concentration of USW-H4 water is 2.7×10^{-7} M, whereas the measured value is 4.24×10^{-4} M. However, for the same water sample the calculated and measured Na^+ concentrations are in excellent agreement (2.9×10^{-3} M versus 3.2×10^{-3} M, respectively). The cause of the disagreement between calculated and measured Ca^{2+} is not clear. One possibility is uncertainty in analytical data; of the seventeen well water data tabulated by Benson et al. (1983), the USW H-4 composition showed the highest charge imbalance

Table 2-17. Comparison of predicted versus measured K^+, Ca^{2+}, and Na^+ molarities for Yucca Mountain well water samples that are possibly spatially correlated with zeolite specimens from the same drillhole

Zeolite Sample No.	# of Zeol. Anal.	wt% Na_2O	wt% K_2O	wt% CaO	wt% MgO	$\bar{X}_K$ K/Na Pseudo-Binary	$\bar{X}_{Ca}$ Ca/Na Pseudo-Binary	M_K Calc. $\times 10^{-3}$	M_K Meas. $\times 10^{-3}$	M_{Ca} Calc. $\times 10^{-3}$	M_{Ca} Meas. $\times 10^{-3}$	M_{Na} Calc. $\times 10^{-3}$ Na/K Param.	M_{Na} Calc. $\times 10^{-3}$ Na/Ca Param.	M_{Na} Meas. $\times 10^{-3}$
UE-25b#1 (863.2 m)	13	0.58 ±0.19	1.28 ±0.12	5.85 ±0.11	0.81 ±0.09	0.592	0.848	0.186 ±0.083	0.072 to 0.095	1.16 ±0.11	0.424 to 0.474	2.81 ±0.08	0.688 ±0.213	2.00 to 2.31
UE-25b#1 (877.5 m)	9	0.64 ±0.23	1.51 ±0.05	6.50 ±0.27	0.37 ±0.14	0.608	0.849	0.206 ±0.084	0.072 to 0.095	1.16 ±0.13	0.424 to 0.474	2.79 ±0.08	0.684 ±0.250	2.00 to 2.31
J-13 (406.9 m)	4	1.05 ±0.29	1.03 ±0.04	4.49 ±0.11	0.53 ±0.11	0.392	0.703	0.054 ±0.018	0.128	0.769 ±0.175	0.299	2.95 ±0.02	1.46 ±0.35	1.83
J-13 (433.1 m)	9	1.22 ±0.08	4.33 ±0.35	2.59 ±0.17	0	0.700	0.540	0.376 ±0.072	0.128	0.310 ±0.072	0.299	2.62 ±0.07	2.38 ±0.15	1.83
J-13 (444.1 m)	9	0.43 ±0.09	2.50 ±0.23	3.01 ±0.21	0.93 ±0.03	0.793	0.795	0.711 ±0.212	0.128	1.02 ±0.12	0.299	2.29 ±0.21	0.953 ±0.257	1.83
USW-H4 (603.8 m)	7	3.45 ±0.38	4.64 ±0.49	0.29 ±0.03	0	0.469	0.044	0.087 ±0.024	0.066	0.00027 ±.00007	0.424	2.91 ±0.02	3.00 ±0.0001	3.18

(0.35 meq/L versus an average of 0.12±0.09 meq/L). Another possibility is that the USW H-4 water sample, which was an integrated sample taken from 600- to 900-m depth, does not represent a composition in equilibrium with the zeolite at 603.5-m depth.

It is interesting to note that Na^+ molarities calculated using Na^+/K^+ binary system parameters are very close (within 3–7 percent) to values derived using Na^+/Ca^{2+} parameters for cases where the Mg content of the zeolite is negligible. On the other hand, where significant amounts of Mg are present in the zeolite, agreement between Na^+ molarities calculated using different binary parameters are not as good. This may indicate that for a ternary system (e.g., $Na^+/K^+/Ca^{2+}$), ion-exchange equilibria may be reasonably calculated using parameters derived from binary systems alone; however, for quaternary and more complex mixtures (e.g., $Na^+/K^+/Ca^{2+}/Mg^{2+}$), additional parameters are likely required. These additional parameters can be easily incorporated into the Margules thermodynamic formulation.

2.5 CONCLUSIONS

Thermodynamic models are important in providing quantitative understanding of ion-exchange interactions between groundwater and zeolite minerals that commonly occur in altered pyroclastic and volcaniclastic rocks, such as those present underneath the proposed HLW repository at Yucca Mountain, Nevada. The results of this study demonstrate that a solid solution model for zeolites based on a Margules formulation, coupled with an activity coefficient model for aqueous solutions (e.g., Pitzer model), can successfully describe and predict ion-exchange equilibria between aqueous solutions and the zeolite mineral clinoptilolite over a wide range of solution composition and concentration, at least for binary ion-exchange reactions. Because the Margules formulation can be easily extended to ternary and more complicated systems, this type of thermodynamic treatment may provide a foundation for modeling ion-exchange equilibria in multicomponent geochemical systems. Using thermodynamic models such as that developed in this study, it may be possible to take into account spatial variations in zeolite composition and natural or repository-induced changes in groundwater chemistry to quantitatively model the transport and retardation of alkali and alkaline earth radionuclides such as ^{135}Cs, ^{137}Cs, and ^{90}Sr, that are important fission products present in HLW.

Furthermore, uncertainties exist in determining groundwater chemistries in the vadose zone of Yucca Mountain due to problems inherent in current techniques for sampling pore waters from unsaturated media. The results of this study show that cationic compositions of aqueous solutions can be predicted very well based only on the composition of zeolites that equilibrated with the solutions and known values for solution normality, at least for binary (two-cation) mixtures. Reasonable predictions can also be obtained for dilute, multicomponent solutions typical of Yucca Mountain groundwaters, using thermodynamic parameters derived from binary systems. However, it is apparent from this study that experimental data on ternary mixtures are needed to better constrain the thermodynamic model and its application to multicomponent aqueous systems.

2.6 REFERENCES

Ames, L.L., Jr. 1964a. Some zeolite equilibria with alkali metal cations. *American Mineralogist* 49: 127-145.

Ames, L.L., Jr. 1964b. Some zeolite equilibria with alkaline earth metal cations. *American Mineralogist* 49: 1,099-1,110.

Argersinger, W.J., A.W. Davidson, and O.D. Bonner. 1950. Thermodynamics and ion-exchange phenomena. *Transactions of the Kansas Academy of Sciences* 53: 404-410.

Barrer, R.M., and J. Klinowski. 1972. Influence of framework charge density on ion-exchange properties of zeolites. *Journal of the Chemical Society Faraday Transactions I* 68: 73-87.

Barrer, R.M., and J. Klinowski. 1974. Ion–exchange selectivity and electrolyte concentration. *Journal of the Chemical Society Faraday Transactions I* 70: 2,080-2,091.

Barrer, R.M., and J. Klinowski. 1977. Theory of isomorphous replacement in aluminosilicates. *Philosophical Transactions Royal Society of London* A 285: 637-676.

Barrer, R.M., and J. Klinowski. 1979. Cation exchangers with several groups of sites. Validity of theoretical base. *Journal of the Chemical Society Faraday Transactions I* 75: 247-251.

Barrer, R.M., J. Klinowski, and H.S. Sherry. 1973. Zeolite exchangers. Thermodynamic treatment when not all ions are exchangeable. *Journal of the Chemical Society Faraday Transactions II* 69: 1,669-1,676.

Benson, L.V., J.H. Robison, R.K. Blankennagel, and A.E. Ogard. 1983. *Chemical Composition of Groundwater and the Locations of Permeable Zones in the Yucca Mountain Area.* Open-File Report 83-854. Reston, VA: U.S. Geological Survey.

Bronsted, J.N. 1922a. Studies on solubility. IV. Principle of the specific interaction of ions. *Journal of the American Chemical Society* 44: 877-898.

Bronsted, J.N. 1922b. Calculation of the osmotic and activity functions in solutions of uni–univalent salts. *Journal of the American Chemical Society* 44: 938-948.

Broxton, D.E., D.L. Bish, and R.G. Warren. 1987. Distribution and chemistry of diagenetic minerals at Yucca Mountain, Nye County, Nevada. *Clays and Clay Minerals* 35: 89-110.

Broxton, D.E., R.G. Warren, R.C. Hagan, and G. Luedemann. 1986. *Chemistry of Diagenetically-Altered Tuffs at a Potential Nuclear Waste Repository.* Report LA-10802-MS. Yucca Mountain, Nye County, NV: Los Alamos, NM: Los Alamos National Laboratory.

Carlos, B. 1989. *Fracture-Coating Minerals in the Topopah Spring Member and Upper Tuff of Calico Hills from Drill Hole J-13.* LANL LA-11504-MS. Los Alamos, NM: Los Alamos National Laboratory.

Clegg, S.L., and M. Whitfield. 1991. Activity coefficients in natural waters. *Activity Coefficients in Electrolyte Solutions.* 2nd Edition. K.S. Pitzer, ed. Boca Raton, FL: CRC Press: 279-434.

Dyer, A., H. Enamy, and R.P. Townsend. 1981. The plotting and interpretation of ion-exchange isotherms in zeolite systems. *Separation Science Technology* 16: 173-183.

Edmunds, W.M., S. Faye, and C.B. Gaye. 1992. Solute profiles in unsaturated Quaternary sands from Senegal: Environmental information and water-rock interaction. Y.K. Kharaka and A.S. Maest, eds. *Water-Rock Interaction.* Rotterdam, Netherlands: Balkema: 719-722.

Ekedahl, E., E. Hogfeldt, and L.G. Sillen. 1950. Activities of the components in ion exchangers. *Acta Chemica Scandinavica* 4: 556-558.

Fletcher, P., and R.P. Townsend. 1981. Ternary ion-exchange in zeolites. Part 3. Activity coefficients in multicomponent electrolyte solutions. *Journal of the Chemical Society Faraday Transactions II* 77: 2,077-2,089.

Fletcher, P., and R.P. Townsend. 1983. Ternary ion-exchange. Part 4. Activity corrections for the solution phase. *Journal of the Chemical Society Faraday Transactions II* 79: 419-432.

Fletcher, P., and R.P. Townsend. 1985. Ion-exchange in zeolites. The exchange of cadmium and calcium in sodium X using different anionic backgrounds. *Journal of the Chemical Society Faraday Transactions I* 81: 1,731-1,744.

Fletcher, P., K.R. Franklin, and R.P. Townsend. 1984. Thermodynamics of binary and ternary ion-exchange in zeolites. The exchange of sodium, ammonium, and potassium ions in mordenite. *Philosophical Transactions Royal Society of London A* 312: 141-178.

Freeman, D.H. 1961. Thermodynamics of binary ion-exchange systems. *Journal of Chemical Physics* 35: 189-191.

Gaines, G.L., Jr., and H.C. Thomas. 1953. Adsorption studies on clay minerals. II. A formulation of the thermodynamics of exchange adsorption. *Journal of Chemical Physics* 21: 714-718.

Ganguly, J., and S.K. Saxena. 1987. *Mixtures and Mineral Reactions.* New York, NY: Springer-Verlag.

Glueckauf, E. 1949. Activity coefficient in concentrated solutions containing several electrolytes. *Nature* 163: 414-415.

Gottardi, G., and E. Galli. 1985. *Natural Zeolites.* New York, NY: Springer-Verlag.

Grant, S.A., and D.L. Sparks. 1989. Method for evaluating exchangeable-ion excess Gibbs energy models in systems with many species. *Journal of Physical Chemistry.* 93: 6,265-6,267.

Grover, J. 1977. Chemical mixing in multicomponent solutions: An introduction to the use of Margules and other thermodynamic excess functions to represent non-ideal behavior. *Thermodynamics in Geology.* D.G. Fraser, ed. Dordrecht-Holland: D. Reidel Publishing Co.: 67-97.

Guggenheim, E.A. 1935. The specific thermodynamic properties of aqueous solutions of strong electrolytes. *Philosophical Magazine* 19: 588-643.

Hardy, H.K. 1953. A "sub-regular" solution model and its application to some binary alloy system. *Acta Metall.* 1: 202-209.

Hay, R.L. 1977. Geology of zeolites in sedimentary rocks. *Reviews in Mineralogy* 4: 53-64.

Hay, R.L. 1978. Geologic occurrence of zeolites. *Natural Zeolites: Occurrence, Properties, Use.* L.B. Sand and F. A. Mumpton, eds. New York, NY: Pergamon Press: 135-143.

Helfferich, F. 1962. *Ion Exchange.* New York, NY: McGraw-Hill.

Howery, D.G., and H.C. Thomas. 1965. Ion exchange on the mineral clinoptilolite. *Journal of Physical Chemistry* 69: 531-537.

Hutchison, C.S. 1974. *Laboratory Handbook of Petrographic Techniques.* New York, NY: John Wiley & Sons.

Kerrisk, J.F. 1985. *An Assessment of the Important Radionuclides in Nuclear Waste.* Report LA-10414-MS. Los Alamos, NM: Los Alamos National Laboratory.

Kerrisk, J.F. 1987. *Groundwater Chemistry at Yucca Mountain, Nevada, and Vicinity.* Report LA-10929-MS. Los Alamos, NM: Los Alamos National Laboratory.

Lahoud, R.G., D.H. Lobmeyer, and M.S. Whitfield, Jr. 1984. *Geohydrology of Volcanic Tuff Penetrated by Test Well UE-25b No. 1.* Report 84-4253. Reston, VA: U.S. Geological Survey.

Mehra, O.P., and M.L. Jackson. 1960. Iron oxide removal from soils and clays by a dithionite-citrate system with sodium bicarbonate. *Proceeding of the 7th Clays and Clay Minerals Conference:* 317-327.

Mumpton, F.A. 1978. Natural zeolites: A new industrial mineral commodity. *Natural Zeolites: Occurrence, Properties, Use.* L.B. Sand and F. A. Mumpton, eds. New York, NY: Pergamon Press: 3-27.

Mumpton, F.A., and W.C. Ormsby. 1978. Morphology of zeolites in sedimentary rocks by scanning electron microscopy. *Natural Zeolites: Occurrence, Properties, Use.* L.B. Sand and F.A. Mumpton eds. New York, NY: Pergamon Press: 113-132.

Ogard, A.E., and J.F. Kerrisk. 1984. *Groundwater Chemistry Along Flow Paths Between a Proposed Repository Site and the Accessible Environment.* Report LA-10188-MS. Los Alamos, NM: Los Alamos National Laboratory.

Pabalan, R.T. 1991. Nonideality effects on the ion-exchange behavior of the zeolite mineral clinoptilolite. *Scientific Basis for Nuclear Waste Management XIV.* T. Abrajano, Jr., and L.H. Johnson, eds. Pittsburgh, PA: Materials Research Society: MRS Symposium Proceedings 212: 559-567.

Pabalan, R.T. 1994. Thermodynamics of ion-exchange between clinoptilolite and aqueous solutions of Na^+/K^+ and Na^+/Ca^{2+}. *Geochimica et Cosmochimica Acta 58.*

Pabalan, R.T., and F.P. Bertetti. 1994. Thermodynamics of ion-exchange between Na^+/Sr^{2+} solutions and the zeolite mineral clinoptilolite. *Scientific Basis for Nuclear Waste Management XVII.* A. Barkatt and R. Van Konynenburg, eds. Pittsburgh, PA: Materials Research Society: MRS Symposium Proceedings 333: 731-738.

Pabalan, R.T., and W.M. Murphy. 1990. Unsaturated mass transport (Geochemistry) *Report on Research Activities for the Quarter April 1 through June 30, 1990.* W.C. Patrick, ed. CNWRA 90-02Q. San Antonio, TX: Center for Nuclear Waste Regulatory Analyses: 2-1 to 2-31.

Pabalan, R.T., and K.S. Pitzer. 1991. Mineral solubilities in electrolyte solutions. *Activity Coefficients in Electrolyte Solutions.* 2nd Edition. K.S. Pitzer, ed. Boca Raton, FL: CRC Press 2: 435-490.

Peters, C.A., I.C. Yang, J.D. Higgins, P.A. Burger. 1992. A preliminary study of the chemistry of pore water extracted from tuff by one-dimensional compression. Y.F. Kharaka, and A.S. Maest, eds. *Water-Rock Interaction.* Rotterdam, Netherlands: Balkema: 741-744.

Pitzer, K.S. 1973. Thermodynamics of electrolytes. 1. Theoretical basis and general equations. *Journal of Physical Chemistry* 77: 268-277.

Pitzer, K.S. 1987. A thermodynamic model for aqueous solutions of liquid-like density. *Reviews in Mineralogy* 17: 97-142.

Pitzer, K.S. 1991. Ion interaction approach: Theory and data correlation. *Activity Coefficients in Electrolyte Solutions.* 2nd Edition. K.S. Pitzer, ed. Boca Raton, FL: CRC Press: 75-153.

Puchelt, H., and B. Bergfeldt. 1992. Major and trace element concentrations in waters centrifuged from unsaturated soils. Y.K. Kharaka, and A.S. Maest, eds. *Water-Rock Interaction.* Rotterdam, Netherlands: Balkema: 751-752.

Reardon, E.J., and D.K. Armstrong. 1987. Celestite ($SrSO_4(s)$) solubility in water, seawater, and NaCl solution. *Geochimica et Cosmochimica Acta* 51: 63-72.

Scatchard, G. 1936. Concentrated solutions of strong electrolytes. *Chemical Reviews* 19: 309-327.

Scatchard, G. 1968. Excess free energy and related properties of solutions containing electrolytes. *Journal of the American Chemical Society* 90: 3,124-3,127.

Smith, S.N., S. Sarada, and R. Palepu. 1993. Activity coefficients of $NaNO_3$ in (Mg, Ca, Sr, and Ba) $(NO_3)_2$ + H_2O systems at 298 K by EMF methods. *Canadian Journal of Chemistry* 71: 384-389.

Sposito, G. 1981. *The Thermodynamics of Soil Solutions.* New York, NY: Oxford University Press.

Sturchio, N.C., J.K. Bohlke, and C.M. Binz. 1989. Radium-thorium disequilibrium and zeolite-water ion-exchange in a Yellowstone hydrothermal environment. *Geochimica et Cosmochimica Acta* 53: 1,025-1,034.

Surdam, R.C. 1977. Zeolites in closed hydrologic systems. *Reviews in Mineralogy* 4: 65-91.

Surdam, R.C. and R.A. Sheppard. 1978. Zeolites in saline, alkaline-lake deposits. *Natural Zeolites: Occurrence, Properties, Use.* L.B. Sand and F.A. Mumpton, eds. New York, NY: Pergamon Press: 145-174.

Townsend, R.P. 1986. Ion exchange in zeolites: Some recent developments in theory and practice. *Pure and Applied Chemistry* 58: 1,359-1,366.

Tschernich, R.W. 1992. *Zeolites of the World.* Phoenix, AZ: Geoscience Press.

Vanselow, A.P. 1932. Equilibria of the base-exchange reactions of bentonites, permutites, soil colloids, and zeolites. *Soil Science* 33: 95-113.

White, A.F., H.C. Claassen, and L.V. Benson. 1980. *The Effect of Dissolution of Volcanic Glass on the Water Chemistry in a Tuffaceous Aquifer.* USGS Open-File Report 1535-Q. Rainier Mesa, NV: U.S. Geological Survey.

White, K.J. 1988. *Ion Exchanges in Clinoptilolite.* Ph.D. Dissertation. Salford, UK: University of Salford.

Whitfield, M.S., Jr., E.P. Eshom, W. Thordarson, and D.H. Schaefer. 1985. *Geohydrology of Rocks Penetrated by Test Well USW H-4.* USGS Water Resource Information Report 85-4030. Yucca Mountain, Nye County, NV. Reston, VA: U.S. Geological Survey.

Yang, I.C., A.K. Turner, T.M. Sayre, and P. Montazer. 1988. *Triaxial-Compression Extraction of Pore Water from Partially-Saturated Tuff.* USGS Water Resource Information Report 88-4189.Yucca Mountain, NV. Denver, CO: U.S. Geological Survey.

3 REACTION KINETICS AND THERMODYNAMICS OF DISSOLUTION AND GROWTH OF ANALCIME AND CLINOPTILOLITE AT 25 °C

3.1 INTRODUCTION

Primary volcanic glass in the natural system at Yucca Mountain is partially altered to clinoptilolite and analcime (see Section 4.2 for a general discussion of mineralogical alteration at Yucca Mountain). These minerals are particularly significant to performance of the proposed geologic repository for nuclear waste because their sorptive characteristics may enhance retardation of radionuclide transport and because their interactions with groundwater could affect its chemistry. In turn, groundwater chemistry would affect waste package and waste form performance, and radioelement speciation and solubility. Despite their significance, the fundamental thermodynamic and kinetic parameters required for predictive modeling and interpretations of chemical interactions among clinoptilolite, analcime, and groundwater are poorly known. The objective of research reported in this section is to advance knowledge of the fundamental properties of these minerals through controlled experimentation, and to interpret the data in the context of the geochemical system at Yucca Mountain. In particular, experiments have been designed and conducted to measure rates and elucidate mechanisms of dissolution and growth of analcime and clinoptilolite. The solubilities of these minerals have been measured, and standard state Gibbs free energies of formation have been derived from the solubility data. The data for clinoptilolite can be combined with ion-exchange data reported in Section 2 of this report to derive standard state Gibbs free energies for binary solid solutions. Derived thermodynamic properties permit evaluations of the state of equilibrium with respect to analcime and clinoptilolite of waters from the Yucca Mountain environment. Also, derived thermodynamic data can be used to evaluate estimated properties for multicomponent clinoptilolite used in modeling studies reported in Section 4.

An idealized reaction between Na-clinoptilolite and analcime can be written

$$\underset{\text{Na-clinoptilolite}}{Na_2Al_2Si_{10}O_{24}\cdot 8H_2O} \rightleftharpoons \underset{\text{analcime}}{2NaAlSi_2O_6\cdot H_2O} + \underset{\text{aqueous silica}}{6SiO_2} + 6H_2O \qquad (3\text{-}1)$$

which indicates that equilibrium between these minerals depends on the concentration of aqueous silica. This observation is consistent with the general coexistence of clinoptilolite with metastable cristobalite and opal CT and absence of cristobalite in the diagenetic zone characterized by analcime at Yucca Mountain (Broxton et al., 1987; see Section 4.2). Recognizing aqueous silica as a possible controlling variable, an experimental strategy was devised to explore the dissolution, precipitation, and aqueous solubilities of analcime and a sodium form of clinoptilolite, and their mutual equilibrium corresponding generally to reaction (3-1). Preliminary computations of experimental conditions using EQ3/6 Version 7.1 with DATA0.COM.R16 (Wolery and Daveler, 1992)[1] indicated that complications associated with variations in aqueous solution composition and precipitation of other phases could be limited by

[1]See Appendix C for a discussion of the EQ3/6 aqueous speciation and reaction path modeling software and data.

conducting experiments in a mixed 0.1 molal sodium chloride and 0.01 molal sodium bicarbonate solution equilibrated at 25 °C with atmospheric CO_2 (Murphy, 1991). Aqueous solutions of this design maintain nearly constant pH near 9 and nearly constant sodium, chloride, and bicarbonate concentrations during the course of reactions with analcime and/or clinoptilolite. At pH near 9 aqueous aluminum is dominated by tetrahedral $Al(OH)_4^-$, which limits possible precipitation of dioctahedral clay minerals with aluminum in octahedral coordination.

3.2 REVIEW OF ANALCIME THERMODYNAMICS AND DISSOLUTION

The occurrence of analcime in a variety of geologic environments has stimulated several studies of its stability and thermodynamic properties. Data for analcime have been derived by three general methods: calorimetry, hydrothermal phase equilibrium determinations, and low-temperature solubility experiments. Evaluation of these data is complicated by variations in the chemical compositions of test specimens. The Si to Al ratio and H_2O content of natural analcime commonly differ from the ideal stoichiometry. Analcime samples collected from Yucca Mountain are enriched in Si relative to the ideal stoichiometry. Analyzed compositions of Yucca Mountain samples (Broxton et al., 1987) generally yield stoichiometries ranging from $(NaAl)_{0.9}Si_{2.1}O_6 \cdot nH_2O$ to $(NaAl)_{0.77}Si_{2.23}O_6 \cdot nH_2O$, and most analyses cluster around $(NaAl)_{0.85}Si_{2.15}O_6 \cdot nH_2O$, where n represents the number of H_2O per formula unit. Even small variations in mineral composition can lead to large differences in derived thermodynamic properties, which is illustrated for analcime in Section 3.6.

3.2.1 Calorimetric Data

Robie et al. (1978) summarized calorimetrically determined standard entropy (S°), standard enthalpy of formation ($\Delta H_f°$), and standard Gibbs free energy of formation ($\Delta G_f°$) for analcime derived from King (1955), Kelly and King (1961), and Barany (1962) (Table 3-1). (Standard state properties of formation are relative to the elements.) The Robie et al. (1978) compilation includes a revised interpretation of the Barany (1962) data for analcime which accounts for a correction in the value for the standard enthalpy of formation of gibbsite, in accord with data reported in Hemingway and Robie (1977). Although the ideal analcime chemical formula is given in the Robie et al. (1978) report, samples used in experiments to generate the data probably deviated from this composition as noted by Johnson et al. (1982).

Johnson et al. (1982) made calorimetric measurements of the properties of analcime including the standard heat capacity ($C_p°$) (Table 3-1). The mineral composition was analyzed and interpreted as $(NaAl)_{0.96}Si_{2.04}O_6 \cdot H_2O$. Johnson et al. (1982) reported that their analcime samples and other test materials closely corresponded to those used in the experimental studies that provided data for the compilations by Robie et al. (1978) and Helgeson et al. (1978). Johnson et al. (1982) used their values for the standard Gibbs free energy and heat capacity for analcime, together with data from Helgeson and Kirkham (1974), Walther and Helgeson (1977), and Helgeson et al. (1978) for the properties of H_2O, aqueous SiO_2, and albite, to show that the analcime calorimetric data are compatible (within limits of uncertainty) with the experimental phase equilibrium data used by Helgeson et al. (1978) to derive analcime properties. Analcime properties in the EQ3/6 composite database (see Appendix C) are derived from the data of Johnson et al. (1982).

Table 3-1. Standard state thermodynamic properties of analcime at 25 °C and 1 bar

$S°$ J/K·mole	$\Delta H_f°$ kJ/mole	$\Delta G_f°$ kJ/mole	$C_p°$ J/K·mole	Reference
234.43 ±2.51	−3,309.839 ±3.598	−3,091.730 ±3.682	—	Robie et al. (1978)
234.30	−3,306.165	−3,088.200	212.13	Helgeson et al. (1978)
226.75 ±0.23	−3,296.9 ±3.3	−3,077.2 ±3.3	211.53 ±0.21	Johnson et al. (1982)
—	−3,298.4 ±2.6	—	—	Johnson et al. (1982)*
—	—	−3,085.4	—	This study

*Reinterpretation of data from Barany (1962)

3.2.2 Hydrothermal Phase Equilibrium Data

Helgeson et al. (1978) compiled thermodynamic properties for analcime (Table 3-1) as part of their comprehensive development of an internally consistent database for minerals. The data were derived primarily from phase equilibrium experiments at elevated temperatures and pressures, but data also depend on experimental and estimated heat capacities and entropies. The Helgeson et al. (1978) values for analcime are compatible with reported hydrothermal phase equilibria for reactions between analcime and albite, and among analcime, nepheline, and albite. However, they are incompatible with published data for equilibria among analcime, quartz, and albite. Helgeson et al. (1978) attributed this discrepancy to major solid solution (excess silica) in the analcime samples used in the analcime-albite-quartz experiments. The analcime data embedded in the program SUPCRT92 (Johnson et al., 1992a) are based on those reported by Helgeson et al. (1978).

3.2.3 Solubility Data

Caullet et al. (1980) reported data for the dissolution of synthetic analcime in 0.02, 0.10, and 0.50 molar NaOH solutions at 25, 60, and 80 °C. Based on their reported analytical data, the composition of the analcime was $Na_{0.984}Al_{1.026}Si_{1.984}O_6 \cdot 1.076H_2O$. However, in their thermodynamic analysis, Caullet et al. (1980) assumed the composition $NaAlSi_{1.94}O_{5.88}$, which has the analytical Al/Si ratio but misrepresents the sodium analysis and neglects the water content. Aqueous solution data were collected after periods of 1 and 2 mo of reaction in nine separate experiments. Measured increases in Si and Al concentrations between 1 and 2 mo fail to demonstrate that equilibrium was achieved in the experiments. Therefore, the thermodynamic data derived by Caullet et al. (1980) from these experiments are unreliable. Furthermore, ambiguities with regard to the bulk chemical compositions of the aqueous solutions and aqueous speciation make analyses of the solubility data untenable. However, the relative

release of aluminum and silicon in the Caullet et al. (1980) experiments corresponds well to the ideal (1 Al to 2 Si) stoichiometric relations (Figure 3-1).

3.2.4 Dissolution Reaction and Aqueous Species

The dissolution reaction for analcime of generalized stoichiometry can be written

$$(NaAl)_{1+x}Si_{2-x}O_6 \cdot nH_2O \rightleftharpoons$$
$$(1+x)Na^+ + (1+x)Al(OH)_4^- + (2-x)SiO_2 + [n-2(1+x)]H_2O \qquad (3\text{-}2)$$

where n and x are coefficients expressing compositional variations. Thermodynamic interpretation of solubility data requires knowledge of the activities of the aqueous species in this reaction, which depend on the bulk solution composition and speciation. Equilibrium calculations with EQ3 (Wolery and Daveler, 1992; see Appendix C) for the dilute, basic sodium bicarbonate solutions in the kinetic and solubility studies reported in this section indicate that important aqueous species in addition to those in reaction (3-2) are: HCO_3^-, CO_3^{2-}, $NaHCO_3$, $NaHSiO_3$, $HSiO_3^-$, H^+, and OH^-. Aqueous species of lesser importance are $NaCO_3^-$ and NaCl. The EQ3 data for most of these species are derived from SUPCRT92 (Johnson et al., 1992a) which provides a recently updated compilation of internally consistent standard-state thermodynamic data for minerals and aqueous species derived largely from solubility studies and empirical correlations. In addition, data for $NaHCO_3$ and $NaCO_3^-$ are taken from Wagman et al. (1982).

3.3 REVIEW OF THE THERMODYNAMIC PROPERTIES OF CLINOPTILOLITE AT 25 °C

Calorimetrically measured thermodynamic properties of two natural, multicomponent clinoptilolites are summarized in Table 3-2. Hemingway and Robie (1984) reported calorimetric data for natural clinoptilolite from Lake Tecopa, Inyo County, California, with the composition $(Na_{0.56}K_{0.98}Ca_{1.50}Mg_{1.23})(Al_{6.7}Fe_{0.3})Si_{29}O_{72}\cdot 22H_2O$. Johnson et al. (1991) reported heat capacity and heat of solution measurements and derived thermodynamic data for clinoptilolite from Malheur County, Oregon. The composition of the clinoptilolite used in their study is $(Na_{0.954}K_{0.543})(Ca_{0.761}Mg_{0.124}Ba_{0.062}Sr_{0.036}Mn_{0.002})(Al_{3.450}\ Fe_{0.017}Si_{14.533})O_{36}\cdot 10.922H_2O$. Johnson et al. (1991, 1992) used silicalite as the Si-containing reference material and (silicalite+hydrofluoric acid) as the reference reaction for the calorimetric measurements, instead of the generally used α-quartz and (α-quartz+hydrofluoric acid) reaction. To reference their values of $\Delta H_f°$ and $\Delta G_f°$ for clinoptilolite to α-quartz, 3.51 kJ/mol should be added for each Si atom in the empirical formula of the zeolite. Furthermore, Johnson et al. (1991, 1992) used a new value of $\Delta H_f°$ for $Al(OH)_3$ (gibbsite) in their thermochemical cycle calculation of the $\Delta H_f°$ and $\Delta G_f°$ of the Oregon clinoptilolite and other zeolites. If consistency with $\Delta H_f°$ and $\Delta G_f°$ of minerals tabulated in databases such as EQ3/6 is desired, a correction of 1.8 kJ/mol for each Al atom in the formula should also be added to the values of Johnson and others (1991, 1992).

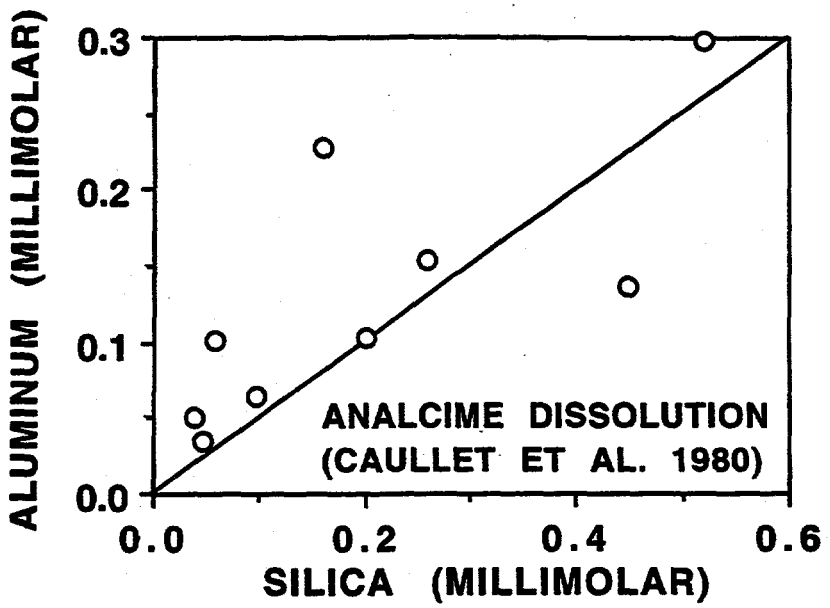

(A)

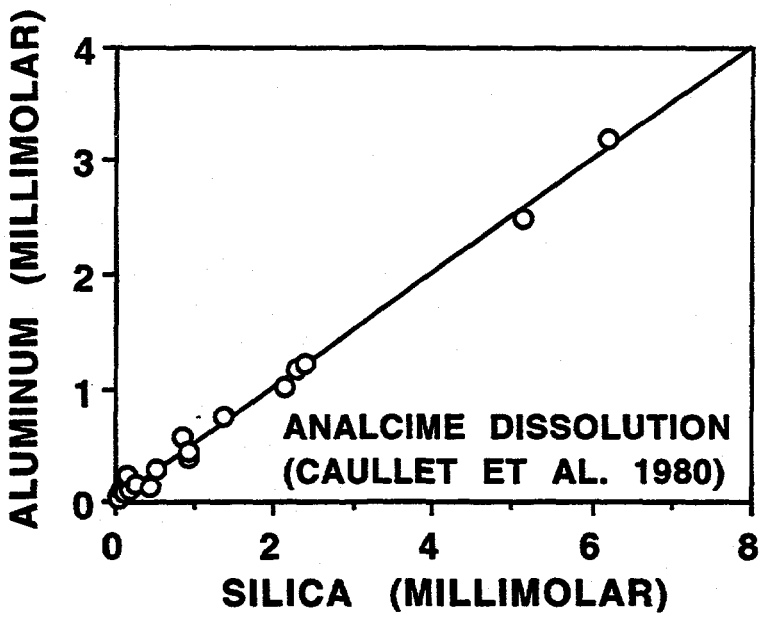

(B)

Figure 3-1. Concentrations of Al and Si in the analcime dissolution experiment reported by Caullet et al. (1980). The initial period of reaction is illustrated in A, and complete data are shown in B. Lines have a slope of 0.5 corresponding to the Al to Si ratio in idealized analcime.

Table 3-2. Standard state thermodynamic properties of clinoptilolite at 25 °C and 1 bar

$S°$[1] J/K·mole	$\Delta H_f°$ kJ/mole	$\Delta G_f°$ kJ/mole	$C_p°$ J/K·mole	Reference
2,872.3 ±9.0	—	—	2,986.5	Hemingway and Robie (1984)[2]
1,483.1	−20,645.0 ±13.5	−19,078.4	1,537.4 ±3.1	Johnson et al. (1991)[3]
—	−20,587.7	−19,021.2	—	Johnson et al. (1991)[3,4]
—	−13,725.1	−12,808.0	—	Johnson et al. (1991)[4,5]
—	—	−12,708.0	—	This study[5]

[1] Reported as S° - S°(0 K) because of unknown configurational disorder.
[2] Based on 72 structural oxygens.
[3] Based on 36 structural oxygens.
[4] Adjusted for α-quartz and $Al(OH)_3$ reference states (see text).
[5] Based on 24 structural oxygens.

3.4 SAMPLE CHARACTERIZATION AND PREPARATION

3.4.1 Analcime

Analcime samples were obtained from Ward's Natural Science Establishment, Inc. These samples are from Mt. St. Hilaire, Quebec, where analcime occurs in coarsely crystalline, late magmatic-stage pegmatites in nepheline syenites. The as-received samples consisted of analcime crystals about 1 to 6 cm in diameter intergrown with accessory K-feldspar, hornblende, and muscovite. Samples were broken into pieces less than 0.5 cm in diameter with a hammer. Essentially pure analcime crystals were separated by hand-picking. Purified samples were crushed and ground in a mortar and pestle, and sieved into four size ranges using a Ro-Tap sieve shaker and 8-in.-diameter stainless steel sieves. The size ranges were: (i) 200–230 mesh (75–63 μm), (ii) 230–325 mesh (63–45 μm), (iii) 325–450 mesh (45–32 μm), and (iv) 450–630 mesh (32–20 μm). Sieving was repeated several times to minimize retention of analcime grains of a particular size with grains in the larger size range. Analcime powders in the first three size ranges were used in dissolution/precipitation kinetics experiments, and analcime in the 450–630 mesh size fraction was used in equilibrium solubility experiments.

XRD analysis of the less than 450 mesh size powder samples was done using a Siemens D-500 x-ray diffractometer and Siemens Kristalloflex 800 x-ray generator to verify that the mineral sample was analcime. A comparison of the pattern with the Joint Committee on Powder Diffraction Standards (JCPDS) mineral powder diffraction file (#19–1180) confirmed that the sample is analcime. No diffraction peaks for other minerals were observed.

All samples were cleaned ultrasonically several times in ultrapure (>17 megaohm resistivity) water to remove fine surface particles. A comparison of SEM photomicrographs of analcime powder before and after ultrasonic cleaning is shown in Figures 3-2A and 3-2B. These images indicate that ultrasonic cleaning removed most of the fine material from the analcime surfaces. A SEM photomicrograph of analcime grains after reaction with NaCl-$NaHCO_3$ solutions in the ACDTIIA experiment is shown in Figure 3-2C.

Surface areas of ultrasonically cleaned analcime powders were determined using both nitrogen and argon gas adsorption methods. Average surface areas calculated using the Brunauer-Emmett-Teller (BET) model are 0.11 ± 0.01, 0.12 ± 0.02, and 0.16 ± 0.04 m^2/g for analcime powders in the 200–230, 230–325 and 325–450 mesh size fraction, respectively, where uncertainties represent one standard deviation in duplicate analyses.

The chemical composition of five analcime powder samples from various size fractions was determined by ICP emission spectrometry subsequent to lithium metaborate fusion and dissolution in an HCl/HNO_3 matrix. The water content of three unreacted and two reacted analcime samples was determined by measuring their weight before and after heating at 900 °C for 2 hr. Results of the chemical analyses are given in Table 3-3.

These chemical analyses were converted to a molar basis by dividing the analytical oxide masses by the oxide molecular weight and normalizing the resulting molar oxide quantities to 6 structural oxygens (excluding oxygen associated with H_2O). The resulting compositions are shown in Figure 3-3 to illustrate the relation between tetrahedral Al (+Fe) and higher coordination Na (+K+2Ca+2Mg) cations as a function of Si (+Ti). The analcime structure accommodates coupled substitution of NaAl for Si, which is illustrated by the line plotted in Figure 3-3. The data reveal some scatter around this line, which is probably an indication of sample heterogeneity as well as analytical error. An intermediate value was selected for the purposes of data interpretation, which can be represented by the formula $Na_{1.02}Al_{1.02}Si_{1.98}O_6$, or Na/Si = Al/Si = 0.515 on a molar basis. Trace quantities of other elements are neglected in this formula. The water analysis for reacted samples shown in Table 3-3, when converted to a molar basis, yields the structurally correct value of 1 H_2O per 6 structural oxygens.

3.4.2 Clinoptilolite

The clinoptilolite material used in the dissolution experiments is the Na form (100–200 mesh size) clinoptilolite also used in the ion-exchange experiments. A description of its characterization and preparation is given in Section 2 of this report. Its chemical formula, calculated from the ICP analysis and based on 24 oxygens per unit cell, is $(Na_{1.804}K_{0.123})(Ca_{0.003}Mg_{0.035})(Al_{1.947}Fe_{0.044})(Si_{10.002}Ti_{0.004})O_{24} \cdot 7.43H_2O$. For comparison, the idealized formula for the sodium endmember of clinoptilolite is $Na_2Al_2Si_{10}O_{24} \cdot 8H_2O$.

3.4.3 Initial Solutions

Dissolution experiments were conducted by reacting weighed amounts of analcime and/or clinoptilolite powder with 0.1 molal NaCl-0.01 molal $NaHCO_3$ solutions continuously equilibrated with atmospheric CO_2 at 25 °C. For the dissolution/precipitation kinetics experiments, 1,000 ml of NaCl-$NaHCO_3$ solutions were used, whereas 250 ml were used for the equilibrium solubility experiments. Before adding the solid to the NaCl-$NaHCO_3$ solutions, the aqueous solutions were pre-equilibrated with

(A)

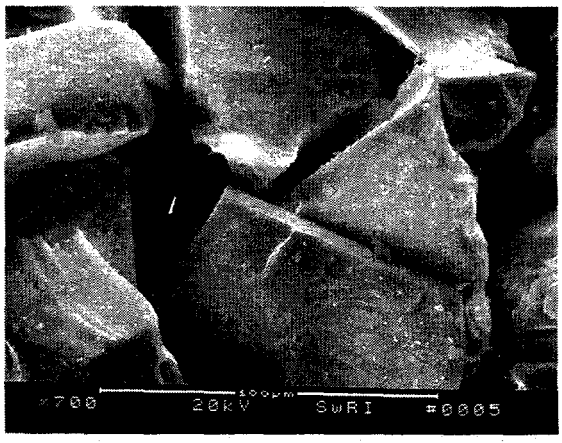

(B)

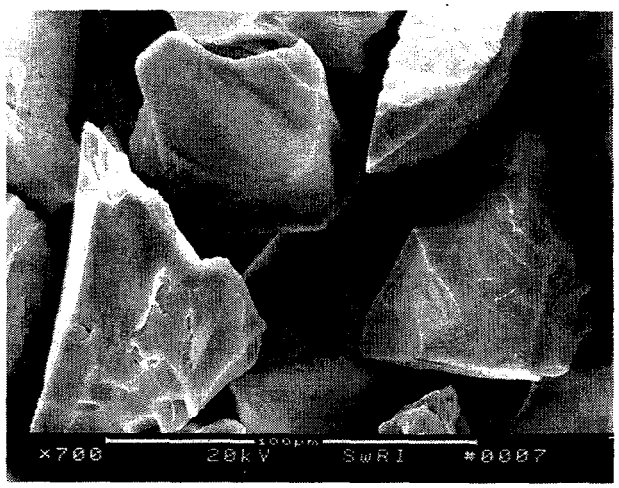

(C)

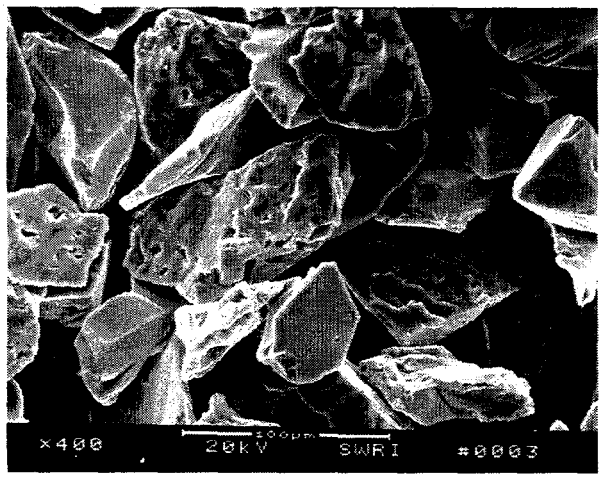

Figure 3-2. Scanning electron photomicrographs of analcime powder: before (A) and after (B) ultrasonic cleaning, and after reaction with NaCl-$NaHCO_3$ solutions in the ACDTIIA experiment (C). Note extensive but selective etch pitting in the reacted samples.

Table 3-3. Analcime chemical analyses (weight percent)

Component	Sample 1 (<325 mesh)	Sample 2 (<325 mesh)	Sample 3 (200-230 mesh)	Sample 4 (450-630 mesh)	Sample 5 (230-325 mesh)
SiO_2	54.36	54.11	54.70	53.77	54.70
Al_2O_3	23.79	23.20	24.54	23.29	24.38
TiO_2	0.01	0.01	0.00	0.00	0.00
Fe_2O_3	0.04	0.02	0.04	0.11	0.04
MgO	0.06	0.06	0.02	0.03	0.02
CaO	0.00	0.00	0.00	0.01	0.00
Na_2O	14.60	14.00	14.50	14.47	14.20
K_2O	0.02	0.05	0.02	0.01	0.04
H_2O[1]	7.89	7.89	7.89	7.89	7.89
H_2O[2]	8.17	8.17	8.17	8.17	8.17
TOTAL[3]	100.78	99.36	101.71	99.58	101.27

1 Average of 3 analyses ($\pm$0.12) for H_2O for ultrasonically cleaned (unreacted) analcime.
2 Duplicate analyses of two samples recovered from the ASE4 solubility experiment (see Section 3.6).
3 Totals based on chemical analyses and H_2O contents for unreacted samples.

atmospheric CO_2 for several days until constant pH values were achieved. The analcime and/or clinoptilolite powder and aqueous solutions were reacted in 500- or 1,000-ml polypropylene bottles which were maintained at 25.0$\pm$0.1 °C and kept under agitation using a constant temperature water bath. To keep the experimental systems open to atmospheric CO_2, the bottles were covered with a porous material (Kimwipes).

3.4.4 Analytical Procedure

The extent of reaction was followed by taking 35- to 50-ml aqueous samples, which were passed through 0.2-micron syringe filters, and analyzing SiO_2 and Al concentrations using a Milton Roy 1201 UV-Vis spectrophotometer. Al was analyzed using the Eriochrome Cyanine R Method [Method 3500-Al D, (APHA, 1989)]. SiO_2 was measured by the Molybdosilicate Method or the Heteropoly Blue Method [Methods 4500-Si D and 4500-Si E, respectively (APHA, 1989)], depending on the expected SiO_2 concentration. The use of glassware in the analysis of SiO_2 was avoided because of demonstrated silica contamination in preliminary tests. The pH and Na^+ concentrations were analyzed using Orion ion selective electrodes. The pH electrode was calibrated using commercially available pH buffers (pH 7.00

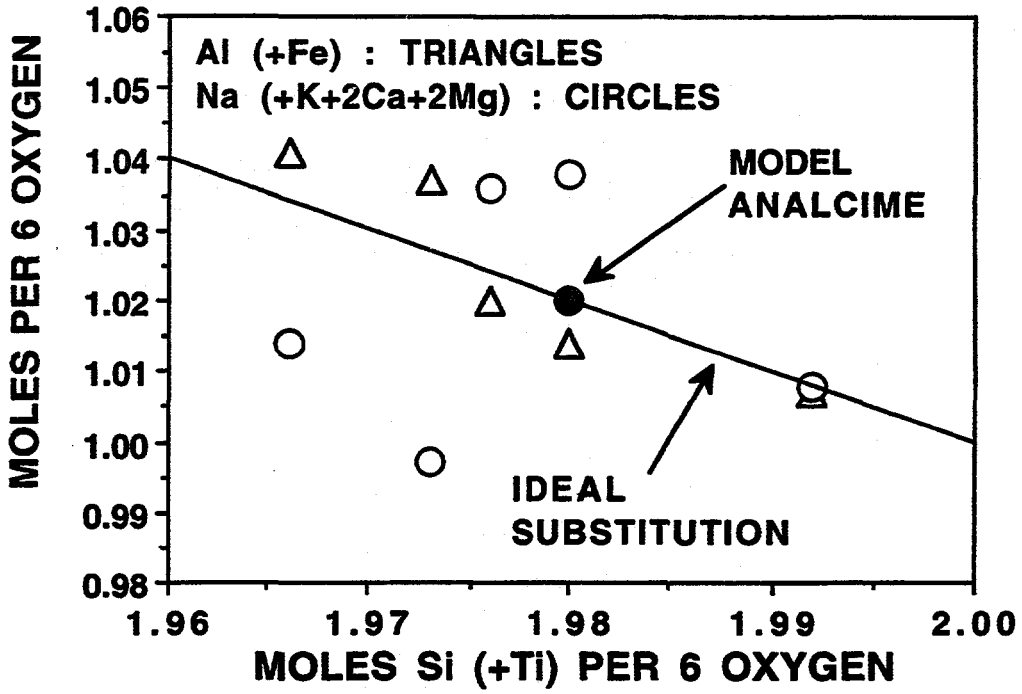

Figure 3-3. Structural interpretation of analcime chemical analyses. Moles of Al (+Fe) and Na (+K+2Ca+2Mg) per 6 moles of structural O are plotted as a function of moles of Si (+Ti) per 6 moles of structural O. The line denotes NaAl for Si substitution. The solid circle represents an intermediate value adopted in the interpretation of dissolution, precipitation, and solubility experimental data.

and 9.00); differences in liquid junction potential between these buffers and the experimental solutions were neglected. The Na^+ ion selective electrode was calibrated using commercially available Na^+ standards; an ionic strength adjustor (4 M NH_4Cl + 4 M NH_4OH) was added to these standards and to the experimental samples prior to analysis. Sample aliquots were not replaced with fresh solutions to avoid discontinuities in the evolution of the solution composition and to facilitate data interpretation. Therefore, each bottle was weighed before and after each sample was taken to record evaporation losses and changes in the mass of the solutions. Analcime and clinoptilolite dissolution and growth experiments are listed in Table 3-4, and characteristics of individual experiments and analytical data are given in Appendix B.

3.5 ANALCIME DISSOLUTION MECHANISM AND RATE

3.5.1 Mass Transfer Relations

Mechanistic and kinetic interpretation of the dissolution and growth data require knowledge of mass transfer (i.e., moles of Si and Al released or precipitated) as a function of time and solution chemistry. The net release to the aqueous solution in a dissolution or precipitation experiment is given by

Table 3-4. Summary of analcime and clinoptilolite experimental studies

Subject and Objective	Test Name*
Mechanism and rate of analcime dissolution and analcime solubility	ACDTIA (B) ACDTIIA (C) ACDTIIIA (D)
Analcime dissolution reaction solubility limit	ASE1 (E) ASE2 (E) ASE3 (E) ASE4 (E)
Analcime dissolution reaction solubility limit	ASEA1 (E) ASEA2 (E) ASEA3 (E)
Analcime precipitation reaction solubility limit	RACDTIA (F) RACDTIIIA (F)
Analcime precipitation reaction solubility limit	RASH1 (G) RASH2 (G) RASH3 (G) RASH4 (G)
Analcime-clinoptilolite mutual equilibrium	ACDTIB (H) ACDTIIB (I) ACDTIIIB (J)
Mechanism and rate of clinoptilolite dissolution and clinoptilolite solubility	CDVSE1 (K) CDVSE2 (K) CDVSE3 (K) CDVSE4 (K)
Clinoptilolite precipitation reaction solubility limit	RCDV1 (L) RCDV2 (L) RCDV3 (L) RCDV4 (L)
*Letters in parentheses refer to data tables in Appendix B; experimental conditions are summarized in Appendix B, Table A.	

$$n_{I,R}(t_s) = m_I(t_s)W(t_s) + n_{I,E}(t_s) - m_I(t_o)W(t_o) \quad (3\text{-}3)$$

where $n_{I,R}(t_s)$ stands for the net number of moles of a particular component, I (e.g., Si or Al), released to solution (which is negative for net precipitation) at the time of sampling, t_s, $m_I(t_s)$ denotes the total molality of I at time t_s, $m_I(t_o)$ represents the molality of I at the time of initiation of the experiment, t_o, $W(t_s)$ stands for the mass of the solvent in the reaction vessel prior to sampling at time t_s. The number of moles of component I extracted in all solution samples removed from the reaction vessel at all times t_p prior to time t_s ($n_{I,E}$) is given by

$$n_{I,E}(t_s) = \sum_{t_p<t_s} m_I(t_p)W_E(t_p) \quad (3\text{-}4)$$

where $W_E(t_p)$ represents the mass of solvent extracted in the sample taken at time t_p. Measurements of experimental solution masses before and after extraction of each solution sample provide values of W and

W_E permitting the effects of variations in solution mass due to sampling and evaporation to be explicitly accounted in calculations of cumulative mass transfer. Differences between solution and solvent masses are negligible for the dilute solutions in these experiments.

Data reported in Appendix B Tables B, C, and D were used in Eqs. (3-3) and (3-4) to calculate values for the cumulative release of Si and Al in analcime dissolution experiments of the ACDT A series. Results are illustrated in the mass release and stoichiometry plots in Figures 3-4 and 3-5. Because of the variable solution mass, cumulative moles released corresponding to each sampling time and analytical measurement depend on measured concentrations for all earlier experimental times. Spurious analytical data can therefore adversely influence calculated values of the total mass released for all subsequent times. To minimize this effect, interpolated concentrations were used in place of a few apparently spurious analytical values to calculate solute masses extracted during sampling. However, the analytical values for concentrations were used in calculations of mass released at each time.

The slopes of the trends of mass release versus time illustrated in Figure 3-4 correspond to rates of reaction, which were rapid at the outset (represented by lines in Figure 3-4 for ACDTIA and ACDTIIA) and slow at the conclusion of the experiments. This is interpreted to be a consequence of the variation of reaction rate with the approach to equilibrium. Upward trailing values for the final experimental times may be a consequence of experimental inaccuracies that are magnified in the calculations of moles released as the remaining solution volume in each reaction vessel becomes small, and the effects of evaporation and solution sample extraction are relatively large. A possibility exists that evaporation can lead to supersaturation of solutions with respect to analcime at extended times in experiments of this design. However, continual net release of Si and Al and the solubility limit evaluated in Section 3.6 indicate that supersaturation was not achieved in the ACDT series experiments.

The data in Figure 3-5 give a strong indication that release of Si and Al from analcime was generally stoichiometric. This result is in accord with the data from Caullet et al. (1980) shown in Figure 3-1. The slopes of lines drawn through the data in Figure 3-5 correspond to the ratio of Al to Si in the adopted formula ($Na_{1.02}Al_{1.02}Si_{1.98}O_6 \cdot H_2O$). The positive intercepts of these lines on the Al axes indicate initial rapid preferential release of Al. This release is likely to be an indication of a change of the surface chemistry of the analcime in contact with the alkaline solution (i.e., silica enrichment). Small increases in the moles of Si released relative to Al released in the final samples of the ACDT series of experiments are indicated by final data points falling consistently below the lines in Figure 3-5. Terminal excess Si release compensates for initial excess Al release resulting in net release that is close to stoichiometric.

The data in Figure 3-5 also suggest that secondary phases did not precipitate, even though the solutions are calculated to be supersaturated with respect to a number of Al-rich minerals. Al concentrations and moles of Al released both increased continuously, even for the final samples. Absence of secondary phase formation is also supported by SEM examinations of the reacted grains from experiment ACDTIIA which revealed no observable secondary products but showed that many analcime grains developed etch pits (Figure 3-2C). Etch pits are a common characteristic of selective dissolution in areas of excess energy such as crystal defects.

Although variations in sodium concentration were small in the dissolution and solubility experiments, the sodium concentration increased by both evaporation of H_2O and dissolution of analcime. Mass transfer analysis permits calculation of the evolution of sodium concentrations, which are required

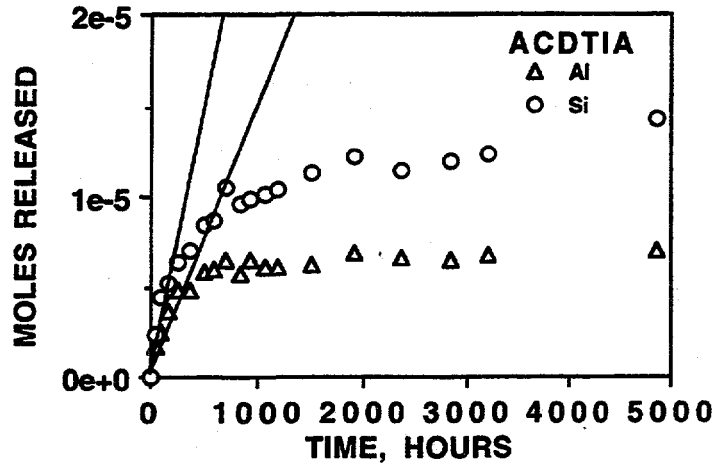

(A)

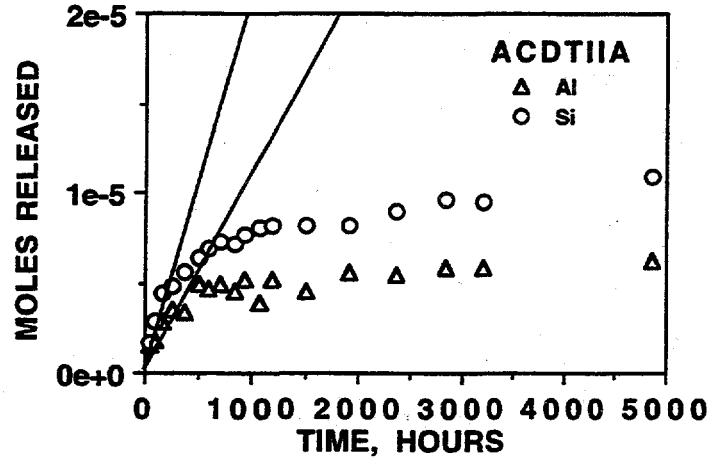

(B)

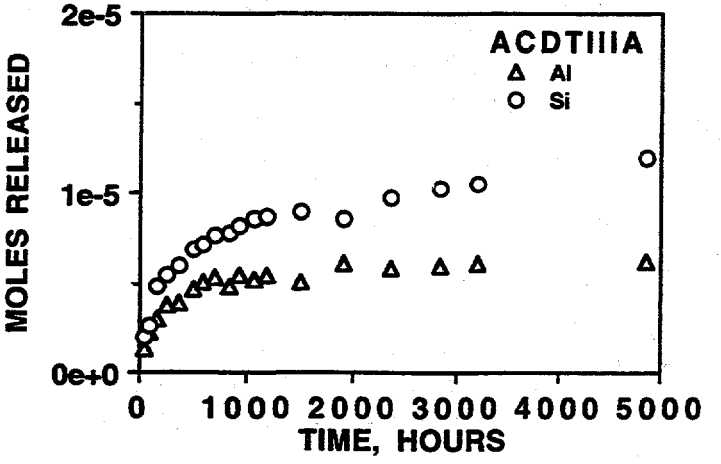

(C)

Figure 3-4. Moles of Al (triangles) and Si (circles) released as a function of time in ACDT A series analcime dissolution experiments. Lines in figures for the ACDTIA and ACDTIIA experiments indicate initial rates of Si and Al release (see text).

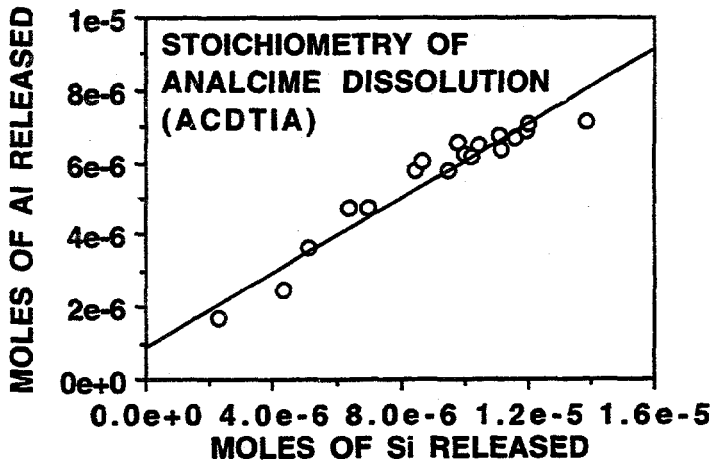

(A)

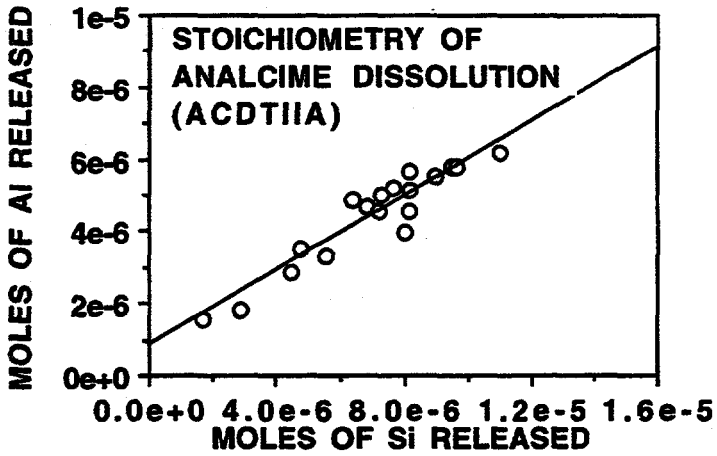

(B)

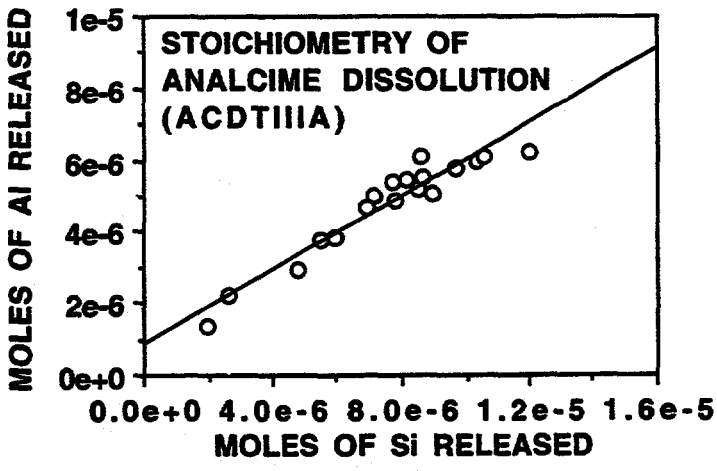

(C)

Figure 3-5. Relative numbers of moles of Al and Si released in ACDT A series analcime dissolution experiments. The slopes of the lines correspond to the analyzed ratio of Al (and Na) to Si in the reactant analcime (0.515). Although dissolution was generally stoichiometric, initial excess Al release and terminal, compensating, excess Si release are indicated.

in kinetic and thermodynamic interpretations. The total number of moles of sodium ($n_{Na,T}$) corresponding to the sum of the amount in the initial solution ($n_{Na,i}$) plus sodium released by dissolution of analcime can be represented by

$$n_{Na,T} = n_{Na,i} + (1 + x)\ \xi \tag{3-5}$$

where ξ stands for the number of moles of analcime dissolved and x represents the stoichiometric coefficient defined in reaction (3-2). The value of $n_{Na,T}$ is a function of time in the experiments because the reaction progress variable, ξ, varies with time. The number of moles of sodium in solution ($n_{Na,S}$) equals the total moles of sodium defined in Eq. (3-5) minus the moles of sodium extracted in solution samples ($n_{Na,E}$), i.e.,

$$n_{Na,S} = n_{Na,T} - n_{Na,E} \tag{3-6}$$

The amount of sodium removed in samples taken prior to time t_s is given by Eq. (3-4) written for Na where the concentration (molality) of sodium (m_{Na}) is simply given by

$$m_{Na} = n_{Na,S}/W_{H_2O} \tag{3-7}$$

Substituting Eqs. (3-4) and (3-5) in Eq. (3-6), and the resulting equation in Eq. (3-7) gives an expression for the sodium molality

$$m_{Na} = \left[n_{Na,i} + (1+x)\,\xi - \sum_{t_p<t_s} m_{Na}(t_p)W_E(t_p)\right] / W_{H_2O} \tag{3-8}$$

Sodium concentrations in the ACDT A series experiments can be calculated as a function of time with Eq. (3-8) using data from Appendix B (Tables B, C, and D) and values of ξ as a function of time, which can be derived from integration of a rate equation for analcime dissolution (see Section 3.5.1) or calculated based on release of Si or Al. Values of Na molality calculated by this method are shown by the solid line in Figure 3-6 for experiment ACDTIA and compared to experimental measurements of sodium concentration made by ISE (Appendix B, Table B). Comparison of measured and calculated values indicates that the calculations provide more accurate representations of the sodium concentration for the purposes of kinetic and thermodynamic interpretations. Chloride concentrations also increased in the experimental solutions due to evaporation, and chloride concentrations were calculated using analogous equations with no input from mineral dissolution. In general, mineral dissolution and/or growth had negligible effects on the sodium concentrations in the experiments compared to evaporation.

3.5.2 Kinetic Analysis

A general rate equation for mineral dissolution can be written as (Aagaard and Helgeson, 1982)

$$\frac{d\xi}{dt} = ks \prod_i a_i^{n_i} (1-(Q/K)^{(1/\sigma)}) \tag{3-9}$$

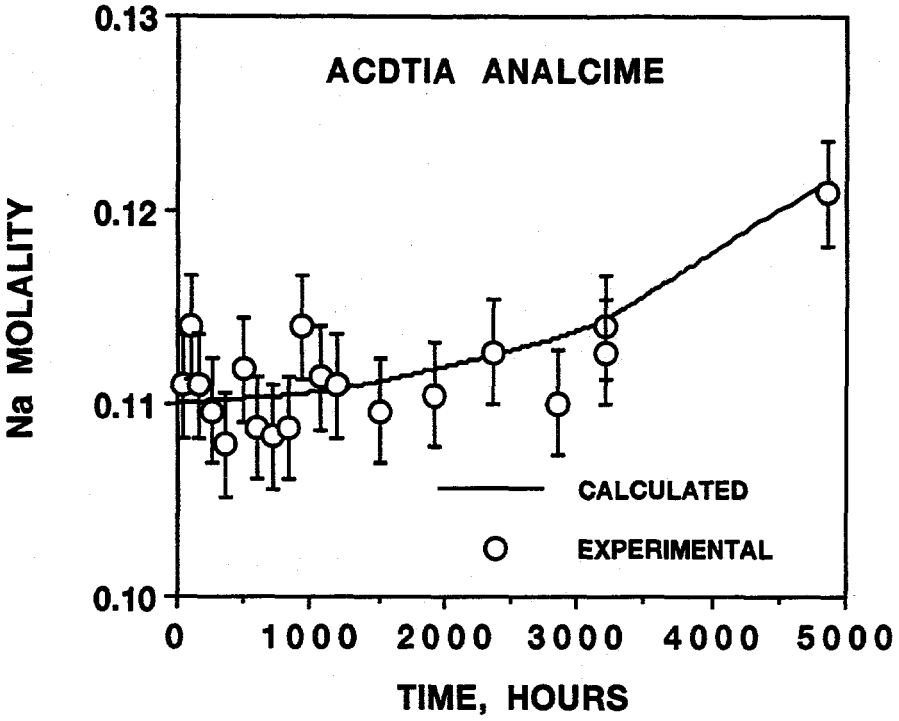

Figure 3-6. Na molality in the ACDTIA analcime dissolution experiment. Circle symbols represent analytical measurements using a sodium ion specific electrode. The curve illustrates calculated values based on initial conditions, reaction progress, and variable solution mass. Errors in the curve are relatively small because it depends primarily on accurate gravimetric analyses with water mass interpolated between measurements. Uncertainties in reaction progress have an insignificant effect on the calculated sodium concentration. Estimated error in experimental measurements is shown by vertical lines.

where ξ stands for the number of moles of dissolved reactant (i.e., the reaction progress variable), t represents time, s denotes the surface area of the reactant, $\prod_i a_i^{n_i}$ represents the product of activities of aqueous species i (e.g., H^+, $Al(OH)_4^-$) that affect the reaction rate independently of their effects on the state of disequilibrium, K stands for the equilibrium constant for the dissolution reaction, and Q denotes the activity product for this reaction. For elementary reactions, the factor σ in Eq. (3-9) is related to the activated complex stoichiometry by transition state theory. However, it may also be regarded as an empirical coefficient. For interpretations of analcime dissolution rates the value of σ was fixed at one. Reasonable fits can also be obtained using values of σ other than 1; however, discrimination between the interpretations is unwarranted given available data. For convenience, the rate constant, k, can be combined with other factors to define the preaffinity factor, k*,

$$k^* = ks \prod_i a_i^{n_i} \qquad (3\text{-}10)$$

The activity product for the general analcime dissolution reaction is given by

$$Q = [(a_{Na^+})(a_{Al(OH)_4^-})]^{(1+x)}(a_{SiO_2})^{(2-x)} \quad (3\text{-}11)$$

where a_{Na^+}, a_{SiO_2}, and $a_{Al(OH)_4^-}$ stand for the thermodynamic activities of the subscripted aqueous species, x is a parameter representing deviation of the analcime from ideal stoichiometry, and analcime and H_2O are assumed to be in their standard states with unit activity. For a reaction at equilibrium, K=Q. By definition, for each species i

$$a_i = m_i \gamma_i \quad (3\text{-}12)$$

where m_i and γ_i represent the molality and activity coefficient of species i.

Kinetic interpretation of the analcime mass transfer data was facilitated by development of a computer code that permits calculations of reaction progress as a function of time by numerically integrating the dissolution rate equation. The code requires an experiment-specific database to account for variable water masses resulting from solution sampling and evaporation. Rate equations are integrated in a stepwise manner for successive small intervals of reaction progress to obtain increments of elapsed time. Between successive steps, values for the solvent mass and the moles of dissolved species in solution are corrected, if necessary, for water sample extraction. Water mass and sodium molality are also stepwise corrected for evaporation by distributing the net evaporation linearly with time between water mass measurements. The number of moles of Si and Al released is calculated as a function of computed cumulative time by summing the moles in solution and the moles extracted in solution samples. The initial Al concentration in the mass transfer model can be set to a finite value to mimic the initial preferential Al release observed in the experiments. EQ3 aqueous speciation calculations indicated that activity coefficients and distributions of elements among aqueous species varied negligibly, and constant values were employed in the mass transfer model.

Dissolution data from ACDT A series experiments were similar, so the kinetic analysis is based primarily on data from experiment ACDTIA. The initial dissolution rate of analcime corresponds to the slope of a line regressed through the Si release data at the beginning of the experiment, divided by the number of moles of Si per mole of analcime (1.98), which equals 4×10^{-12} moles/s. Lines approximating Si and Al release corresponding to this initial rate of release are shown in Figure 3-4(A). During this initial period of reaction, the system was far from equilibrium with regard to reaction (3-2), and Q/K in Eq. (3-9) was close to zero. The chemical affinity for the dissolution reaction [$A = -RT\ln(Q/K)$] diminished to 8675 J/mole at 3,200 hr in experiment ACDTIA. At this state of undersaturation the theoretical impact of affinity on the net reaction rate is less than 3 percent. The initial rate, therefore, equals the preaffinity factor k* in Eq. (3-10). The surface area specific initial rate of reaction under conditions that are far from equilibrium is commonly interpreted as an apparent rate constant (e.g., Murphy and Helgeson, 1989). Dividing the initial rate determined for experiment ACDTIA by the specific surface area (1,100 cm^2/g) and the mass of material (3.75 g) yields an initial surface area specific dissolution rate of 10^{-15} moles/cm^2/s. This value was used together with appropriate surface areas, sample masses, and stoichiometric coefficients to calculate initial moles of Si and Al released per time in the ACDTIIA and ACDTIIIA experiments. Correspondence to the ACDTIIA data is good and indicated by lines in Figure 3-4 for initial Si and Al release. Correspondence with the ACDTIIIA data is not good, partially due to the high and relatively uncertain specific surface area determined for the fine grain size material used in this experiment (Section 3.4.1). The experimentally determined initial rate of

analcime dissolution corresponds well to that estimated by Brady and Walther (1989), which is $10^{-15.4}$ moles/cm^2/s at pH 9.

Assuming k* equal to 4×10^{-12} moles/s is constant throughout the experiment, its use in Eq. (3-10) substituted in Eq. (3-9) to calculate moles released at later stages of reaction progress provides a poor correspondence between calculated and experimental results. The constant value of k* leads to calculation of excessive mass transfer in early stages of reaction. Discovery of this effect was a fortuitous consequence of the reduction in water mass during the experiment. Because of significantly decreasing water mass, solution concentrations in the experiments grew at an increasing rate with time even though the surface reaction rate diminished as equilibrium was approached. Extrapolation of the rate derived from the initial stage of reaction leads to predictions of a large mass transfer to large masses of dilute solution early in the experiment. This result is inconsistent with the experimental results. The important observation with regard to reaction kinetics is that reaction rates diminished significantly for conditions that were relatively far from equilibrium. Two alternate mechanisms have been postulated and tested to account for these results. These are called the variably reactive materials hypothesis and the aqueous aluminate dependence hypothesis.

3.5.2.1 Variably Reactive Materials Hypothesis

Sample preparation, for example, grinding the original analcime crystal to powder, generates reactive surface materials with large corresponding values of k*, which are incompletely removed by ultrasonic cleaning (e.g., Holdren and Berner, 1979). Extra-reactive material may consist of fine particles and edges and corners and defects (e.g., dislocations) at the surface induced by grinding. SEM images of reacted grains show that rounding of edges occurred in dissolution experiments (e.g., Figure 3-2C). This material would have reacted quickly and possibly to completion in the early stages of the experiment. Later stages of reaction would have been dominated by materials characterized by a smaller value of k*. If this hypothesis is correct, application of the value of k* extracted from the initial reaction rate data throughout the experiment (or, notably, also to reactions in nature) would be inappropriate.

To examine the hypothesis that material of variable reactivity contributed to the experimental results for analcime dissolution, mass transfer data have been regressed assuming two distinct types of material existed and that they reacted simultaneously. One material is assumed to have a higher reactivity and limited mass (10^{-3} g). The ultrareactive material is postulated to dissolve completely in the initial stages of the experiment according to a relation for diminishing surface area for identical grains (Helgeson et al., 1984). The second material is assumed to have a lower reactivity and a constant preaffinity factor for the duration of the experiment. A reasonable data regression is illustrated in Figure 3-7, where the curve was calculated by stepwise integration of two expressions of Eq. (3-9) combined with Eq. (3-10) using $\sigma = 1$. For the less reactive material, k* was set to 1.98×10^{-13} moles/s. The value for k* for the more reactive material was taken initially to be 4×10^{-12} moles/s, and it decreased to zero as the extra reactive material dissolved completely and its surface area went to zero. The value for the equilibrium constant in Eq. (3-9) was based on results of the analcime solubility analysis given in Section 3.6. Activities of the aqueous species in the rate equation were calculated based on the initial conditions for water mass and species concentrations, calculated mass released due to analcime dissolution, solute and solvent extraction due to sampling and evaporation, and activity coefficients and aqueous species distributions from thermodynamic modeling of the equilibrium solution properties using EQ3. The relatively poor fit of the data for Al release shown in Figure 3-7 is largely a consequence of the inaccurate representation in the model of the deviation from stoichiometric dissolution of analcime

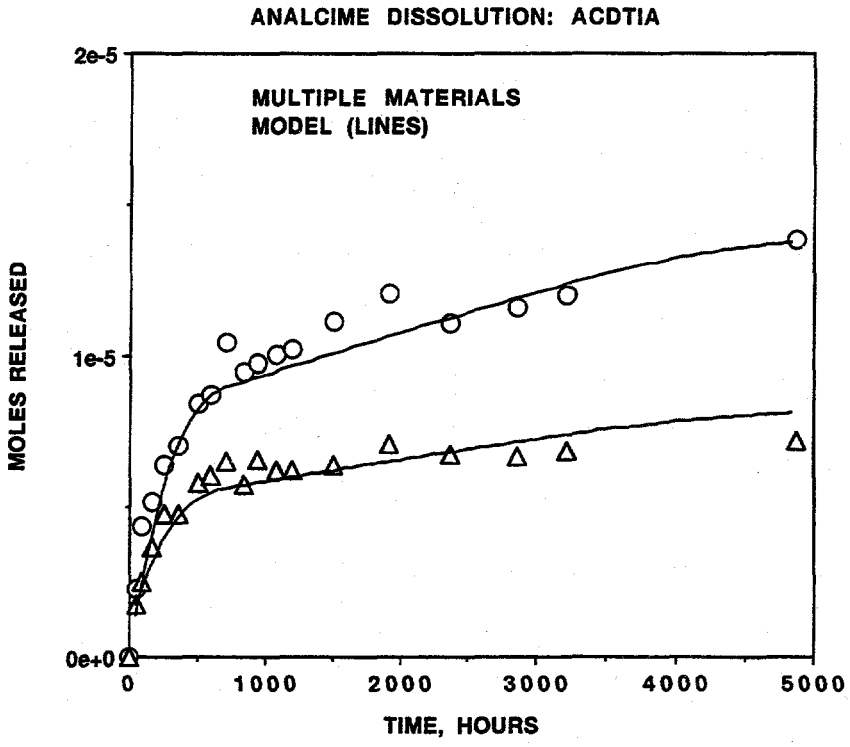

Figure 3-7. Calculated moles of Si (circles) and Al (triangles) released based on analytical data from experiment ACDTIA. Curves are computed by numerical integration of rate Eq. (3-9) assuming an initial instantaneous nonstoichiometric release of Al and two sources of material, one that is highly reactive and limited in mass, and the other with lower reactivity and constant surface area.

observed in the experiments. A small quantity of 10^{-6} moles of Al was assumed in the model to be released instantaneously at the outset of the reaction. This initial condition accounts reasonably well for the preferential release of Al that occurred in the first 50 hr of the experiment. At the end of the experiment, the cumulative release of Al relative to Si tended to approach the stoichiometric ratio in the reactant analcime (Figure 3-5). This effect was neglected in the model, which resulted in the overestimation of Al at long times provided by the model calculations. Nevertheless, the resulting curves give a reasonable fit to the experimental data for Si and Al release.

3.5.2.2 Aluminate Dependence Hypothesis

Recent experimental studies have shown that dissolution rates of the aluminosilicate minerals albite and kaolinite are inversely related to the aqueous aluminum ion concentration under conditions that are relatively far from equilibrium (Chou and Wollast, 1985; Devidal et al., 1992; Oelkers et al., 1994). A similar mechanism could provide an interpretation for the data for analcime dissolution at pH 9. Rate dependence on dissolved aluminum was examined in regressions of the rate data using postulated rate expressions that involve an aluminate ion-activity dependence. Reasonable data regressions have been obtained using

$$\prod_i a_i^{n_i} = a_{Al(OH)_4^-}^{-2} \qquad (3\text{-}13)$$

Curves for Si and Al release were generated from numerical integration of the analcime dissolution rate equation [Eq. (3-9)] with substitution of Eq. (3-13). For this regression, the parameter ks was adjusted to 1.3×10^{-23} moles/s to obtain a good fit to the data (Figure 3-8).

The alternate kinetic models each provide reasonable interpretations of the experimental data. Nevertheless, each has its limitations. Validity of the model that adopts the premise of multiple materials with different reactivity could be tested by subjecting reacted analcime to a fresh solution. Rate dependence on the inverse square of the aluminate ion activity could be tested in steady-state, flow-through experiments in which the aluminum concentration could be varied. Each of these models is clearly a simplification, and other models and mechanisms could be postulated. For example, the silica activity also increased in the experimental solutions. The rate data could probably be rationalized by assuming a rate dependence on the aqueous silica activity, or on both aluminate and silica activities, independently of their effects on the degree of disequilibrium. Nevertheless, some mechanisms appear to be ruled out. Attempts at regressions using a rate equation similar to Eq. (3-9), but with the aluminate ion-activity to the -1 power, gave poor fits to the data. Also, one essential and significant conclusion is that the preaffinity factor in the rate equation under conditions that are far from equilibrium cannot be reasonably extrapolated to more advanced conditions of reaction progress and near-equilibrium conditions in the absence of other mechanisms. This observation provides a possible rationale for the commonly observed discrepancy between laboratory determined rate constants and those evaluated from mass balance relations in systems undergoing natural weathering (e.g., Velbel, 1991; Brantley, 1992). Neglect of inverse rate dependence on aluminum concentrations would lead to overestimations of rates in models for natural systems.

3.6 ANALCIME SOLUBILITY

The ACDT A series experiments were permitted to react until solution compositions approached equilibrium as indicated by a slow rate of release. In addition, separate sets of experiments were conducted with solid mass-to-solution ratios about five times greater (Appendix B, Table A) to test analcime solubility limits. Analcime solubility was approached by dissolution in undersaturated solutions in the ASE and ASE A series experiments, and solubility was approached by precipitation from supersaturated solutions in RACDT and RASH series experiments (Table 3-4). Initial conditions for dissolution experiments were the same as for the kinetics experiments described in Section 3.4.3. Initial conditions for precipitation experiments RACDT were close to estimated solubility limits. To confirm that precipitation occurred in the RACDT series experiments, moles of Si and Al precipitated were calculated using Eq. (3-3), taking into account the depletion of solution mass and solute removal in samples (Figure 3-9). The data confirm precipitation of both species. Rapid initial decrease in reaction rate and effective arrest of precipitation for a period of 10,000 hr or more at the end of the experiments indicate close approach to chemical equilibrium. The relative amounts of Al and Si precipitated in the RACDT series experiments correspond closely to the ratio of these species in the unreacted analcime (Figure 3-10). However, within the uncertainty of the data, precipitation could be either slightly richer in silica (e.g., as in the idealized analcime stoichiometry, $NaAlSi_2O_6 \cdot H_2O$), or more likely poorer in silica than the unreacted material.

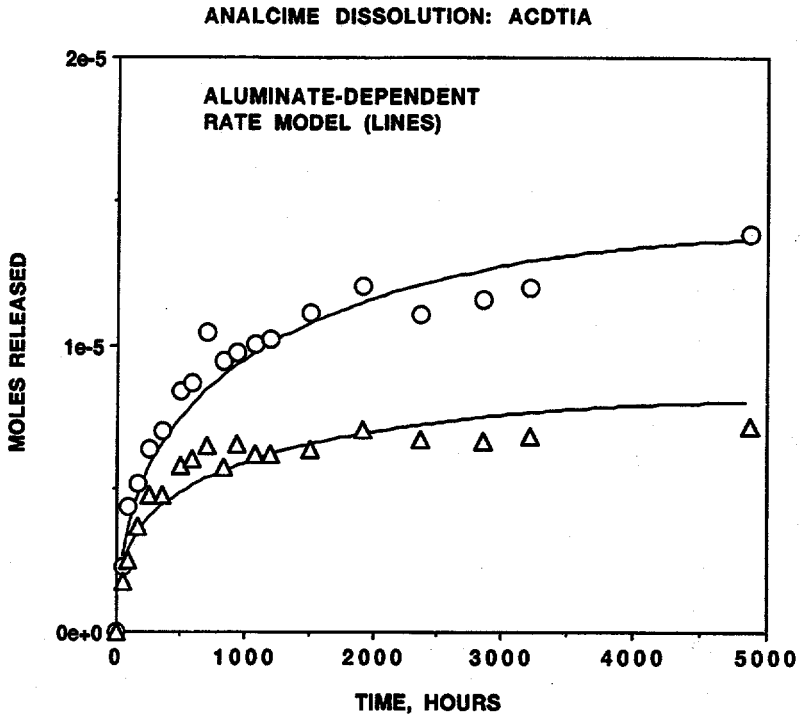

Figure 3-8. Calculated moles of Si (circles) and Al (triangles) released based on analytical data from experiment ACDTIA. Curves are computed by numerical integration of rate Eq. (3-9) assuming an initial instantaneous nonstoichiometric release of Al and a reaction mechanism in which the reaction rate is inversely proportional to the square of the aqueous $Al(OH)_4^-$ activity.

Equilibrium distributions of aqueous species were computed from aqueous solution analyses with EQ3. Analytical measurements were used to constrain total Si and Al concentrations and pH. Total Na concentrations were calculated based on initial solution compositions corrected for concentration of Na due to evaporation. The bicarbonate content of the solutions was calculated by adjusting its value to achieve electroneutrality in the speciated solutions. Calculated equilibrium fugacities of CO_2 were similar and close to atmospheric values which provides a check of the accuracy of the data and interpretation. Thermodynamic activities of aqueous species obtained in the speciation computations illustrate reaction paths taken by the solid-solution mixtures when plotted on logarithmic activity diagrams. Analcime solubility is conveniently illustrated in the coordinates of Figure 3-11. Equilibrium between analcime and aqueous species according to the reaction

$$\begin{aligned} &Na_{1.02}Al_{1.02}Si_{1.98}O_6 \cdot H_2O + 1.04H_2O \rightleftharpoons \\ &1.02Na^+ + 1.02Al(OH)_4^- + 1.98SiO_2 \end{aligned} \qquad (3\text{-}14)$$

is described by the law of mass action, which can be written as

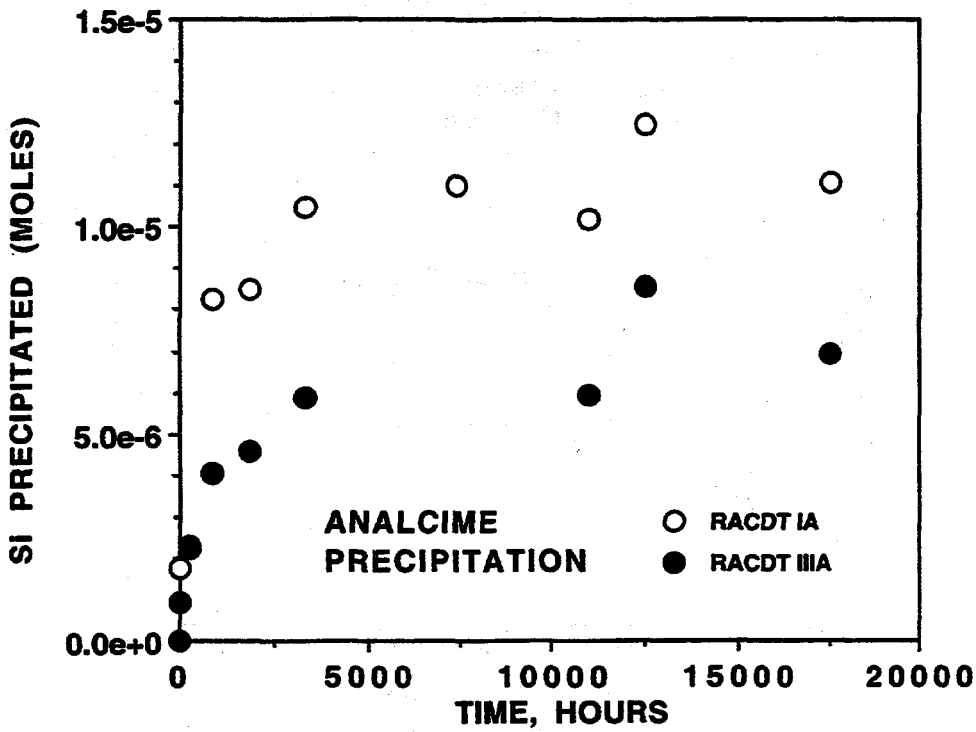

(A)

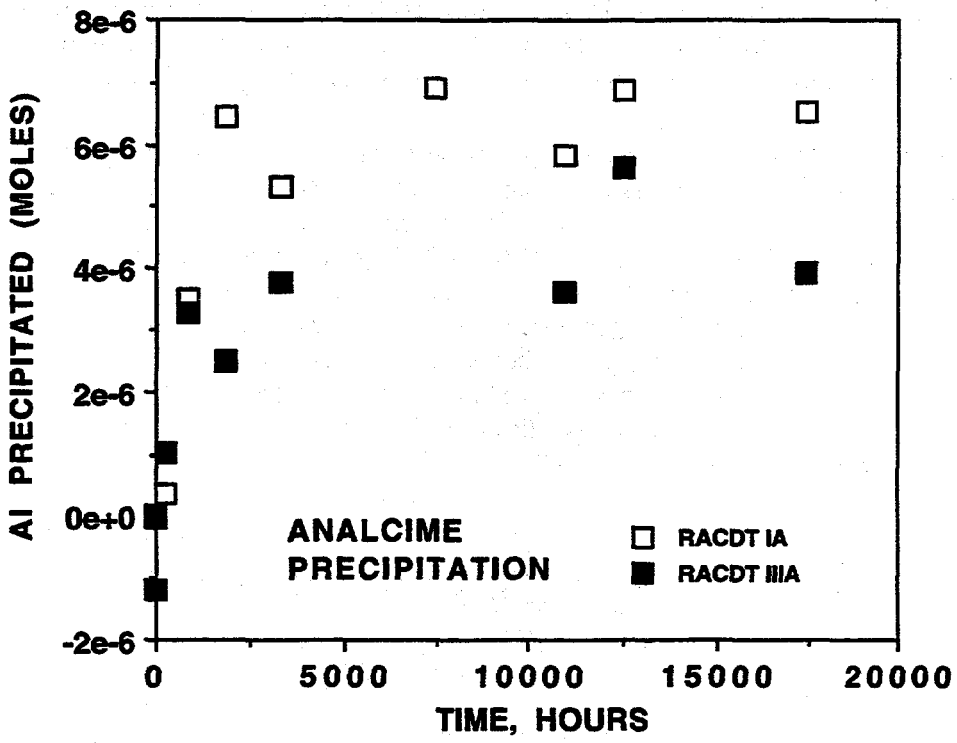

(B)

Figure 3-9. Moles of Si (A) and Al (B) precipitated in RACDT series analcime precipitation experiments as a function of time

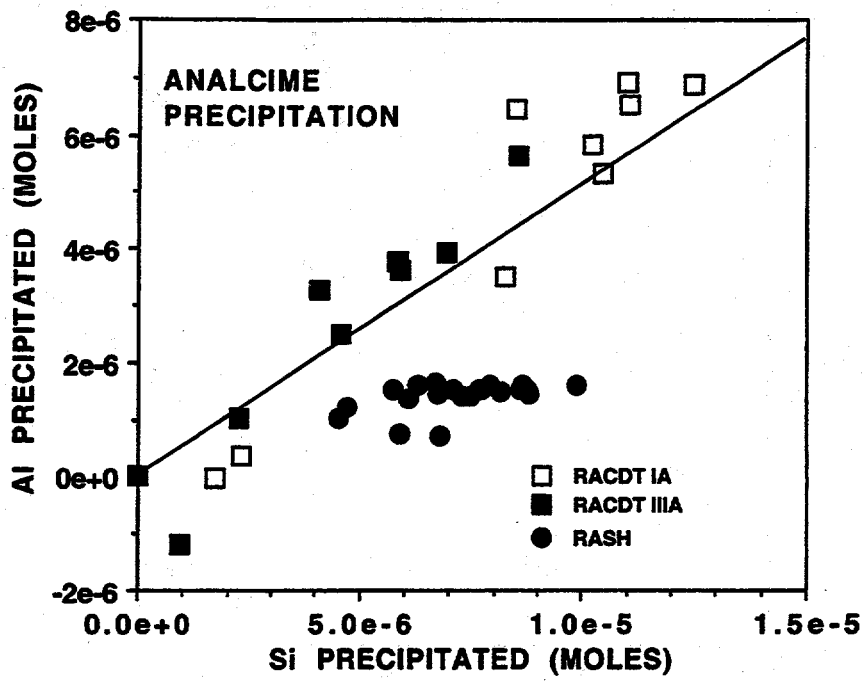

Figure 3-10. Moles of Al precipitated as a function of moles of Si precipitated in RACDT and RASH series analcime precipitation experiments. The line has a slope corresponding to the Al/Si ratio inferred for the reactant analcime (0.515). The data provide an indication that analcime precipitated in the RACDT series experiments, but a different phase precipitated in the RASH series experiments.

$$K = \left(a_{Na^+}\right)^{1.02}\left(a_{Al(OH)_4^-}\right)^{1.02}\left(a_{SiO_2}\right)^{1.98} \tag{3-15}$$

where K denotes the equilibrium constant for the reaction, and H_2O and the nonstoichiometric analcime are assumed to be in standard states with unit activities. Eq. (3-15) can be rewritten as

$$\log\left[\left(a_{Na^+}\right)\left(a_{Al(OH)_4^-}\right)\right] = -\frac{1.98}{1.02}\log\left(a_{SiO_2}\right) + \frac{1}{1.02}\log K \tag{3-16}$$

which is the equation for analcime solubility in the coordinates of Figure 3-11. The line in Figure 3-11 has been drawn between the data derived from analcime dissolution and precipitation experiments, and corresponds to Eq. (3-16). The value of log K for reaction (3-14) consistent with this line is -14.67. The narrowly defined experimental reversibility illustrated in Figure 3-11 indicates that uncertainty associated with disequilibrium is approximately ± 0.2 in the value of log K, which corresponds to the range of potential y-intercepts of lines drawn between the forward and reverse data in Figure 3-11.

Final solution compositions in dissolution experiments ASE1 and ASEA 1-3 fall to the supersaturated side of the equilibrium curve in Figure 3-11 because of evaporative concentration of the solutions. Supersaturation is confirmed by decreasing Si and Al concentrations in ASE1 during the last interval between sample extractions (which was 9 mo). Si and Al concentrations increased in the last interval of the ASEA experiments (which was 14 mo). However, in all cases, the final increases in concentration were less than those that would be a consequence of evaporation alone, confirming net

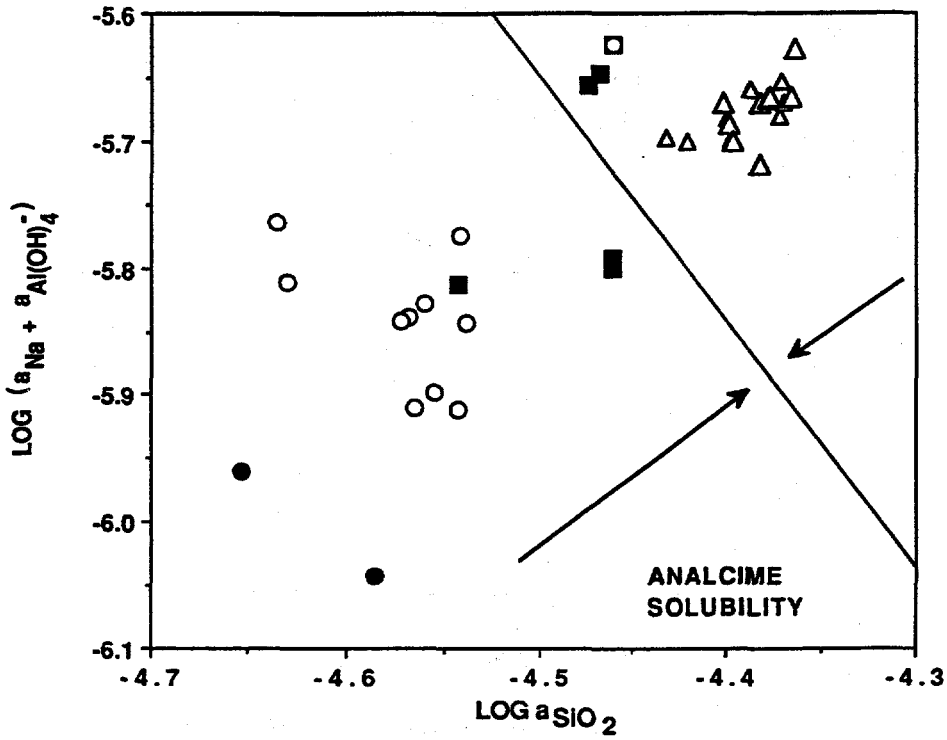

Figure 3-11. Logarithmic activity diagram illustrating experimental reversal of the analcime solubility limit. Symbols represent solution properties derived from ACDT, ASE, and ASEA series analcime dissolution experiments (solid circles, open circles, and solid squares, respectively) and RACDT series analcime precipitation experiments (open triangles). The line drawn between these sets of data represents analcime solubility and has a slope corresponding to the negative Si to Al (or Na) ratio in the reactant analcime (1.98/1.02). Solutions exceeded the solubility limit at the end of some dissolution experiments because of evaporation (see text).

precipitation. Therefore, equilibrium with analcime was approached both by dissolution and precipitation, successively in these experiments.

In the RASH series experiments, an attempt was made to precipitate analcime from a supersaturated solution at a higher silica concentration than in the RACDT series experiments to provide an additional constraint on analcime solubility. Data are summarized in Appendix B Table G. Moles of Si and Al precipitated in these experiments, calculated using Eq. (3-3), are illustrated in Figure 3-10. In contrast to the RACDT series experiments, these data show that the ratio of Si to Al precipitated was approximately 5. This ratio indicates that the precipitate in these experiments was not uniquely analcime of a typical stoichiometry. EQ3 computations of aqueous speciation in these experiments indicate that the aqueous silica activity was close to that of cristobalite. However, cristobalite nucleation and growth under low-temperature conditions are slow (e.g., Rimstidt and Barnes, 1980). Also, aqueous $Al(OH)_4^-$ activities evolved to values below those compatible with the extrapolation of the reversed analcime solubility determination, precluding equilibrium with both cristobalite and analcime. It seems likely that at the higher silica concentrations of the RASH experiments, a higher silica phase (e.g., clinoptilolite) possibly together with another aluminum-bearing phase precipitated. A process of this type apparently

occurred in experimental studies of clinoptilolite dissolution and growth (see Section 3.7). Therefore, reasonable constraints on analcime solubility cannot be derived from the RASH series data.

Aluminum hydrolysis can be expressed as

$$Al^{3+} + 4H_2O \rightleftharpoons Al(OH)_4^- + 4H^+ \qquad (3\text{-}17)$$

The equilibrium constant for this reaction at 25 °C is $10^{-22.1477}$ according to the DATA0.COM.R16 database associated with EQ3/6 and SUPCRT92 (Wolery and Daveler, 1992; Johnson et al., 1992a). Subtracting reaction (3-17) (multiplied by 1.02) from reaction (3-14) yields

$$Na_{1.02}Al_{1.02}Si_{1.98}O_6 \cdot H_2O + 4.08H^+ \rightleftharpoons 1.02Na^+ + 1.02Al^{3+} + 1.98SiO_2 + 3.04H_2O \qquad (3\text{-}18)$$

The base ten logarithm of the equilibrium constant for reaction (3-18) is given by $-14.67-(1.02)\times(-22.1477)=7.92$. Standard-state Gibbs free energies of formation in kilojoules per mole for the aqueous species in reaction (3-18) at 25 °C calculated with SUPCRT92 (Johnson et al., 1992a) are −261.9, −482.7, −833.4, −237.2, and 0.0 for Na^+, Al^{3+}, SiO_2, H_2O, and H^+, respectively. Standard-state free energies are related to the equilibrium constant for reaction (3-18) by

$$-RT\ln K_{Anc} = \Delta G^\circ_{Anc} = 1.02\Delta G^\circ_{Na^+} + 1.02\Delta G^\circ_{Al^{3+}} + 1.98\Delta G^\circ_{SiO_2} + 3.04\Delta G^\circ_{H_2O} - 4.08\Delta G^\circ_{H^+} - \Delta G^\circ_{Analcime} \qquad (3\text{-}19)$$

where R and T stand for the gas constant and absolute temperature, ΔG°_{Anc} stands for the standard Gibbs free energy for reaction (3-18), and ΔG_i° denotes standard Gibbs free energies of formation for the subscripted species. Using the standard state data, Eq. (3-19) can be solved for the standard Gibbs free energy of formation for analcime, which is −3,085.4 kJ/mole. This value compares favorably with values reported in the literature (Table 3-1). However, it depends critically on evaluation of the precise analcime stoichiometry.

The composition of analcime with which solutions approached or achieved equilibrium in the experimental studies may differ from the bulk composition of the starting material. Equilibration of the aqueous solution may in effect occur with a limited mass of material near mineral grain surfaces. Data for the relative net release or precipitation of Si and Al in the experiments used to establish analcime solubility are generally sufficient to confirm analcime dissolution and growth. However, these data are insufficiently accurate to identify the precise composition of the analcime. Small variations in composition have little effect on derived equilibrium constants. For example, in dilute solutions with H_2O activities close to one, the equilibrium constant is effectively independent of the number of H_2O in the mineral structure. Small variations in the Al/Si ratio also have negligible effects on derived equilibrium constants. Analcime solubility data were interpreted assuming the analcime to have the composition $Na_{1.02}Al_{1.02}Si_{1.98}O_6 \cdot H_2O$, which is based on analytical data for the bulk mineral (Table 3-3). This slightly nonstoichiometric form was taken to be the standard state for derivation of the equilibrium constant for the dissolution reaction and the standard state Gibbs free energy of formation of analcime. The solubility data shown in Figure 3-10 could be interpreted alternatively using the nominal stoichiometric form and the dissolution reaction

$$NaAlSi_2O_6 \cdot H_2O + H_2O \rightleftharpoons Na^+ + Al(OH)_4^- + 2SiO_2 \quad (3\text{-}20)$$

The slope of the solubility limit based on this reaction would differ slightly from that shown in Figure 3-11. However, the equilibrium constant consistent with the equilibrium reversal and reaction (3-20) is $10^{-14.65}$, in contrast to the value of $10^{-14.67}$ derived using the aluminum-rich stoichiometry. This is a small difference. Similarly, the standard state Gibbs free energy of the dissolution reaction derived from the reversal illustrated in Figure 3-10 differs only between 8,374 J/mole and 8,362 J/mole for the slightly Al-rich and nominal stoichiometric forms [reactions (3-14) and (3-20), respectively]. However, primarily because of the different number of atoms in the alternate mineral formulas, the derived standard state Gibbs free energy of formation for analcimes of the two stoichiometries derived from the same solubility data differ by over 5 kJ/mole between −3,085.4 kJ/mole (Section 3.6) and −3,080.1 kJ/mole for the slightly Al-rich and nominal stoichiometric forms, respectively.

Derived thermodynamic properties also depend on properties of all major aqueous species involved in aqueous speciation computations to determine thermodynamic activities. For example the database employed for computations in this section [DATA0.COM.R16 of Wolery and Daveler (1992)] includes data for the aqueous complex $NaHSiO_3$ which indicate that it is fairly stable in the Na-rich and pH 9 solutions of the experiments. The base ten logarithm of equilibrium constant for the reaction

$$NaHSiO_3 + H^+ \rightleftharpoons Na^+ + SiO_2 + H_2O \quad (3\text{-}21)$$

is 8.304 at 25 °C. Data for this reaction are derived from SUPCRT92 (Johnson et al., 1992a) and are based primarily on correlations of properties among similar species. Uncertainty in this equilibrium constant is unestablished. If the stability of this complex has been overestimated, then extrapolation of the derived properties of analcime for interpretations of data may be jeopardized for conditions that are different than those of the experiments (e.g., conditions of lower pH and Na concentration).

3.7 CLINOPTILOLITE DISSOLUTION AND GROWTH

Bulk chemical analyses indicate that the purified sodium-exchanged clinoptilolite composition can be represented as $(Na_{1.804}K_{0.123})(Ca_{0.003}Mg_{0.035})(Al_{1.947}Fe_{0.044})(Si_{10.002}Ti_{0.004})O_{24} \cdot 7.43H_2O$. Grouping divalent cations (times 2) together with monovalent cations, the clinoptilolite formula can be expressed in terms of cations of equivalent charge as $M^{(I)}_{2.003}M^{(III)}_{1.991}T^{(IV)}_{10.006}O_{24} \cdot 7.43\ H_2O$. With the exception of the water content, which is likely to be variable and dependent on humidity, this stoichiometry corresponds almost identically, and certainly within experimental uncertainty, to the idealized silica-rich clinoptilolite formula which can be written for the sodium end member as $Na_2Al_2Si_{10}O_{24} \cdot 8H_2O$.

Clinoptilolite dissolution in the standard initial NaCl-$NaHCO_3$ solution was examined in the CDVSE series of experiments. Elemental release in these experiments was calculated using Eq. (3-3). Release of Si followed a trend of decreasing rate of reaction, corresponding to the variation in the slope of the curve in Figure 3-12A. This result is consistent with a close approach to equilibrium. Calculated moles of release of Al (Figure 3-12B), based on aqueous solution data, are approximately three orders of magnitude lower than the release of Si, although the Si/Al atomic ratio in the primary clinoptilolite is approximately 5. An initial period of net Al release is followed by a net decrease in Al release. Net Al decrease begins at approximately the time that Si release effectively stops (and clinoptilolite

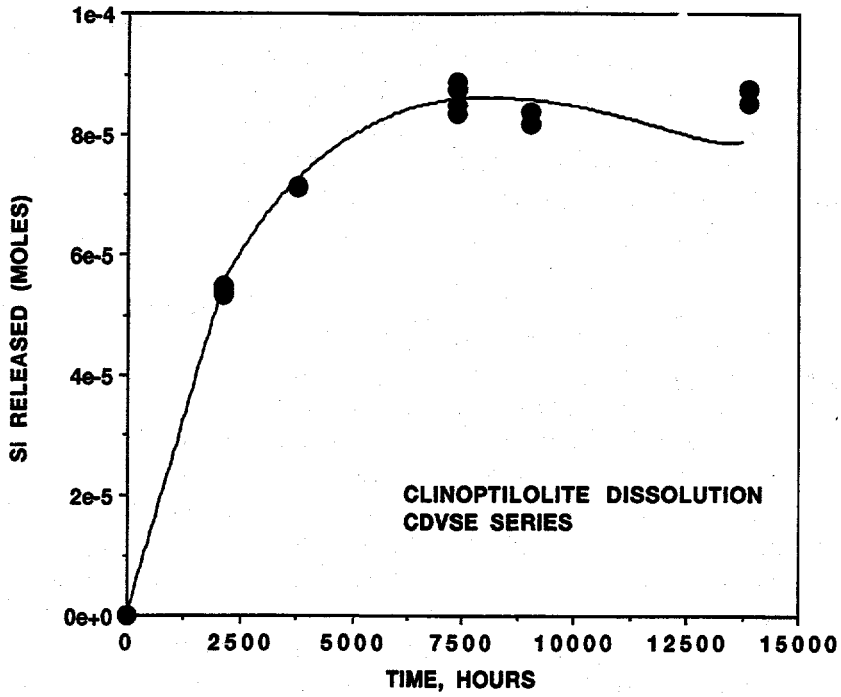

(A)

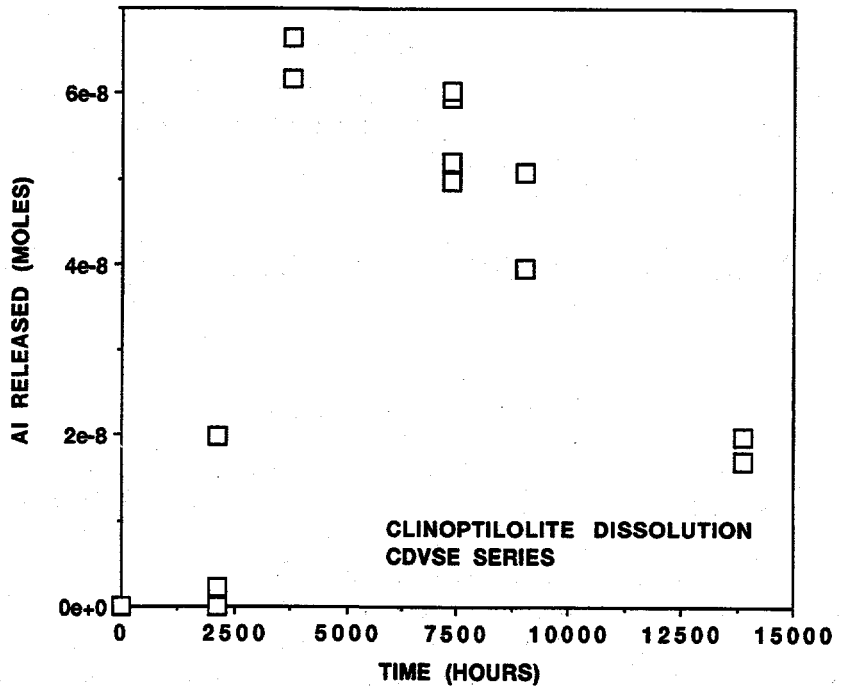

(B)

Figure 3-12. Moles of Si (A) and Al (B) released in CDVSE series clinoptilolite dissolution experiments as a function of time. Al release is roughly three orders of magnitude less than Si release indicating incongruent dissolution. The curve in A was generated by integration of rate Eq. (3-9).

equilibrium is inferred to be closely approached). The large discrepancy between the amounts of release of Si and Al and the eventual decrease in Al release indicates that clinoptilolite dissolution is incongruent and a secondary unidentified Al phase precipitated in the experiments. Other processes that could contribute to this effect are selective leaching of Si or contamination of the clinoptilolite with silica (e.g., amorphous silica), which is preferentially released. No attempt was made to calculate solubility products for potential unknown aluminous phases because final Al concentrations were below analytical detection limits (Appendix B, Tables K and L).

The Na-exchanged clinoptilolite starting material contains appreciable potassium and calcium. However, these species would occur at negligibly small concentrations in the experimental systems relative to sodium, which is a major aqueous component at 0.11 molal and greater. It can be reasonably assumed that equilibrium between clinoptilolite and the experimental solutions would involve a sodium endmember clinoptilolite phase, with negligible amounts of potassium and calcium corresponding to their trace concentrations in solution. Similarly the preponderance of aluminum over iron in the starting material suggests that iron can also be neglected in determining solubility relations. The water activity in the experiments is close to 1; EQ3 speciations for the most evaporated solutions in the clinoptilolite solubility studies indicate a water activity of 0.996. Therefore, the water content of the clinoptilolite would not affect the equilibrium constant for the dissolution reaction (although it would affect the value of the standard state Gibbs free energy derived from the equilibrium constant). These considerations, together with the ideal structural formula determined for the starting clinoptilolite, justify provisional use of the idealized sodium endmember stoichiometry for interpretation of the data, which is $Na_2Al_2Si_{10}O_{24}\cdot 8H_2O$.

Although the data for release of Si from clinoptilolite (Figure 3-12A) are not definitive with respect to reaction mechanism, the systematic variation in Si release rate suggests that the general rate equation (Eq. 3-9) may be appropriate for modeling clinoptilolite dissolution kinetics. The curve in Figure 3-12A was generated by a regression of the Si release data using a numerical integration of Eq.(3-9) for the reaction

$$Na_2Al_2Si_{10}O_{24}\cdot 8H_2O \rightleftharpoons 2Na^+ + 2Al(OH)_4^- + 10SiO_2 + 4H_2O \qquad (3\text{-}22)$$

for which

$$Q = \left(a_{Na^+}\right)^2\left(a_{Al(OH)_4^-}\right)^2\left(a_{SiO_2}\right)^{10} \qquad (3\text{-}23)$$

For the regression, the values for the $Al(OH)_4^-$ molality were interpolated between analytical points, and aqueous Na^+ molality was calculated by mass balance accounting for initial conditions in the experiments, evaporation, solute extraction due to sampling, and Na^+ release from clinoptilolite in proportion to Si [e.g., Eq. (3-8)]. Activity coefficients and relative distributions of species of the same component (which remained constant) were based on an extended Debye-Huckel algorithm and calculated in EQ3 speciations for the aqueous solutions. The value of the equilibrium constant used in the regression is based on the provisional clinoptilolite solubility measurement described in Section 3.8. A constant value of $k^* = 7.2\times10^{-13}$ moles/s in Eq. (3-10) substituted in Eq. (3-9) with $\sigma=20$ yields the good fit to the data shown in Figure 3-12A. The net release of Al does not correspond to the same expression presumably because of precipitation of another aluminum phase. The large value of σ is related to the clinoptilolite formula adopted. If reaction (3-22) were written for clinoptilolite containing one Si, the same kinetic regression of the Si release data would be obtained using a value of $\sigma=2$.

Clinoptilolite growth from a supersaturated solution was conducted in RCDV series experiments. Based on experience from the CDVSE and ACDT series clinoptilolite dissolution experiments, initial solutions were prepared to contain 30 ppm SiO_2 and 200 ppb Al. In these experiments Al concentrations dropped precipitously to near the analytical detection limit at approximately 1 ppb. Using Eq. (3-3), Si was calculated initially to be precipitated as Al was precipitated, but when Al reached very low levels, net release of Si was observed (Figure 3-13). Apparently, precipitation of a secondary aluminum phase was a dominant feature of these experiments which precludes a reasonable interpretation of the clinoptilolite growth rate from these data. The mass of the secondary phase was necessarily small because of the small amount of aluminum; and no secondary phases were observed in SEM examinations. EQ3 computations show final solutions in these experiments to be close to saturation with respect to the zeolite natrolite ($Na_2Al_2Si_3O_{10}\cdot 2H_2O$) which could be the secondary phase.

3.8 CLINOPTILOLITE SOLUBILITY

Equilibrium aqueous speciations for solutions in clinoptilolite dissolution and growth experiments were calculated with EQ3 using analytical values for Al and Si concentrations, analytical pH (Appendix B), and sodium and chloride concentrations calculated using equations accounting for concentration changes due to evaporation and dissolution [e.g., Eq. (3-8)]. Precipitation of a secondary aluminum phase and uncertainty in the composition of the clinoptilolite complicate determination of its solubility. Furthermore, evaporation in the experiments can drive initially undersaturated solutions in dissolution experiments to states of supersaturation. In contrast, precipitation of a secondary aluminum phase can drive initially supersaturated solutions in precipitation experiments to states of undersaturation with respect to clinoptilolite. Nevertheless, a provisional solubility that depends on a few crucial assumptions has been determined.

The time-dependent data illustrated in Figure 3-12A and the associated kinetic interpretation suggest a close approach to a relatively stable equilibrium state. Although the number of moles of Si released remains nearly constant over the period from 7,500 to 14,000 hr, the Si concentrations increase markedly during this period due to evaporation (Appendix B Table K). The increase in Si concentration is slightly less than that due purely to evaporation indicating that solutions attained states of supersaturation due to evaporation and that clinoptilolite precipitated. Continuously increasing Si (and Na) concentrations are nevertheless compatible with maintenance of a state close to equilibrium because of decreasing concentrations of Al.

In contrast, calculated release of Si in the clinoptilolite precipitation experiments (RCDV series; Figure 3-13) is initially negative and subsequently positive. Clinoptilolite is the only source of silica in the experiments. Therefore, net release of silica indicates dissolution of clinoptilolite and undersaturation of the aqueous solution with respect to clinoptilolite in the period after 1,000 hr of reaction. In contrast to the CDVSE series dissolution experiments, silica concentrations increased in the nominal precipitation experiments at a rate that was slightly greater than that due purely to evaporation, which is also consistent with clinoptilolite dissolution.

Ironically, equilibrium with clinoptilolite seems to have been finally approached from supersaturation in the dissolution experiments and from undersaturation in the precipitation experiments. This result appears to be confirmed by calculations of the ion-activity product Q for the provisional dissolution reaction which is defined in Eq. (3-23). Values of the logarithm of Q calculated for solutions in the CDVSE and RCDV series experiments using activities from aqueous speciation computations with

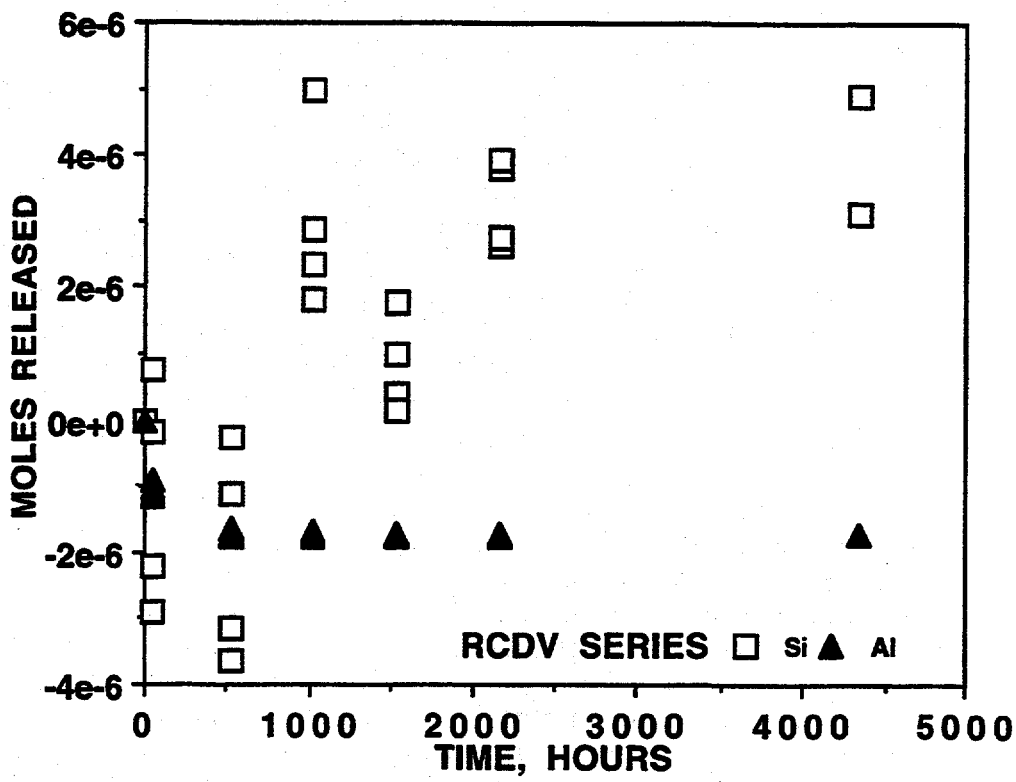

Figure 3-13. Net moles of Si and Al released in RCDV series clinoptilolite precipitation experiments as a function of time. Net precipitation is indicated by negative values and dissolution by positive values. Initially, Al precipitated rapidly followed by a long period of slow precipitation. Si precipitated initially, but then was released indicating clinoptilolite dissolution.

EQ3 are shown in Figure 3-14 as a function of elapsed time in the experiments. For the dissolution experiments (CDVSE series), the ion-activity product increases to a value that remains approximately constant after 7,000 hr, corresponding to the period of minimal change in net moles of silica released illustrated in Figure 3-12A. For the precipitation experiments (RCDV series), the ion-activity product decreases to values somewhat lower than the maximum values from the CDVSE series experiments. These combined data appear to indicate the determination of a *reverse reversal* of the equilibrium state. The logarithm of the provisional equilibrium constant for the dissolution reaction corresponds to the horizontal line in Figure 3-14 and equals -51. Within reasonable limits of uncertainty, this value is equivalent to the value generated by combining the estimated properties of clinoptilolite of Kerrisk (1983) with aqueous solution species properties consistent with the EQ3/6 database, which is approximately -52. The latter value is used in modeling studies reported in Section 4 of this report.

Subtracting two times reaction (3-17) from reaction (3-22) expresses the provisional dissolution reaction in terms of Al^{3+}. The logarithm of the provisional equilibrium constant for the resulting reaction is $-51-2\times(-22.1477)=-6.705$. This value can be related to the standard Gibbs free energy of formation of clinoptilolite ($\Delta G^\circ_{\text{Clinoptilolite}}$) by

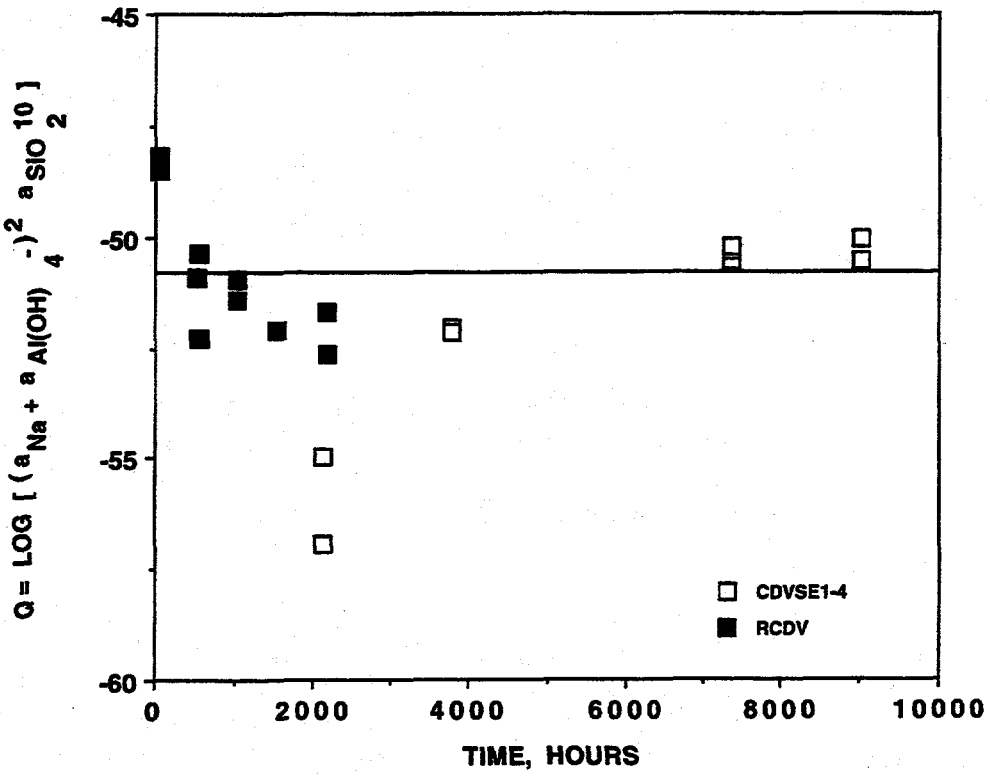

Figure 3-14. Ion-activity product for clinoptilolite dissolution and precipitation reactions derived from CDVSE and RCDV series experimental results as a function of time. The line is drawn as a provisional equilibrium constant for the reaction.

$$\Delta G_r^\circ = -RT\ln\left(10^{-6.705}\right) = 2\Delta G_{Na^+}^\circ + 2\Delta G_{Al^{3+}}^\circ + 10\Delta G_{SiO_2}^\circ + 12\Delta G_{H_2O}^\circ - 8\Delta G_{H^+}^\circ - \Delta G_{Clinoptilolite}^\circ \quad (3\text{-}24)$$

where symbols are defined as in Eq. (3-19). Using the data given after reaction (3-18), Eq. (3-24) can be solved for the provisional value of $\Delta G^\circ_{Clinoptilolite}$, which is $-12{,}708$ kJ/mole.

The EQ3/6 database DATA0.COM.R16 contains a value for the equilibrium constant for dissolution of a Na-rich clinoptilolite. This value is based on calorimetric data from Johnson et al. (1991) for a natural multicomponent specimen (see Section 3.3) and ion-exchange data from the literature and estimated (Viani and Bruton, 1992). This Na-exchanged clinoptilolite has a formula, $Na_{3.467}Al_{3.45}Fe_{0.017}Si_{14.533}O_{36}\cdot 10.922H_2O$. Because the clinoptilolite contains ferric iron, its calculated solubility based on calorimetric data can be compared with the interpretation of experimental solubility data of this study only with additional approximations. Equilibrium with hematite provides a conservative lower limit for the total iron concentration in natural, low-temperature aqueous systems. Assuming equilibrium with hematite, EQ3 computations indicate that solutions in the clinoptilolite dissolution and

precipitation studies that fall on the provisional equilibrium curve in Figure 3-14 would contain iron at 1.13×10^{-12} molal and would be supersaturated with respect to the Na-(Fe)-clinoptilolite by approximately 46 kJ/mole. Higher iron concentrations would lead to even greater calculated supersaturations. It seems highly unlikely that a trace amount of iron substituting for Al in clinoptilolite would increase its stability by this amount. This apparent inconsistency between the experimental clinoptilolite dissolution and precipitation data reported in this study and the Na-clinoptilolite thermodynamic properties in the EQ3/6 database suggests significant uncertainty in the appropriate properties for clinoptilolite to be used in modeling water-rock interactions at Yucca Mountain.

3.9 EQUILIBRATION OF ANALCIME AND CLINOPTILOLITE

Equilibration of analcime, clinoptilolite, and a NaCl-$NaHCO_3$ solution was attempted in ACDT B series experiments. Analcime was first reacted with the standard initial solution, then clinoptilolite was added to the reaction vessel. In preliminary experimental design computations with EQ3/6, aqueous silica was predicted to rise continuously to a value defining analcime-clinoptilolite equilibrium according to reaction (3-1) (Murphy, 1991).

Experimental data for successive analcime dissolution and analcime-clinoptilote-solution reaction can be interpreted using mass balance relations given in Eqs. (3-3) and (3-4). Results of net Si and Al release are shown in Figure 3-15. Analcime dissolution is initially similar to that observed in the ACDT A series experiments. On addition of clinoptilolite to the analcime-solution mixture in the ACDT B series tests after 5,640 hr of reaction, Si concentrations sharply increased and Al concentrations decreased. This is consistent with simultaneous clinoptilolite dissolution and analcime precipitation. However, growth of analcime under these conditions conflicts with the measurement of analcime solubility. The Si release and Al precipitation data are consistent with clinoptilolite dissolution and precipitation of another secondary Al-bearing product of lower solubility than analcime. EQ3 computations suggest that aqueous solutions evolved to states of metastable supersaturation with respect to Al phases during initial analcime dissolution. On addition of clinoptilolite to the system, the clinoptilolite crystals, or a silica-depleted residual clinoptilolite substrate, may have provided for nucleation of the secondary product. As in the RCDV series experiments, final solutions in the ACDT B series experiments are close to equilibrium with natrolite according to EQ3 speciation computations. Natrolite could be the secondary Al phase in these experiments.

Aqueous solution data from a subset of the analcime and clinoptilolite experiments are plotted in Figure 3-16 along with the solubility limits of analcime and Na-clinoptilolite derived from these data as described in Sections 3.6 and 3.8. The intersection of the analcime and clinoptilolite solubility limits represents the predicted point of their mutual equilibrium. Results of the independent analcime plus clinoptilolite experiments (ACDT B series) clearly follow a trend to near this point. The precipitous drop in Al concentration at the end of these experiments drives the final solutions away from the predicted analcime-clinoptilolite equilibration point. This result is consistent with ultimate precipitation of a less soluble aluminous phase. The postulated ultimate supersaturation of solutions in the clinoptilolite dissolution (CDVSE series) experiments and undersaturation of solutions in clinoptilolite precipitation (RCDV series) experiments is also apparent from the distribution of data from these experiments in Figure 3-16 relative to the provisional Na-clinoptilolite solubility limit.

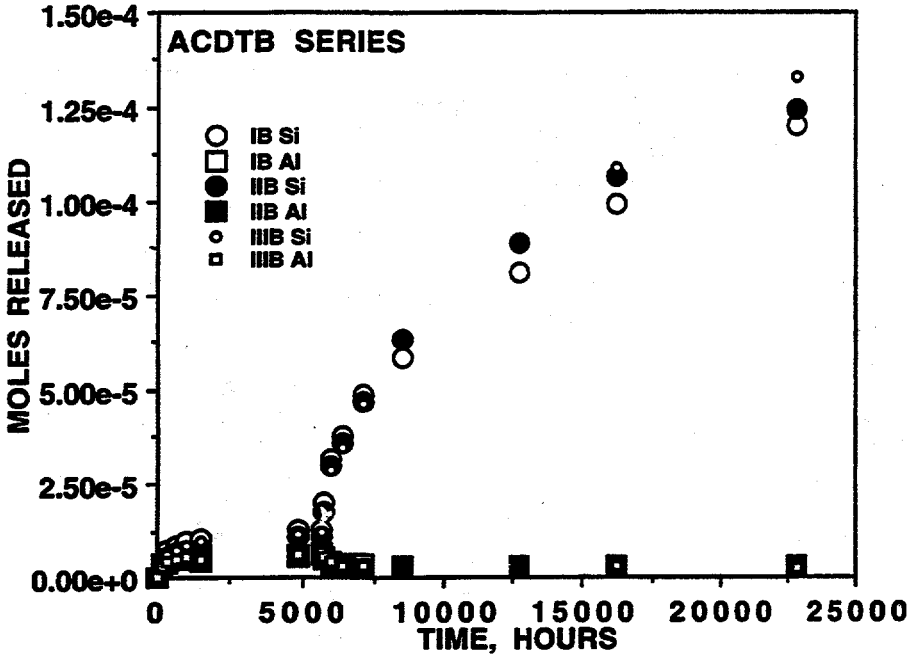

Figure 3-15. Moles of Si and Al released in ACDT B series experiments as a function of time. Analcime dissolved during the first 5,640 hr. Then clinoptilolite was added to the reaction vessel. It dissolved and a secondary Al-bearing phase precipitated.

3.10 GROUNDWATER IN THE VICINITY OF YUCCA MOUNTAIN

Most analyses of groundwater chemistry from the vicinity of Yucca Mountain do not include data for aluminum. Exceptions comprise water analyses reported by Young (1972) for wells J-11, J-12, and J-13, by Daniels et al. (1982) for wells UE25b-1, UE29a-2, H1-4000, and J-13 from the saturated-zone tuffaceous aquifer in the vicinity of Yucca Mountain, and by White (1979) for the Oasis Valley area northwest of Yucca Mountain. Equilibrium aqueous speciation computations were performed with EQ3 using these chemical analyses. The bicarbonate concentrations for the aqueous speciation calculations were based on charge balance in the solutions, and analytical data were used to constrain total concentrations of other species and pH. Calculated bicarbonate values are reasonably consistent with analytical data (e.g., for alkalinity). Results of these speciation calculations are plotted as open squares (Yucca Mountain data) and open circles (Oasis Valley data) in Figures 3-17 and 3-18.

Data for waters from Yucca Mountain and Oasis Valley show small variations in the aqueous silica activity (Figure 3-17). Silica activities are near 10^{-3}, and generally lie between the cristobalite and amorphous silica solubilities at 25 °C to 40 °C (which is the general range of the groundwater temperatures) based on data from EQ3/6. This trend and the difference between the silica activities in the natural solutions and that consistent with clinoptilolite-analcime equilibrium suggest that silica activities are buffered naturally by metastable equilibrium with a silica phase (e.g., leached volcanic glass or opal) and not by clinoptilolite-analcime equilibrium. Values for the product of the Na^+ and $Al(OH)_4^-$ ion activities in the Yucca Mountain and Oasis Valley waters are mainly between 10^{-8} and 10^{-9}, which is a fairly restricted relative and absolute variation. In the coordinates of Figure 3-17, the groundwater data center near the intersection of the natural silica buffer concentration and the experimental analcime solubility limit. This result indicates that analcime may provide a control on water compositions in the tuffaceous aquifers.

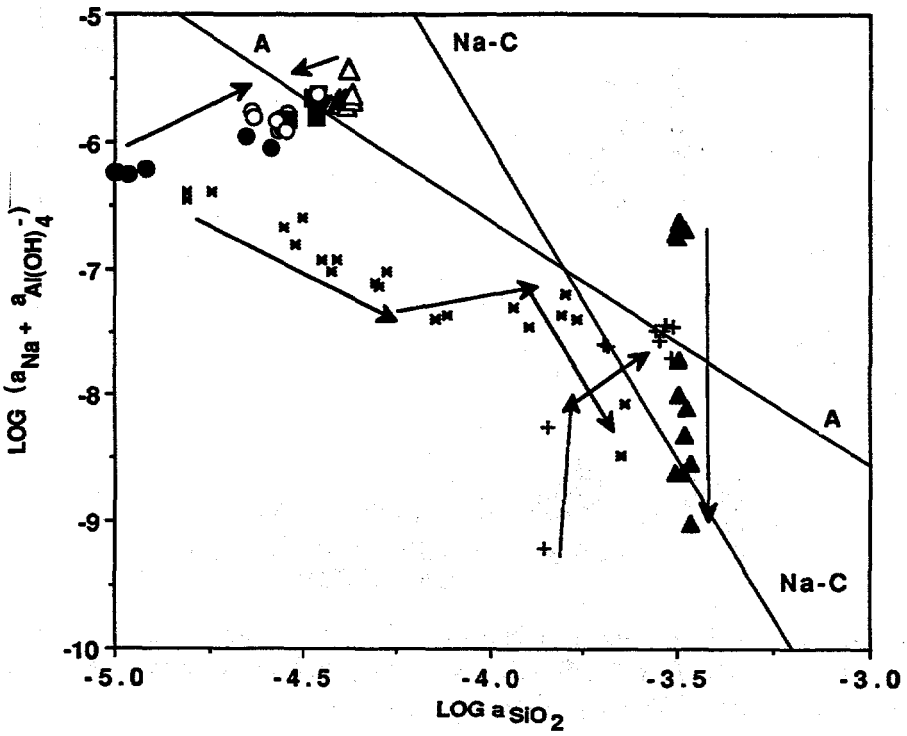

Figure 3-16. Interpretation of analcime and clinoptilolite dissolution and precipitation experiments in logarithmic activity coordinates. Arrows mimic the evolution of solution compositions in individual series of experiments. Line A corresponds to the reversed analcime solubility limit based on aqueous solution data (circles, squares, and open triangles; symbols as in Figure 3-10) and the stoichiometry of the starting material. Line Na-C is the provisional Na-clinoptilolite solubility limit based on data from dissolution and precipitation experiments (crosses and solid triangles, respectively) and the idealized stoichiometry for clinoptilolite. Barred x's represent experimental aqueous solutions reacted with both analcime and clinoptilolite.

Lines H and J in Figure 3-17 are analcime solubility limits calculated using published thermodynamic data for analcime (Table 3-1) and mineral stoichiometries adopted by Helgeson et al. (1978) and Johnson et al. (1982), respectively. Helgeson et al. (1978) adopted the nominal analcime stoichiometry $NaAlSi_2O_6 \cdot H_2O$, and Johnson et al. (1982) adopted a silica rich stoichiometry based on analytical data; $Na_{0.96}Al_{0.96}Si_{2.04}O_6 \cdot H_2O$. Solubility limits derived from the literature data are significantly smaller than those based on the present study and incompatible with the experimental data.

An additional test of analcime equilibrium control of groundwater compositions is provided in an activity diagram showing relations between Na^+ and $Al(OH)_4^-$ activities at 25 °C (Figure 3-18). To plot analcime solubility limits in the coordinates of this figure, the aqueous silica activity was fixed at 10^{-3}, which corresponds to the apparent natural buffer in the Yucca Mountain area tuffaceous aquifer system (Figure 3-17). Thermodynamic interpretations of groundwater data from near Yucca Mountain and Oasis Valley are plotted in Figure 3-18 as open squares and circles, respectively. Analcime solubility based on the equilibrium constant adduced above is plotted in this figure as line A. The trend of the groundwater data and their magnitudes closely follow the line, suggesting that the natural water chemistries are controlled by equilibrium with analcime. Some deviation of the groundwater data from the plotted analcime solubility line would be expected even if there were no uncertainty in the analyses

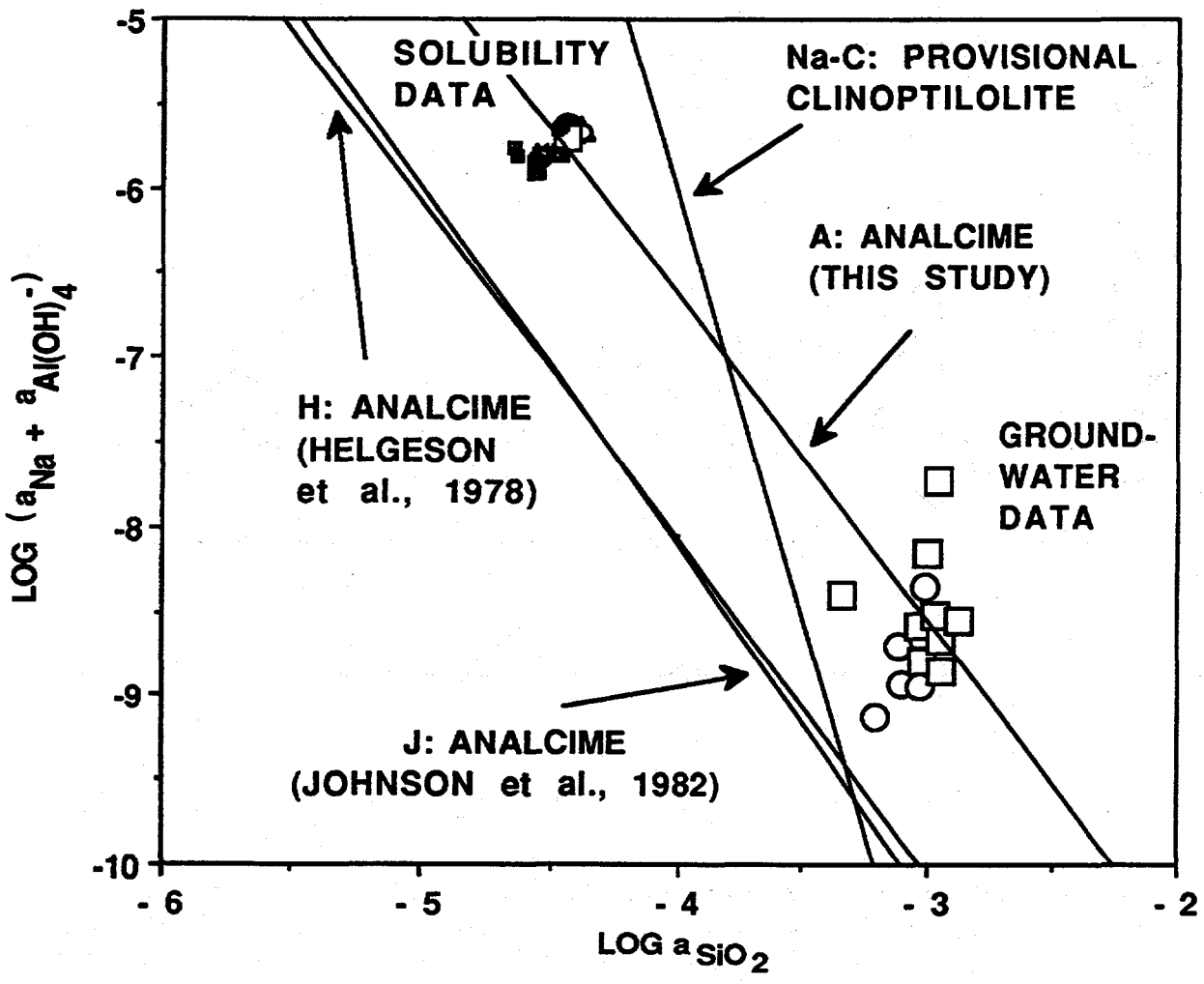

Figure 3-17. Logarithmic activity diagram representing natural groundwater chemistry from the vicinity of Yucca Mountain (open squares) and Oasis Valley (open circles) in relation to solubility limits for analcime and clinoptilolite at 25 °C. Line A represents the analcime solubility limit based on data from this study. Lines labeled H and J are analcime solubility limits based on thermodynamic data reported by Helgeson et al. (1978) and Johnson et al. (1982), respectively. Line Na-C is based on the provisional Na-clinoptilolite solubility determination in this study.

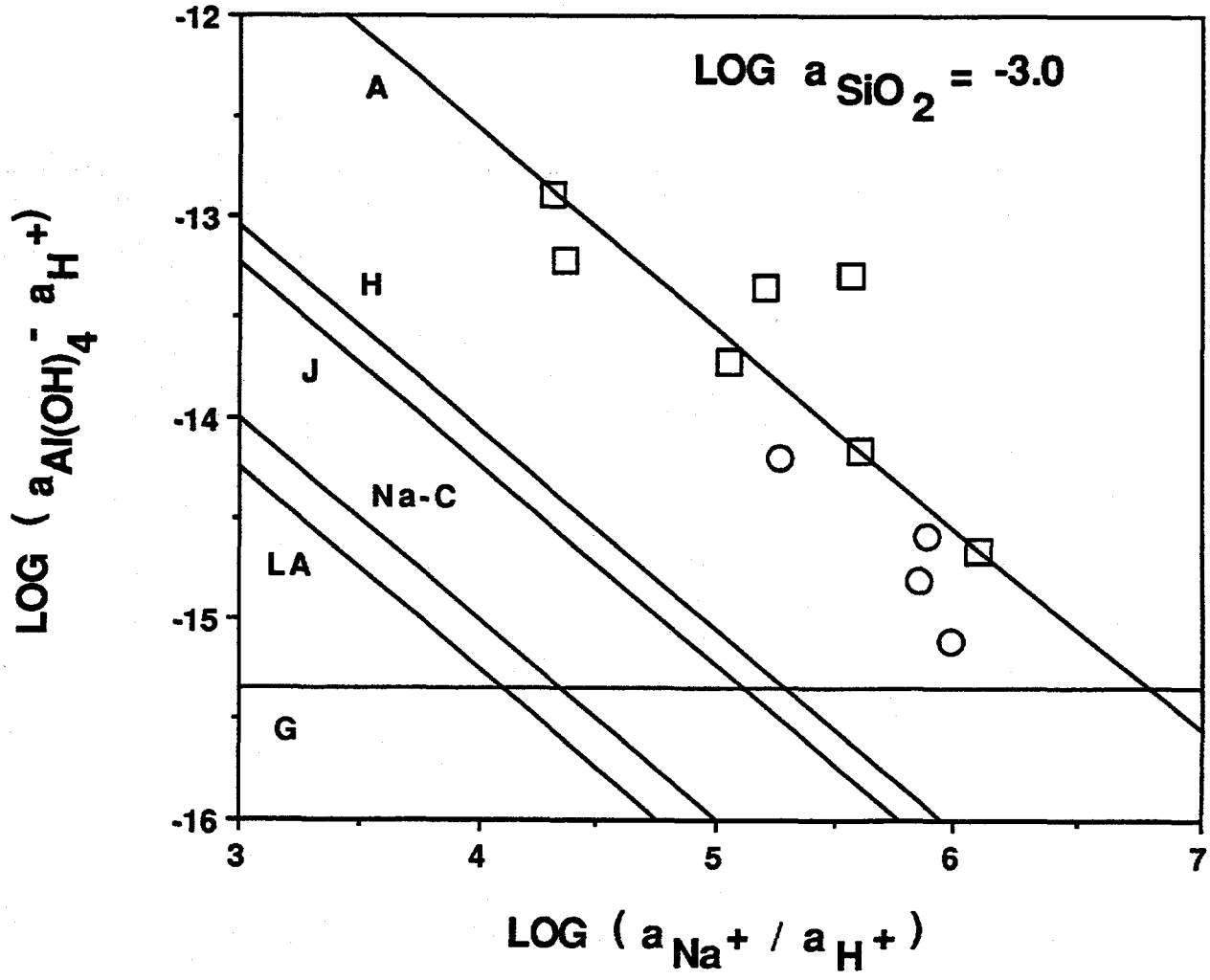

Figure 3-18. Logarithmic activity diagram representing natural groundwater chemistry from the vicinity of Yucca Mountain (open squares) and Oasis Valley (open circles) in relation to mineral solubility limits at 25 °C. Line A represents the analcime solubility limit based on data from this study. Lines labeled H and J are analcime solubility limits based on data reported by Helgeson et al. (1978) and Johnson et al. (1982), respectively. Line Na-C is based on the provisional Na-clinoptilolite solubility determination in this study. Lines LA and G represent solubility limits of low albite and gibbsite, respectively, based on data from Helgeson et al. (1978) and Johnson et al. (1992a). Solubility limits are based on log $a_{SiO_2} = -3$. Groundwater data can be compared to the plotted solubility limits of aluminosilicates only to the extent that their aqueous silica activities are reasonably approximated by this value.

of water from the field and all the waters were in equilibrium with analcime. The aqueous silica activities in the groundwaters were not all equal to 10^{-3} (though they were all close), and the temperatures of the waters were not all 25 °C (though they were all close). However, the solubility limits plotted as lines in Figure 3-18 are based on these conditions. Also, variable Al/Si ratios of analcimes would lead to small variations in equilibrium solubility limits (see Section 3.6). Analcimes at Yucca Mountain tend to be relatively silica rich (Broxton et al., 1987).

Analcime has been identified at depth in core from boreholes J-13 and UE25b#1 (and many others for which aqueous aluminum values are unavailable), but not in core from borehole J-12 (Bish and Chipera, 1989). Other minerals that could play a role in control of groundwater chemistry include low albite and gibbsite whose solubilities are also plotted in Figure 3-18 as lines LA and G, respectively, based on data from the EQ3/6 database DATA0.COM.R16. Clinoplilolite at Yucca Mountain occurs as a solid solution of several components in addition to Na (especially K and Ca). For these natural conditions the activity of the Na component would be less than one, and the solubility limits for multicomponent clinoptilolite would plot at lower levels in Figure 3-18. The natural groundwaters appear to be supersaturated to a greater degree with respect to multicomponent clinoptilolite than with respect to the pure Na form. The equilibrium aqueous speciations at field temperatures indicated the natural groundwaters represented in Figure 3-18 are all 50 to 100 kJ/mole supersaturated with respect to the Na (-Fe) clinoptilolite of the EQ3/6 database.

3.11 SUMMARY OF CONCLUSIONS

Analcime and clinoptilolite are critical diagenetic minerals in the Yucca Mountain environment. Several series of low-temperature (25 °C), long-term (up to 2.6 yr) batch-type dissolution and precipitation experiments have been designed, conducted, and interpreted to examine interactions between analcime, Na-clinoptilolite, and aqueous solutions. Preliminary experimental design facilitated data interpretation by limiting the number of important components, by establishing aqueous solution compositions that limited the potential for secondary phase formation, and by providing for relatively stable chemical conditions in the experiments. Experiments were conducted in 0.1 molal NaCl-0.01 molal $NaHCO_3$ solutions continuously equilibrated with atmospheric CO_2, which maintained pH close to 9.

Small changes in Na and Cl concentrations as a consequence of evaporation were calculated from initial conditions and measurements of water mass as a function of time. Mass transfer of Si and Al among solid and aqueous phases was determined from measurements of Si and Al concentrations as a function of time taking account of solutes removed in solution samples and evaporative concentration.

Analcime dissolution and growth were approximately stoichiometric in the experiments. A slight initial excess Al release in dissolution experiments was compensated as equilibrium was approached by a slight excess Al precipitation. Mass transfer data indicate that no solid phases other than analcime influenced analcime dissolution and growth experiments at aqueous Si concentrations less than approximately 4 ppm. However, attempts to precipitate analcime from supersaturated solutions at Si concentration of approximately 30 ppm apparently led to precipitation of a mineral other than analcime with lower solubility.

The rate of release of Si and Al in analcime dissolution studies decreased systematically with increasing Si and Al concentrations and the approach to equilibrium. However, the dissolution rate data cannot be rationalized using a constant preaffinity factor based on the initial rate of release under

conditions that are far from equilibrium. The dissolution rate in the experiments decreased significantly with increasing reaction progress and increasing Si and Al concentrations even under conditions that were far from equilibrium. Two dissolution mechanisms have been hypothesized to account for this result, and both provide reasonable regressions of the mass transfer rate data. The variably reactive materials hypothesis invokes the presence of a significant mass of high-reactivity material (e.g., ultrafine particles and damaged surface material such as structural defects) that reacts rapidly and dissolves completely. Its rate of dissolution decreases as its mass and surface area decrease. The bulk material is hypothesized to react in parallel with the ultrareactive material but accords to a much smaller preaffinity rate constant. In the aluminate-dependent reaction hypothesis the reaction rate is presumed to depend on the activity of the dominant aqueous Al species, $Al(OH)_4^-$. Rate data are reasonably regressed assuming that the preaffinity factor is inversely proportional to the square of the $Al(OH)_4^-$ activity. Existing data do not permit a selection among these models or other possible mechanisms that would decrease reaction rate under conditions that are far from equilibrium.

A point of controversy in recent literature has been an apparent discrepancy between dissolution rate parameters deduced from laboratory studies and those evaluated by mass transfer modeling of natural systems. Experimentally determined rate constants seem to be consistently in excess of field deduced rate constants by an order of magnitude or more (e.g., Velbel 1991; Brantley, 1992). Laboratory dissolution studies are commonly conducted under conditions that are far from equilibrium. The analysis of dissolution data collected under conditions that are both far from and near to equilibrium illustrates the potential for misapplication of laboratory data to natural phenomena. The analysis also provides a possible rationale for discrepancies between experimentally determined and field deduced mass transfer rate constants.

The equilibrium solubility of analcime has been closely approached from both undersaturation and supersaturation (i.e., reversed). In several long-term experiments, initially undersaturated solutions were driven to states of supersaturation by evaporative concentration. Evaluations of net precipitation of Si and Al in the last stages of these experiments confirmed precipitation. Interpretation of the aqueous solution data using EQ3 (Wolery and Daveler, 1992) permits extraction of the equilibrium constant and standard state Gibbs free energy for the analcime dissolution reaction. The standard state Gibbs free energy of formation of analcime can also be extracted using established properties for the aqueous species. However, this value depends fairly strongly on the stoichiometry adopted for the equilibrated analcime. Small variations in the mineral composition (e.g., the Na and Al to Si ratio) are reflected by fairly large differences in the standard state Gibbs free energy of formation of the analcime derived from the solubility measurements. The equilibrium solubility of analcime obtained in this study differs significantly from values based on thermodynamic data reported in the literature.

Release of Si in Na-clinoptilolite dissolution studies follows a systematic pattern of decreasing rate with increasing solution concentration and approach to equilibrium. The time-dependent data can be rationalized using a conventional dissolution rate equation. Release of Al, however, is orders of magnitude less than that of Si indicating incongruent dissolution.

Attempts to determine the solubility of Na-clinoptilolite were complicated by precipitation of an unidentified, low-solubility, Al-bearing phase in the experiments, as indicated by mass transfer relations and thermodynamic interpretation of the data. Furthermore, solutions in clinoptilolite dissolution experiments evolved to states of supersaturation due to evaporative concentration, and solutions in clinoptilolite precipitation experiments evolved to states of undersaturation due to precipitation of the low-solubility phase(s). Nevertheless, the data have been interpreted to provide an ironic reverse reversal of

the equilibrium state. A provisional equilibrium constant and corresponding standard Gibbs free energy for the dissolution reaction have been extracted from the data, adopting plausible assumptions about the composition of the equilibrated clinoptilolite. Within limits of reasonable uncertainty, this value is equivalent to one based on theoretical estimates of the properties of Na-clinoptilolite by Kerrisk (1983) and employed in reaction-path modeling in Section 4 of this report.

Simultaneous equilibration of analcime and Na-clinoptilolite with an aqueous solution generated solution compositions that evolved toward the theoretical equilibration point for these two minerals as determined from thermodynamic data extracted in the solubility studies. However, eventual precipitation of an unidentified, low-solubility, Al-bearing phase also complicated interpretation of these data.

Natural groundwater chemical data from the vicinity of Yucca Mountain and from Oasis Valley have been interpreted thermodynamically. The solutions have aqueous silica activities that vary over a small range suggesting buffering by mineral-solution equilibrium. The value of aqueous silica activity is greater than that determined for mutual equilibration of analcime and Na-clinoptilolite. The magnitude and trend of the natural water chemistry data correspond closely to analcime equilibrium using thermodynamic data derived in this study. However, the natural waters are supersaturated with respect to the provisional Na-clinoptilolite solubility and with respect to the solubility of analcime based on thermodynamic data reported in the literature.

3.12 REFERENCES

Aagaard, P., and H.C. Helgeson. 1982. Thermodynamic and kinetic constraints on reaction rates among minerals and aqueous solutions. I. Theoretical considerations. *American Journal of Science* 282: 237-285.

American Public Health Association (APHA). 1989. *Standard Methods for the Examination of Water and Wastewater*. 17th Edition. Washington, DC: American Public Health Association.

Barany, R. 1962. *Heats and Free Energies of Formation of Some Hydrated and Anhydrous Sodium- and Calcium-Aluminum Silicates*. U.S. Bureau of Mines Report Inv. 5900.

Brady, P.V., and J.V. Walter. 1989. Controls of silicate dissolution rates in neutral and basic pH solutions at 25 °C. *Geochimica et Cosmochimica Acta*. 53: 2,823-2,830.

Brantley, S.L. 1992. Kinetics of dissolution and precipitation—experimental and field results. *Water-Rock Interactions*. Y.K. Kharaka and A.S. Maest, eds., Rotterdam, Netherlands: Balkema: 3-12.

Broxton, D.E., D.L. Bish, and R.G. Warren. 1987. Distribution and chemistry of diagenetic minerals at Yucca Mountain, Nye County, Nevada. *Clays and Clay Minerals*. 35: 89-110.

Caullet, P., J.-L. Guth, and R. Wey. 1980. Solubilité de la zéolite Y et de l'analcite dans des solutions aqueuses basiques. Grandeurs thermodynamiques de dissolution. *Camptes Rendus de l' Académie Scientifique de Paris*. 291D: 117-120.

Chou, L., and R. Wollast. 1985. Steady-state kinetics and dissolution mechanisms of albite. *American Journal of Science* 285: 963-993.

Daniels, W.R., et al. 1982. *Summary Report on the Geochemistry of Yucca Mountain and Environs.* LA-9328-MS. Los Alamos, NM: Los Alamos National Laboratory.

Devidal, J.L., J.L. Dandurand, and J. Schott. 1992. Dissolution and precipitation kinetics of kaolinite as a function of chemical affinity (T=150 °C, pH=2 and 7.8). *Proceedings of the 7th International Symposium on Water-Rock Interaction.* Park City, UT: 1: 93-96

Helgeson, H.C., and D.H. Kirkham. 1974. Theoretical prediction of the thermodynamic behavior of aqueous electrolytes at high pressures and temperatures. I. Summary of the thermodynamic/electrostatic properties of the solvent. *American Journal of Science* 274: 1,089-1,198.

Helgeson, H.C., J.M. Delany, H.W. Nesbitt, and D.K. Bird. 1978. Summary and critique of the thermodynamic properties of rock-forming minerals. *American Journal of Science* 278A: 229.

Helgeson, H.C., W.M. Murphy, and P. Aagaard. 1984. Thermodynamic and kinetic constraints on reaction rates among minerals and aqueous solutions. II. Rate constants, effective surface area, and the hydrolysis of feldspar. *Geochimica et Cosmochimica Acta* 48: 2,405-2,432.

Hemingway, B.S. and R.A. Robie. 1977. Enthalpies of formation of low albite, $NaAlSi_3O_8$, gibbsite, $Al(OH)_3$, and $NaAlO_2$; revised values for $\Delta H_{f,298}$ and $\Delta G_{f,298}$ of some aluminosilicate minerals. *U.S. Geological Survey Journal of Research* 5: 413-429.

Hemingway, B.S., and R.A. Robie. 1984. Thermodynamic properties of zeolites: low-temperature heat capacities and thermodynamic functions for phillipsite and clinoptilolite. Estimates of the thermochemical properties of zeolitic water at low temperature. *American Mineralogist* 69: 692-700.

Holdren, G.R., Jr., and R.A. Berner. 1979. Mechanism of feldspar weathering - I. Experimental Studies. *Geochimica et Cosmochimica Acta* 43: 1,161-1,171.

Johnson, G.K., H.E. Flotow, and P.A.G. O'Hare. 1982. Thermodynamic studies of zeolites: analcime and dehydrated analcime. *American Mineralogist* 67: 736-748.

Johnson, G.K., I.R. Tasker, R. Jurgens, and P.A.G. O'Hare. 1991. Thermodynamic studies of zeolites: clinoptilolite. *Journal of Chemical Thermodynamics* 23: 475-484.

Johnson, J.W., E.H. Oelkers, and H.C. Helgeson. 1992a. SUPCRT92: (A software package for calculating the standard molal thermodynamic properties of minerals, gases, aqueous species, and reactions from 1 to 5000 bars and 0° to 1000 °C.) *Computer and Geosciences* 18: 899-947.

Johnson, G.K., I.R. Tasker, H.E. Flotow, and P.A.G. O'Hare. 1992b. Thermodynamic studies of mordenite, dehydrated mordenite, and gibbsite. *American Mineralogist* 77: 85-93.

Kelly, K.K., and E.G. King. 1961. *Contributions to the Data on Theoretical Metallurgy. XIV. Entropies of the Elements and Inorganic Compounds.* U.S. Bureau of Mines Bulletin 592: 149.

Kerrisk, J.F. 1983. *Reaction-path Calculations of Groundwater Chemistry and Mineral Formation at Rainier Mesa, Nevada.* LANL LA-9912-MS. Los Alamos, NM: Los Alamos National Laboratory: 41.

King, E.G. 1955. Low-temperature heat capacity and entropy at 298.16 K of analcite. *American Chemical Society Journal* 77: 2,193.

Murphy, W.M. 1991. Geochemical modeling. *Report on Research Activities for Calendar Year 1990.* W.C. Patrick, ed. NUREG/CR-5817. Washington, DC: Nuclear Regulatory Commission: 2-24 to 2-54.

Murphy W.M., and H.C. Helgeson. 1989. Thermodynamic and kinetic constraints on reaction rates among minerals and aqueous solutions. IV. Retrieval of rate constants and activation parameters for the hydrolysis of pyroxene, wollastonite, olivine, andalusite, quartz, and nepheline. *American Journal of Science* 289: 17-101.

Oelkers, E.H., J. Schott, and J.-L. Devidal. The effect of aluminum, pH, and chemical affinity on the rates of aluminosilicate dissolution reactions. *Geochimica et Cosmochimica Acta* 58: 2,011-2,024.

Rimstidt, J.D., and H.L. Barnes. 1980. The kinetics of silica-water reactions. *Geochimica et Cosmochimica Acta* 40: 537-548.

Robie, R.A., B.S. Hemingway, and J.R. Fisher. 1978. *Thermodynamic Properties of Minerals and Related Substances at 298.15 K and 1 bar (10^5 Pascals) Pressure and at Higher Temperatures.* U.S. Geological Survey Bulletin 1452. Reston, VA: U.S. Geological Survey.

Velbel, M.A. 1991. Differences between natural and experimental feldspar weathering rates. *Geological Society of America Abstracts with Program.* 23: A258.

Viani, B.E., and C.J. Bruton. 1992. Modeling ion exchange in clinoptilolite using EQ3/6 geochemical modeling code. *Water-Rock Interactions.* Y.K. Kharaka and A.S. Maest, eds. Rotterdam, Netherlands: Balkema: 73-77.

Wagman, D.D., W.H. Evans, V.B. Parker, R.H. Schumm, I. Halow, S.M. Bailey, K. L. Churney, and R.L. Nuttall. 1982. The NBS tables of chemical thermodynamic properties, selected values for inorganic and C1 and C2 organic substances in SI units. *Journal of Physical Chemistry Reference Data.* 11 (Sup. 2): 392.

Walther, J.V., and H.C. Helgeson. 1977. Calculation of the thermodynamic properties of aqueous silica and the solubility of quartz and its polymorphs at high pressures and temperatures. *American Journal of Science* 277: 1,315-1,351.

White, A.F. 1979. *Geochemistry of Ground Water Associated with Tuffaceous Rocks, Oasis Valley, Nevada.* Geological Survey Professional Paper 712–E. Washington, DC: U.S. Printing Office.

Wolery, T.J., and S.A. Daveler. 1992. EQ3/6, *A Software Package for Geochemical Modeling of Aqueous Systems*. UCRL-MA-110772 PT I-IV. Livermore, CA: Lawrence Livermore National Laboratory: 4 volumes.

Young, R.A. 1972. *Water Supply for the Nuclear Rocket Development Station at the U.S. Atomic Energy Commission's Nevada Test Site*. Geological Survey Water-Supply Paper 1938. Washington, DC: U.S. Geological Survey.

4 CONCEPTUAL AND NUMERICAL GEOCHEMICAL MODELING OF THE ENVIRONMENT OF THE PROPOSED NUCLEAR WASTE REPOSITORY AT YUCCA MOUNTAIN

4.1 INTRODUCTION

Yucca Mountain in southern Nevada was selected by the government of the United States to be studied as a potential site for geologic disposal of HLW. The geochemistry of Yucca Mountain could impact performance of a nuclear waste repository through effects on containment (e.g., corrosion of engineered containers), waste form behavior (e.g., dissolution and alteration of spent nuclear fuel and vitrified nuclear waste), and transport of wastes (e.g., aqueous speciation and distribution of radioactive species among solid, liquid, and gas phases and solid surfaces, and effects of dissolution and precipitation on fluid flow). Conceptual and numerical modeling of the environment of the proposed repository at Yucca Mountain can provide insights into geochemical processes of significance to repository performance. Modeling can also aid predictions of the evolution of the geochemical environment through the period of repository perturbations and regulatory concern. The first objective of this section is to provide a general description of the geochemical system at Yucca Mountain based on literature review and to identify geochemical processes that are important in the evolution of this system. This framework is then used to develop the conceptual basis for quantitative reaction-path models for the natural Yucca Mountain system and the heated repository system. Employing principles of thermodynamics, reaction kinetics, mass transfer, and mass transport, computational models are developed to explore the evolution, the natural geochemical system, and the geochemical processes that are likely to occur under repository conditions.

The natural system at Yucca Mountain consists structurally of silicic volcanic strata that are variably bedded, welded, and fractured. Mineralogically the rocks are variably vitric, devitrified to an alkali feldspar and silica mineral assemblage, and diagenetically altered mainly to zeolite minerals (Broxton et al; 1987; Bish and Chipera, 1989). Groundwater at the site is dilute and its chemistry is dominated by sodium bicarbonate in the saturated zone where it is relatively well analyzed (McKinley et al., 1991). However, limited data indicate that pore waters from the unsaturated zone are somewhat more concentrated and enriched particularly in calcium, chloride, and sulfate (Yang et al., 1988; Yang, 1992). The groundwater table is at a depth of 500 to 700 m below the ground surface under Yucca Mountain. The proposed repository horizon is 200 to 300 m above the saturated zone in the lower densely welded zone of the Topopah Spring Tuff member of the Paintbrush Tuff (U.S. Department of Energy, 1988). The matrix porosity of the rocks varies widely with degree of welding and alteration from as low as 1 percent to over 50 percent, but it is generally in the range of 20 to 35 percent for bedded and zeolitized tuffs and 5 to 20 percent for welded tuffs (Nelson and Anderson, 1992). Fractures are abundant in welded units, but uncommon in bedded rocks. Above the water table, the matrix porosity is commonly 60 to 90 percent saturated with water in welded units, and 20 to 50 percent saturated with water in bedded units (A. Flint, written communication, 1992). The unsaturated porosity is filled with atmospheric air with excess CO_2 (Thorstenson et al., 1990). Although extensive data on the geochemistry of the Yucca Mountain system have been collected, subsurface data (e.g., mineralogy, mineral chemistry, groundwater chemistry, and gas chemistry) are presently based on samples from few drill holes, and water chemistry data from the unsaturated zone are particularly sparse.

Introduction of radioactive wastes and engineering materials in Yucca Mountain would have extensive and complicated impacts on the geochemical system. The temperature of the near field may increase to over 200 °C. Major effects would be due to thermally induced water and gas flow, changes in mineral stabilities, accelerated reaction rates at elevated temperatures, and contamination of the system with engineering materials and chemical components derived from nuclear waste forms. Complexity in the repository system stems notably from coupled thermal-hydrological-chemical effects, transience of the thermal regime, reaction kinetics resulting in characteristic times for important chemical reactions that range from seconds to millennia, system heterogeneity, and the numerous important chemical species of the system, many with poorly or incompletely known properties. These complexities must be considered in developing realistic models for the geochemical system at Yucca Mountain.

4.2 SUMMARY OF THE NATURAL GEOCHEMICAL SYSTEM AT YUCCA MOUNTAIN

4.2.1 Bulk Rock Geochemistry and Mineralogy

Typical bulk rock compositions from Yucca Mountain are given in Table 4-1. The rocks are rhyolitic zoning upward to quartz latitic in composition, rich in silica, alumina, and alkali metals (Lipman et al., 1966). Alkali feldspars and silica minerals (cristobalite, tridymite, and quartz) constitute the dominant primary mineralogy of devitrified tuffs (Bish and Chipera, 1989). The bulk composition of unaltered rocks can be reasonably approximated (to greater than 97 percent) by two components, approximately 1 mole of alkali feldspar with the composition $Or_{53}Ab_{45}An_{02}$ and 2 moles of a silica phase.

Mineralogical characterization of the rocks (Bish and Chipera (1989) and petrographic interpretation (Broxton et al., 1989) reveal general patterns of mineral occurrences. Margins of individual volcanic units were quenched to glass on eruption while the insulated flow interiors mostly devitrified. Subsequently, glassy units have been partially to completely altered to secondary minerals. Four vertically disposed diagenetic zones have been described at Yucca Mountain based on the degree and nature of alteration (Smyth, 1982; Broxton et al., 1987). The top zone (zone I) retains unaltered glass with minor clay minerals, zeolites, and opal. In zone II, glass is completely replaced by clinoptilolite and sometimes mordenite with lesser opal, potassium feldspar, clay, and quartz. In zone III, the alteration assemblage is dominated by analcime with lesser potassium feldspar and quartz, and minor calcite and clay. Zone IV, which occurs in the lowest members of the volcanic strata, contains the mineralogy of zone III but with analcime replaced by albite. Data from Bish and Chipera (1989) indicate that cristobalite is generally abundant in devitrified rocks associated with diagenetic zones I and II, but is absent in the lower zones. Conversely, kaolinite occurs only below the mineralogic discontinuity between zones II and III.

Zone II of Broxton et al. (1987) generally straddles the water table at Yucca Mountain and largely occupies a position between the proposed repository horizon and the water table. The geochemical characteristics and evolution of this zone are of particular significance because this zone occurs along a path of possible radionuclide migration. Zeolite minerals, notably clinoptilolite, which is the dominant alteration mineral in zone II, are widely cited as a favorable condition for radioactive waste disposal at the Yucca Mountain site because of their high ion exchange capacities (U.S. Department of Energy, 1988). It is also likely that as the first alteration product of volcanic glass, zeolites would play an important role in controlling groundwater chemistry that may interact with engineered repository components or released radionuclides.

Table 4-1. Bulk rock compositions for tuffs at Yucca Mountain (Broxton et al., 1986)

	Pah Canyon Member, Paintbrush Tuff		Topopah Spring Member, Paintbrush Tuff		Tuff of Calico Hills		
	Densely Welded Devitrified Tuff	Partially Welded, Clay-and Zeolite- Rich Tuff	Unaltered Lower Vitrophyre	Altered Lower Vitrophyre	Nonwelded Vitric Tuff	Nonwelded Zeolitic Tuff, Alkalic Suite	Nonwelded Zeolitic Tuff, Calcic Suite
Diagenetic Zone	—	I	—	I	—	II	II
SiO_2	72.9	64.3	74.0	70.2	74.5	69.1	69.1
TiO_2	0.28	0.33	0.10	0.14	0.10	0.06	0.11
Al_2O_3	13.9	16.8	12.4	16.7	11.7	11.5	13.4
Fe_2O_3	1.4	1.83	1.07	1.44	1.10	0.81	1.13
FeO	0.04	—	—	—	—	0.04	—
MnO	0.06	0.17	0.08	0.09	0.08	0.03	0.05
MgO	0.33	1.77	0.31	0.90	0.12	0.03	0.94
CaO	0.92	2.60	0.66	3.51	0.77	0.75	3.22
Na_2O	3.8	1.38	3.40	1.90	3.20	2.82	1.23
K_2O	5.1	2.72	4.00	0.72	4.34	4.10	2.64
P_2O_5	2.02	0.05	0.01	0.02	0.01	0.00	0.01
LOI	0.97	8.0	3.79	5.91	3.58	10.6	8.90
TOTAL	99.7	100.0	99.8	101.5	99.5	99.8	100.7

Broxton et al. (1986) report extensive chemical analytical data for clinoptilolites from Yucca Mountain determined by microprobe analyses. In general, clinoptilolites are relatively rich in silica (Si/Al = 4 to 5 on an atomic basis) and have a wide variety of alkali and alkaline earth contents, which are generally correlated with their geographic distribution (Broxton et al., 1986, 1987). Clinoptilolites near the surface from zone I are rich in calcium (and magnesium). In zones II and III, clinoptilolites tend to vary from sodium and potassium rich varieties in the west to calcium (and magnesium) varieties in the east. In potassium rich rocks in the northern part of Yucca Mountain, clinoptilolites are rich in potassium, but also trend from relatively calcium (and magnesium) rich varieties nearer the ground surface to potassium rich varieties at depth.

Clay minerals tend to occur in all stratigraphic and diagenetic zones, but in relatively small quantities. Based on XRD data, clay minerals in rocks above the water table at Yucca Mountain are randomly interstratified illite/smectite with less than 25-percent illite (Bish, 1989). The potassium content and the illite fraction of the interstratified clays tend to increase with depth. However, in the unsaturated zone, the sodium and calcium components of the smectites predominate (Bish, 1989).

Calcite also occurs locally both above and below the water table at Yucca Mountain and is prevalent in caliche near the ground surface and in fracture fillings. It is generally the most recently precipitated mineral at Yucca Mountain, with sample ages predominantly between 26,000 and 310,000 yr (Szabo and Kyser, 1990). Stable isotope and trace element compositions of calcites generally denote a distinction between those below the water table and those above it (Whelan and Stuckless, 1992; Vaniman, 1993). Unsaturated zone calcites generally have chemical characteristics similar to those in soil-zone caliche at Yucca Mountain (Whelan and Stuckless, 1992).

Fracture mineralogy differs from bulk rock mineralogy (Carlos et al., 1991). Tridymite occurs in early fractures related to lithophysal cavities and is increasingly replaced by cristobalite or quartz with depth. Manganese oxides with nonlithophysal quartz and later mordenite are common coating planar cooling fractures. Zeolites, mordenite, heulandite/clinoptilolite, and stellerite are dominant in later forming fractures. Smectite and calcite occur commonly in fractures as late forming minerals in variable amounts (Carlos et al., 1991). Whereas mordenite and euhedral heulandite are common fracture minerals in the Topopah Spring Tuff above the water table, mordenite is rare and heulandite is absent from fractures in this member below the water table taken from borehole J-13 (Carlos, 1989).

4.2.2 Origin of Alteration at Yucca Mountain

Studies of natural mineral assemblages at Yucca Mountain are likely to provide the most realistic indications of alteration that may develop due to repository heating and fluid circulation. The notion of Yucca Mountain as a "self analog" is well established (Levy, 1993; Bish and Aronson, 1993). Hypotheses for the origin of major mineral alteration features at Yucca Mountain generally invoke three types of mechanisms: (i) geothermal alteration at elevated temperatures shortly following or coincident with Timber Mountain Caldera volcanic activity, (ii) low-temperature weathering and diagenesis under conditions similar to those that exist at present, and (iii) repeated hydrothermal inundation.

Hydrothermal activity is indicated by clay diagenetic relations supported by fluid inclusion data in the northern region of Yucca Mountain, particularly in samples taken from depths greater than 1,000 m in drill hole USW G-2 (Bish, 1989; Bish and Aronson, 1993). However, hydrothermal effects are not evident in rocks within approximately 1,000 m of the surface in USW G-2 and are subtly expressed at

even greater depths in areas to the south. Based on potassium-argon dating of illite and smectite, a hydrothermal alteration event is likely to have occurred 10 to 11.5 ma at the time of Timber Mountain Caldera volcanic activity (Bish, 1989; Bish and Aronson, 1993).

Hydrothermal formation of zeolites, clays, and silica phases occurs along fractures in zones of transition between devitrified and vitric rocks in the lower densely welded Topopah Spring Tuff at Yucca Mountain (Levy and O'Neil, 1989). Textural and mineralogical relations and oxygen isotope geothermometry for these materials indicate that alteration occurred contemporaneously with cooling of the primary volcanic deposits. Concretionary structures and breccia dikes at the ground surface in the vicinity of Yucca Mountain were also interpreted by Levy (1991) to have formed by water infiltrating into still hot volcanic deposits. In contrast, J.S. Szymanski[1] contends that these and similar deposits are a consequence of repeated injections of hydrothermal solutions into the unsaturated zone at Yucca Mountain and even to the ground surface.

Systematic diagenetic transitions (e.g., transitions from glass to clinoptilolite to analcime) occur in borehole USW G-2 where hydrothermal activity is evident at depth and are also apparent in other borehole samples showing no sign of hydrothermalism. Normal diagenesis does not require hydrothermal alteration, and may be occurring slowly at present. Coexistence of lower temperature, randomly interstratified illite/smectite with higher temperature, more ordered clays of hydrothermal genesis, indicates that clay formation continued after the end of the hydrothermal event recorded in samples from borehole USW G-2 (Bish and Aronson, 1993).

Levy and O'Neil (1989) and Levy (1991) concluded that most zeolitization, particularly in nonwelded tuffs, occurred early in the history of Yucca Mountain under ambient diagenetic conditions below the groundwater table. Evidence from textures of precipitated minerals indicates tilting of volcanic strata following primary zeolitization. The deformation is proposed to have occurred prior to 11.6 ma, establishing a minimum age limit for most zeolitization.

Mineralogic variations at Yucca Mountain may be related to the variation of silica content of groundwater under ambient conditions (Kerrisk, 1983; Duffy, 1993). Metastable glass, opal, tridymite, and cristobalite disappear with depth, indicating a decrease in aqueous silica activity. Lithophysal tridymite, which is preserved in fractures in the Topopah Springs member from boreholes J-13 and USW G-4 above the water table, is absent in fractures in this member from the J-13 well where it is below the water table (Carlos, 1989). Disappearance of metastable silica phases is correlated with the transition in dominant alteration mineralogy from clinoptilolite to analcime, which also corresponds to a decrease in silica activity (Kerrisk, 1983; Bish and Aronson, 1993).

Several lines of evidence indicate that altered rocks at Yucca Mountain are enriched in calcium derived from the ground surface and transported to depth in infiltrating groundwater. Calcite is an occasional secondary mineral, occurring notably in fractures and as coatings near the surface where a substantial caliche layer is developed (Vaniman et al., 1984). Young calcite with isotopic characteristics similar to soil-zone calcite occurs at depth in the unsaturated zone. Unaltered Paintbrush Tuff from Yucca Mountain generally contains less than 1 percent CaO by weight, whereas rocks that have been partially

---

[1]Jerry S. Szymanski, "The Origin and History of Alternation and Carbonatization of the Yucca Mountain Ignimbrites." U.S. Department of Energy, DOE Nevada Field Office, Yucca Mountain Site Characterization Project Office; Las Vegas, Nevada, April 1992.

altered to zeolites and/or clays typically contain CaO at 3 to 4 percent (Broxton et al., 1986; see Table 4-1). Although the altered rocks may have silica depletions of 10 to 20 percent, and alumina enrichments of up to 30 percent suggesting limited preferential leaching, the large differences in calcium concentrations indicate that it is added to the altered rocks from an external source. In general, alteration minerals, notably zeolites, are enriched in calcium at higher positions in the volcanic section above the water table, and become richer in potassium and sodium with depth. Similar relations are observed for other alkaline earth metals, magnesium and strontium. Variations in groundwater chemical compositions also support a mechanism of alkaline earth metasomatism (Section 4.2.5.8).

4.2.3 Gas Chemistry

Analyses of gases collected from the vadose zone at Yucca Mountain at depths up to 140 m show them to be indistinguishable from atmospheric air with regard to major components (78 percent N_2, 21 percent O_2, and approximately 1 percent Ar). However, the CO_2 content is elevated typically at 0.1 to 0.13 percent, and CH_4 is depleted with little to none present, relative to atmospheric values (Thorstenson et al., 1990). For reference, the CO_2 content of air is approximately 0.03 percent. The CO_2 contents of gases calculated to be at equilibrium with saturated zone well waters from tuffaceous aquifers generally range from 0.13 to 1.4 percent (Kerrisk, 1987). Hence, the maximum CO_2 content of the unsaturated zone gas phase corresponds approximately to the minimum CO_2 content calculated for gases in equilibrium with saturated zone waters. This observation suggests that degassing of saturated zone water could provide CO_2 to the unsaturated zone. The relatively light carbon isotopic character of the gas at Yucca Mountain (e.g., $\delta^{13}C$ normally between –15 and –23 PDB [Thorstenson et al. (1990); Yang et al. (1993)] indicates a biogenic origin for the carbon. Ground gas that escapes from borehole UZ6S and gas collected from shallow "neutron holes" on Yucca Mountain have ^{14}C contents generally in excess of 100-percent modern carbon (pmc) indicating that the carbon is derived dominantly from testing of nuclear devices (Thorstenson et al., 1990). However, gas collected from depths up to 350 m in borehole UZ1 have progressively lower ^{14}C activities with depth (Yang et al., 1993) indicating that the carbon becomes progressively older with depth.

Because of the generally large liquid saturation in the natural vadose zone, the ground gas would be expected to be close to chemical saturation with water at ambient temperatures. For repository conditions at and within the boiling point isotherm surrounding the waste packages, the large amount of water in the mountain would tend to drive the gas composition toward pure H_2O vapor. Large-scale gas convection or binary diffusion of air and water vapor would tend to disrupt this regime.

4.2.4 Hydrochemical Characteristics

Waters contained in tuffaceous rocks at and near Yucca Mountain have chemical compositions formulated primarily by interactions with soil-zone materials, silicic tuffaceous rocks, and Paleozoic carbonate rocks that underlie the tuffs. Groundwater taken from saturated zone tuffaceous aquifers in the Yucca Mountain area have compositions that are uniformly dilute (e.g., generally less than 400 mg/l total dissolved salts), rich in sodium (with lesser potassium and calcium), bicarbonate, and silica, oxidizing (except at depth), and intermediate in pH (e.g., 7 to 8) (Ogard and Kerrisk, 1984; Kerrisk, 1987; McKinley et al., 1991). Kerrisk (1987) summarized and interpreted water chemistry from a subset of wells that tap the saturated zone and identified 15 wells from "Yucca Mountain and vicinity." Water chemistry data from this set of wells have been adopted in this study as representative of the saturated tuffaceous aquifer at Yucca Mountain. However, water from well UE-25p#1 was excluded from the set

because this well taps water from the Paleozoic carbonate aquifer and was collected at 44 to 56 °C. Locations of boreholes are shown in Figure 4-1, and water chemistry data from the Yucca Mountain vicinity are illustrated in Figure 4-2 (A through L).

Variations in water chemistry in the saturated zone are significant and geographically dependent. Notably, the Ca content of tuffaceous aquifer waters is relatively low to the west of the Ghost Dance Fault (which divides the proposed repository area) and higher to the east of this fault, leading to corresponding variations in the Na to Ca ratio (Kerrisk, 1987). Gravity and borehole data indicate that the depth to Paleozoic carbonate rocks increases from east to west under Yucca Mountain (Snyder and Carr, 1984) which could contribute to the variation in Ca content of the saturated zone tuffaceous aquifer waters. Deeper, saturated zone waters that have apparently reacted with rocks containing abundant carbonate minerals (e.g., those from regional aquifers in carbonate rocks underlying the tuffs) have a chemical composition that is substantially different from the tuffaceous aquifer waters notably having higher calcium and carbonate and lower sulfate and chloride concentrations (Winograd and Thordarson, 1975). Water has been extracted from the Topopah Spring Tuff (the proposed host rock for the repository) from well J-13 where this stratum dips below the water table. The chemical composition of J-13 well water has been adopted as a reference composition in Yucca Mountain Project studies (U.S. Department of Energy, 1988).

Although analogous processes have affected water chemistry in the saturated tuffaceous aquifers and in the unsaturated zone at Yucca Mountain, they are not strictly from the same source, and their environments are different. The dominant recharge area for saturated zone water under Yucca Mountain is probably at higher elevations to the north such as Pahute Mesa (Winograd and Thordarson, 1975). In contrast, the unsaturated zone waters must have a more local meteoric source. Unlike the saturated zone groundwaters, the chemistry of vadose zone water is continuously affected by interactions with the gas phase (e.g., evaporation/condensation of H_2O and exchange with gaseous CO_2). Because of these hydrologic differences, the composition of the ambient groundwater in the unsaturated zone may differ substantially from the saturated zone water chemistry, including that from the J-13 well.

Chemical data for pore water samples extracted by triaxial compression of core samples from unsaturated zone rocks at Yucca Mountain have been reported by Yang and coworkers (Yang et al., 1988; Yang, 1992; Peters et al., 1992). These data show wide variability and suggest substantial chemical differences from saturated zone tuffaceous aquifer waters (Figure 4-2). In part this may be due to the formidable technical difficulties associated with collection and preservation of unaltered samples of partially saturated rock and extraction of pristine water samples.

An additional set of unsaturated zone groundwater chemistry data is available from Rainier Mesa (Benson, 1976; White et al., 1980), which is approximately 30 km north of Yucca Mountain in a similar geologic setting but at higher elevation with greater rainfall and groundwater recharge. Pore water samples were extracted from core samples taken from Rainier Mesa by centrifugation (for unzeolitized, friable, vitric Paintbrush Tuff samples) or by triaxial compression (primarily for zeolitized beds). Fracture waters were collected from perched water flowing into tunnels from the zeolitized Tunnel Beds (White et al., 1980). Interstitial (pore) waters are notably higher in calcium, chloride, and sulfate than fracture waters. Pore waters from the vadose zone at Rainier Mesa reported by White et al. (1980) have lower bicarbonate to chloride plus sulfate ratios than saturated zone waters from the vicinity of Yucca Mountain. Pore waters from Rainier Mesa also have lower equilibrium CO_2 pressures for a given pH than fracture waters at Rainier Mesa or saturated zone well waters from the vicinity of Yucca Mountain (Kerrisk, 1987). Chemical differences between unsaturated and saturated zone waters at Yucca Mountain are

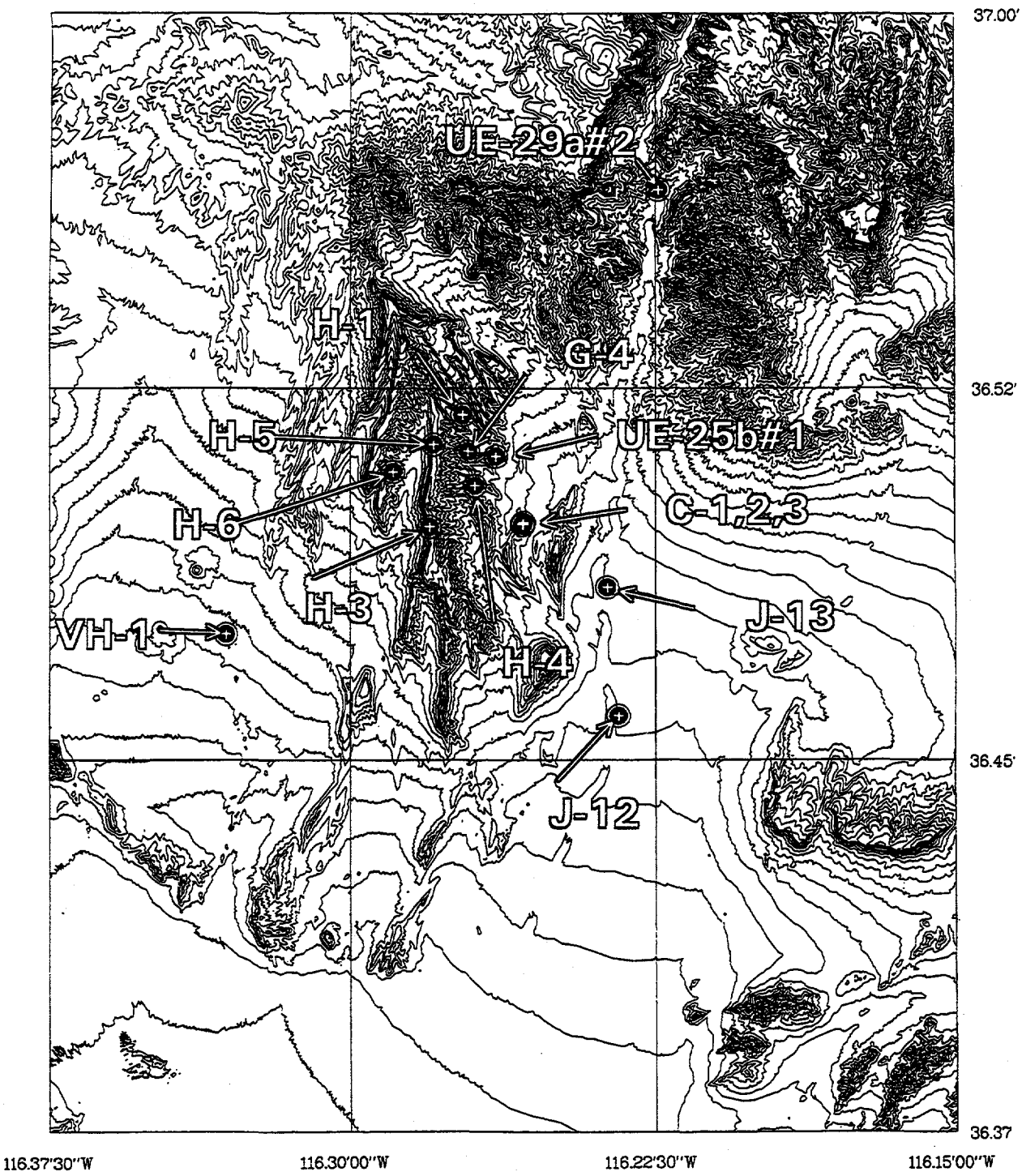

Figure 4-1. Locations of wells in the vicinity of Yucca Mountain for which water chemistry is regarded as characteristic of the saturated zone tuffaceous aquifer. Topography is represented by contours of 100-ft intervals. Yucca Mountain is located in the center of the figure.

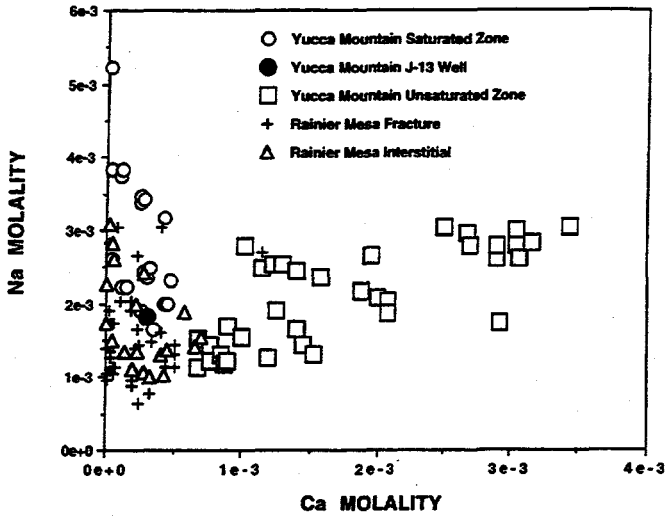

(A)

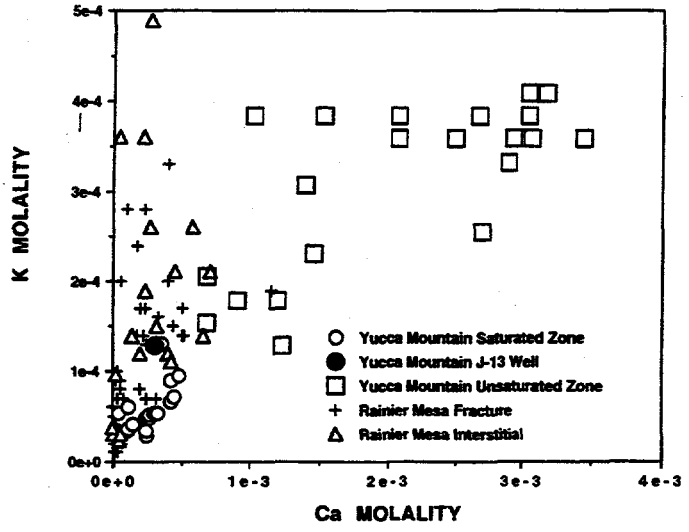

(B)

Figure 4-2. Comparison of water chemistry from the saturated zone tuffaceous aquifer in the vicinity of Yucca Mountain highlighting J-13 well water (Kerrisk, 1987) from unsaturated zone core samples from Yucca Mountain (Yang et al., 1988; Yang, 1992; Peters et al., 1992); from interstices (pores) in unsaturated zone core samples from Rainier Mesa; and from saturated fractures above the water table at Rainier Mesa (White et al., 1980). Na, K, Mg, Si, Cl, HCO_3^-, and pH are plotted as a function of Ca in A through G, respectively; SO_4^{2-} is plotted as a function of Cl in H; and Cl, HCO_3^-, SO_4^{2-}, and pH are plotted as a function of Na in I through L, respectively. Lines in E and J have slopes of one for reference.

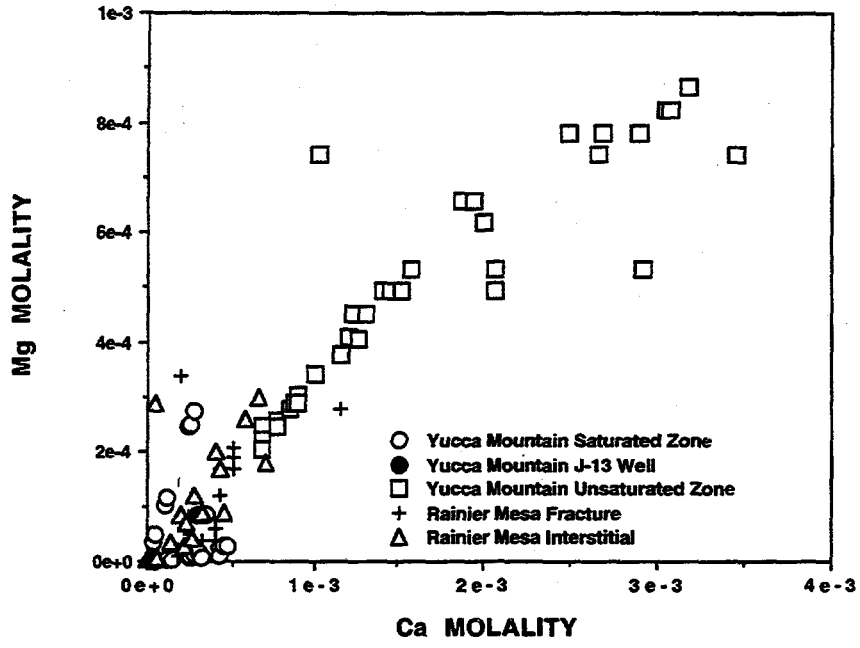

(C)

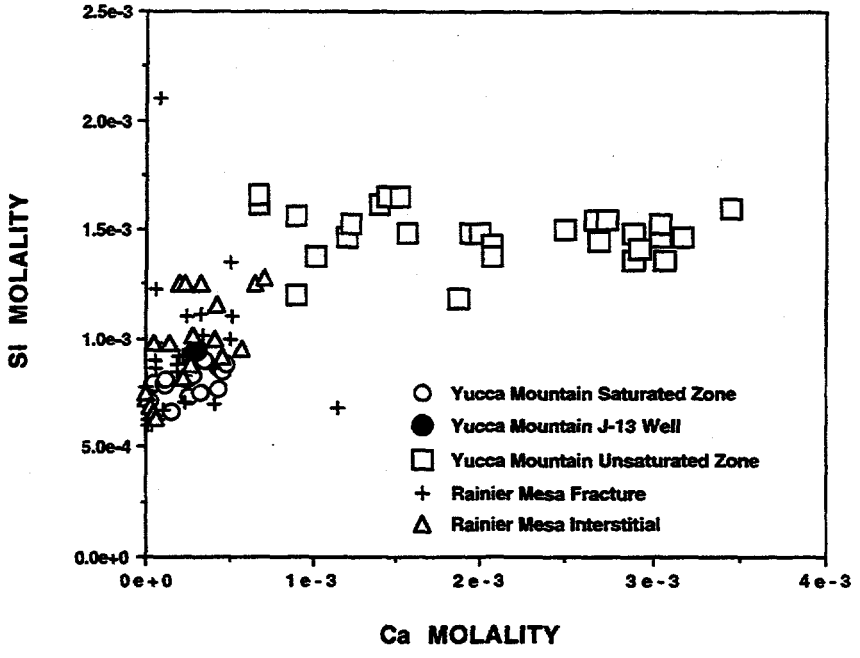

(D)

Figure 4-2. Cont'd

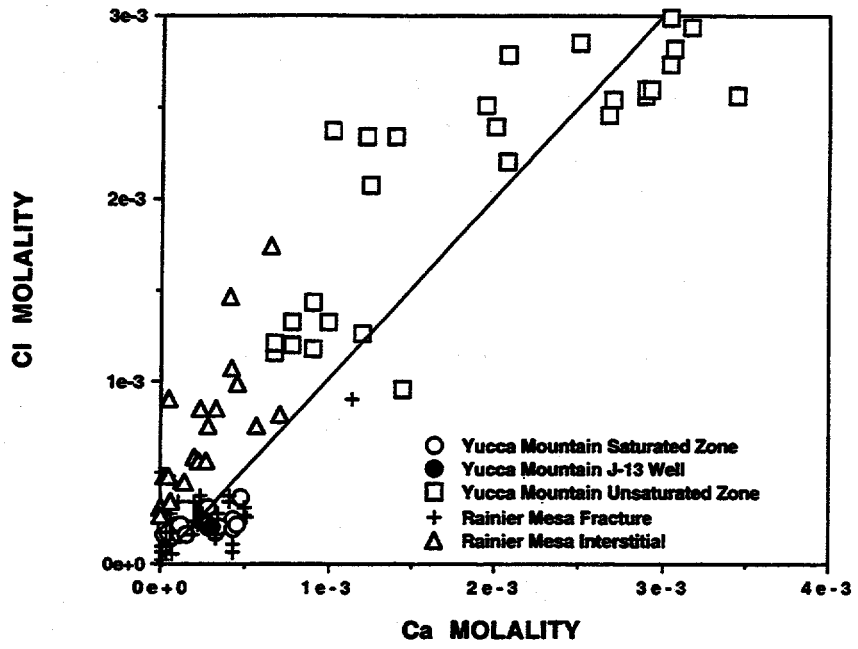

(E)

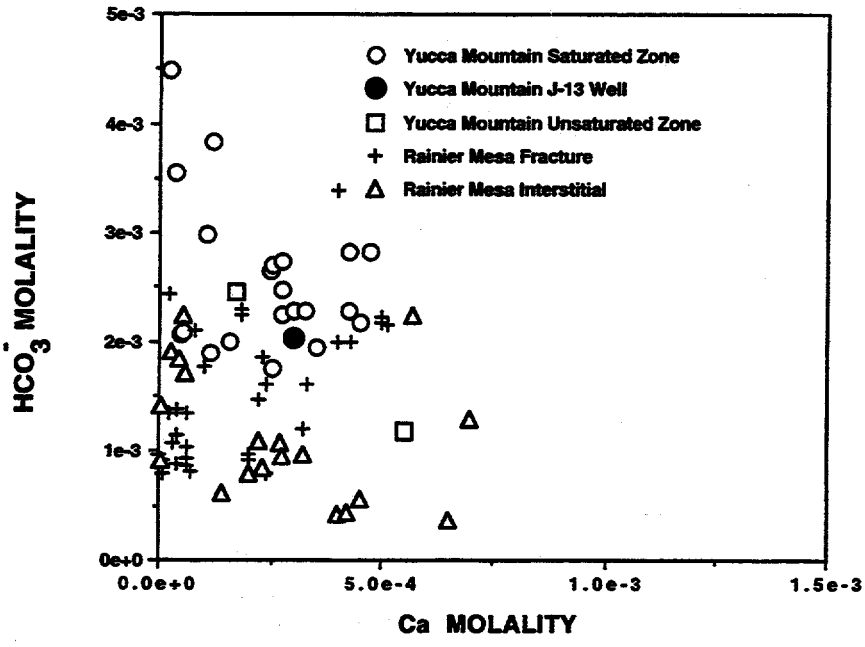

(F)

Figure 4-2. Cont'd

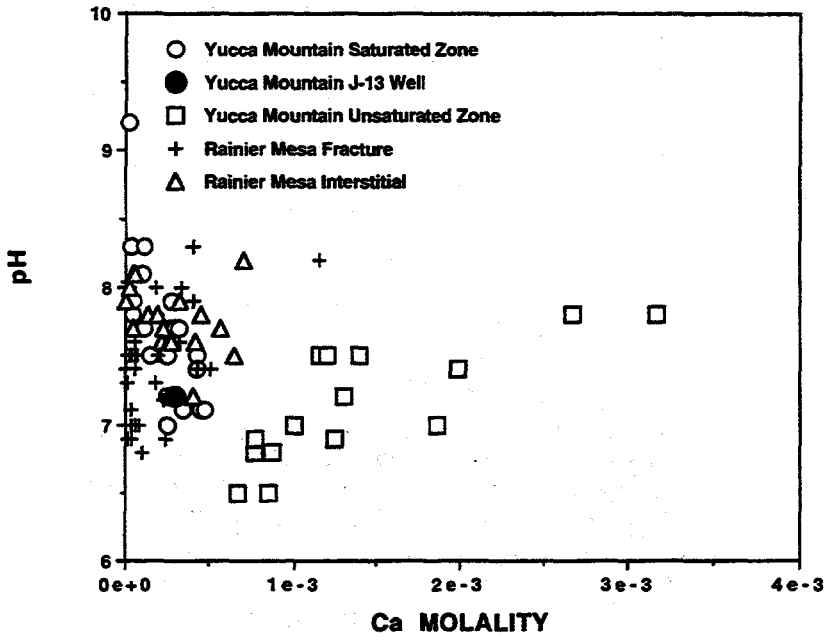

(G)

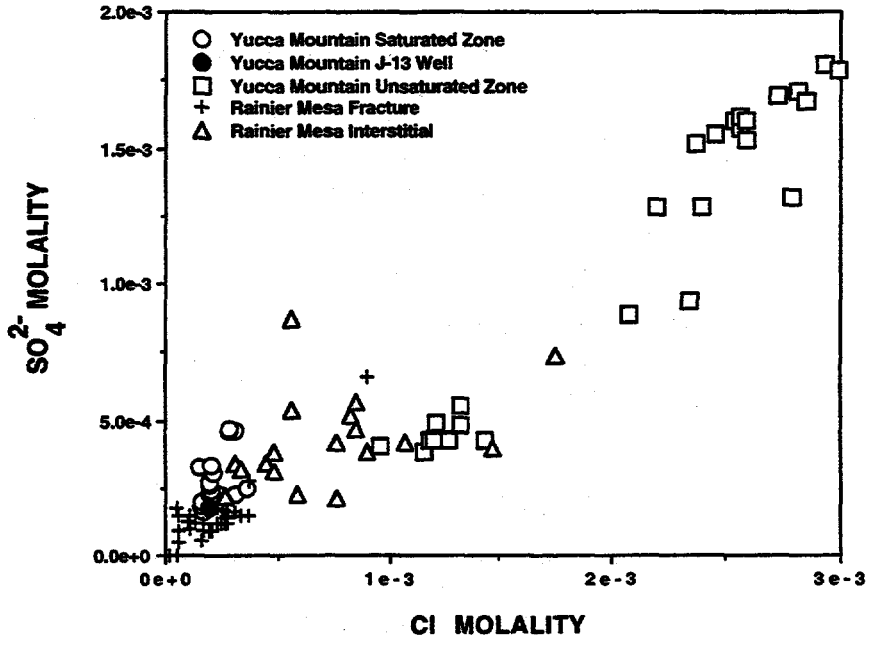

(H)

Figure 4-2. Cont'd

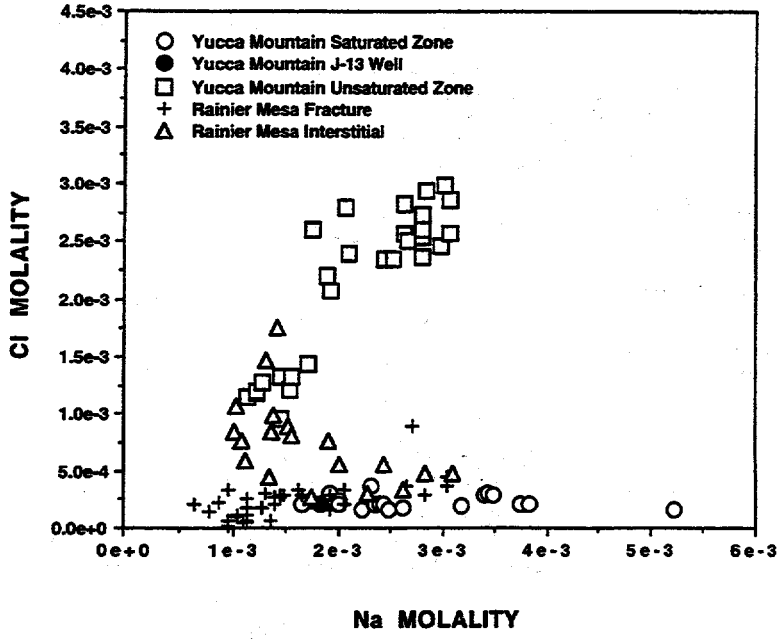

(I)

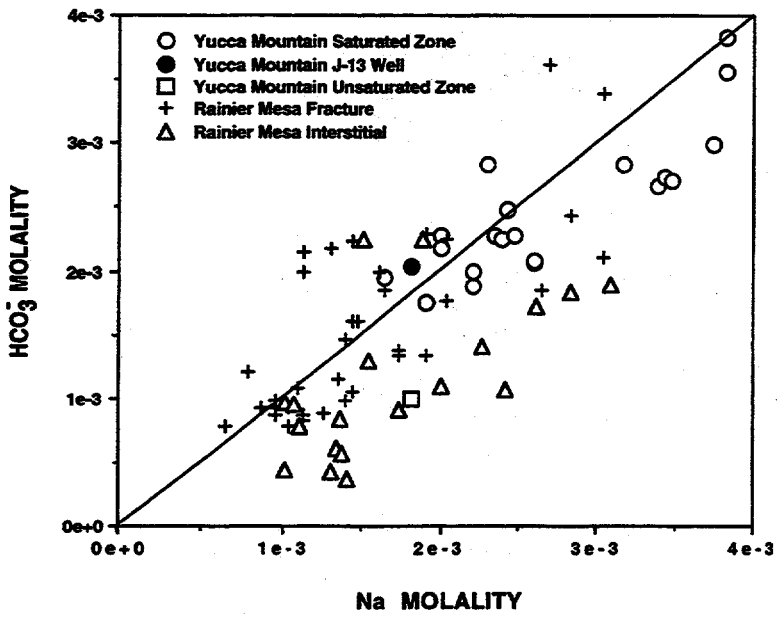

(J)

Figure 4-2. Cont'd

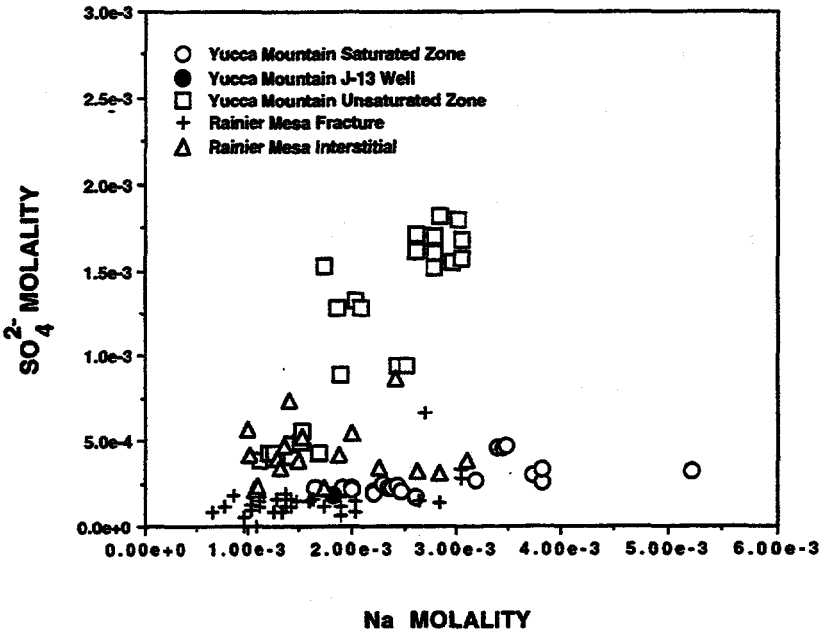

(K)

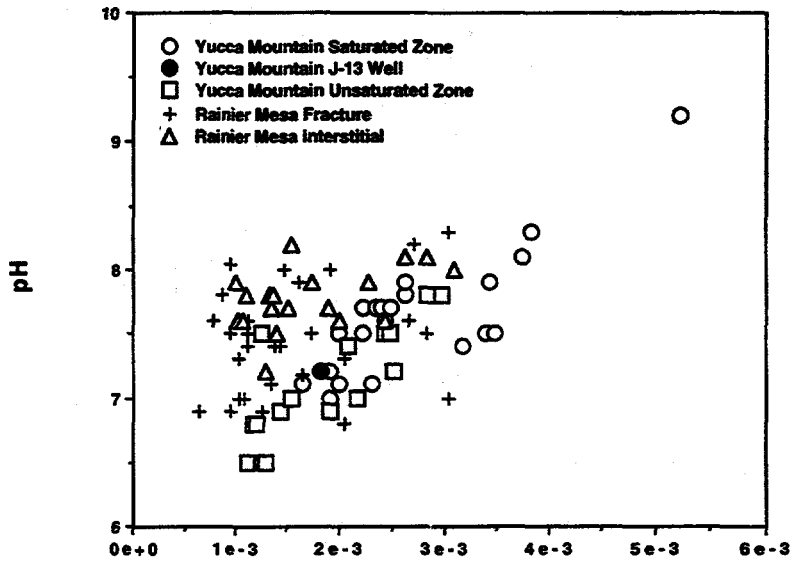

(L)

Figure 4-2. Cont'd

analogous to differences at Rainier Mesa between pore waters from unsaturated tuffs and waters from saturated fractures above the water table. Chemical similarities between the fracture water at Rainier Mesa and saturated zone groundwater at Yucca Mountain suggest that the latter is recharged by fracture flow through unsaturated tuffs.

4.2.5 Aqueous Geochemistry in the Saturated and Unsaturated Zones

Water in the partially saturated zone at Yucca Mountain is of particular concern because the proposed repository is to be located above the water table. However, water is difficult to sample there and few data are available. In contrast, water chemistry data are available from a variety of boreholes in the vicinity of Yucca Mountain which tap the saturated tuffaceous aquifer. A summary of characteristics and constraints on individual properties of saturated and unsaturated zone waters is provided in this section. Inferences are drawn from mineralogical data, gas composition data, and water chemistry data from both the saturated and unsaturated zones at Yucca Mountain, and from the unsaturated zone at Rainier Mesa. Likely thermodynamic, kinetic, and mass transfer controls on gas-water-rock interactions and water chemistry are identified. Also, qualitative scenarios for repository evolution are examined for their implications for the consequent evolution of unsaturated zone groundwater properties. Relations among dissolved species discussed in the following sections are illustrated in Figure 4-2. Ca is a useful component for comparison in these figures because it varies over a large range of concentrations.

4.2.5.1 Oxidation State

The dominant control on the oxidation state in the vadose zone is the gas phase which provides abundant oxygen. Few reducing agents exist in the natural system. Petrographic analyses of Yucca Mountain tuff indicate that ferrous iron is significant only in primary glass in small concentrations (Bish and Vaniman, 1985), and that ferrous iron is isolated from water (Caporuscio and Vaniman, 1985). Bish and Vaniman (1985) speculate that accelerated alteration of glass during a thermal pulse could oxidize this iron. However, its quantity is so small that this would have a negligible effect on the oxidation state of the system. Analyses of saturated zone groundwater from near the static water table show oxidizing conditions (Kerrisk, 1987). Reducing groundwaters have been extracted from depth in the saturated zone (Ogard and Kerrisk, 1984), but they are unlikely to affect the unsaturated zone or the repository system.

Metallic waste containers and spent nuclear fuel represent an enormous reducing potential and would generate local reducing conditions. The spatial disposition, intensity, and evolution of reducing plumes which could emanate from waste packages would be a function of corrosion and spent fuel oxidation rates and transport rates of oxidants and reductants (notably oxygen, water, and hydrogen). Reducing plumes and released radionuclides may ultimately migrate by similar mechanisms, raising the possibility of radionuclide transport under locally reducing conditions, particularly in the near field.

4.2.5.2 pH

The measured pH of groundwater from the saturated zone in the vicinity of Yucca Mountain is generally between 6.5 and 8.5, and J-13 well water has a pH of approximately 7 (McKinley et al., 1991). Water extracted from unsaturated rock from Yucca Mountain by triaxial compression has pH measured in the range of 6.5 to 7.8 (Yang et al., 1988; Yang, 1992). Measurements of pH for pore water and fracture water from the unsaturated zone at Rainier Mesa are also in this range (White et al., 1980).

Aqueous carbonate equilibria provide a primary control on pH. Repository heating and consequent exsolution of dissolved CO_2 and accelerated silicate hydrolysis would cause the pH of unsaturated zone solutions to increase (Arthur and Murphy, 1989; see Section 4.7.3). Also, interactions of groundwater with cementitious construction materials (e.g., grout) could cause pH to increase to high values (e.g., Reardon, 1992).

4.2.5.3 CO_2 and Bicarbonate

The dominant aqueous carbonate species is HCO_3^- throughout the pH range for natural waters at Yucca Mountain, and aqueous carbonate speciation is a weak function of temperature below 100 °C. Bicarbonate concentrations in saturated zone waters in the vicinity of Yucca Mountain vary within a relatively narrow range from approximately 2×10^{-3} to 5×10^{-3} molal, but most waters contain between 2×10^{-3} and 3×10^{-3} molal bicarbonate as the dominant anion (McKinley et al., 1991). Similar bicarbonate concentrations characterize water samples from the unsaturated zone at Rainier Mesa. However, some Rainier Mesa water analyses indicate significantly lower bicarbonate contents down to 0.5×10^{-3} to 1×10^{-3} molal particularly in interstitial waters (White et al., 1980). Averaged values for bicarbonate from unsaturated zone waters at Yucca Mountain range from 1×10^{-3} to 2.5×10^{-3} molal (Peters et al., 1992).

Saturated zone groundwaters in the vicinity of Yucca Mountain groundwaters are calculated generally to be undersaturated with respect to calcite (Kerrisk, 1987). Water infiltrating to the vadose zone is likely to encounter secondary calcite mineralization in the caliche (soil) zone, and to leave that zone in a state close to equilibrium with respect to calcite. Calcite solubility according to the reaction

$$CaCO_3 + CO_2 \rightleftharpoons 2\ HCO_3^- + Ca^{2+} \qquad (4\text{-}1)$$

together with the CO_2 partial pressure and a constraint on the Ca^{2+} content, offers a reasonable upper limit to carbonate concentrations in the unsaturated zone.

A strong positive correlation between sodium and bicarbonate among all tuffaceous groundwaters from Yucca Mountain and vicinity [Figure 4-2(J)] is consistent with traditional views of groundwater evolution. Dissolution of primary sodium aluminosilicates liberates Na^+, and consumes carbonic acid forming bicarbonate.

An important contribution to water chemistry at Yucca Mountain is CO_2 derived primarily from soil-zone biological processes such as root respiration. Rainwater saturated with respect to atmospheric CO_2 at a partial pressure of approximately $10^{-3.5}$ bar has a bicarbonate content of approximately 10^{-5} molal and a pH of approximately 5. In contrast, groundwaters from tuffaceous aquifers in the vicinity of Yucca Mountain have chemistries consistent with 10^{-2} to 10^{-3} bar of CO_2 pressure, which is significantly greater than the atmospheric value (Kerrisk, 1987). Vadose zone gases in the upper 140 m at Yucca Mountain contain CO_2 in excess of atmospheric values (Thorstenson et al., 1990), corresponding to approximately $10^{-2.9}$ bar of CO_2 pressure.

It seems likely that unsaturated zone water readily exchanges carbon isotopes with the gas phase. Because mobility of the ground gas may be greater than that of water in the vadose zone, and because gas phase diffusion of CO_2 is relatively rapid, carbon in the gas may be younger than the water. Under these conditions, the apparent ^{14}C age of water that has interacted with the gas would be less than its true age. Alternatively, if CO_2 in the unsaturated zone is derived by degassing of underlying saturated zone

waters, the apparent ^{14}C age could reflect the age and history of these waters including their interactions with older carbonate-bearing rocks. Unsaturated zone groundwaters taken from approximately a 100-m depth in UE-25 UZ#4, and UE-25 UZ#5 wells on the east side of Yucca Mountain yield apparent ^{14}C ages of 1,000 and 4,900 yr, respectively (Yang, 1992). Notably, gas collected from a 100-m depth in USW UZ-1 at the crest of Yucca Mountain contains 70-percent modern carbon (Yang et al., 1993), which corresponds to an apparent age of 2,950 yr. Murphy (1994)[2] has shown that gas phase diffusion of $^{14}CO_2$ coupled with gas-water carbonate equilibrium could reasonably account for the observed ^{14}C distribution in the gas phase at Yucca Mountain in the absence of net fluid advection.

4.2.5.4 Chloride and Sulfate

Groundwater from saturated zone tuffaceous aquifers in the vicinity of Yucca Mountain contains up to 0.5×10^{-3} molal chloride and sulfate [Figure 4-2(H)]. A rough correlation between saturated zone sulfate and chloride concentrations corresponds to a molar ratio of 0.82 (Kerrisk, 1987). Data for water extracted from unsaturated tuff (Yang et al., 1988; Yang, 1992) show a similar correlation between sulfate and chloride, with a somewhat lower molar ratio of approximately 0.6. However, sulfate and chloride concentrations from unsaturated zone water samples range from approximately the maximum values measured for the saturated zone at Yucca Mountain up to approximately 2×10^{-3} molal sulfate and 3×10^{-3} molal chloride. Fracture waters at Rainier Mesa (White et al., 1980) have chloride concentrations similar to saturated zone waters at Yucca Mountain, but lower sulfate to chloride ratios [Figure 4-2(H)].

Interstitial waters at Rainier Mesa have greater chloride and sulfate concentrations (and greater ratios of these species to bicarbonate) than fracture waters collected within the same depth intervals (White et al., 1980). Nevertheless, chloride and sulfate from pore waters at Rainier Mesa are generally less than values obtained from unsaturated rocks at Yucca Mountain. Increased concentrations in pore waters in the unsaturated zone could be accomplished by occasional volatilization of CO_2 and H_2O from the interstitial water, with associated concentration of the soluble anions. During periods of recharge, fractures could be flooded with relatively dilute, CO_2-charged water descending from the soil-zone. According to this interpretation, unsaturated zone pore waters may be substantially older than waters in saturated fractures above and below the water table. Higher soluble anion concentrations in Yucca Mountain pore waters than in Rainier Mesa pore waters may indicate that the process of evaporative concentration is more advanced at Yucca Mountain where rainfall and presumably recharge is significantly lower. The high solubilities of chloride and sulfate salts in contrast to silicates and carbonate minerals suggests that, as waters evaporate extensively due to repository heating, their chemistries would become dominated by chloride and sulfate rather than bicarbonate as in the natural system.

4.2.5.5 Fluoride

Fluoride tends to increase with increasing Na^+ and HCO_3^-, ranging from 5×10^{-5} to 3×10^{-4} molal in saturated zone waters (Kerrisk, 1987). Saturated zone waters range up to chemical saturation with respect to fluorite, which has been observed in fractures at Yucca Mountain (Bish and Vaniman, 1985). Together with constraints on calcium, fluorite saturation may provide a reasonable upper

---

[2]Murphy, W.M. (1994). Contributions of thermodynamic and mass transport modeling to evaluation of groundwater flow and groundwater travel time at Yucca Mountain, Nevada. Materials Research Society Symposium Proceedings. In Review.

limit to fluoride concentrations in groundwater at Yucca Mountain. The chlorine content of the tuffaceous rocks at Yucca Mountain is low (approximately 500 ppm) and the molar fluorine-to-chlorine ratio in unaltered tuffs is approximately 10 (Kerrisk, 1987). In contrast, chloride is the second most abundant anion in groundwaters from the tuffaceous aquifer, where its molality usually exceeds the fluoride molality. Enrichment of groundwater in chloride relative to fluoride suggests an external source of chlorine, although it may also be due to preferential incorporation of fluoride in secondary minerals such as zeolites, clays, and apatite. An external source of chloride is likely to be aerosol or dust halite derived from seawater or the numerous playas in the region and deposited at the surface of the mountain.

4.2.5.6 Nitrate

The nitrate content of saturated groundwater in the vicinity of Yucca Mountain ranges up to 3×10^{-4} molal (Kerrisk, 1987). Nitrite as well as nitrate has been observed in reducing water from depth at Yucca Mountain (Ogard and Kerrisk, 1984), but nitrite is unlikely under ambient oxidizing conditions in the unsaturated zone. The nitrate/nitrite couple may be significant in characterizing the redox state of the system where it tends toward reducing conditions, because reduction of carbonate and sulfate is kinetically slow, and because the concentrations and buffering capacities of aqueous iron and manganese are minimal. Nitrate is a major product of radiolysis in air, and could become significant in the radiation field of a repository at Yucca Mountain. Hypothetically, condensation of nitric acid generated by radiolysis along with early condensation of small volumes of water on cooling containers (or other materials including rocks) could generate relatively concentrated nitric acid solutions. Decomposition of nitrate could lead to persistence of oxidizing conditions in some circumstances, e.g., below the water table.

4.2.5.7 Silica

Aqueous silica contents of saturated zone waters in the Yucca Mountain vicinity vary in a narrow range from about 0.6×10^{-3} to 1.3×10^{-3} molal. At these concentrations, the water is in the range of cristobalite to amorphous silica saturation (e.g., Kerrisk, 1987). Similar silica contents are typical of waters from both interstitial and fracture waters from above the water table in Rainier Mesa, although some samples from Rainier Mesa range to slightly higher concentrations (White et al., 1980). In contrast, the silica contents of water extracted from cores from the unsaturated zone at Yucca Mountain vary over a narrow but elevated range from 1.3×10^{-3} to 1.7×10^{-3} molal (Yang et al., 1988; Yang, 1992).

Low-temperature waters, including those at Yucca Mountain, are commonly supersaturated with respect to quartz (the stable silica polymorph at low temperature and pressure) because of its slow nucleation and growth rates. The more soluble silica phases, cristobalite and opal, are common silica minerals at Yucca Mountain particularly above the water table and in diagenetic zones I and II, whereas, quartz is common below the water table (Carlos, 1985; Bish and Chipera, 1989). Generation of aqueous silica activities in excess of cristobalite saturation requires dissolution of silica-bearing phases such as feldspars or glass. With conservation of aluminum, dissolution of feldspars and growth of clay minerals results in a net release of silica. However, dissolution of feldspars coupled with precipitation of clinoptilolite, which generally has a higher silica to alumina ratio, would result in removal of silica from solution. Feldspar alteration to clinoptilolite is unlikely to generate the high silica concentrations in Yucca Mountain groundwaters. In contrast, the silica to alumina ratio in rhyolite glass exceeds that in clinoptilolite. Alteration of glass is a likely mechanism for generation of secondary clinoptilolite and elevated aqueous silica activities as concluded by other researchers (White et al., 1980). This conclusion

is supported by petrographic evidence indicating that clinoptilolite forms predominantly by alteration of rhyolitic glass at Yucca Mountain. However, feldspar alteration to clay minerals is another possible mechanism.

Alteration of clinoptilolite to analcime is a critical process at Yucca Mountain and is related closely to the aqueous silica content of groundwater. Experimental studies of relations between these minerals are presented in Section 3 of this report. A reaction between idealized mineral components can be written as

$$\underset{\text{Na-clinoptilolite}}{Na_2Al_2Si_{10}O_{24}\cdot 8H_2O} \rightleftharpoons \underset{\text{Na-analcime}}{2NaAlSi_2O_6\cdot H_2O} + \underset{\text{aqueous silica}}{6SiO_2} + 6H_2O \qquad (4\text{-}2)$$

Na and Al are conserved in mineral phases in this reaction, and equilibrium in dilute solutions at a constant temperature depends only on the concentration of aqueous silica. Control of the relative stability of clinoptilolite and analcime at Yucca Mountain by aqueous silica activity is indicated by the correlation of cristobalite and/or opal with clinoptilolite in shallower rocks, and the absence of cristobalite with analcime in deeper rocks (Kerrisk, 1983; Bish and Chipera, 1989; Duffy, 1993). However, the data presented in Section 3 of this report indicate that reaction (4-2) does not generally control aqueous silica activities.

Equilibrium for reaction (4-2) shifts to the right, that is, to higher silica activities, with increasing temperature primarily because it is a dehydration reaction. With increasing temperature, if the equilibrium silica activity for reaction (4-2) exceeds the value of the aqueous system, then Na-clinoptilolite becomes unstable relative to analcime and aqueous silica. For example, higher temperatures may activate growth of quartz leading to reduced silica activities and destabilization of clinoptilolite. In nature, clinoptilolite frequently replaces volcanic glass, and subsequently analcime replaces clinoptilolite with increasing depth (and temperature) (Hay and Sheppard, 1977). On this basis, Smyth (1982) recommended limiting repository temperatures at Yucca Mountain below 85 °C to protect favorable clinoptilolite. Preliminary reaction-path models analogous to those in Section 4.7 show the feasibility of destabilization of clinoptilolite at repository temperatures below 50 °C under hypothetical conditions of rapid, open-system volatilization of CO_2 and corresponding increase in pH, and kinetic growth of quartz (Murphy, 1991). Bish and Aronson (1993) speculate, however, that the abundance of glass and opal in the unsaturated zone and the limited duration of repository heating would preclude important reductions of aqueous silica concentrations at Yucca Mountain. In contrast, Glassley (1994) concluded from kinetic considerations that time would be sufficient in the environment of a repository at Yucca Mountain for most of the system to reach equilibrium with respect to quartz. This basic issue has not been resolved.

4.2.5.8 Major Cations: Na, K, Ca, Mg

Major dissolved cations are derived from dissolution of volcanic glass and minerals and are controlled to some extent by precipitation and ion exchange reactions among secondary minerals such as zeolites, clays, and calcite. Relations between the major exchangeable cation chemistry of zeolites and water at Yucca Mountain are analyzed in Section 2 of this report. Dissolution of soil-zone materials, for example, carbonate minerals, is also an important source for some groundwater species, notably alkaline

earths and possibly chloride. In the saturated zone of tuffaceous aquifers near Yucca Mountain, Na^+ ranges from 2×10^{-3} to 5×10^{-3} molal and varies in proportion to total carbonate [Figure 4-2(J)]; Ca^{2+} ranges up to 5×10^{-4} molal and tends to decrease with increasing Na^+ and pH [Figure 4-2(A) and (G)]; Mg^{2+} is generally less than 1×10^{-4} molal; and K^+ is generally less than 1.5×10^{-4} molal. Interstitial waters from the Paintbrush Tuff at depths between 100 and 200 m taken from core U12T3 at Rainier Mesa have Na^+ contents that range from 1×10^{-3} to 2×10^{-3} molal, K^+ between 2×10^{-4} and 4×10^{-4} molal, Ca^{2+} from 5×10^{-5} to 6×10^{-4} molal, and Mg^{2+} from 1×10^{-4} to 3×10^{-4} molal (White et al., 1980). Mg^{2+} and Ca^{2+} concentrations in water from the unsaturated zone at Rainier Mesa decrease systematically with depth, which is correlated with a decrease in Cl^- and an increase in HCO_3^- with depth (Benson, 1976; White et al., 1980). The pattern of decreasing alkaline earth cation concentrations with depth was attributed by White et al. (1980) to progressive formation of calcium containing montmorillonite and clinoptilolite. The relations between chloride and bicarbonate could reflect greater evaporation of pore waters retained closer to the ground surface (see Section 4.2.5.4).

In unsaturated zone pore water at Yucca Mountain, Ca^{2+} ranges from 1×10^{-3} to nearly 4×10^{-3} molal, and Mg^{2+} ranges from 2×10^{-4} to almost 1×10^{-3} molal (Yang et al., 1988; Yang, 1992). Both of these species, which show a strong positive correlation in the unsaturated zone waters, are significantly more concentrated there than in saturated zone waters at Yucca Mountain [Figure 4-2(C)]. In contrast, Na^+ ranges from 1×10^{-3} to 3×10^{-3} molal in the unsaturated zone (Yang et al., 1988; Yang, 1992), which is typical of saturated zone water. Ca^{2+} dominates over Na^+ in about half the unsaturated zone waters analyzed from Yucca Mountain [Figure 4-2(A)]. Potassium is also elevated in unsaturated waters from Yucca Mountain relative to the saturated zone, ranging from 1×10^{-4} to 4×10^{-4} molal (Yang et al., 1988; Yang, 1992), and shows a rough correlation with calcium.

Geologic and geochemical data indicate that Ca^{2+}, Mg^{2+}, and possibly Cl^- in Yucca Mountain groundwaters are derived partially or dominantly from sources other than the tuffs. The source of Ca^{2+} is likely to be the prevalent near-surface caliche zone at Yucca Mountain, which is rich in calcite ($CaCO_3$). A likely origin of the calcium near the surface is widespread exposures of Paleozoic rocks in the region, some of which are dominantly or partially calcite and/or dolomite [$CaMg(CO_3)_2$]. Dust particles derived from carbonates and other exposed rocks can be transported by wind and deposited on the ground surface elsewhere. Aeolean deposited calcium carbonate dust would rapidly dissolve in meteoric water. Dissolved calcium bicarbonate would be transported into and through the soil-zone by infiltrating water generating caliche, which is characteristic of the soil-zone at Yucca Mountain. Water that enters the deeper vadose zone from the soil-zone would be expected to be saturated with respect to calcite. Magnesium is also low in unaltered tuffs of Yucca Mountain and enriched by several times in altered tuffs (Table 4-1), and may be supplied similarly by dissolution of dolomite deposited at the surface. The concept of recharge waters initially enriched with calcium and magnesium is supported by data showing that calcium and magnesium concentrations generally decrease with depth in waters extracted from core taken in the unsaturated zone at Rainier Mesa (White et al., 1980). Introduction of calcium from the ground surface is also consistent with generally decreasing calcium contents of secondary clinoptilolite with depth at Yucca Mountain (Broxton et al., 1986). Also, the relatively large range of calcium contents of the natural groundwaters from the vicinity of Yucca Mountain is consistent with varying amounts of input from different sources. However, these sources could also include water from the Paleozoic carbonate aquifer underlying tuffaceous rocks at Yucca Mountain.

4.2.5.9 Minor Components: Al, Fe, Sr, Mn

Young (1972) and Daniels et al. (1982) provide data for minor aqueous species from a subset of wells in the vicinity of Yucca Mountain that tap saturated zone water, and Yang et al. (1988) report data for a few minor species in water squeezed from rocks from the unsaturated zone at Yucca Mountain. Data for aluminum, iron, strontium, and manganese are of particular interest. Measured aluminum concentrations in saturated zone groundwaters are in the range of 0.6×10^{-6} to 5×10^{-6} molal, and appear to be compatible with the solubility of analcime (see Section 3 of this report).

Iron concentrations range from 0.2×10^{-6} to 4×10^{-6} molal in saturated zone waters and similarly from 0.1×10^{-6} to 2×10^{-6} molal in unsaturated zone waters. Iron concentrations are critical to evaluating reported thermodynamic data for clinoptilolite (see Section 3.10 of this report). The solubility of iron increases by orders of magnitude in reducing conditions, which could occur locally around metallic waste packages, and waste packages could be a source of iron. A common alteration product of metallic iron is magnetite, which may provide local constraints on iron concentrations in the near field.

Strontium concentrations in saturated zone groundwaters have been measured at 0.3×10^{-6} to 1.2×10^{-6} molal and at significantly higher values from 6×10^{-6} to 17×10^{-6} molal in unsaturated zone waters. Also, like calcium and magnesium, altered rocks at Yucca Mountain are enriched in strontium. For example, unaltered vitrophyre of the Topopah Spring Tuff from borehole USW G-1 contains less than 760 ppm Sr, whereas smectite- and zeolite-rich vitrophyric rock taken less than 10 m higher in the section contains 1,650 ppm Sr (Broxton et al., 1986). These differences are analogous to those of other alkaline earth cations, calcium and magnesium, and indicate similar external sources for strontium.

Measured manganese concentrations in oxidizing saturated zone waters at Yucca Mountain range over at least two orders of magnitude up to about 4×10^{-6} molal. In unsaturated zone waters from Yucca Mountain, manganese concentrations also vary by an order of magnitude or more up to 1.3×10^{-6} molal. Manganese concentrations are probably limited by the solubility of secondary manganese oxides, which have widespread occurrences and great variability at Yucca Mountain. The distribution of manganese oxide minerals depends in part on their disposition relative to the water table. Only rancieite and lithiophorite have been observed above the water table, and aurorite, pyrolusite, todorokite, and cryptomelane occur only below the water table (Carlos et al., 1993).

4.2.6 Construction of a Quantitative Geochemical Model for the Natural System

The general summary of the geochemical system at Yucca Mountain presented in preceding sections provides a basis for development of simplified scenarios for dominant gas-water-rock interactions that may be implemented in quantitative, and to some extent predictive, reaction-path models. Geochemical models for repository systems possess a degree of validity only when shown to be compatible with data from site characterization. Therefore, modeling of the ambient geochemical and mineralogical system at a site is a prerequisite for valid simulations of repository-induced perturbations to the system.

A reaction-path simulation of the evolution of groundwater and mineral chemistry at Yucca Mountain requires a conceptual model for the initial water chemistry and the set of reactions that affect the system. Previously reported conceptual and numerical models for groundwater and mineral chemistry

at Yucca Mountain and similar environments (Benson, 1976; White et al., 1980; Kerrisk, 1983; Murphy, 1994) have generally invoked dissolution of primary unstable materials such as volcanic glass, and growth of products such as smectite and zeolite as basic controls. This framework is adopted in the present study with the additional recognition that interactions between source water (i.e., rainfall) and caliche and/or dust deposited at the ground surface have an important effect.

To facilitate comparisons of model results with the saturated zone groundwater compositions, which are relatively well characterized, the model is constructed to constrain several aspects of water chemistry to be similar to analyzed waters from the saturated zone in the vicinity of Yucca Mountain. Initial water chemistry is fixed in the model to contain 2×10^{-4} molal NaCl to yield a chloride content typical of tuffaceous groundwaters in the vicinity of Yucca Mountain. The CO_2 pressure is buffered at $10^{-2.2}$ bar throughout the reaction-path simulation. Saturated zone groundwaters have CO_2 fugacities close to this value. All groundwater samples analyzed from tuffaceous aquifers contain elevated silica concentrations and appear to be buffered at approximately 8×10^{-4} molal aqueous silica. Water chemistry in the natural system model is fixed at this value, and solutions are assumed to maintain metastable supersaturation with respect to silica polymorphs of lower solubility. The initial water is also taken to be saturated with calcite providing an external source of calcium to the system.

For simplicity, only dominant elements and those required for dominant water-rock reactions are included in the model. These are sodium, potassium, calcium, aluminum, silicon, carbon, chlorine, hydrogen, and oxygen. Magnesium, iron, manganese, fluorine, nitrogen, and other components are eliminated, and no oxidation-reduction reactions are included in the model. A temperature of 30 °C was selected because it corresponds closely to water at depth in the vadose zone and near the top of the saturated zone. Using these constraints, an equilibrium model for the initial aqueous solution can be computed with EQ3 (Wolery and Daveler, 1992; see Appendix C). This computation yields a model solution with Ca^{2+} and HCO_3^- contents of 1.3×10^{-3} and 2.55×10^{-3} molal, respectively, at a pH of 7.42. These appear to be realistic values for solutions exiting the soil-zone.

The primary solid reactant in the model is taken to have the composition of an intermediate alkali feldspar with the composition $Na_{0.44}K_{0.56}AlSi_3O_8$. Together with silica, this feldspar closely represents the bulk composition of the primary rock at Yucca Mountain. Therefore, from the standpoint of chemical mass transfer, dissolution of this phase in a solution buffered with silica is comparable to dissolution of primary volcanic glass. Feldspar dissolution kinetics do not give a fair representation of glass alteration rates. Although the model as constructed gives a fairly good representation of mass transfer due to glass alteration, no kinetic interpretation is given for the natural system model.

The mass transfer model for the genesis and evolution of groundwaters like those at Yucca Mountain consists of irreversible dissolution of the alkali feldspar analog of volcanic glass in water with the initial composition described previously, coupled with reversible growth of a secondary stable or metastable solid phase assemblage. Dominant secondary minerals in the upper diagenetic levels of Yucca Mountain are clinoptilolite, mordenite, and smectite. Calcite also occurs in many horizons. Uncertainty in thermodynamic data does not permit a reasonable distinction to be made between clinoptilolite and mordenite for modeling purposes. Therefore, clinoptilolite and mordenite can be considered equivalent in the model. This set of minerals is permitted to precipitate in the model when solutions are calculated to be saturated with respect to them. Chemical formulas of all minerals included in the model are given in Table 4-2. Reaction-path computations were performed using the EQ3/6 software package (Wolery and Daveler, 1992; see Appendix C).

Table 4-2. Reactants and products in reaction-path models

Reactants		Products	
Alkali Feldspar	0.54 $KAlSi_3O_8$ + 0.46 $NaAlSi_3O_8$	Clinoptilolite	$CaAl_2Si_{10}O_{24}\cdot 8H_2O$ $Na_2Al_2Si_{10}O_{24}\cdot 8H_2O$ $K_2Al_2Si_{10}O_{24}\cdot 8H_2O$
Cristobalite (heated repository model only)	SiO_2	Smectite	$Na_{0.33}Al_{2.33}Si_{3.67}O_{10}(OH)_2$ $K_{0.33}Al_{2.33}Si_{3.67}O_{10}(OH)_2$ $Ca_{0.165}Al_{2.33}Si_{3.67}O_{10}(OH)_2$
		Calcite	$CaCO_3$

Uncertainties in thermodynamic and kinetic properties, variations in stoichiometries of secondary clinoptilolite and smectite, and limitations of solid solution modeling capabilities in EQ6 require several assumptions and approximations to be invoked in the model. Theoretically based estimates for standard state properties of endmember smectites are taken from the EQ3/6 database (Wolery and Daveler, 1992). For clinoptilolite, theoretical estimates from Kerrisk (1983) are employed with one exception. Preliminary studies using the estimated data showed the modeled secondary clinoptilolite to be unrealistically dominated by the potassium component. Therefore, the equilibrium constant for the dissolution reaction for this component was increased by a factor of 10 relative to the value estimated by Kerrisk (1983). With this modification, the range of compositions of secondary clinoptilolites computed in the model corresponds reasonably to that observed at Yucca Mountain. Smectite and clinoptilolite are represented as ideal three component solid solutions of endmember components in the model. Given uncertainties in the standard state properties of these minerals, the suite of other model uncertainties and approximations, and the small excess energies of mixing (see Section 2 of this report), this approximation is justified. Therefore, in the set of models presented in this section, data for the ternary clinoptilolite are not fully compatible with data generated in Section 2 of this report for binary solid solutions. Nevertheless, the value for Na-clinoptilolite estimated by Kerrisk (1983) and used in the models is consistent with the provisional value for Na-clinoptilolite solubility as reported in Section 3.8 of this report. Refinement of models for clinoptilolite solutions of three or more components to incorporate data from binary exchange reactions is an apparent area for future research (e.g., Viani and Bruton, 1992).

Lack of understanding of detailed reaction mechanisms and kinetic data prompts an additional assumption that secondary minerals maintain continuous equilibrium with aqueous solutions. Although it is apparent from natural mineral heterogeneities that ideal equilibrium conditions are not attained in the natural system, this approximation is commonly invoked and accepted in modeling water-rock interactions. It tends to be justified, in the natural system model for Yucca Mountain, by the long time periods available for equilibration, the slow alteration rates of primary phases, and the large surface areas of fine grained secondary minerals. Continuous homogeneous equilibrium within the aqueous phase and between gas and aqueous phases is also assumed in the model, which is a good assumption given the rapidity of the relevant reactions and the absence of important oxidation-reduction processes in the natural inorganic system.

4.2.7 Natural System Model Results

Modeled evolution of the system as a function of reaction progress primarily involves variations in the compositions of the aqueous solution and continuous formation of secondary clinoptilolite in response to dissolution of feldspar. The solution remains slightly undersaturated with respect to calcite. At very advanced stages of reaction the solution becomes saturated with a smectite solid solution that precipitates along with clinoptilolite.

The absence of calcium in the reactant assemblage requires the initially high aqueous calcium concentration to decrease as calcium is incorporated in secondary clinoptilolite. The decrease in aqueous calcium with increasing reaction progress is a useful monitor to illustrate variations in model aqueous solution composition (Figures 4-3 and 4-4). The sodium concentration increases progressively with reaction progress, which is consistent with the general hydrogeological observation that sodium introduced in natural groundwater systems remains in solution and reflects the "maturity" of groundwater. Modeled potassium concentrations initially increase due to dissolution of alkali feldspar (representing volcanic glass) to maximum values near 2×10^{-4} molal. However, as the aqueous solution becomes depleted in calcium, secondary clinoptilolite incorporates an increasing amount of potassium, and the aqueous potassium concentration diminishes. The pH and aqueous silica and bicarbonate concentrations remain at nearly constant values because of the silica and CO_2 pressure buffers imposed in the model and because the dominant reactions of alkali feldspar components and silica to clinoptilolite, for example

$$2\ Na_{0.5}K_{0.5}AlSi_3O_8 + 4SiO_2 + 8H_2O + K^+ \rightleftharpoons K_2Al_2Si_{10}O_{24}\cdot 8H_2O + Na^+ \qquad (4\text{-}3)$$

and

$$2\ Na_{0.5}K_{0.5}AlSi_3O_8 + 4SiO_2 + 8H_2O + Ca^{2+} \rightleftharpoons CaAl_2Si_{10}O_{24}\cdot 8H_2O + Na^+ + K^+ \qquad (4\text{-}4)$$

do not consume protons. However, as aqueous calcium drops to low concentrations and aqueous sodium becomes increasingly concentrated, the solution becomes saturated with a sodium-rich smectite. Incongruent dissolution of feldspar and precipitation of smectite consumes protons, for example, according to the reaction

$$2.33\,Na_{0.5}K_{0.5}AlSi_3O_8 + 2H^+ \rightleftharpoons Na_{0.33}Al_{2.33}Si_{3.67}O_{10}(OH)_2 + 0.835\,Na^+ + 1.165\,K^+ + 3.32\,SiO_2 \qquad (4\text{-}5)$$

Initiation of smectite precipitation causes a discontinuity in the trend of evolution of the aqueous solution. Bicarbonate and pH increase as carbonic acid is consumed.

The reaction-path model reasonably represents observed ranges and relative variations of major groundwater components of the saturated zone tuffaceous aquifer at Yucca Mountain (Figures 4-3 and 4-4). Computed clinoptilolite compositions also correspond well to those observed at Yucca Mountain, particularly for diagenetic zone II in the Topopah Spring basal vitrophyre (Broxton et al., 1987). The absence of calcite precipitation is consistent with its sparse occurrence in tuffs at Yucca Mountain, particularly in the Topopah Spring Tuff (Bish and Chipera, 1989), and general undersaturation with

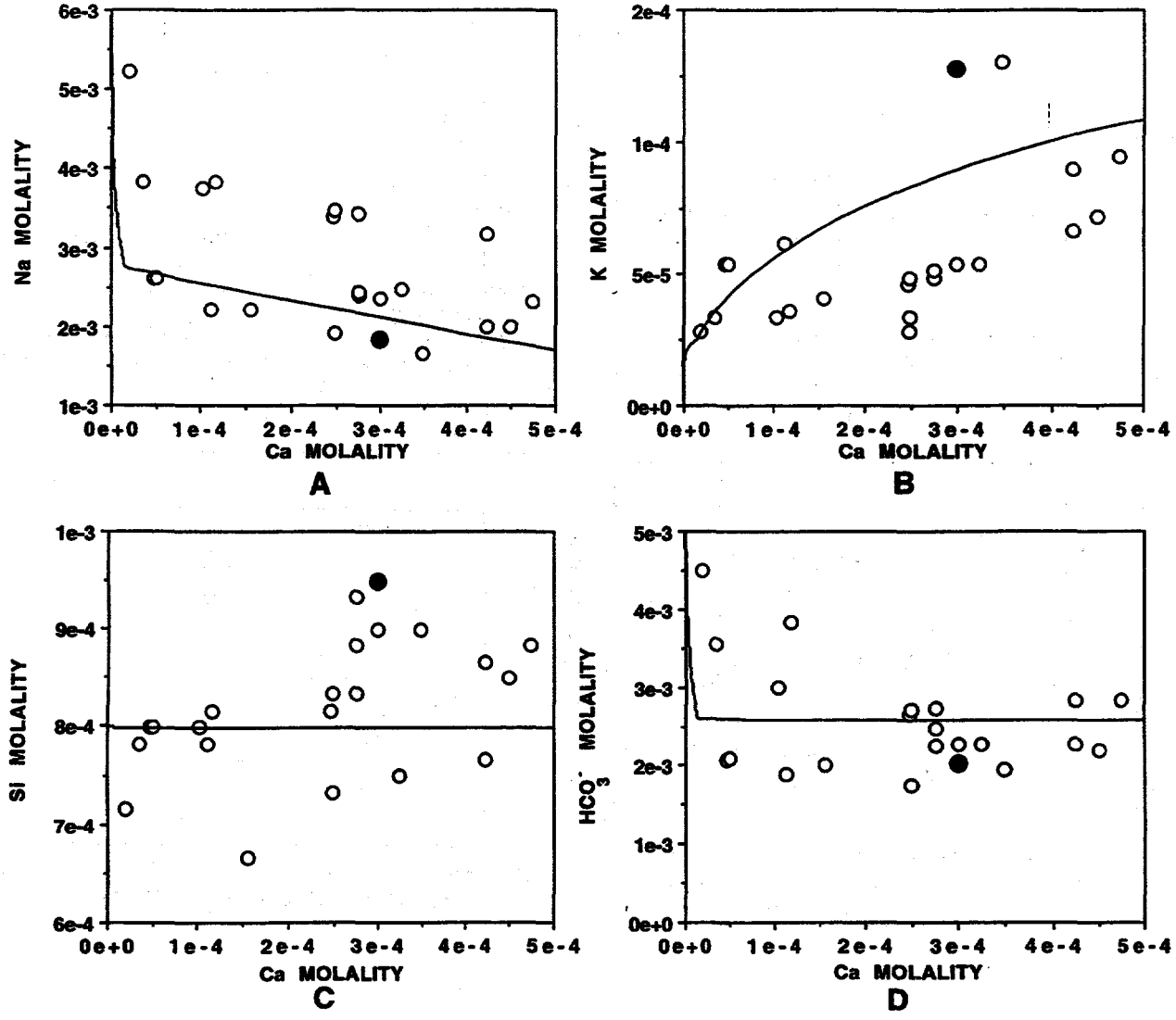

Figure 4-3. Isothermal reaction-path model results and analytical solution compositions. Aqueous concentrations of Na (A), K (B), Si (C), and HCO_3^- (D) are shown as functions of the concentration of Ca. Lines result from the isothermal reaction path model described in the text. Calcium is a measure of reaction progress, decreasing with increasing reaction in the simulation. Circle symbols represent groundwater compositions from the saturated tuffaceous aquifer at Yucca Mountain; water from the J-13 well is indicated by solid symbols (Kerrisk, 1987).

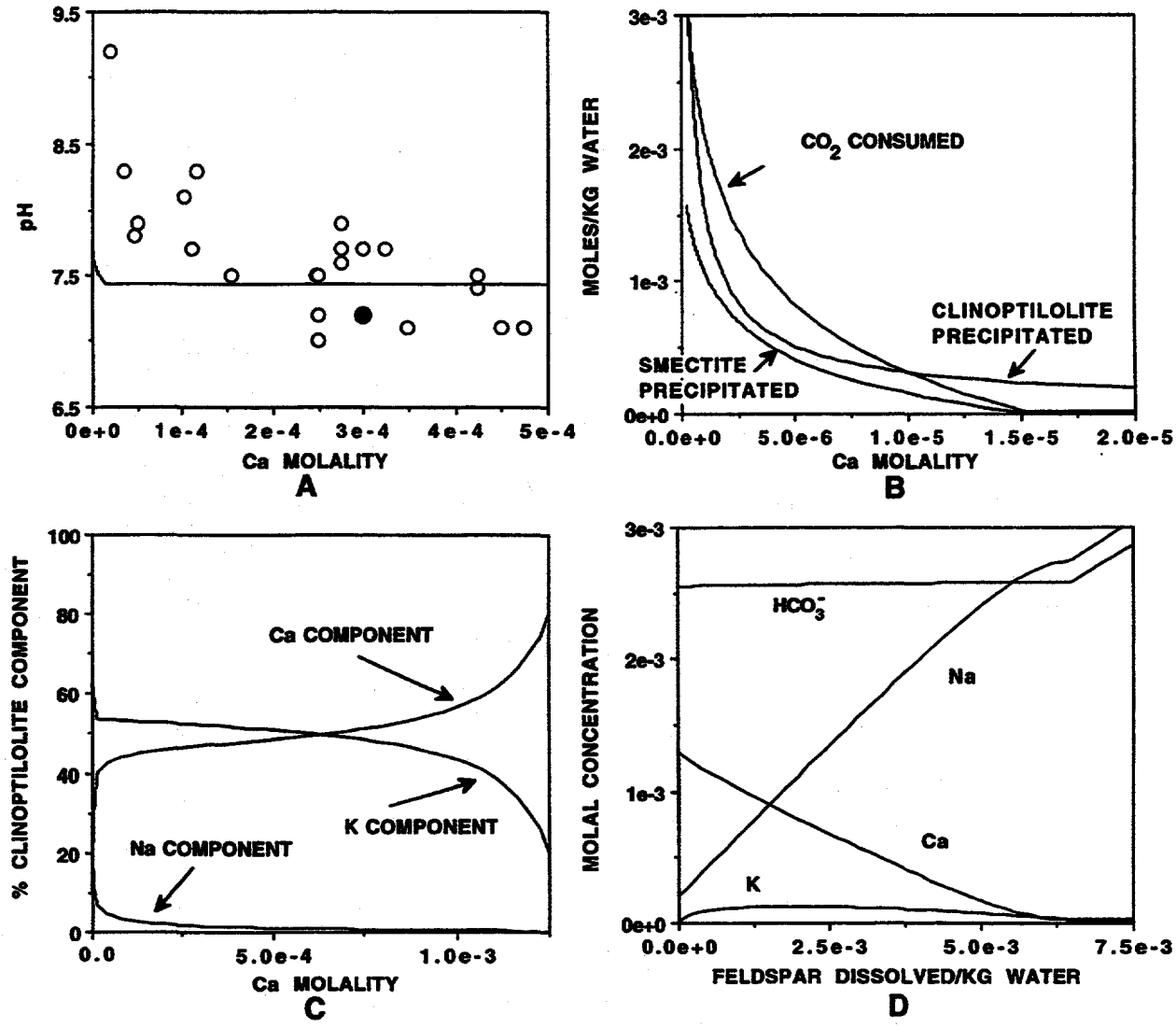

Figure 4-4. Isothermal reaction-path model results. Solution pH (A), moles of secondary minerals (B), and secondary clinoptilolite (C) are shown as functions of the concentration of Ca. Calcium is a measure of reaction progress, decreasing with increasing reaction in the simulation. Circle symbols (A) represent groundwater compositions from the saturated tuffaceous aquifer at Yucca Mountain; water from the J-13 well is indicated by a solid symbol (Kerrisk, 1987). Moles of aqueous species (D) are shown as a function of the moles of dissolved feldspar, which increases with reaction progress. Lines result from the isothermal reaction path model described in the text. Note that the x-axis scales differ among the figures.

respect to calcite of the saturated zone tuffaceous aquifer groundwaters at Yucca Mountain. Smectites in the unsaturated zone at Yucca Mountain are commonly rich in sodium (Bish, 1989), which is also consistent with model results.

Some features of the natural geochemical system are only approximately represented by the model, such as the inverse relation between pH and calcium content of groundwater, and the positive correlation between aqueous sodium and bicarbonate. The model indicates that evolved aqueous solutions are close to equilibrium with respect to potassium feldspar, kaolinite, pyrophyllite, and mesolite, and significantly supersaturated with respect to quartz and stilbite. In part, calculated supersaturations with respect to aluminosilicate minerals may be a consequence of errors in estimated data for clinoptilolite, which is the aluminum-bearing mineral modeled to be at equilibrium with the solutions. Near-saturation with respect to potassium feldspar and kaolinite is reasonable as both are secondary mineral products at Yucca Mountain. Mesolite is an uncommon mineral in silicic tuffaceous rocks so its elimination from the model is reasonable. Slight saturation with respect to pyrophyllite may be a consequence of inaccurate thermodynamic data at low temperature for that mineral, which normally forms at elevated temperatures in metamorphic rocks that are poor in alkali metals. It does not occur in the low-temperature, alkali metal-rich diagenetic system at Yucca Mountain. Strong supersaturation with respect to stilbite, a zeolite solid solution of nominal fixed composition in the EQ3/6 database ($Ca_{1.019}Na_{0.136}K_{0.006}Al_{2.81}Si_{6.92}O_{18}\cdot 7.33H_2O$), may be an indication of incompatibility of tabulated thermodynamic data for this mineral with data for other minerals. Stilbite commonly occurs in hydrothermally altered mafic rocks unlike the silicic rocks at Yucca Mountain. Model waters are undersaturated with respect to analcime, and calculated aqueous aluminum concentrations are significantly below those measured in the Yucca Mountain vicinity (see Section 3.10). This discrepancy also points to uncertainties in aluminosilicate properties and phase relations in the natural system. Despite good correspondence between many model results and observations of the natural system, evident areas for model and database refinements persist.

The design and calibration of the model for the natural geochemical system are strongly based on site data, including the conceptual basis for the model, the components and phases included in it, initial conditions, system buffering, and even the thermodynamic properties of secondary clinoptilolite. Natural open-system behavior is approximated by CO_2 buffering and the initially elevated calcium concentration in solution with progressive mass transfer of calcium to secondary minerals. This process of model calibration contributes to the good correspondence between model results and natural system data. The model, however, is not intended to be a specific representation of the evolution of any particular groundwater sample. Neither does the model address the amount, spatial distribution, or timing of alteration that characterize natural open-system processes. Rather, it is a hypothetical ensemble of plausible and generally observed geochemical processes that are quantitatively integrated using principles of reaction-path chemistry and an established thermodynamic database. It can be regarded as a partially validated, although imperfect, quantitative representation of dominant chemical reactions that characterize the evolution and status of the natural gas-water-rock system at Yucca Mountain. Its principal utility is in testing conceptual models for the chemical evolution of the gas-water-rock system, for testing the applicability of thermodynamic data, and for construction of predictive models that may be useful in performance assessments for a nuclear waste repository.

4.3 HEATED REPOSITORY MODEL

4.3.1 Geochemical Scenario for a Heated Repository Environment

Heating Yucca Mountain by emplacement of radioactive wastes would alter the geochemistry with important potential impacts on repository performance. Geochemical variations would result notably from thermohydrological effects on fluid flow, fluid flow effects on mass distribution, and thermodynamic and chemical kinetic effects on mass transfer among phases. In a heated unsaturated repository, water would vaporize with elevating temperatures, water vapor would be transported by gas flow, and water would condense with decreasing temperatures, for example, in cooler areas. Vaporization would continue to completion in areas where temperatures exceed the boiling point and even at lower temperatures depending on moisture fluxes. Complete vaporization would result in precipitation of salts and scale. Gas would flow in response to thermal buoyancy and pressure gradients due to vaporization and condensation, and as a consequence of multicomponent gaseous diffusion. Liquid water would flow in response to suction pressure gradients and gravity. Thermodynamic properties of fluid and solid phases vary as a function of temperature, which would stimulate chemical reactions among components in gas, liquid, and solid phases. Chemical reaction rates generally increase with increasing temperature and depend strongly on the presence or absence of water and variations in water chemistry.

The repository environment would differ from most natural geological systems because variations in temperature would occur on a relatively short time scale relative to metamorphic or major hydrothermal systems, but on a long scale relative to most volcanic or hypabyssal systems. The near field would heat rapidly to maximum temperatures and then cool continuously. With increasing distance in the far field, temperature would increase over progressively longer periods of time to progressively lower maximum values and then cool slowly. Continual variations in temperature (and fluid fluxes and fluid compositions and liquid saturation states) would have important consequences for the geochemical system. Reaction progress for slow chemical reactions would be governed predominantly by chemical kinetics and would lag behind evolving theoretical equilibrium states. Fast reactions would tend to maintain states close to transient local equilibrium conditions.

Fluid chemistry would be expected to change readily with changes in thermal conditions because most reactions among aqueous species and between liquid and gas phases are rapid. Water chemistry changes would include increases in concentration of dissolved species due to vaporization of water or dilution due to condensation. Increasing fractionation of CO_2 into the gas phase with increasing temperature would lead to increases in pH (Arthur and Murphy, 1989) and variations in mineral paragenesis (Criscenti and Arthur, 1991). Accelerated dissolution of glass and other minerals would tend to increase aqueous concentrations of soluble species. Variations in mineral-solution ion exchange equilibria with temperature, for example, involving zeolites, would be likely to affect dissolved cation ratios.

Two likely changes to the mineralogical system at Yucca Mountain due to repository heating would be precipitation of calcite and partial alteration of zones of bedded tuffs composed of glass to secondary minerals such as zeolites. Calcite precipitation would be motivated by: (i) its retrograde solubility, (ii) the decreasing solubility of CO_2 in water with increasing temperature and the consequential rise in pH, and (iii) concentration of solutions by evaporation. Transient calcite precipitation due to heating may occur over widespread areas of the mountain over long time periods (Codell and Murphy, 1992). Alteration of volcanic glass is the dominant diagenetic process that has occurred naturally at Yucca

Mountain, and additional alteration would be likely to be provoked by heating and heat induced fluid circulation. Other important reactions are also possible, notably dehydration of pre-existing hydrated minerals, including zeolites, and alteration of more hydrous minerals to less hydrous minerals (e.g., alteration of clinoptilolite to analcime plus silica). Also, abundant metastable silica polymorphs in the natural system (e.g., opal, cristobalite, and tridymite) could alter to more stable phases (e.g., quartz). Mineralogical changes would in turn have potential effects on fluid flow and retardation of radionuclide migration as well as on water chemistry.

Recirculating water could cause significant disruption to the mineralogical system and the hydrologic properties of a heated environment at Yucca Mountain. Major effects are observed in natural hydrothermal systems, which are, however, generally of much larger scale and duration than anticipated perturbations at Yucca Mountain. Liquid condensates are likely to be chemically aggressive due to their distilled and slightly acidic (dilute carbonic acid) character. However, fairly limited reaction with silicate phases would generate relatively stable dilute solutions characteristic of fresh groundwater systems in tuffaceous rocks even at somewhat elevated temperatures. Also, complete vaporization of water would lead to formation of salts and scale. However, desiccation of the system would arrest most mineralogical transformations because their rates, even at repository temperatures, are negligibly slow in the absence of water. Detailed analyses of the complex consequences of the coupling of two-phase fluid flow and chemical reactions are poorly developed at this time, and are beyond the scope of numerical modeling in this study.

Interactions of natural and engineered materials could also have strong impacts on geochemistry, particularly in the near field. However, these interactions are also beyond the scope of modeling exercises in this report, which focuses on theoretical characterization of the natural system and its perturbations due to thermal loading.

4.3.2 Construction of a Geochemical Model for the Heated Repository

Construction of a quantitative model for the evolution of the heated repository requires general consideration of the complex coupled processes noted in the preceding section, and abstraction of important processes that can be incorporated feasibly in numerical simulations. The strategy adopted in this study is to neglect certain processes and to couple others sequentially. The objective of this effort is to generate simulations that provide insight into the processes that are likely to occur and their possible impacts on repository performance, and to develop and test components of more comprehensive models for the repository. Aspects of the problem that require more detailed examination and model and code development can be identified by this effort.

The following model structures are adopted. The chemical system is simplified to incorporate only major components of the natural system and essential components of important reactions, using the natural system model described in Section 4.2.7 as a basis. Engineering materials are assumed not to impact the system. Detailed consideration is made of the evolution of the gas-water-rock system at one representative point located 75 m above a hypothetical repository. Temperature is assumed to vary continuously according to a transient model for conductive heat flow. For SCP design thermal loading of 57 kW/acre (U.S. Department of Energy, 1988) and heat transfer by conduction, the temperature at the 75-m point is predicted to rise to approximately 78 °C over a period of 900 yr, and then to decrease slowly during subsequent millennia (Figure 4-5). Complete vaporization would not be expected at this point, and the model assumes a constant mass of liquid water. Effects of diffusion of chemical species, liquid flow, and evaporation/condensation of water are neglected as a simplification.

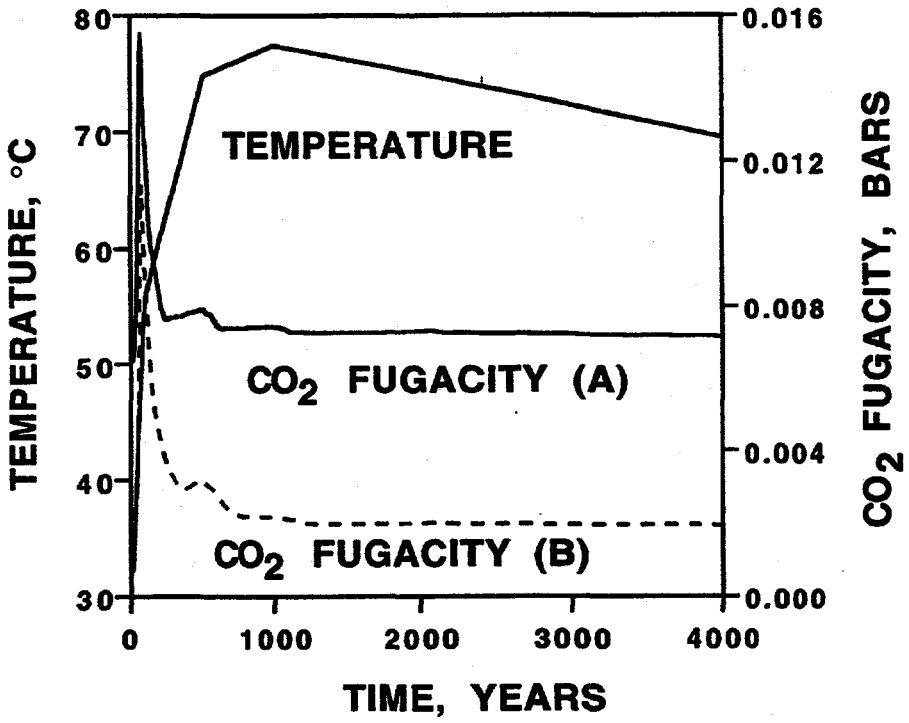

Figure 4-5. Model temperature and CO_2 fugacity at a point 75 m above the repository horizon as a function of time (Codell and Murphy, 1992). CO_2 fugacity shown as curve A was used in the heated repository model; CO_2 fugacity shown as curve B was used in sensitivity tests (Section 4.3.4).

Gas flow and open-system behavior is manifested in the heated repository model by assuming that the local CO_2 fugacity is controlled externally. Variable CO_2 fugacity is based on results of an independent gas flow and carbon system geochemical model (Codell and Murphy, 1992). The carbon system model includes simplified chemistry assumed to maintain local equilibrium. The carbon system geochemical model is coupled to a schematic model for uniform, vertical gas flow in one dimension, which was abstracted from results of more detailed thermohydrological modeling. CO_2 is considered to be transported in the gas phase and to interact at equilibrium with the local geochemical system. The carbon system model predicts complex temporal and spatial variations in CO_2 pressures and widespread precipitation and subsequent dissolution of calcite. It also predicts that a pulse of CO_2-rich gas is generated by an initial purge of CO_2 from the aqueous system in the near field. This pulse rises in the gas phase at a retarded velocity and eventually exits the system (Codell and Murphy, 1992). At a point 75 m above the repository horizon, the CO_2 pressure rises initially as the CO_2 pulse moves through the point over the first 250 yr. Subsequently, the CO_2 pressure stabilizes at an elevated level due to the increased temperature of the repository as shown in curve A of Figure 4-5.

Time- and temperature-dependent CO_2 buffering is accomplished computationally for the heated repository model by defining a fictive single-component phase with thermodynamic properties as a function of temperature that correspond to the CO_2 fugacities derived from the simple carbon system model. Forcing the system to maintain continuous equilibrium with the fictive phase buffers the CO_2 fugacity at values that vary with time and temperature (see Appendix C). A variation of this EQ6 technique was described previously for systems of constant gas fugacity (Delany and Wolery, 1984).

Primary reactants in the heated repository model comprise the alkali feldspar of intermediate composition used in the natural system model and cristobalite, which are close representations of the natural primary mineralogy in the devitrified Topopah Spring Tuff. Sources of thermodynamic data are the same as those used for the natural system model. As in the natural system model, clinoptilolite and smectite solid solutions and calcite are the only secondary minerals permitted to form. The chemical system in the heated repository system is modeled to respond continuously to perturbations in temperature and CO_2 fugacity using EQ6 (Wolery and Daveler, 1992; see Appendix C). Primary minerals dissolve (or precipitate) irreversibly. Unlike the natural system model in which the aqueous silica concentration is buffered, cristobalite is also assumed to dissolve irreversibly in the heated repository model. However, formation of more stable silica polymorphs, for example, quartz, is suppressed. Reactions among aqueous and gas species and secondary minerals are assumed to be adequately described by relations for local equilibrium as a function of temperature. Secondary silicates are treated as ideal, homogeneous solid solutions with compositions that vary in time. The initial water and mineral chemistries and relative abundances for the nonisothermal model are based on natural system model results illustrated in Figures 4-3 and 4-4 at reaction progress corresponding to 4×10^{-3} moles of feldspar dissolved (per kilogram of water) and an aqueous calcium concentration of 3×10^{-4} molal. System characteristics at this stage of the model represent a rough average of the range of water compositions illustrated in Figures 4-3 and 4-4.

Results of the carbon system reaction and transport model (Codell and Murphy, 1992) and the multicomponent local reaction-path model are linked through the time parameter. Elapsed time is computed in the EQ6 reaction-path model by integrating rate equations for the rate-limiting steps, which are irreversible dissolution of feldspar and cristobalite (see Appendix C). Dissolution rate expressions and kinetic data derived from laboratory experiments were taken from the literature (Table 4-3). Unlike the natural system model where feldspar and silica were treated as proxies for volcanic glass, the heated repository model explicitly includes feldspar and cristobalite, which are the dominant minerals in the area surrounding the repository horizon. The relative dissolution rate constants for cristobalite and feldspar and the dependence of reaction rates on pH, temperature, and solution composition are likely to be reasonably represented by the kinetic formulations for conditions that are far from equilibrium. However, significant uncertainty exists with regard to reactive surface areas in the Yucca Mountain system, reaction mechanisms, and rate expressions, especially under conditions that are relatively close to equilibrium. For example, experimentally determined dissolution rate constants are commonly greater than those deduced from field observations (Brantley, 1992). Hence, relatively small reactive surface areas were selected for the simulations (Table 4-3). Sensitivity of model results to variations in rate parameters is explored in Section 4.3.4.

4.3.3 Heated Repository Model Results

Heated repository model results are shown in Figure 4-6. Elevated temperatures promote feldspar dissolution, and secondary growth of clinoptilolite and smectite. Precipitation of calcite occurs because of its retrograde solubility and the increase in solution pH. However, the mass of calcite precipitation is limited by the supply of calcium. The initial increase in CO_2 pressure causes a transient decrease in pH from 7.45 to 7.2. The pH then increases over 4,000 yr toward a value of 8 because of continuous bicarbonate production accompanying incongruent alteration of feldspar to smectite. As the temperature increases, the solution almost immediately becomes undersaturated with respect to cristobalite, which thereafter dissolves. The silica concentration reaches a maximum value at about 1,000 yr corresponding approximately to the time the maximum temperature is achieved. The solution remains close to equilibrium with cristobalite, and almost no cristobalite dissolves. Smectite retains a calcium-rich

Table 4-3. Rate expressions and parameters

RATE EXPRESSIONS (Helgeson et al., 1984)

$$\frac{d\xi}{dt} = \sum \left\{ ks(a_{H^+})^n \left[1 - \exp\left(\frac{-A}{RT}\right) \right] \right\} \qquad \frac{d \ln (k/T)}{d(1/T)} = \frac{-\Delta H^{\ddagger}}{R}$$

(summation over parallel mechanisms)

ξ	reaction progress variable (moles dissolved per kg H_2O)	n	reaction order with respect to aqueous H^+
t	time	A	chemical affinity for dissolution reaction
k	apparent rate constant	R	gas constant
s	surface area per kg H_2O	T	absolute temperature
a_{H^+}	aqueous H^+ activity	$\Delta H^{\ddagger}$	activation enthalpy

RATE PARAMETERS

Mineral	k	$\Delta H^{\ddagger}$	n	s
	$\frac{moles}{cm^2 s}$	$\frac{kJ}{mole}$		$\frac{cm^2}{kgH_2O}$
Alkali Feldspar (Helgeson et al., 1984; Knauss and Wolery, 1986; Murphy and Helgeson, 1989)				200
Mechanism 1	3.00×10^{-16}	35.3	0.0	
Mechanism 2	2.51×10^{-19}	32.1	−0.4	
Cristobalite (based on data for quartz) (Knauss and Wolery, 1988; Murphy and Helgeson, 1989)				100
Mechanism 1	1.58×10^{-18}	75.3	0.0	
Mechanism 2	5.01×10^{-21}	105.8	−0.5	

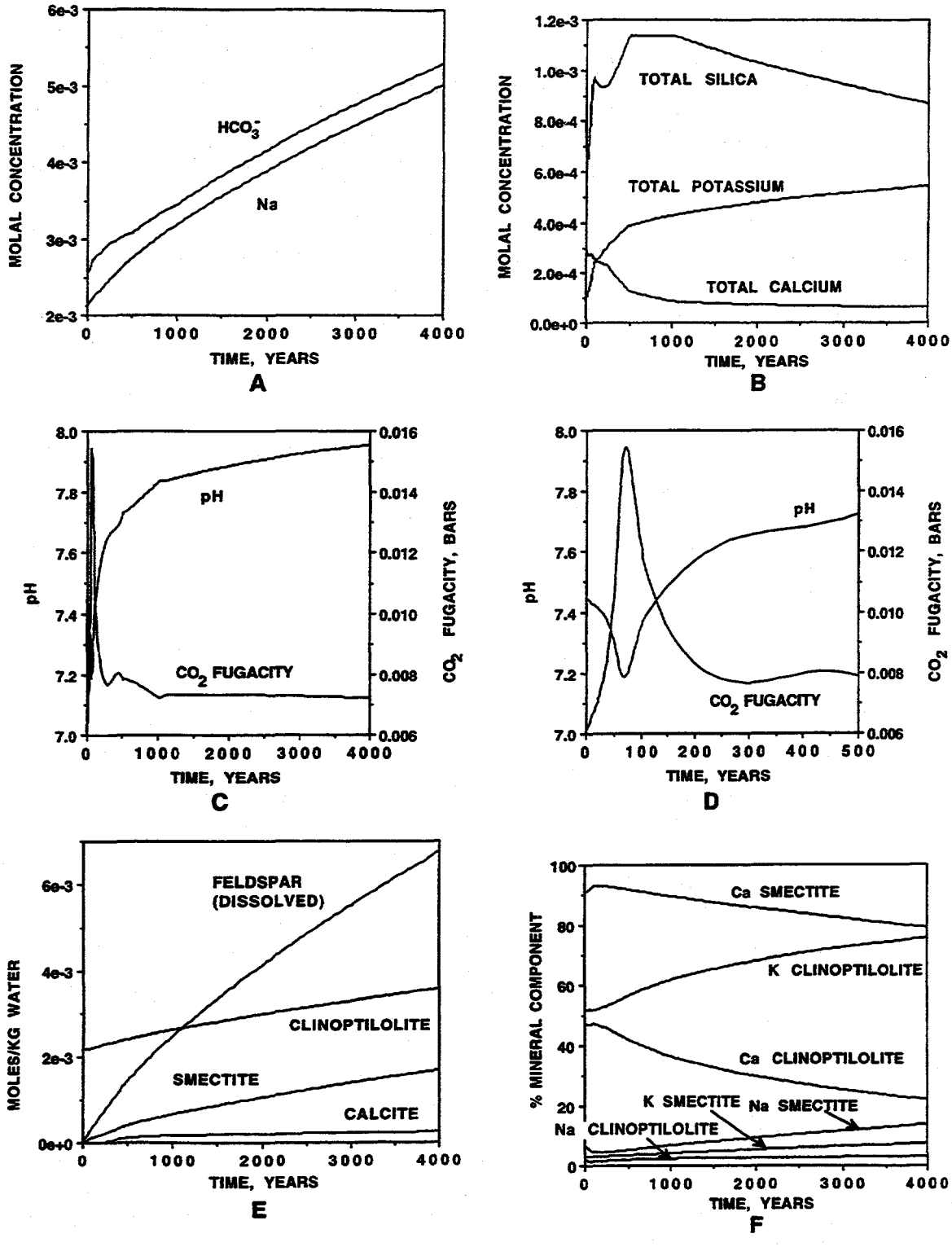

Figure 4-6. Heated repository model results for the aqueous (A, B, C, D) and mineral systems (E, F) as a function of time

composition throughout the simulation. The initial clinoptilolite has an intermediate potassium and calcium composition, but transforms toward lower calcium contents as calcium is consumed by smectite and calcite precipitation, and the aqueous solution evolves toward higher ratios of sodium and potassium to calcium. The aqueous solution becomes increasingly dominated by sodium bicarbonate, the concentration of which roughly doubles over 4,000 yr, increasing ionic strength to 5.7×10^{-3} molal. Simulated volumes of dissolved and precipitated minerals correspond to a small fraction of the water-filled porosity. Approximately 4 cm^3 of feldspar dissolves per 1,000 cm^3 of liquid water over 4,000 yr in the simulation, and is accompanied by precipitation of approximately 2 cm^3 of clinoptilolite, 1.5 cm^3 of smectite, and 0.1 cm^3 of calcite. Modeled solutions become supersaturated with the same set of minerals described for the natural system model in Section 4.2.7: silica minerals, potassium feldspar, stilbite, and mesolite. However, solutions are calculated to be supersaturated with muscovite rather than pyrophyllite at the elevated temperatures. Greater uncertainty attends the heated repository model results because they are relatively unconstrained relative to the natural system model.

4.3.4 Heated Repository Model Sensitivity to Reaction Rates and CO_2 Pressures

The product of the rate constant and surface area for feldspar and cristobalite reactions has a likely uncertainty of at least an order of magnitude. Additional uncertainty stems from an incomplete understanding of reaction mechanisms, particularly for conditions near equilibrium. Sensitivity of model results to reaction rate parameters was investigated in alternate heated repository model computations with the product of rate constants and surface areas increased by a factor of two. The same initial conditions and temporal evolution of CO_2 pressure and temperature were employed in both models. Results are compared to those generated with lower rates in Figure 4-7. Higher reaction rates cause a faster initial increase in the dominant dissolved species, sodium and bicarbonate, slightly greater potassium and calcium concentrations and pH, slightly smaller concentrations of aqueous silica, and moderately more feldspar dissolution and smectite and clinoptilolite precipitation. An increase in reaction rates by a factor of two does not have a dramatic effect on the geochemical model for the heated repository.

An additional study of model sensitivity shows that model results depend strongly on CO_2 pressures. Lower CO_2 values given by curve B in Figure 4-5 were computed in an alternate simplified carbon system reaction and transport model with an initial CO_2 pressure that more closely corresponds to that measured in the vadose zone at Yucca Mountain (Murphy and Codell, 1993, unpublished results). Using the evolution of CO_2 pressure, shown as curve B in Figure 4-5, and the doubled products of rate constants and surface areas, an alternate heated repository model was generated. Initial conditions for this model were modified slightly to obtain realistic values of pH at the lower CO_2 pressures. This model leads to the same general pattern of alteration; however, it produces significantly smaller increases in sodium and bicarbonate concentrations, higher pH, diminished feldspar dissolution, and reduced growth of secondary silicate minerals (Figure 4-7).

The sensitivity of the models to simplifications is also indicated by comparison of the relatively detailed chemical models described previously with the more simplified but related model for the carbon system in the heated repository of Codell and Murphy (1992). In the latter model, all silicate system reactions are neglected, that is, there is no feldspar dissolution or clinoptilolite and smectite precipitation. Results from the simplified carbon system model are therefore an indication of the geochemical evolution in the limit of slow rates in the silicate system. Temperature and CO_2 fugacity are constrained to be equivalent in the two models as a function of time. Results for the two models are generally comparable. Results of the simplified carbon system model differ most significantly in that the calculated aqueous

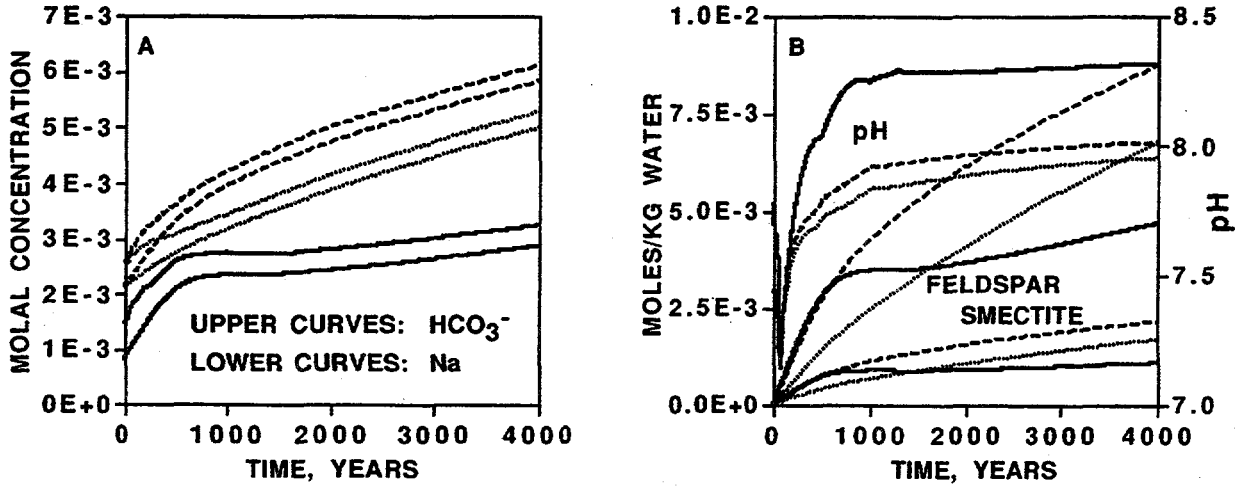

Figure 4-7. Sensitivity of the heated repository model results to reaction rate and CO_2 pressure. Dotted curves are results from the heated repository model based on higher CO_2 pressures corresponding to curve A in Figure 4-5 and the results in Figure 4-6. Dashed lines are based on the same initial conditions and CO_2 pressures as the heated repository model, but with the products of rate constants and surface areas double those consistent with data in Table 4-3. Solid lines are based on a model with similar initial conditions, but with lower CO_2 pressures corresponding to curve B in Figure 4-5, and doubled rate parameters. (A) The upper and lower curves of each pair represent aqueous bicarbonate and total aqueous sodium molalities, respectively. (B) Feldspar dissolution and smectite precipitation (moles/kg H_2O) are plotted from the origin; pH (scale on right) initially decreases and than increases.

sodium concentration is constant and, after an initial rise, the pH decreases toward its initial value with decreasing temperature. In the multicomponent model, the pH increases to somewhat higher values and continues to rise up to 4,000 yr. Silicate hydrolysis contributes to the additional pH increase. The maximum amount of calcite precipitated is similar in the two models, limited by the calcium content of the system. However, calcite continues to precipitate longer in the multicomponent model, in part due to the continuous increase in pH. Because of these differences, use of CO_2 pressures generated in the simplified carbon system model is not fully compatible with the set of carbon plus silicate system reactions in the heated repository model. The distribution of CO_2 and aqueous carbon species would be affected by reactions in the silicate system.

4.3.5 Geochemical Model for Boiling Evolved Water

Boiling to dryness would occur in a potential repository at Yucca Mountain where temperatures exceed the boiling point, taking account of vapor pressure lowering due to suction pressures and solution concentration. Complete vaporization of water is possible even in the absence of boiling, depending on

moisture fluxes. Vaporization of water could lead to several speculative consequences relevant to repository performance. Aqueous solutions would become concentrated as vaporization occurs, and eventually solids such as salts and scale would precipitate. Solutions in a rewetting front would be likely to dissolve previously precipitated salts and become concentrated in soluble species such as sodium, chloride, and sulfate. Concentrated solutions could affect container and waste form alteration processes and radionuclide speciation and distribution. Vapor pressure lowering at equilibrium with salt saturated solutions could affect moisture distribution. Also, growth of relatively insoluble precipitates such as silica and calcite in rocks enclosing the repository could affect hydrologic properties or water and gas flow paths.

The water and mineral chemistry model developed for the natural and heated repository system can be extended to examine some effects of boiling. The boiling model is based on the following scenario. After 1,000 yr, the water that has evolved at a point 75 m above the repository horizon is mobilized and drops on a component of the engineered barrier or natural rock system where the temperature is 100 °C. This effect is represented in the model by an instantaneous change in the temperature from approximately 75 °C to 100 °C. As the water boils it is assumed to be unaffected by reaction with the substrate, but it reacts reversibly with precipitating secondary phases and with CO_2 in the gas phase, which is buffered at 7.2×10^{-3} bar by contact with the gas phase. Computationally this model is implemented in EQ6 by progressively removing pure water from the system, such that reaction progress corresponds to the amount of water removed.

In the simulation, calcite begins immediately to precipitate and is followed by clinoptilolite and cristobalite after 47 and 57 percent of the water has vaporized, respectively. Changes in solution composition (Figure 4-8) are small until over 80 percent of water is removed. Dramatic changes occur between 95- and 99.6-percent evaporation. Ionic strength and pH increase to 1.1 and 9.6, respectively, at 99.6-percent evaporation, and the solution becomes dominated by mixed sodium bicarbonate and sodium carbonate. Solution properties beyond this concentration are poorly represented by the extended Debye-Huckel (b dot) formulation for activity coefficients. This limitation may be overcome eventually by development of a database of ion interaction parameters for relevant aqueous species and temperatures. Preliminary computations using an ion interaction model for simplified chemistry indicate precipitation of calcium and magnesium carbonates, sodium bicarbonate and sulfate, and sodium chloride (halite) with advanced stages of boiling.

4.4 DISCUSSION OF MODEL APPROXIMATIONS AND UNCERTAINTY

Although model results for the natural system and their correspondence to field data appear reasonable, numerous simplifications and approximations have been adopted in the models, and important aspects of the natural and repository systems are incompletely represented. Major model approximations and uncertainties are summarized in this section to place model results in a fair context, and to indicate areas where future model developments would be valuable.

The system chemistry has been simplified by elimination of relatively minor species including magnesium, sulfate, nitrate, and fluoride, and by neglect of oxidation-reduction reactions. Although calcium is neglected as a reactant in the primary phase assemblage, calcium metasomatism is represented by the initially high calcium content of the solution in the natural system model. These simplifications to the chemical system seem unlikely to have major effects on the modeled evolution of the system. The most significant species that has been neglected may be magnesium, particularly because this component

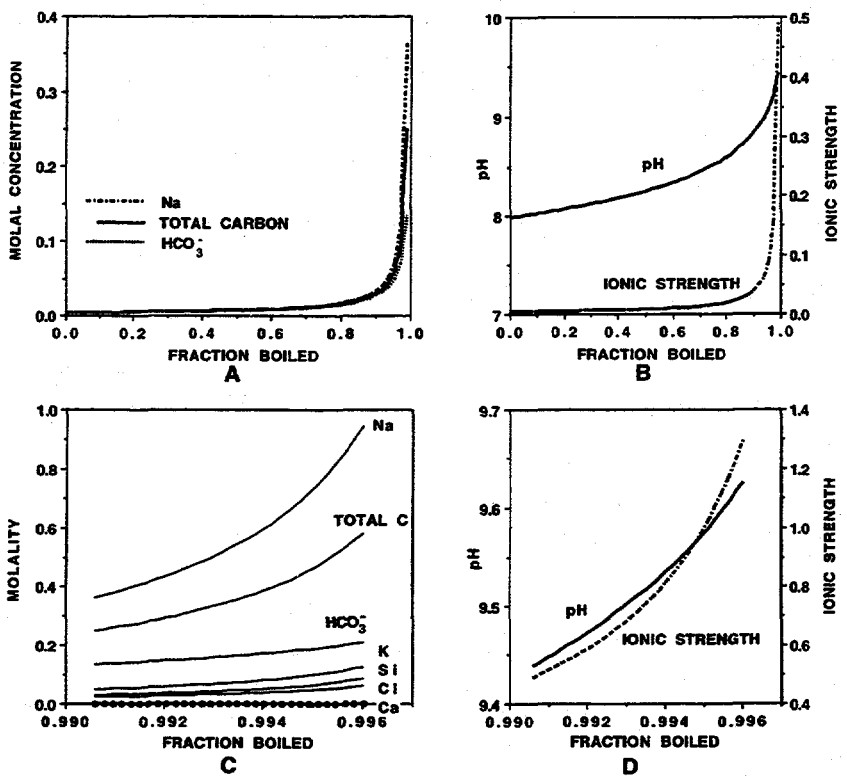

Figure 4-8. Boiling reaction-path model. Solution characteristics are shown as a function of the fraction of the original H_2O that has been volatilized.

is enriched in unsaturated zone groundwater and secondary minerals relative to the saturated zone at Yucca Mountain (Section 4.2.2). Inclusion of magnesium in the model would tend to stabilize clinoptilolite and smectite, and would lead to precipitation of a magnesium carbonate mineral in the boiling model. Although aluminum occurs in small concentrations in the aqueous solutions it is included in the models because it is a component of aluminosilicate minerals. However, the models fail to give reasonable representations of the limited aqueous aluminum concentrations measured in the field. Low model aluminum concentrations result in model solutions that are undersaturated with respect to analcime in contrast to results shown in Section 3.10.

An important uncertainty involves the suite of secondary mineral phases permitted in the model and thermodynamic properties of secondary minerals. Thermodynamic properties for smectite and clinoptilolite adopted in the models are estimated and subject to significant uncertainty. Validity of the data for clinoptilolite is examined in detail in Sections 2 and 3 of this report. The provisional solubility measurement for Na-clinoptilolite (Section 3.8) yields thermodynamic properties for this mineral that are within experimental uncertainty of the estimated value adopted in the reaction-path models of this section. Ion-exchange data (Section 2) were interpreted for binary systems adopting a set of endmember components that are not implemented in Version 7.1 of EQ3/6 and employing an alternate model for aqueous solution activity coefficients. Therefore, the binary system ion-exchange data of Section 2 have not been employed for the ternary clinoptilolite solution in the system modeling. Rather, data for K-clinoptilolite have been adjusted to provide model results for aqueous and solid solutions that correspond closely to these phases as observed at Yucca Mountain.

Modeled solutions become supersaturated with respect to quartz, potassium feldspar, pyrophyllite, stilbite, scolectite, plus mesolite and muscovite in the heated repository model, plus dolomite in the boiling model. Precipitation of these minerals is suppressed in the models on the following basis. Nucleation and growth kinetics of quartz and potassium feldspar are generally slow at the temperatures considered (e.g., less than 100 °C). Thermodynamic data for stilbite, scolectite, and mesolite are highly uncertain, and these minerals are uncommon in nature at Yucca Mountain and in similar systems. Saturation with respect to pyrophyllite may be a consequence of inaccurate thermodynamic data at low temperature for that mineral, which normally occurs in metamorphic rocks that are poor in alkali metals. Muscovite may be regarded as an analog of illite, formation of which could be a reasonable consequence of heating in the Yucca Mountain system. However, studies of sedimentary diagenesis indicate that temperatures in excess of 200 °C are generally required prior to illite formation even on geologic time scales. Dolomite formation is generally inhibited by slow nucleation kinetics, evidenced by difficulty in its experimental synthesis.

Suppression of quartz in the natural system model is well justified on the basis of field data (e.g., Section 4.2.5.7). However, possible formation of quartz and its potential control on silica activities and secondary mineral stability in the heated repository model has not been addressed in the models. It has been assumed that the duration of repository heating is too short for significant quartz precipitation. Speculatively, however, if the heated system would come to equilibrium with quartz as proposed by Glassley (1994), the lowered aqueous silica activity would have a strong effect on the stability of clinoptilolite. Effects of kinetic precipitation of quartz and equilibrium precipitation of K-feldspar at elevated temperatures were examined by Murphy (1991) in a model that included open-system volatilization of CO_2. A transient lowering of the aqueous silica activity occurred due to quartz growth and a strong increase in pH. The lowered silica activity resulted in destabilization of clinoptilolite. Precipitation of K-feldspar reduced the potassium concentration, with the main consequence that secondary clinoptilolite was richer in calcium than in the model shown previously.

Reaction rate parameters and reaction mechanisms, for example, the functional dependence of reaction rates on solution chemistry, have been based on theoretical formalism and limited experimental data, but are nevertheless approximate. The reaction rates of feldspar and cristobalite in the heated repository models depend on a somewhat arbitrary surface area parameter, and the validity of the rate expression is particularly uncertain for conditions that are relatively close to equilibrium. Supersaturation with respect to potassium feldspar may have significance with respect to the dissolution rate of the primary multicomponent alkali feldspar. Back-reaction of a stable potassium-rich phase by an asymmetric dissolution mechanism (Murphy and Smith, 1988) could limit or arrest feldspar dissolution. This process would be incompletely represented by the stoichiometric release and reaction affinity dependence of rate expressions used in the model. Nevertheless, the feldspar reaction rate is a significant factor in the heated repository model as the principal couple between temperature (as a function of time) and reaction progress (as a function of time). For example, the amount of secondary phase formation and the increase in solution pH depend on the feldspar dissolution rate as illustrated in Section 4.3.4.

Open-system behavior is treated in a simplified fashion in the models. Introduction of calcium to the system is simulated by initially high calcium concentrations in the natural system model. Open-system conditions for the gas phase are approximated by CO_2 buffering, either at a constant value in the natural system model and boiling model, or at time-dependent values for the heated repository model. Also, in the boiling model, the system is open with respect to loss of water. However, effects of liquid flow, diffusion, water condensation, and (except in the boiling model) water evaporation are neglected.

An additional uncertainty concerns calibration of the natural system model on water chemistry from the saturated zone, and applications of the model to processes anticipated for the unsaturated zone. Differences have been noted between unsaturated zone pore water compositions and saturated zone water chemistry at Yucca Mountain (Section 4.2.5). However, considerable uncertainty is associated with the unsaturated zone water chemistry because of sampling difficulties, and because relatively few data are available. For example, water chemistry tends to vary with the magnitude of the stresses used for pressure extraction of the water samples (Yang et al., 1988; Yang, 1992), suggesting that experimental artifacts may be introduced. Complete chemical analyses are generally unavailable because the water sample size is limited, which precludes tests of charge balance in the analyzed solutions. Also, fracture water from above the water table at Rainier Mesa is generally similar to saturated zone waters at Yucca Mountain, and unlike unsaturated zone pore waters either from Rainier Mesa or Yucca Mountain (Section 4.2.5). Fracture waters have not been sampled and analyzed at Yucca Mountain, although they may have greater significance than pore waters for repository performance because of the potential for relatively short fracture water travel times. Chemical similarities between fracture water at Rainier Mesa and saturated zone groundwater suggest that if fracture water exists at Yucca Mountain, it may resemble saturated zone water more closely than unsaturated zone pore waters at Yucca Mountain. For these reasons, reaction-path models have been calibrated and evaluated using better established data from the saturated zone.

4.5 CONCLUSIONS

Geochemical interactions among solid, liquid, and gas phases at the proposed nuclear waste repository at Yucca Mountain would affect waste form and container stability, and the transport of radioelements. Performance assessments rely on geochemical models to provide predictions of the evolution of repository systems, or at least to provide estimates of bounds on the possible behavior of these systems. Geochemical models for repository systems possess a degree of validity only when shown to be compatible with data from site characterization. Therefore, modeling of the ambient geochemical and mineralogical system at a site is a prerequisite for valid simulations of repository-induced perturbations to the system. A general description of the geochemical characteristics of Yucca Mountain was developed based on literature review to identify geochemical processes that are important in the evolution of this system. This framework was used to develop the conceptual basis for quantitative reaction-path models for the natural Yucca Mountain system and the heated repository system. Employing principles of thermodynamics, reaction kinetics, mass transfer, and mass transport, computational models were developed using EQ3/6 to explore the evolution of the natural geochemical system, and the geochemical processes that are likely to occur under repository conditions.

The dominant natural geochemical process at Yucca Mountain is alteration of volcanic glass to clinoptilolite and, with increasing depth, to analcime. Smectite also forms as a minor alteration product throughout much of the mountain. Several lines of evidence indicate that altered rocks at Yucca Mountain are enriched in calcium derived from the ground surface and transported to depth in infiltrating groundwater. Unaltered Paintbrush Tuff from Yucca Mountain generally contains less than 1 percent CaO by weight, whereas rocks that have been partially altered to zeolites and/or clays typically contain CaO at 3 to 4 percent. The large differences in calcium concentrations indicate that it is added to the altered rocks from an external source. In general, alteration minerals, notably zeolites, are enriched in calcium at higher positions in the volcanic section above the water table, and become richer in potassium and sodium with depth. Similar relations are observed for other alkaline earth metals, magnesium and

strontium. Variations in groundwater compositions also support a mechanism of alkaline earth metasomatism.

Natural groundwaters from the saturated and unsaturated zones span a range of compositions reflecting extent of reaction progress and (especially in the unsaturated zone) evaporation and volatilization of CO_2. The range of water chemistries and their modifications in the repository system suggest that a single reference water composition would have limited utility in site characterization, engineering design, and performance assessment activities.

A numerical mass-transfer model for the genesis and evolution of groundwater and alteration minerals like those at Yucca Mountain consists of irreversible dissolution of an alkali feldspar, as a chemical analog of volcanic glass in a silica-buffered system, in water with a calcium enriched initial composition, coupled with reversible growth of a secondary stable or metastable solid phase assemblage. Dominant secondary minerals in the upper diagenetic levels of Yucca Mountain are clinoptilolite and smectite. This set of minerals precipitates in the model when solutions are calculated to be saturated with respect to them. After calibration the natural system reaction-path model reasonably represents observed ranges and relative variations of major groundwater components of the saturated zone tuffaceous aquifer at Yucca Mountain. Computed clinoptilolite compositions also correspond well to those observed at Yucca Mountain. The absence of calcite precipitation is consistent with its sparse occurrence in tuffs at Yucca Mountain, and general undersaturation with respect to calcite of the saturated zone tuffaceous aquifer groundwaters at Yucca Mountain. Smectites in the unsaturated zone at Yucca Mountain are commonly rich in sodium, which is also consistent with model results.

Two likely changes to the mineralogical system at Yucca Mountain due to repository heating would be precipitation of calcite and partial alteration of glass or feldspars to secondary minerals such as zeolites. Transient calcite precipitation due to heating may occur over widespread areas of the mountain over long time periods. Alteration of volcanic glass is the dominant diagenetic process that has occurred naturally at Yucca Mountain, and additional alteration is likely to be provoked by heating and heat-induced fluid circulation. Mineralogical changes would in turn have potential effects on fluid flow and retardation of radionuclide migration as well as on water chemistry.

Reaction-path models of the heated repository system, and for a boiling groundwater solution, illustrate plausible variations in gas, water, and rock geochemistry that could affect container and waste form performance and radionuclide migration in a repository at Yucca Mountain. Initial conditions for the heated repository model were based on results of the natural system model. Temperature and CO_2 fugacity variations as a function of time were imposed on the modeled geochemical system at a point above the repository horizon. Dominant model predictions include feldspar dissolution, precipitation of calcite, clinoptilolite and smectite, and evolution of solution compositions toward increased sodium bicarbonate concentrations and pH. Alternate computations showed that model results for the heated repository system are somewhat sensitive to reaction rate parameters. Model results are strongly sensitive to CO_2 pressures which affect pH and mineral alteration rates. A reaction-path model for vaporization of water in the heated repository indicates precipitation of calcite, clinoptilolite, and cristobalite. Changes in aqueous solution composition are relatively small until over 80 percent of water is vaporized. Dramatic changes occur between 95- and 99.6-percent evaporation, as the solution becomes dominated by mixed sodium bicarbonate and sodium carbonate at $pH > 9$.

Approximations adopted in the system modeling include neglect of magnesium and other minor species, limitation of the secondary phase assemblage to minerals common at Yucca Mountain,

approximation of ternary clinoptilolite solid solution properties by ideal endmember mixing, use of generalized rate expressions, estimation of unknown effective surface areas, and neglect of complete effects of open-system behavior and fluid flow (Section 4.4). Nevertheless, the reaction-path models based on principles of thermodynamics, reaction kinetics, mass transfer, and mass transport offer unprecedented, theoretically based, long-term projections of the geochemical evolution of the potential repository at Yucca Mountain. The natural system model reasonably reflects the ranges and variations of observed groundwater and mineral chemistry at Yucca Mountain, which is an important prerequisite for extrapolations to repository conditions. The models account for unsaturated zone processes particularly through open-system CO_2 behavior and CO_2 buffering. The heated repository model explicitly accounts for the transience of the thermal regime and its effects on geochemical changes through coupled reaction kinetics. The models provide indications of significant geochemical variations which would be expected in a repository at Yucca Mountain, and which could impact repository performance through effects on containment, waste form behavior, and radionuclide transport.

4.6 REFERENCES

Arthur, R.C., and W.M. Murphy. 1989. An analysis of gas-water-rock interactions during boiling in partially saturated tuff. *Sciences Géologiques Bulletin* 42: 313-327.

Benson, L.V. 1976. *Mass transport in Vitric Tuffs of Rainier Mesa, Nye County, Nevada.* DRI NVO-1253-10. Las Vegas, NV: Desert Research Institute.

Bish, D.L. 1989. *Evaluation of Past and Future Alterations in Tuff at Yucca Mountain, Nevada, Based on Clay Mineralogy of Drill Cores USW G-1, G-2, and G-3.* LA-10667-MS. Los Alamos, NM: Los Alamos National Laboratory.

Bish, D.L., and J.L. Aronson. 1993. Paleogeothermal and paleohydrologic conditions in silicic tuff from Yucca Mountain, Nevada. *Clays and Clay Minerals* 41: 148-161.

Bish, D.L., and S.J. Chipera. 1989. *Revised Mineralogic Summary of Yucca Mountain, Nevada.* LA-11497-MS. Los Alamos, NM: Los Alamos National Laboratory.

Bish, D.L., and D.T. Vaniman. 1985. *Mineralogic Summary of Yucca Mountain, Nevada.* LA-11497-MS. Los Alamos, NM: Los Alamos National Laboratory.

Brantley, S.L. 1992. Kinetics of dissolution and precipitation—Experimental and field results. *Water-Rock Interactions*. Y.K. Kharaka and A.S. Maest., eds. Rotterdam Netherlands: Balkema: 3-12.

Broxton, D.E., R.G. Warren, R.C. Hagan, and G. Luedemann. 1986. *Chemistry of Diagenetically Altered Tuffs at a Potential Nuclear Waste Repository, Yucca Mountain, Nye County, Nevada.* LA-10802-MS. Los Alamos, NM: Los Alamos National Laboratory.

Broxton, D.E., D.L. Bish, and R.G. Warren. 1987. Distribution and chemistry of diagenetic minerals at Yucca Mountain, Nye County, Nevada. *Clays and Clay Minerals* 35: 89-110.

Broxton, D.E., F.M. Byers, Jr., and R.G. Warren. 1989. *Petrography and Phenocryst Chemistry of Volcanic Units at Yucca Mountain, Nevada,: A Comparison of Outcrop and Drill Hole Samples.* LA-11403-MS. Los Alamos, NM: Los Alamos National Laboratory.

Caporuscio, F.A., and D.T. Vaniman. 1985. *Iron and Manganese in Oxide Minerals and in Glasses: Preliminary Consideration of Eh Buffering Potential at Yucca Mountain, Nevada.* LA-10369-MS. Los Alamos, NM: Los Alamos National Laboratory.

Carlos, B.A. 1985. *Minerals in Fractures of the Unsaturated Zone from Drill Core USW G-4, Yucca Mountain, Nye County, Nevada.* LA-10415-MS. Los Alamos, NM: Los Alamos National Laboratory.

Carlos, B.A. 1989. *Fracture-Coating Minerals in the Topopah Spring Member and Upper Tuff of Calico Hills from Drill Hole J-13.* LA-11504-MS. Los Alamos, NM: Los Alamos National Laboratory.

Carlos, B.A., D.L. Bish, and S.J. Chipera. 1991. Fracture-lining minerals in the lower Topopah Spring Tuff at Yucca Mountain. *Proceedings of the International High-Level Radioactive Waste Conference.* La Grange Park, IL: American Nuclear Society: 486-493.

Carlos, B.A., S.J. Chipera, D.L. Bish, and S.J. Craven. 1993. Fracture-lining manganese oxide minerals in silicic tuff, Yucca Mountain, Nevada, U.S.A. *Chemical Geology* 107: 47-69.

Codell, R.B., and W.M. Murphy. 1992. Geochemical model for ^{14}C transport in unsaturated rock. *Proceedings of the International High-Level Radioactive Waste Conference.* La Grange Park, IL: American Nuclear Society: 1,959-1,965.

Criscenti, L.J., and R.C. Arthur. 1991. The calculated effects of isothermal boiling on tuff-water interactions. *Special Issue of: Radiochimica Acta, International Journal for Chemical Aspects of Nuclear Science and Technology.* R. Oldenbourg Verlag, eds. München, Germany: 1: 513-517.

Daniels, W.R. et al. 1982. *Summary Report on the Geochemistry of Yucca Mountain and Environs.* LA-9328-MS. Los Alamos, NM: Los Alamos National Laboratory.

Delany, J.M., and T.J. Wolery. 1984. *Fixed-Fugacity Option for the EQ6 Geochemical Reaction Path Code.* UCRL-53598. Livermore, CA: Lawrence Livermore National Laboratory.

Duffy, C.J. 1993. *Preliminary Conceptual Model for Mineral Evolution in Yucca Mountain.* LA-12708-MS. Los Alamos, NM: Los Alamos National Laboratory.

Glassley, W. 1994. Coupled Processes in the Altered Zone. *Focus '93.* La Grange Park, IL: American Nuclear Society.

Hay, R.L., and R.A. Sheppard. 1977. Zeolites in open hydrologic systems. *Mineralogy and Geology of Natural Zeolites, Reviews in Mineralogy.* F.A. Mumpton, ed. American Mineralogical Society: 4: 93-102.

Helgeson, H.C., W.M. Murphy, and P. Aagaard. 1984. Thermodynamic and kinetic constraints on reaction rates among minerals and aqueous solutions. II. Rate constants, effective surface area, and the hydrolysis of feldspar. *Geochimica et Cosmochimica Acta* 48: 2,405-2,432.

Kerrisk, J.F. 1983. *Reaction-Path Calculations of Groundwater Chemistry and Mineral Formation at Rainier Mesa, Nevada.* LA-10560-MS. Los Alamos, NM: Los Alamos National Laboratory.

Kerrisk, J.F. 1987. *Groundwater Chemistry at Yucca Mountain, Nevada, and Vicinity.* LA-10929-MS. Los Alamos, NM: Los Alamos National Laboratory.

Knauss, K.G., and T.J. Wolery. 1986. Dependence of albite dissolution kinetics on pH and time at 25 °C and 70 °C. *Geochimica et Cosmochimica Acta* 50: 2,481-2,497.

Knauss, K.G., and T.J. Wolery. 1988. The dissolution of quartz as a function of pH and time at 70 °C. *Geochimica et Cosmochimica Acta* 52: 43-53.

Levy, S.S. 1991. Mineralogic alteration history and paleohydrology at Yucca Mountain, Nevada. *Proceedings of the International High-Level Radioactive Waste Conference.* La Grange Park, IL: American Nuclear Society: 477-485.

Levy, S.S. 1993. Surface-discharging hydrothermal systems at Yucca Mountain—examining the evidence. *Material Research Society Symposium Proceedings.* 294: 543-548.

Levy, S.S., and J.R. O'Neil. 1989. Moderate-temperature zeolitic alteration in a cooling pyroclastic deposit. *Chemical Geology* 76: 321-326.

Lipman, P.W., R.L. Christiansen, and J.T. O'Connor. 1966. *A Compositionally Zoned Ash-Flow Sheet in Southern Nevada.* USGS Professional Paper 524-F, F1-F47. Washington, DC: U.S. Geological Survey.

McKinley, P.W., M.P. Long, and L.V. Benson. 1991. *Chemical Analyses of Water from Selected Wells and Springs in the Yucca Mountain Area, Nevada and Southeastern California.* USGS Open-File Report 90-355. Denver, CO. U.S. Geological Survey: 47.

Murphy, W.M. 1991. *Geochemical modeling.* Report on Research Activities for Calendar Year 1990. W.C. Patrick, ed. NUREG/CR-5817. Washington, DC: Nuclear Regulatory Commission: 2-24 to 2-54.

Murphy, W.M. 1994. Geochemical models for gas-water-rock interactions in a proposed nuclear waste repository at Yucca Mountain, Nevada. *Focus '93.* La Grange Park, IL: American Nuclear Society.

Murphy W.M., and H.C. Helgeson. 1989. Thermodynamic and kinetic constraints on reaction rates among minerals and aqueous solutions. IV. Retrieval of rate constants and activation parameters for the hydrolysis of pyroxene, wollastonite, olivine, andalusite, quartz, and nepheline. *American Journal of Science* 289: 17-101.

Murphy, W.M., and R.A. Smith. 1988. Irreversible dissolution of solid solutions: A kinetic and stoichiometric model. *Radiochimica. Acta* 44/45: 395-401.

Nelson, P.H., and L.A. Anderson. 1992. Physical properties of ash flow tuff from Yucca Mountain, Nevada. *Journal of Geophysical Research* 97: 6,823-6,841.

Ogard, A.E., and J.F. Kerrisk. 1984. *Groundwater Chemistry Along Flow Paths Between a Proposed Repository Site and the Accessible Environment.* LA-10188-MS. Los Alamos, NM: Los Alamos National Laboratory.

Peters, C.A., I.C. Yang, J.D. Higgins, and P.A. Burger. 1992. A preliminary study of the chemistry of pore water extracted from tuff by one-dimensional compression. *Water-Rock Interaction.* Y.K. Kharaka, and A.S. Maest, eds. Rotterdam, Netherlands: Balkema: 741-745.

Reardon, E.J. 1992. Problems and approaches to the prediction of the chemical composition in cement/water systems. *Waste Management* 12: 221-239.

Smyth, J.R. 1982. Zeolite stability constraints on radioactive waste isolation in zeolite-bearing volcanic rocks. *Journal of Geology* 90: 195-201.

Snyder, D.B., and W.J. Carr. 1984. Interpretation of gravity data in a complex volcano-tectonic setting, southwestern Nevada. *Journal of Geophysical Research* 89: 10,193-10,206.

Szabo, B.J., and T.K. Kyser. 1990. Ages and stable-isotope compositions of secondary calcite and opal in drill cores from the Tertiary volcanic rocks of the Yucca Mountain area, Nevada. *Geological Society of America Bulletin* 102: 1,714-1,719.

Thorstenson, D.C., E.P. Weeks, H. Haas, and J.C. Woodward. 1990. *Proceedings of Nuclear Waste Isolation in the Unsaturated Zone, Focus '89.* La Grange Park, IL: American Nuclear Society: 256-270.

U.S. Department of Energy. 1988. *Site Characterization Plan.* DOE/RW-0199. Washington, DC: U.S. Department of Energy: 8 volumes.

Vaniman, D.T. 1993. Calcite deposits in fractures at Yucca Mountain, Nevada. *Proceedings of the International High-Level Radioactive Waste Conference.* La Grange Park, IL: American Nuclear Society: 1,935-1,939.

Vaniman, D.T., D.L. Bish, D.E. Broxton, F. Byers, G. Heiken, B.A. Carlos, E. Semarge, F.A. Caporuscio, and R. Gooley. 1984. *Variations in Authigenic Mineralogy and Sorptive Zeolite Abundance at Yucca Mountain, Nevada, Based on Studies of Drill Cores USW GU-3 and G-3.* LA-9707-MS. Los Alamos, NM: Los Alamos National Laboratory.

Viani, B.E., and C.J. Bruton. 1992. Modeling ion exchange in clinoptilolite using EQ3/6 geochemical modeling code. *Water-Rock Interactions.* Y.K. Kharaka and A.S. Maest, eds. Rotterdam, Netherlands: Balkema: 73-77.

Whelan, J.F., and J.S. Stuckless. 1992. Paleohydrologic implications of the stable isotopic composition of secondary calcite within the tertiary volcanic rocks of Yucca Mountain, Nevada. *Proceedings of the International High-Level Radioactive Waste Conference.* La Grange Park, IL: American Nuclear Society: 1,572-1,581.

White, A.F., H.C. Claassen, and L.V. Benson. 1980. *The Effect of Dissolution of Volcanic Glass on the Water Chemistry in a Tuffaceous Aquifer, Rainier Mesa, Nevada.* Geological Survey Water-Supply Paper 1535-Q. Washington, DC: U.S. Geological Survey.

Winograd, I.J., and W. Thordarson. 1975. *Hydrogeologic and Hydrochemical Framework, South-Central Great Basin, Nevada-California, with Special Reference to the Nevada Test Site.* Geological Survey Professional Paper. 712-C. Washington, DC: U.S. Geological Society.

Wolery, T.J., and S.A. Daveler. 1992. EQ3/6, *A Software Package for Geochemical Modeling of Aqueous Systems.* UCRL-MA-110772 PT I-IV. Livermore, CA: Lawrence Livermore National Laboratory: 4 volumes.

Yang, I.C. 1992. Flow and transport through unsaturated rock—Data from two test holes, Yucca Mountain, Nevada. *Proceedings of the International High-Level Radioactive Waste Conference.* La Grange Park, IL: American Nuclear Society: 732-737.

Yang, I.C., A.K. Turner, T.M. Sayre, and P. Montazer. 1988. *Triaxial-Compression Extraction of Pore Water from Unsaturated Tuff, Yucca Mountain, Nevada.* USGS Water-Resources Investigations Report 884,189. Denver, CO: U.S. Geological Survey: 68.

Yang, I.C., C.A. Peters, and D.C. Thorstenson. 1993. Carbon isotopic data from test hole USW UZ-1, Yucca Mountain, Nevada. *Proceedings of the International High-Level Radioactive Waste Conference.* La Grange Park, IL: American Nuclear Society: 401-406.

Young, R.A. 1972. *Water Supply for the Nuclear Rocket Development Station at the U.S. Atomic Energy Commission's Nevada Test Site.* Geological Survey Water-Supply Paper 1938. Washington, DC: U.S. Geological Survey.

5 PROGRAMMATIC CONCLUSIONS

The Geochemistry Research Project was undertaken with broad objectives to address issues related to the proposed geologic disposal of HLW at Yucca Mountain, Nevada. Specific topics of investigation were chosen to help resolve technical uncertainties concerning fundamental aspects of the geochemical system at Yucca Mountain. Experimental studies and data interpretation focused on interactions between aqueous solutions and the zeolite minerals analcime and clinoptilolite. The abundance of these secondary minerals at Yucca Mountain, their relations in the field, and the relationship between their chemistries and those of other minerals and of groundwaters suggest that they play a controlling role in water-rock interactions. In addition, clinoptilolite is widely cited as a natural barrier to radionuclide migration because of its sorptive characteristics. Thus, knowledge of the fundamental thermodynamic and kinetic properties of these minerals and their interactions with aqueous solutions is required to make defensible projections of the evolution of the water-rock system and retardation of radionuclide transport in the Yucca Mountain repository system. At the inception of this project, major uncertainties existed concerning these properties. Geochemical modeling studies focused on development of multicomponent system models calibrated on mineral, water, and gas chemistry from the site and extrapolated to predict the geochemical evolution of the nonisothermal repository system over thousands of years. Geochemical modeling of the repository system provides a necessary basis for assessments of waste package and waste form alteration processes, radioelement solubilities and speciation, and retardation of radionuclide migration. Nevertheless, only limited attempts previously had been made to use thermodynamic and kinetic reaction-path modeling to predict the evolution of unsaturated zone gas, groundwater, and mineral chemistry in a repository at Yucca Mountain. The results presented in Sections 2 to 4 demonstrate that significant advances have been achieved in these areas as a result of research activities conducted in the Geochemistry Research Project. Publications documenting this work are referenced in Section 1 of this report.

5.1 PROJECT OBJECTIVES AND ACCOMPLISHMENTS

The objectives that were established at the outset of this project were substantially achieved through an integrated approach comprising literature review, experimental studies, interpretive analyses, and theoretical modeling. These objectives are reiterated below, including a brief indication of how they were addressed and references to specific sections of this report and to other products related to this research project.

- Establish similarities and differences between chemical compositions of groundwater in the hydrologically unsaturated zone of Yucca Mountain tuff and groundwater in nearby, geochemically similar but hydrologically saturated rocks.

Published data on chemical compositions of groundwaters from saturated and unsaturated tuffaceous rocks from Yucca Mountain, and from similar tuffaceous rocks from the unsaturated zone at Rainier Mesa, were compared and examined in Section 4.2.4. Although currently available data from the unsaturated zone at Yucca Mountain appear to be subject to considerable uncertainty, important differences between unsaturated and saturated zone groundwaters seem to exist as discussed in Section 4.2.4. Efforts to directly measure the chemistry of water in unsaturated rocks using cryoelectron microscopy met with limited success (Birnbaum and Murphy, 1993).

- Establish a reference chemical composition (or range of compositions) for water in unsaturated fractured rock that can be used to constrain the initial solution composition for geochemistry experiments and for corrosion studies performed in the CNWRA Integrated Waste Package Research Project.

Examination of the range of chemical compositions from the saturated and unsaturated zones at Yucca Mountain (Section 4.2.4) and the possible changes to water chemistry as a consequence of repository-induced perturbations (Section 4.3) led to the conclusion that a reference water composition, such as the often used J-13 well water composition, is unlikely to be a useful concept. A better alternative is to develop thermodynamic models that allow predictions over a range of geochemical conditions. For example, experimental data on clinoptilolite/aqueous-solution ion exchange were used to develop a thermodynamic model that can be used to predict ion exchange equilibria as a function of solution composition and concentration (Section 2). Water compositions for zeolite dissolution and solubility experiments were selected to maximize the potential to obtain thermodynamic data (Section 3.1) that can be extrapolated, based on theoretical principles, for a range of possible geochemical conditions and water chemistries (Section 3.10). In addition, the approach adopted in the CNWRA Integrated Waste Package Research Project has been to examine the functional dependence of corrosion processes on variations in water chemistry (e.g., Sridhar et al., 1993). Nevertheless, the possible range of water chemistries in the proposed Yucca Mountain repository environment has been specifically provided through kinetic and thermodynamic modeling of nonisothermal effects, including boiling and open system variations in CO_2 pressure for proposed repository conditions (Section 4.3).

- Assess potential effects of open-system CO_2 behavior on the chemical composition of fluids and solids in unsaturated fractured tuff.

The potential effects of open-system CO_2 behavior on the chemical composition of fluids and solids in the unsaturated geologic media of Yucca Mountain has been addressed theoretically for both natural conditions (Section 4.2) and repository conditions (Section 4.3). Volatilization of CO_2 due to repository heating has important geochemical consequences, particularly with regard to pH. These processes have been evaluated from several points of view. One endmember process is rapid, open-system volatilization with no back reaction (Rayleigh fractionation). Techniques for computer modeling of Rayleigh fractionation have been developed in this project (Appendix C) and applied to preliminary scenarios for the potential repository environment (e.g., Murphy, 1991). An alternative treatment, which may be more realistic, is based on open-system behavior of CO_2 in a gas flow system, which would develop due to thermal perturbations in an unsaturated repository (Codell and Murphy, 1992), together with local equilibrium between the gas phase and the aqueous phase (Section 4.3).

- Identify and characterize solid phases in the tuff that may control groundwater chemistry and/or radionuclide mobility.

The properties of clinoptilolite, which is widely cited as a solid phase that may control groundwater chemistry and/or radionuclide mobility at Yucca Mountain, were a principal objective of several related aspects of this project, including ion exchange experiments (Section 2); dissolution, precipitation, and solubility studies (Sections 3.7 and 3.8); and modeling of multicomponent variations in a potential repository system (Section 4.3). Experimental studies

indicate that clinoptilolite would readily incorporate radioactive alkali and alkaline earth metals (Section 2) and retard their migration in the aqueous phase. Relations between clinoptilolite and groundwater chemistry were addressed by an evaluation of cation concentrations in potentially coexisting Yucca Mountain groundwaters and clinoptilolites (Section 2.4.3), and through modeling of the evolution of coexisting clinoptilolite and groundwater for the natural and repository systems (Sections 4.2 and 4.3). However, interpretation of solubility data suggests that groundwaters are metastably supersaturated with respect to clinoptilolite and at equilibrium with analcime (Section 4.4). A review of mineralogical data for Yucca Mountain and system modeling exercises also indicate that dissolution of feldspars and/or glass and precipitation of calcite and smectite are also likely to control groundwater compositions (Section 4.2).

- Evaluate conceptual models of the geochemical evolution of water in the unsaturated fractured tuffs at the repository candidate site from periods prior to waste emplacement through operation, closure, and post-emplacement.

A variety of conceptual models for the natural geochemical system at Yucca Mountain have been reported in the literature, notably by researchers of the U.S. Department of Energy. These models were summarized and expanded as described in Section 4.2. Detailed evaluation of a conceptual model for the natural system was effected through its implementation in numerical reaction-path models and through comparison of model results with natural system data (Sections 4.2.6 and 4.2.7). Conceptual models for the geochemical system under repository conditions have not been well developed previously. Repository system models presented in Section 4.3 should provide a basis for evaluation of DOE conceptual models as they are proposed.

- Develop a theoretically based understanding of relevant gas-water-rock reactions, and the capacity to make predictions of the evolution of the geochemical systems of concern.

Theoretically based understanding of gas-water-rock interactions was a dominant theme of this project, including thermodynamic and kinetic interpretations of ion exchange, dissolution, and precipitation data (Sections 2 and 3). Predictive capability was developed for calculations of ion exchange equilibria (Section 2) and for predictions of geochemical behavior of the potential repository system (Section 4.3).

- Interpret and evaluate experimental and field data from studies of gas-water-rock interactions, including those conducted for and by the DOE HLW program.

Field geochemical data from the Yucca Mountain area have been extensively reviewed and interpreted in Section 4, where they have been used to condition system modeling. Field groundwater and clinoptilolite data have been evaluated in the context of ion exchange properties generated in this project (Section 2). Also, groundwater data have been examined in the context of clinoptilolite and analcime solubility (Section 3). Experimental data from the literature relevant to the thermodynamic properties of analcime and clinoptilolite have been reviewed in Sections 2, 3, and 4.

- Identify and directly measure key parameters for characterizing the relevant geochemical systems and their evolution for which necessary data are either lacking or of insufficient accuracy.

Identification and evaluation of key parameters motivated experimental studies of clinoptilolite and analcime (Sections 2 and 3). Key parameters measured were binary ion exchange properties of clinoptilolite in the Na-K, Na-Ca, and Na-Sr systems (Section 2); analcime dissolution mechanism and rate; analcime solubility; clinoptilolite dissolution mechanism and rate; and provisional solubility for clinoptilolite (Section 3).

- Develop constraints of initial conditions, time periods, water-rock ratios, fluid and gas compositions, etc., in order to support and direct experimental activities in this project and research in other CNWRA projects such as natural analog and waste package performance studies.

In general, experimental studies were preceded by predictions of expected behavior (e.g., Murphy, 1991) using the speciation and reaction-path modeling codes EQ3/6 (Wolery and Daveler, 1992). Successive experimental studies were calibrated in advance using data from previous experiments. Geochemical modeling tools developed in this project have also been used in the interpretation of experimental and field data in other CNWRA projects, including Integrated Waste Package Experiments (e.g., Murphy, 1991) and Natural Analogs (e.g., Murphy and Pearcy, 1992).

- Support and validate the geochemical modeling described in the modeling task.

The provisional Na-clinoptilolite solubility value generated in this project (Section 3.8) compares favorably with data used in system modeling studies (Section 4). Ion exchange data (Section 2) have been used to evaluate estimated properties for ternary clinoptilolite solid solutions in system models (Section 4).

- Provide an experimental database with which to independently judge the geochemical work by the DOE on HLW isolation.

An independent set of data was developed on clinoptilolite ion exchange properties (Section 2), analcime dissolution mechanism and rate, analcime solubility, clinoptilolite dissolution mechanism and rate, and provisional solubility for clinoptilolite (Section 3).

5.2 PROJECT RESULTS AND NRC REGULATORY NEEDS

As stated in Section 1, the goal of the Geochemistry Research Project was to support the NRC program relevant to licensing a HLW geologic repository. Information developed in the project will be used to support specific sections of the License Application Review Plan (LARP), particularly the following regulatory requirement topics (RRTs).

RRT 3.1.3: Description of Individual Systems and Characteristics of the Site, Geochemical System

RRT 3.2.3.1: Assessment of Compliance with Siting Criteria, Geochemical System, Individual Favorable Conditions, Nature and Rates of Geochemical Processes

RRT 3.2.3.2: Assessment of Compliance with Siting Criteria, Geochemical System, Individual Favorable Conditions, Geochemical Conditions

RRT 3.2.3.3: Assessment of Compliance with Siting Criteria, Geochemical System, Individual Favorable Conditions, Mineral Assemblages

RRT 3.2.3.4: Assessment of Compliance with Siting Criteria, Geochemical System, Potentially Adverse Conditions, Groundwater Conditions and the Engineered Barrier System

RRT 3.2.3.5: Assessment of Compliance with Siting Criteria, Geochemical System, Potentially Adverse Conditions, Geochemical Processes

RRT 3.2.3.6: Assessment of Compliance with Siting Criteria, Geochemical System, Potentially Adverse Conditions, Not Reducing Groundwater Conditions

RRT 3.2.3.7: Assessment of Compliance with Siting Criteria, Geochemical System, Potentially Adverse Conditions, Gaseous Radionuclide Movement.

Key Technical Uncertainties (KTUs) with regard to compliance determination for several of the LARP sections listed above have been initially identified during a recently completed process of developing Compliance Determination Strategies (CDSs) for the LARP. Many of these KTUs relate to fundamental geochemical problems associated with gas-water-rock interactions and their effects on containment, waste form behavior, and radionuclide transport. Notably, LARP Sections 3.2.3.1, 3.2.3.2, 3.2.3.3, 3.2.3.4, 3.2.3.5, and 3.2.3.7 have been identified to pose KTUs associated with the geochemical system. Development of Compliance Determination Methodologies (CDMs) in this area is currently in progress. Although the Geochemistry Research Project was designed prior to identifying KTUs as main tools in the NRC regulatory strategy, by focusing on clear issues relating to the gas-water-rock evolution of the natural and repository systems at Yucca Mountain, the project has produced results that have contributed significantly to the development of CDSs and to the identification of KTUs. Results of the project will directly contribute to the development of CDMs and help in the resolution of KTUs. A summary of major accomplishments of the Geochemistry Research Project is provided below, together with CDSs with associated KTUs to which the results are most directly related:

- Experimental Data
  - Clinoptilolite ion exchange isotherms were determined at 25 °C for the Na-K, Na-Ca, and Na-Sr systems as a function of aqueous solution composition and concentration (3.2.3.2, 3.2.3.5)
  - Analcime dissolution rate was measured, and dissolution mechanism was evaluated at 25 °C and pH 9 (3.2.3.1)
  - Reversed solubility limit for analcime was determined (3.2.3.4, 3.2.3.5)
  - Dissolution rate was measured, and dissolution mechanism was evaluated for clinoptilolite at 25 °C and pH 9 (3.2.3.1, 3.2.3.5)
  - Provisional solubility limit for clinoptilolite was determined (3.2.3.4, 3.2.3.5)
- Kinetic and Thermodynamic Parameters

- A Margules thermodynamic model for clinoptilolite solid solutions was developed and demonstrated to be successful in predicting binary ion exchange equilibria over wide ranges of solution composition and concentration (3.2.3.2, 3.2.3.5)

- The Margules model was shown to be useful in predicting aqueous solution cationic composition based on zeolite analytical data (3.2.3.2, 3.2.3.5)

- Gibbs free energy of mixing parameters for clinoptilolite solid solutions were regressed from experimental data (3.2.3.2, 3.2.3.5)

- Rate constants and rate laws were determined for analcime and Na-clinoptilolite dissolution (3.2.3.1, 3.2.3.5)

- Equilibrium constant for the analcime dissolution reaction and standard Gibbs free energy of formation for analcime were derived from experimental data (3.2.3.4, 3.2.3.5)

- Provisional equilibrium constant for the clinoptilolite dissolution reaction and standard Gibbs free energy of formation for Na-clinoptilolite were derived from experimental data (3.2.3.4, 3.2.3.5)

- Reaction-Path Modeling Capabilities

  - The EQ3/6 geochemical modeling software and thermodynamic data package were acquired from the DOE and brought under configuration control (3.2.3.1, 3.2.3.2, 3.2.3.3, 3.2.3.4, 3.2.3.5, 3.2.3.7)

  - Open-system, equilibrium (Rayleigh) gas fractionation modeling capabilities were implemented in EQ6 (3.2.3.3, 3.2.3.4, 3.2.3.5, 3.2.3.7)

  - Nonisothermal, variable, imposed fugacity modeling was implemented with EQ6 (3.2.3.3, 3.2.3.4, 3.2.3.5, 3.2.3.7)

- System Models

  - System models were developed for Yucca Mountain groundwater and mineral chemistry (3.2.3.1, 3.2.3.2, 3.2.3.4, 3.2.3.5, 3.2.3.7)

  - System models were developed for nonisothermal, repository-induced chemical variations at Yucca Mountain (3.2.3.3, 3.2.3.4, 3.2.3.5, 3.2.3.7)

  - System models were developed for water and mineral variations during boiling of Yucca Mountain groundwater (3.2.3.3, 3.2.3.4, 3.2.3.5)

In addition to the research results presented in Sections 2 to 4 and the input to the identification of KTUs and the development of CDSs, interactions of the principal investigators in the Geochemistry Project with researchers in other CNWRA research and technical assistance activities have demonstrated the utility of the research results. Direct relations with other CNWRA research projects include: acquisition and preparation of materials and design and interpretation of experiments for the Sorption

Modeling for HLW Performance Assessment Research Project, use of techniques and expertise for geochemical modeling of aqueous solutions in the Integrated Waste Package Experiments Research Project, use of modeling techniques for modeling of aqueous uranium chemistry at the Peña Blanca site for the Geochemical Analogs Research Project, and application of general knowledge of Yucca Mountain area geochemistry in development of the Regional Hydrology Research Project. For the Iterative Performance Assessment, techniques and expertise have been derived from the Geochemistry Research Project for the computation of solubilities of radionuclide-bearing solids and for the development of conceptual and simplified numerical models for the carbon system for use in modeling coupled heat flow, gas flow, and carbon-14 transport. Furthermore, expertise and information developed in the Geochemistry Research Project have been useful for numerous technical reviews of DOE prelicensing submittals.

5.3 REFERENCES

Birnbaum, S.J., and W.M. Murphy. 1993. Cryoelectron microscopy of pore fluids. *NRC High-Level Radioactive Waste Research at CNWRA*. NUREG/CR-5817. Washington, DC: Nuclear Regulatory Commission. (3)1: 2-18 to 2-24.

Codell, R.B., and W.M. Murphy. 1992. Geochemical model for ^{14}C transport in unsaturated rock. *High-Level Radioactive Waste Management Proceedings of the Third International Conference Las Vegas, Nevada, April 12-16, 1992*. La Grange Park, IL: American Nuclear Society, Inc: 2: 1,959–1,965.

Murphy, W.M. 1991. Geochemical modeling. *Report for Research Activities for Calendar Year 1990*. W.C. Patrick, ed. NUREG/CR-5817. Washington, DC: Nuclear Regulatory Commission: 2-24 to 2-54.

Murphy, W.M., and E.C. Pearcy. 1992. Source-term constraints for the proposed repository at Yucca Mountain, Nevada, derived from the natural analog at Peña Blanca, Mexico. *Materials Research Symposium Proceedings*. Pittsburgh, PA: Materials Research Society 257: 521–527.

Sridhar, N., G.A. Cragnolino, and D. Dunn. 1993. *Experimental Investigations of Localized Corrosion of High-Level Waste Container Materials*. CNWRA 93-004. San Antonio, TX: Center for Nuclear Waste Regulatory Analyses.

Wolery, T.J., and S.A. Daveler. 1992, EQ3/6, *A Software Package for Geochemical Modeling of Aqueous Systems*. UCRL-MA-110772 PT I-IV. Livermore, CA: Lawrence Livermore National Laboratory: 4 volumes.

APPENDIX A

ESTIMATED OVERALL UNCERTAINTY IN ISOTHERM DATA

The general equation for normalized uncertainty of an experimental result, r, that is a function of J variables X_i, for example

$$r = r(X_1, X_2, \ldots, X_J) \tag{A-1}$$

is given by (Coleman and Steele, 1989)

$$(U_r/r)^2 = \left[(1/r)(\partial_r/\partial X_1)U_{X_1}\right]^2 + \left[(1/r)(\partial r/\partial X_2)U_{X_2}\right]^2 + \ldots \left[(1/r)(\partial r/\partial X_J)U_J\right]^2 \tag{A-2}$$

where U is the uncertainty in the measured variable X. Thus the uncertainties in $\bar{E}_K$ and E_K (or $\bar{E}_{Ca}$ and E_{Ca} or $\bar{E}_{Sr}$ and E_{sr}) calculated from the K^+ (or Ca^{2+} or Sr^{2+}) data [Eq. (2-18)] are given by

$$\left(U_{\bar{E}_A}/\bar{E}_A\right)^2 = \left[U_{M_{A,i}}/(M_{A,i} - M_{A,f})\right]^2 + \left[U_{M_{A,f}}/(M_{A,i} - M_{A,f})\right]^2 + (U_V/V)^2$$

$$+ (U_W/W)^2 + (U_{CEC}/CEC)^2 \tag{A-3}$$

$$\left(U_{E_A}/E_A\right)^2 = \left(U_{M_{A,f}}/M_{A,f}\right)^2 + \left(U_{TN}/TN\right)^2 \tag{A-4}$$

where the subscript A refers to K^+, Ca^{2+}, or Sr^{2+}. The equation for the uncertainties in $\bar{E}_K$ (or $\bar{E}_{Ca}$ or $\bar{E}_{Sr}$) calculated from the Na^+ data (Eq. 2-19) is the same as Eq. (A-3), except the molarities are those for Na^+. The uncertainty equation for E_K, E_{Ca}, or E_{Sr} is slightly different from Eq. (A-4), and is given by

$$\left(U_{E_A}/E_A\right)^2 = \left[z_B M_{B,f}/(TN - z_B M_{B,f})\right]^2 \left[\left(U_{M_{B,f}}/M_{B,f}\right)^2 + \left(U_{TN}/TN\right)^2\right] \tag{A-5}$$

Note that Eq. (A-3) has terms with concentration differences in the denominator. Where the difference in initial and final concentration is small the uncertainty in the calculated parameter becomes large. Therefore, errors in $\bar{E}_K$, $\bar{E}_{Ca}$, or $\bar{E}_{Sr}$ calculated from the K^+, Ca^{2+}, or Sr^{2+} analysis become large as $\bar{E}_K$, $\bar{E}_{Ca}$, or $\bar{E}_{Sr}$ approach one. On the other hand, errors in $\bar{E}_K$, $\bar{E}_{Ca}$, or $\bar{E}_{Sr}$ calculated from the Na^+ data become large as $\bar{E}_K$, $\bar{E}_{Ca}$, or $\bar{E}_{Sr}$ approach zero. This explains why it is important to analyze the solution concentrations of both cations participating in the exchange reaction when constructing ion exchange isotherms. In this manner the ion-exchange isotherm is well-constrained throughout the whole isotherm range.

Uncertainties in the selectivity coefficient, K_v, derived using either K^+, Ca^{2+}, or Sr^{2+} analytical data (Eq. 2-20) can be calculated from

$$\left(U_{K_v}/K_v\right)^2 = \left[z_A U_{\bar{X}_A}/\left(1-\bar{X}_A\right) + z_B U_{\bar{X}_A}/\bar{X}_A\right]^2 + \left[z_A^2 U_{M_A}/\left(TN-z_A M_A\right) + z_B U_{M_A}/M_A\right]^2$$

$$+ \left[z_A U_{\gamma_B}/\gamma_B\right]^2 + \left[z_B U_{\gamma_A}/\gamma_A\right]^2 \qquad \text{(A-6)}$$

The corresponding uncertainty equation for K_v calculated from the Na^+ data (Eq. 2-21) can be derived by interchanging coefficients A and B in Eq. (A-6). Also,

$$U_{\ln K_v} = U_{K_v}/K_v \qquad \text{(A-7)}$$

and

$$U_{\bar{X}_A}/\bar{X}_A = \left(z_A - z_B\right)U_{\bar{E}_A}/\left[\left(z_A + \left(z_B - z_A\right)\bar{E}_A\right)\right] + U_{\bar{E}_A}/\bar{E}_A \qquad \text{(A-8)}$$

The error bars plotted for some of the isotherm points in the figures were calculated from the above equations using estimated overall uncertainties in the Na^+, K^+, Ca^{2+}, and Sr^{2+} analytical data of ± 2, ± 3, ± 4, and ± 1 percent, respectively, overall relative errors in V and γ_i of 1 and 3 percent, respectively, and overall absolute errors in W and CEC of 10^{-4} g and 0.02 meq/g respectively. For calculation purposes, rounded-off values of TN (0.005, 0.05, or 0.50 N) were used. TN was assigned an overall uncertainty of ± 3 percent based on deviations from the measured $Na^+ + K^+$, $Na^+ + Ca^{2+}$, and $Na^+ + Sr^{2+}$ normalities.

REFERENCES - APPENDIX A

Coleman, H.W., and W.G. Steele. 1989. *Experimentation and Uncertainty Analysis for Engineers.* New York, NY: John Wiley and Sons.

APPENDIX B

EXPERIMENTAL CONDITIONS AND ANALYTICAL DATA FOR ANALCIME AND CLINOPTILOLITE DISSOLUTION AND PRECIPITATION STUDIES

Appendix B. Table A. Experimental Conditions

Mixture Label	Initial Solution Volume 0.1 M NaCl + 0.01 M $NaHCO_3$ preequilibrated with atmospheric CO_2 (initial pH = 9.00±0.02)	Solid Involved			
		Analcime		Clinoptilolite	
		Grain size based on nominal sieve opening	Mass, g	Grain size based on nominal sieve opening	Mass, g
ACDTIA	1,000 ml	75-63 µm (200-230 mesh)	3.7502		
ACDTIIA		63-45 µm (230-325 mesh)	2.5002		
ACDTIIIA		45-32 µm (325-450 mesh)	2.2501		
ASE1	250 ml	32-20 µm (450-635 mesh)	3.9999		
ASE2			4.0001		
ASE3			4.0000		
ASE4			4.0001		
ASEA1	250 ml	32-20 µm (450-635 mesh)	3.9995		
ASEA2			3.9996		
ASEA3			4.0001		
RACDTIA	1,000 ml (4000 ppb SiO_2 and 900 ppb Al)	75-63 µm (200-230 mesh)	3.7502		
RACDTIIIA			2.2501		
RASH1	250 ml (30 ppm SiO_2 and 200 ppb Al)	32-20 µm (450-635 mesh)	4.0017		
RASH2			4.0051		
RASH3			4.0044		
RASH4			4.0089		
ACDTIB	1,000 ml	75-63 µm (200-230 mesh)	3.7503		1.0010
ACDTIIB		63-45 µm (230-325 mesh)	2.5007	150-75 µm (100-200 mesh)	1.0008
ACDTIIIB		45-32 µm (325-450 mesh)	2.2506		1.0001
CDVSE1	250 ml				1.0004
CDVSE2				150-75 µm (100-200 mesh)	1.0012
CDVSE3					1.0006
CDVSE4					1.0001
RCDV1	250 ml (30 ppm SiO_2 and 200 ppb Al)				0.9607
RCDV2				150-75 µm (100-200 mesh)	0.9751
RCDV3					0.9611
RCDV4					0.9606

Appendix B. Table B. Analytical Data

Mixture Label	Elapsed Time (hours)	Mass (g) before sampling	Mass (g) after sampling	Solution pH	Na (ppm)	SiO_2 (ppb)	Al (ppb)
ACDTIA	48	1,094.20	1,043.40	8.98	2,550	136.8	46.25
	95	1,043.30	992.70	9.00	2,620	267.9	62.75
	168	922.60	941.80	8.99	2,550	322.0	103.75
	261	941.50	890.90	8.99	2,520	410.4	138.25
	358	890.60	839.80	8.97	2,480	456.0	138.75
	497	839.30	788.60	8.98	2,570	570.0	175.25
	594	788.40	737.70	8.99	2,500	592.8	184.75
	713	737.40	686.70	9.00	2,490	758.1	205.75
	834	686.20	635.30	8.98	2,500	666.9	171.25
	934	635.00	584.11	8.98	2,620	698.2	208.50
	1074	583.68	532.95	9.00	2,560	732.4	189.25
	1,193	532.57	481.88	9.00	2,550	763.8	186.25
	1,505	480.39	429.71	9.01	2,520	906.3	194.75
	1,915	427.80	377.29	9.00	2,540	1,088.7	250.25
	2,369	375.38	324.63	9.00	2,590	920.5	224.50
	2,849	322.87	272.24	9.02	2,530	1,063.0	219.00
	3,209-a	270.85	169.93	8.99	2,620	1,202.7	249.00
	3,209-b	270.85	169.93	9.00	2,590	1,151.4	224.50
	4,870	165.08	114.27	9.00	2,780	2,884.2	383.25

Appendix B. Table C. Analytical Data

Mixture Label	Elapsed Time (hours)	Mass (g) before sampling	Mass (g) after sampling	Solution pH	Na (ppm)	SiO_2 (ppb)	Al (ppb)
ACDTIIA	48	1,094.30	1,043.70	8.99	2,540	119.7	32.75
	95	1,043.50	992.90	9.00	2,580	173.8	49.50
	168	992.60	941.90	8.95	2,560	282.1	80.00
	261	941.60	890.90	8.99	2,520	304.9	101.00
	358	890.60	840.00	8.99	2,490	367.6	92.25
	497	839.50	788.90	8.97	2,520	433.2	152.50
	594	788.60	737.90	8.99	2,510	470.2	142.75
	713	737.40	686.50	9.00	2,510	513.0	157.25
	834	686.00	635.50	8.97	2,490	501.6	135.75
	934	635.10	584.28	8.98	2,590	555.7	166.75
	1,074	583.07	532.74	9.00	2,520	601.3	99.50
	1,193	532.14	481.39	9.00	2,540	615.6	165.25
	1,505	479.56	428.95	9.02	2,670	627.0	124.00
	1,915	427.05	376.42	9.01	2,530	621.3	202.75
	2,369	373.87	323.21	9.00	2,600	789.4	193.25
	2,849	320.73	269.46	9.02	2,500	969.0	230.50
	3,209-a	267.29	166.55	9.00	2,650	943.3	229.00
	3,209-b	267.29	166.55	9.01	2,630	931.9	230.25
	4,870	160.39	109.40	9.02	2,910	2,194.5	410.00

Appendix B. Table D. Analytical Data

Mixture Label	Elapsed Time (hours)	Mass (g) before sampling	Mass (g) after sampling	Solution pH	Na (ppm)	SiO_2 (ppb)	Al (ppb)
ACDTIIIA	48	1,089.80	1,039.50	8.98	2,540	116.8	36.25
	95	1,039.30	988.70	8.99	2,530	159.6	60.25
	168	988.50	937.90	8.97	2,500	307.8	82.75
	261	937.60	886.90	8.97	2,500	356.2	110.50
	358	886.60	835.90	9.01	2,480	390.4	112.50
	497	835.40	784.80	8.98	2,500	467.4	143.00
	594	784.40	733.70	8.98	2,500	487.3	155.75
	713	733.20	682.50	8.99	2,510	541.5	171.25
	834	682.00	631.30	8.97	2,500	552.9	147.75
	934	630.90	579.94	8.98	2,540	589.9	175.75
	1,074	579.38	528.71	9.00	2,530	641.2	161.25
	1,193	528.19	476.90	9.00	2,530	658.3	178.75
	1,505	475.11	424.23	9.01	2,600	706.8	147.75
	1,915	422.25	372.05	9.01	2,570	649.8	225.75
	2,369	369.70	319.11	9.00	2,590	863.5	205.25
	2,849	316.90	266.06	9.02	2,500	1,040.2	226.25
	3,209-a	264.10	163.35	9.00	2,600	1,142.8	246.75
	3,209-b	264.10	163.35	9.00	2,650	1,157.1	244.50
	4,870	158.00	106.81	9.02	2,850	2,556.4	343.50

Appendix B. Table E. Analytical Data

Mixture Label	Elapsed Time (hours)	Mass (g) before sampling	Mass (g) after sampling	Solution pH	Na (ppm)	SiO_2 (ppb)	Al (ppb)
ASE1	1,104	300.39	249.63	8.85	2,490	2,408.2	508.0
	1,203	249.26	228.49			2,972.0	573.0
	2,567	223.00	172.17	8.97	2,620	2,473.8	582.5
	9,075	160.00	109.35	9.03	3,140	2,348.4	570.0
ASE2	1,104	301.42	250.64	8.94	2,550	2,442.4	505.7
	1,203	250.30	229.78			3,144.0	598.0
	2,567	224.90	174.17	8.99	2,630	2,545.0	581.0
	9,075	161.84	111.05	9.04	3,040	2,793.0	632.0
ASE3	1,773	298.58	247.92	8.96	2,630	2,542.2	522.0
	2,567	244.83	193.98	9.00	2,680	2,604.9	604.5
	9,075	185.20	134.53	9.02	2,840	2,810.1	646.5
ASE4	1,773	299.05	248.48	8.97	2,630	2,656.2	590.2
	2,567	245.12	194.37	9.00	2,620	2,713.2	623.5
ASEA1	5,556	291.90	241.20	9.00	2,920	3,343.0	617.0
	15,637	182.62	132.34	9.13	3,900	4,212.3	700.0
ASEA2	5,556	294.08	243.34	8.99	2,920	3,243.3	654.0
	15,637	188.81	138.06	9.12	3,710	3,961.5	676.0
ASEA3	5,556	290.96	240.41	9.00	2,760	3,283.2	635.0
	15,637	189.30	138.68	9.12	3,620	4,007.1	694.0

Appendix B. Table F. Analytical Data

Mixture Label	Elapsed Time (hours)	Mass (g) before sampling	Mass (g) after sampling	Solution pH	Na (ppm)	SiO_2 (ppb)	Al (ppb)
RACDTIA	21	1,112.00	1,061.40	8.99	2,500	3,898.9	901.0
	256	1,054.80	1,003.90	8.96	2,520	3,890.2	896.5
	882	917.80	866.90	9.00	2,590	3,861.7	887.5
	1,842	862.40	811.80	9.02	2,610	3,864.6	788.5
	3,282	805.00	754.30	9.05	2,590	3,733.5	839.0
	7,393	738.00	686.70	8.99	2,840	3,779.1	794.0
	10,969	667.20	616.50	8.98	2,850	3,992.8	871.5
	12,500	611.30	559.65	9.05	2,730	3,767.7	826.0
	17,473	538.42	487.67	9.04	2,840	4,143.9	886.0
RACDTIIIA	21	1,103.80	1,053.20	8.99	2,510	3,944.4	932.0
	265	1,050.90	1,000.20	8.96	2,550	3,873.1	871.5
	882	981.80	931.00	9.00	2,520	3,830.4	821.5
	1,842	926.80	876.50	9.02	2,540	3,813.3	851.5
	3,283	871.40	820.50	9.05	2,600	3,739.2	812.0
	10,969	786.80	736.20	9.00	2,780	3,915.9	858.0
	12,500	731.00	679.60	9.05	2,840	3,699.3	780.0
	17,473	656.30	604.70	9.04	2,800	4,024.2	893.0

Appendix B. Table G. Analytical Data

Mixture Label	Elapsed Time (hours)	Mass (g) before sampling	Mass (g) after sampling	Solution pH*	Na (ppm)	SiO_2 (ppm)	Al (ppb)
RASH1	49	304.81	269.23	8.96	2,620	28.38	125.0
	525	268.23	232.77	9.06		28.71	38.1
	1,028	231.64	195.96	9.07	2,560	29.02	16.5
	1,536	194.55	159.09	9.07		28.87	33.0
	2,179	157.47	121.98	9.08	2,520	29.02	38.3
	4,341	114.40	78.36	9.11	2,960	31.40	4.2
RASH2	49	304.87	269.38	8.96	2,640	28.60	118.0
	525	268.44	232.83	8.96		28.27	36.3
	1,028	231.68	196.03	8.96	2,540	28.59	20.2
	1,536	194.58	158.96	8.97		28.16	32.0
	2,179	157.60	121.88	8.98	2,560	28.90	28.5
	4,341	116.08	80.53	9.04	2,930	31.04	6.8
RASH3	49	305.31	269.84	8.96	2,630	28.93	88.0
	525	268.84	233.18	8.96		28.16	25.8
	1,028	231.95	196.42	8.96	2,560	28.84	17.4
	1,536	194.95	159.51	8.97		28.54	26.0
	2,179	157.85	122.46	8.99	2,520	29.57	18.5
RASH4	49	305.30	270.96	8.96	2,610	28.87	70.2
	525	268.81	233.35	8.96		28.27	22.2
	1,028	232.06	196.74	8.97	2,560	28.90	15.8
	1,536	195.22	159.77	8.98		27.83	24.5
	2,179	158.06	122.44	8.99	2,540	29.02	22.2

*pH estimated from correlation between pH and Na established for ASEA series experiments

Appendix B. Table H. Analytical Data

Mixture Label	Elapsed Time (hours)	Mass (g) before sampling	Mass (g) after sampling	Solution pH	Na (ppm)	SiO_2 (ppb)	Al (ppb)
ACDTIB	168	1,093.70	1,043.00	8.96	2,540	265.1	104.25
	358	1,042.10	991.40	8.98	2,490	461.7	131.00
	664	989.70	939.00	9.01	2,520	544.3	171.00
	1,001	937.10	886.30	9.00	2,560	627.0	190.75
	1,505	883.20	832.50	9.01	2,550	672.6	160.25
	4,870	812.00	761.20	8.97	2,530	866.4	174.75
	5,637	756.70	706.10	8.97	2,560	903.4	214.00
	5,708	705.60	654.80	8.96	2,590	1,647.3	160.50
	6,017	649.30	598.13	8.95	2,610	2,889.9	102.25
	6,377	594.12	542.40	8.98	2,620	3,665.1	46.25
	7,121	536.91	486.08	9.03	2,750	5,204.1	37.75
	8,561	479.79	429.15	9.00	2,730	6,817.2	15.53
	12,670	420.88	370.28	8.99	2,980	11,132.1	18.80
	16,247	360.49	309.69	9.02	3,060	15,709.2	23.38
	22,751	294.32	243.47	9.03	3,140	23,320.0	3.00

Appendix B. Table I. Analytical Data

Mixture Label	Elapsed Time (hours)	Mass (g) before sampling	Mass (g) after sampling	Solution pH	Na (ppm)	SiO_2 (ppb)	Al (ppb)
ACDTIIB	168	1,093.60	1,042.90	8.96	2,540	190.9	67.25
	358	1,042.40	991.60	8.97	2,460	336.6	96.75
	664	990.60	940.00	8.99	2,510	416.1	130.75
	1,001	938.70	887.90	9.00	2,580	475.9	142.75
	1,505	885.70	835.10	9.00	2,630	518.7	125.50
	4,870	822.60	771.80	8.97	2,580	749.5	154.00
	5,637	767.00	716.10	8.97	2,520	778.0	180.25
	5,708	716.80	666.20	8.95	2,580	1,405.5	143.75
	6,017	663.30	612.40	8.96	2,590	2,750.2	62.50
	6,377	609.90	559.07	8.96	2,590	3,451.3	38.25
	7,121	554.77	503.96	9.03	2,720	4,939.0	29.00
	8,561	497.34	446.59	9.02	2,700	7,415.7	17.20
	12,670	435.05	384.42	9.00	2,920	12,198.0	13.40
	16,247	373.19	322.66	9.00	3,030	16,564.2	14.86
	22,751	305.71	255.04	9.04	3,120	22,935.0	1.17

Appendix B. Table J. Analytical Data

Mixture Label	Elapsed Time (hours)	Mass (g) before sampling	Mass (g) after sampling	Solution pH	Na (ppm)	SiO_2 (ppb)	Al (ppb)
ACDTIIIB	168	1092.50	1041.90	8.95	2,510	259.3	79.25
	358	1041.30	990.40	9.00	2,500	387.6	108.75
	664	989.30	938.70	8.99	2,510	456.0	145.00
	1001	937.30	886.00	9.00	2,600	530.1	161.00
	1505	883.40	832.20	9.01	2,600	644.1	140.75
	4870	819.60	768.80	8.99	2,520	792.3	190.75
	5637	763.80	713.20	8.97	2,570	837.9	197.00
	5708	712.80	661.90	8.95	2,590	1,402.2	162.25
	6017	656.60	605.60	8.96	2,600	2,573.5	87.50
	6377	600.90	549.99	8.98	2,610	3,308.8	47.75
	7121	546.94	496.28	9.04	2,740	4,904.8	31.50
	8561	467.00	416.50	9.03	3,000	15,458.4	16.03
	2,2751	402.40	351.64	9.03	2,960	20,790.0	0.00

Appendix B. Table K. Analytical Data

Mixture Label	Elapsed Time (hours)	Mass (g) before sampling	Mass (g) after sampling	Solution pH	Na (ppm)	SiO_2 (ppb)	Al (ppb)
CDVSE1	2,113	289.71	249.21	9.03	2,630	13,571.7	0.25
	3,797	236.40	185.84	9.02	3,080	20,223.6	9.00
	7,375	146.19	95.44	9.15	4,210	36,850.0	9.35
	9,031	82.26	54.08		6,180	49,280.0	4.25
CDVSE2	2,113	289.47	249.06	9.03	2,650	13,851.0	2.25
	3,797	236.81	185.70	9.01	3,020	20,116.6	9.20
	7,375	151.53	100.81	9.13	3,960	35,200.0	10.69
	9,031	86.32	53.38	9.22	5,550	48,070.0	7.75
CDVSE3	2,113	291.79	251.29	9.03	2,610	13,395.0	0.00
	7,375	207.83	157.07	9.07	3,420	30,800.0	9.02
	13,879	102.37	54.35	9.26	7,140	60,390.0	0.00
CDVSE4	2,113	290.83	250.43	9.02	2,640	13,634.4	0.00
	7,375	204.78	153.94	9.09	3,630	30,910.0	10.52
	13,879	100.69	60.39	9.25	7,340	64,790.0	0.00

Appendix B. Table L. Analytical Data

Mixture Label	Elapsed Time (hours)	Mass (g) before sampling	Mass (g) after sampling	Solution pH*	Na (ppm)	SiO_2 (ppm)	Al (ppb)
RCDV1	49	302.21	266.17	9.00	2,750	30.19	86.75
	524	264.97	229.39	9.00		30.08	4.20
	1,027	227.85	192.38	9.01	2,550	32.14	0.00
	1,536	190.45	154.66	9.01		31.18	0.00
	2,179	152.60	117.00	9.02	2,560	33.05	0.00
	4,340	108.39	72.48	9.06	3,100	39.29	0.00
RCDV2	49	302.22	266.51	9.00	2,650	29.97	99.75
	524	265.36	229.76	9.00		29.86	8.10
	1,027	228.05	192.62	9.00	2,560	31.53	3.30
	1,536	190.78	155.29	9.01		31.13	0.00
	2,179	153.40	117.84	9.02	2,520	32.69	0.40
	4,340	108.51	72.94	9.06	3,140	38.61	0.00
RCDV3	49	302.47	266.75	9.00	2,620	29.31	81.50
	524	265.92	230.20	9.00		29.37	0.00
	1,027	229.18	193.56	9.00	2,540	31.22	2.00
	1,536	192.25	156.55	9.01		30.80	0.00
	2,179	155.30	119.56	9.01	2,520	32.69	1.20
RCDV4	49	302.31	266.67	9.00	2,630	29.48	76.50
	524	265.77	230.08	9.00		29.20	1.00
	1,027	229.07	193.40	9.00	2,540	31.40	0.00
	1,536	192.10	156.58	9.01		30.85	1.00
	2,179	155.13	119.47	9.01	2,520	33.36	0.00

*pH estimated from correlation between pH and Na established for CDVSE series experiments

APPENDIX C

SUMMARY AND USE OF THE EQ3/6 SOFTWARE PACKAGE

Numerical geochemical models presented in this report were generated with the EQ3/6 computer software package Version 7.1 operating on the Southwest Research Institute VAX 8700 computer. The R16.com database associated with the package was used for all thermodynamic data, except for clinoptilolite as noted in Section 4.6. The codes and databases of the EQ3/6 package are described in detail by Wolery and Daveler (1992). EQ3 generates models for equilibrium speciation in an aqueous phase and calculates mineral saturation indices relative to the aqueous solution. EQ6 generates reaction-path models consisting of a series of equilibrium aqueous speciation states associated with the evolution of a system undergoing a change such as mineral dissolution and precipitation or evaporation. Principles of modeling with EQ3/6 are summarized in this section, with an emphasis on techniques used in generating the models presented in this report.

Equilibrium speciation (or equilibrium distribution of species) is a thermodynamic model for the properties of an aqueous solution. The fundamental phenomenon is the reversible chemical reaction in which reactants are continuously forming products and vice versa. The model postulates that all chemical reactions among aqueous species are at equilibrium. The state of the system can be described by equations that simultaneously impose mass balance, charge balance, and mass action constraints. Simultaneous solution of these equations is the basic means of calculating an equilibrium aqueous speciation and the fundamental function that EQ3 accomplishes.

These principal relations are shown mathematically as:

Mass conservation (for all elements, i):

$$n_i = \sum_j \nu_{ij} n_j$$

Charge conservation (for the aqueous phase):

$$0 = \sum_j z_j n_j$$

Mass action (for all reactions, r, that are at equilibrium):

$$K_r = \prod_j a_j^{c_{jr}}$$

where

- n_i = moles of element i
- n_j = moles of species j
- ν_{ij} = stoichiometric number of moles of element i in species j
- z_j = electric charge of species j
- K_r = equilibrium constant for reaction r
- a_j = thermodynamic activity of species j, which is related to the species concentration
- c_{jr} = reaction coefficient for species j in reaction r, which is positive for products and negative for reactants

The thermodynamic activity is related to the number of moles of a species by the definition

$$a_j = m_j \gamma_j = (n_j / W_{H_2O})_{\gamma_j}$$

where

m_j = molality of species j (moles of j per kilogram of solvent)
γ_j = activity coefficient of species j
W_{H_2O} = mass of H_2O in kilograms

Activity coefficients are mainly a function of the ionic strength of the solution.

To define the equilibrium state of an aqueous system, one constraint is required for each independent chemical component. Commonly, this is accomplished by specifying the total number of moles of the component in 1 kg of the solvent, H_2O. Additional means to constrain a component are to specify a heterogeneous equilibrium, or to specify that a species concentration is to be adjusted to achieve charge neutrality. For example, the component silica can be constrained by specifying its total molality. Alternatively, the solution can be specified to be in equilibrium with cristobalite. In the latter case, silica is constrained by the law of mass action for the reaction

$$SiO_2 \text{ (cristobalite)} \rightleftharpoons SiO_2 \text{ (aqueous)} \qquad K_{Cris} = a_{SiO_2}$$

Once a component is constrained, activities of additional aqueous species containing the component are related by laws of mass action. For example, if the activities of Na^+ and HCO_3^- have been fixed, then the activity of the neutral aqueous species $NaHCO_3$ can be calculated using the law of mass action for the reaction

$$NaHCO_3 \rightleftharpoons Na^+ + HCO_3^- \quad K_{NaHCO_3} = (a_{Na^+})(a_{HCO_3^-})/a_{NaHCO_3}$$

Knowing the equilibrium aqueous speciation of a solution and the activities of the aqueous species permits calculation of the saturation state of the solution with respect to various mineral and gas phases. For each mineral, the saturation index can be represented by Q_r/K_r where Q_r represents the activity product for the mineral dissolution reaction whether or not it is at equilibrium

$$Q_r = \sum_j a_j^{c_{jr}}$$

and K_r stands for the equilibrium constant for the reaction. At equilibrium $Q_r/K_r = 1$. For undersaturated solutions $Q_r/K_r < 1$, and for supersaturated solutions $Q_r/K_r > 1$.

For gas species g, the thermodynamic fugacity is defined by $f_g = \chi_g p_g$, where χ_g stands for the fugacity coefficient and p_g denotes the partial pressure of the gas species. The law of mass action for the reaction between the gas species and species in the aqueous solution permits calculation of the fugacity of a gas species that would be in equilibrium with the solution. For example, for the reaction

$$CO_2(gas) + H_2O \rightleftharpoons HCO_3^- + H^+$$

The fugacity of CO_2 is given by

$$f_{CO_2} = \frac{a_{HCO_3^-}\ a_{H^+}}{a_{H_2O}\ \ K_{CO_2}}$$

If the fugacity of a gas species at equilibrium with an aqueous solution exceeds the fugacity of that gas species in a gas phase in contact with the solution, then there will be a thermodynamic drive for the gas species to exsolve from the aqueous solution.

EQ6 goes beyond EQ3 by introducing reaction progress. In a closed system at chemical equilibrium such as that modeled by EQ3, there is no net reaction progress; all reactions are reversible. Systems that are not at equilibrium may evolve spontaneously by irreversible reactions to states of lower free energy. In general, geochemical systems evolve continually, albeit slowly toward an equilibrium state. Geochemical systems can also evolve as conditions such as temperature change. Other systems change as fluids of different compositions mix. The sequence of states through which a system evolves by chemical reactions is called the reaction path. EQ6 can be used to model reaction paths in systems involving minerals (glasses, rocks, etc.), gases, and aqueous solutions.

Partial equilibrium is a basic conceptual model at the foundation of reaction path modeling with EQ6. A subset of chemical reactions in a system is assumed to be at equilibrium while other reactions are out of equilibrium with respect to the equilibrium subset. The irreversible (disequilibrium) reactions continually progress toward equilibrium with the equilibrium subsystem, altering its state, for example, by adding mass and changing the governing mass balance relations. As the irreversible reactions progress, the equilibrium subsystem moves along a reaction path. The partial equilibrium conceptual model can be illustrated by the irreversible dissolution of a rock into an aqueous solution which is in continuous homogeneous equilibrium. As mass from the rock is added to the aqueous solution the solution composition changes, and reactions among the solution species proceed instantaneously to maintain continuous equilibrium.

In practice, EQ6 solves a reaction path problem by solving equations describing a series of sequential partial equilibrium states that are closely spaced along the reaction path. At each step, an aqueous speciation is calculated for the equilibrium subsystem in the manner that EQ3 would calculate a static system model. EQ6 keeps track of the mass transfer between phases that are out of equilibrium and phases that are part of the equilibrium subsystem, including the aqueous phase.

At each step of the reaction path model, the saturation state of the equilibrium aqueous phase is computed with respect to minerals. If the solution is supersaturated with respect to a mineral it can be added to the equilibrium subsystem. A mass action relation for the heterogeneous equilibrium between

the mineral and the aqueous phase is incorporated in the system of equations describing the equilibrium subsystem. The mass of the new mineral is also included in mass conservation relations. The equilibrium distribution of aqueous species is recalculated to include precipitation of some mass of the new mineral at equilibrium with the solution. With progress along the reaction path, this mineral may continue to precipitate or dissolve, but it always remains at equilibrium with the aqueous solution. If the mass of the mineral goes to zero, then it is removed from the equilibrium subsystem by removing the relevant mass action and mass conservation relations. Minerals (glasses, rocks, solutions, etc.) that are part of the disequilibrium subsystem are referred to as primary phases or reactants. Reaction products generated by precipitation from the aqueous phase are referred to as secondary phases.

EQ6 computes fluid-centered models; the equilibrium aqueous phase is the reference frame. Mass transfer is modeled in and out of this aqueous phase. Mass transport equations are not solved by EQ6. Models can also be calculated for stationary open systems. For example, evaporation can be modeled by allowing the reactant assemblage to be a negative mass of H_2O. The EQ6 reaction path describes the progressive increases in concentration of the aqueous solution and precipitation of secondary minerals from it.

An implicit assumption in partial equilibrium reaction path models is that some reactions occur rapidly (indeed instantaneously) such that they can be considered to be in continuous equilibrium. Other reactions fail to go to equilibrium because their rates are relatively slow. The slow reactions control the changes in the system, and are the rate-determining processes. Fortunately for ease of modeling geochemical systems, some reactions like most homogeneous reactions among aqueous species are fast relative to other reactions such as mineral dissolution. Reaction path models computed with EQ6 depend critically on assumptions regarding the relative rates of the various processes included in the model.

If the kinetics of the rate-limiting steps are known (i.e., rate laws and rate constants), then EQ6 can be used to make reaction path calculations as a function of reaction time. The absolute rate of reaction of each reactant (i.e., moles per second) is calculated at each reaction progress step using the kinetic data. Mass is transferred to the equilibrium subsystem from each reactant in proportion to its absolute rate. The elapsed time for the reaction progress step is computed in EQ6 by integrating the rate law over the amount of mass transferred in the step. For example, a simple rate law for the mineral dissolution reaction r is given by

$$\text{rate}_r = \frac{d\xi_r}{dt} = k_r\left(1 - \frac{Q}{K}\right)$$

where ξ denotes the reaction progress variable for reaction r, and k_r is a parameter that depends on surface area, temperature, solution composition, etc. Elapsed time for a reaction progress step is given by

$$\Delta t = \int_{\xi_{r1}}^{\xi_{r2}} \frac{d\xi_r}{rate_r}$$

Variations in k_r and Q over the ξ_{r2} - ξ_{r1} interval are accommodated in EQ6 by fitting a polynomial to the variation in $rate_r$ as a function of ξ_r and performing the integration over this polynomial (e.g., Helgeson and Murphy, 1983).

EQ6 also has the capability to model precipitation (growth) kinetics in a manner similar to dissolution kinetics. Secondary products that are modeled using precipitation kinetics are treated like primary reactants in that they are not part of the equilibrium subsystem. The capability for nonisothermal kinetic modeling is also provided, for which rate parameters are specified functions of temperature.

Aqueous solutions that vaporize rapidly may not maintain continuous equilibrium with gaseous components in an external reservoir, as they do in the buffered systems of the models presented in this report. Modifications were performed on an early version of EQ6 to allow simulations of open-system fractionation of volatile components from a vaporizing aqueous solution. In these computations, gases are continuously removed from the liquid system in relative amounts controlled by gas-liquid equilibrium, and no back reaction of the gas with the liquid is permitted. This limiting model for multicomponent volatilization is equivalent to Rayleigh distillation. Program modifications make use of kinetic coding in EQ6. Rates of volatilization of gas reactants, for example, H_2O and CO_2, are specified to be proportional to their equilibrium fugacities. The proportionality constant is the same for all volatilizing species, hence, the ratios of gas species in each increment of gas removed from the liquid correspond to the ratios in a gas phase at equilibrium with the liquid. For instance the rates of CO_2 and H_2O volatilization can be expressed as

$$\frac{d\xi_{CO_2}}{dt} = k_v f_{CO_2} \quad \text{and} \quad \frac{d\xi_{H_2O}}{dt} = k_v f_{H_2O}$$

where k_v stands for the volatilization constant, and f_{CO_2} and f_{H_2O} denote fugacities of CO_2 and H_2O. Equilibrium, open-system volatilization does not require that k_v remain constant in time. However, k_v must have the same value for all volatilizing species at each increment of reaction progress. In practice, the volatilization constant may be related to the heat flux in the system that provides energy for vaporization. The primary code modification required to enable open-system, equilibrium volatilization is to allow pseudo-kinetic volatilization rates to be proportional to equilibrium fugacities. Examples of the use of a modified version of EQ6 to perform Rayleigh fractionation calculations are given in Pabalan and Murphy (1990) and Murphy (1991).

The basic content of the EQ3/6 database is a tabulation of logarithms of equilibrium constants for reactions between basis species and all other species, including aqueous complexes, minerals, solid solutions, and gases. One basis species represents each chemical component in the database. Equilibrium constants are for pressures of 1 bar at temperatures below 100 °C, and for pressures along the steam saturation curve at temperatures up to 300 °C. The database contains over 1,700 species covering nearly all of the periodic table including many radioelements. Data come from over 100 references which are

carefully noted in the database. Many of the data are estimated. Notably, the composite database includes the well reviewed uranium species database recently compiled by the Nuclear Energy Agency (Grenthe et al., 1992).

Much of the data in the composite database comes from SUPCRT, which is a program for calculating standard-state thermodynamic properties of minerals, gases, aqueous species, and reactions to 5 kb and 1,000 °C (Johnson et al., 1992). An alternate database is provided with the EQ3/6 package which contains exclusively SUPCRT data.

Data are provided in DATA0 (and DATA1) for coefficients in the "b dot" extension of the Debye-Huckel equation for activity coefficients for aqueous species. This formulation is generally good for solutions of ionic strength less than 0.5 to 1 molal. Activity coefficients depend on the ionic strength of the solution, which depends on the equilibrium aqueous speciation. Part of the iterative solution of a distribution of species problem is to simultaneously solve equations for activity coefficients and ionic strength, as well as mass conservation, charge conservation, and mass action equations.

Values of log K for each reaction between basis species and all other aqueous species, minerals, and gases are tabulated for 0.01, 25, 60, 100, 150, 200, 250, and 300 °C in the primary database called DATA0. The data processor program EQPT reads these values and fits a polynomial to each set as a function of temperature. The polynomial coefficients are written to a file called DATA1 which is the required input for EQ3 and EQ6. EQPT must be run only when a change is made to the primary database. The equilibrium constants for reactions among species in the database can be modified by a constant value for particular runs using the EQ3 and EQ6 input decks without modification of the database. The fictive CO_2 phase used to buffer CO_2 fugacity as a function of temperature was entered in the database for each run with properties characteristic of the run. Because temperature in the heated repository models increased and then decreased, CO_2 fugacity was not a unique function of temperature throughout the simulation. Each heated repository model was compiled from six sequential segments for which CO_2 fugacity-temperature relations were unique.

REFERENCES - APPENDIX C

Grenthe, I., J. Fuger, R. Konings, R. Lemire, A. Muller, C. Nguyen-Trung, and H. Wanner. 1992. *Chemical Thermodynamics of Uranium.* North-Holland Elsevier, Amsterdam, Holland.

Helgeson, H.C., and W.M. Murphy. 1983. Calculation of mass transfer among minerals and aqueous solutions as a function of time and surface area in geochemical processes. I. Computational approach. *Mathematical Geology* 15: 109–130.

Johnson, J.W., E.H. Oelkers, and H.C. Helgeson. 1992. SUPCRT92: A software package for calculating the standard molal thermodynamic properties of minerals, gases, aqueous species, and reactions form 1 to 5000 bars and 0° to 1000 °C. *Computers & Geoscience* 18: 899–947.

Murphy, W.M. 1991. Geochemical modeling. *Report on Research Activities for Calendar Year 1990.* W.C. Patrick, ed. NUREG/CR-5817. Washington, DC: Nuclear Regulatory Commission: 2-24 to 2-54.

Pabalan, R.T., and W.M. Murphy. 1990. Unsaturated mass transport (geochemistry). *Report on Research Activities for Calendar Year 1990.* W.C. Patrick, ed. NUREG/CR-5817. Washington, DC: Nuclear Regulatory Commission.

Wolery, T.J., and S.A. Daveler. 1992, EQ3/6, *A Software Package for Geochemical Modeling of Aqueous Systems.* UCRL-MA-110772 PT I-IV. Livermore, CA: Lawrence Livermore National Laboratory: 4 volumes.

NRC FORM 335 (2-89) NRCM 1102, 3201, 3202

U.S. NUCLEAR REGULATORY COMMISSION

BIBLIOGRAPHIC DATA SHEET

(See instructions on the reverse)

1. REPORT NUMBER (Assigned by NRC, Add Vol., Supp., Rev., and Addendum Numbers, if any.)

NUREG/CR-6288

2. TITLE AND SUBTITLE

Geochemical Investigations Related to the Yucca Mountain Environment and Potential Nuclear Waste Repository

3. DATE REPORT PUBLISHED

MONTH: November YEAR: 1994

4. FIN OR GRANT NUMBER

B6666

5. AUTHOR(S)

W. M. Murphy, R. T. Pabalan

6. TYPE OF REPORT

Technical

7. PERIOD COVERED *(Inclusive Dates)*

8. PERFORMING ORGANIZATION – NAME AND ADDRESS *(If NRC, provide Division, Office or Region, U.S. Nuclear Regulatory Commission, and mailing address; if contractor, provide name and mailing address.)*

Center for Nuclear Waste Regulatory Analyses
Southwest Research Institute
6220 Culebra Road
San Antonio, TX 78228

9. SPONSORING ORGANIZATION – NAME AND ADDRESS *(If NRC, type "Same as above"; if contractor, provide NRC Division, Office or Region, U.S. Nuclear Regulatory Commission, and mailing address.)*

Division of Regulatory Applications
Office of Nuclear Regulatory Research
U.S. Nuclear Regulatory Commission
Washington, DC 20555-0001

10. SUPPLEMENTARY NOTES

11. ABSTRACT *(200 words or less)*

Research is reported which focused on experimental determinations and theoretical interpretations of fundamental thermodynamic and kinetic properties of minerals and reactions that characterize geochemical processes at the proposed nuclear waste repository site at Yucca Mountain and that could affect the capacity of the site to isolate nuclear waste. Cation exchange equilibria were determined for clinoptilolite and binary solutions of NA^{+} with K^{+}, Ca^{2+}, and Sr^{2+}. Results were interpreted using a Margules solid solution model. Dissolution rate data for analcime can be rationalized by mechanisms which invoke either ultrareactive material or rate dependence on aqueous aluminum. Solubility determinations were interpreted to obtain equilibrium constants for dissolution reactions of analcime and of Na-clinoptilolite. Chemical analytical data indicate that natural groundwaters at Yucca Mountain appear to be at equilibrium with analcime. Employing principles of thermodynamics, reaction kinetics, mass transfer, and mass transport, computational models were developed using EQ3/6 to explore the evolution of the natural geochemical system, and the geochemical processes that are likely to occur under repository conditions.

12. KEY WORDS/DESCRIPTORS *(List words or phrases that will assist researchers in locating the report.)*

geochemistry, Yucca Mountain, clinoptilolite, analcime, ion exchange dissolution kinetics, solubility, reaction-path model, groundwater chemistry, geologic disposal of nuclear waste

13. AVAILABILITY STATEMENT

Unlimited

14. SECURITY CLASSIFICATION

(This Page) Unclassified

(This Report) Unclassified

15. NUMBER OF PAGES

16. PRICE